Characterization and modeling of Carbide-Free Bainite transformations along isothermal and anisothermal heat treatments

Cécile Rampelberg

UNIVERSITÉ DE LORRAINE

Ecole doctorale C2MP Lorraine

Thèse

Présentée et soutenue publiquement le 20 Octobre 2022

pour l'obtention du titre de

DOCTEUR DE l'UNIVERSITE DE LORRAINE

Mention : Sciences des Matériaux

par **Cécile Rampelberg**

Characterization and modeling of Carbide-Free Bainite transformations along isothermal and anisothermal heat treatments

Membres du jury :

Rapporteurs :	**Francisca Garcia Caballero**	**Directrice de recherche, CENIM-CSIC, Madrid, Espagne**
	Mohamed Gouné	**Professeur, Université de Bordeaux, France**
Présidente de jury :	**Sabine Denis**	**Professeure, Institut Jean Lamour, Nancy, France**
Examinateur :	**Hugo Van Landeghem**	**Chargé de recherche du CNRS, SIMAP, Grenoble, France**
Directeur de thèse :	**Sébastien Allain**	**Professeur, Institut Jean Lamour, Nancy, France**
Co-directeur de thèse :	**Julien Da Costa Teixeira**	**Chargé de recherche du CNRS, Institut Jean Lamour, Nancy, France**
Membres invités :	**Guillaume Geandier**	**Chargé de recherche du CNRS, Institut Jean Lamour, Nancy, France**
	Thomas Sourmail	**Docteur-Ingénieur, Ascometal (CREAS), Hagondange, France**

Remerciements

Je tiens à remercier mes encadrants de thèse : Sébastien Allain, Julien Teixeira , Guillaume Geandier et Thomas Sourmail. Tout d'abord je remercie mon directeur de thèse Sébastien Allain pour ses précieux conseils, son aide, le partage de toutes ses connaissances et son investissement tout au long de ma thèse. Je tiens ensuite à remercier mon co-directeur Julien Teixeira pour son aide pour la partie modélisation. Je remercie mon co-encadrant de thèse Guillaume Geandier pour son aide et le temps consacrait pour la partie synchrotron. Merci « Guillauuuuume » pour ses moments de partage passé au synchrotron et pour m'avoir fait confiance pour participer à de nombreuses sessions. Je voudrais remercier mon encadrant industriel Thomas Sourmail pour la confiance qu'il m'a faite pour ce beau projet ainsi que pour son investissement dans le projet.

Je voudrais remercier les membres du jury en commençant par les rapporteurs Francisca Garcia Caballero et un merci particulier à Mohamed Gouné. Je les remercie pour leurs commentaires fournis dans leurs rapports sur le manuscrit de thèse, ainsi que pour les discussions très intéressantes que nous avons pu avoir lors de la soutenance. Je tiens à remercier Hugo Van Landeghem d'avoir accepté d'être examinateur de la thèse. Merci pour les discussions riches que nous avons pu avoir lors de la soutenance et je tiens à le remercier d'avoir lu avec attention le manuscrit et fait des remarques constructives. Un grand merci à Sabine Denis de m'avoir fait l'honneur d'accepter de présider mon jury de thèse, merci pour tous vos conseils, discussions très intéressantes et riches que nous avons pu avoir lors de la soutenance de thèse. Merci pour l'intérêt que vous avez portez à mon sujet de thèse depuis son commencement. Merci pour le partage de votre savoir sur les transformations de phase et bien d'autres sujets tout au long de ma thèse.

Je tiens ensuite à remercier toutes les personnes qui m'ont aidé et suivi tout au long de ma thèse (un merci au personnel de DESY). Un merci à mes collègues d'Ascometal pour leur aide, leur soutien et leur disponibilité. Grâce à mes nombreuses venues j'ai pu grâce à eux découvrir le monde du travail en industrie et développer mon sens du travail au sein d'un groupe. Merci à mes collègues qui sont devenus de vrai amis (ils se reconnaîtront).

Je tiens à remercier l'ensemble du personnel de l'IJL qui ont pu contribuer de près ou de loin à cette thèse. En particulier les membres de l'équipe et du département. Un merci à l'atelier mécanique, le CC3M un merci particulier à Erwan Etienne pour son aide et sa bonne humeur, Philippe Masschelein et Bertrand Lenoir pour les traitements thermiques, Jean-Marc Fiorani pour les discussions très intéressantes sur la thermodynamique et un grand merci à Florimonde Lebel de l'équipe pour le temps passé avec moi au MEB à l'IJL. Je tiens aussi à remercier les stagiaires qui ont pu contribuer à l'avancement du projet général : Fanta Kaba, Clément Lintilhac, Mahel Voulhoux et Nicolas Liouville.

Un merci à mes membres de comité de suivi Alain Jardy et Nathalie Gey pour avoir suivi l'avancement de mes travaux pendant l'intégralité de la thèse. Je tiens aussi à remercier les membres de l'école doctorale Dominique Daloz, Christine Sartori et Juliette Barbat.

Enfin, un grand merci à mes ami(e)s et co-bureau : Steve Gaudez, Rafael Paiotti, Hélène Quehen et Widad Ayadh avec qui j'ai pu passer beaucoup de temps, partager des bons (et mauvais) moments, merci pour leur soutien. Je remercie aussi Juan Macchi, Clélia Couchet, Madhumanti Mandal, Mathias Lamari, Thomas Girardet et Arthur Tausch pour leur aide, leur bonne humeur et les bons moments passés ensemble. Je tiens à remercier aussi mes ami(e)s de l'IJL avec qui j'ai pu passer de bons moments tout au long de thèse : Lucile, Litan, Nazim, Ivan, Marc, Ilia, Valentin, Gatien, Miguel, Italo, Ahmadou, Julien, Savya, Thomas, Nicolas, Lucie, Victor, Félix, Arthur, Azise, Sébastien, Loris, Kilian, Adèle, Clovis, Pavel, Solenne, Jérémy, Manoj, Fares, Harshad, Sharma, Bassem, et ceux que j'ai oublié, last but not least Rabeh.

Je tiens à remercier ma famille de cœur pour leur soutien, ainsi que ma Mamouc Rose et ma sœur Mathilde alias Janine qui m'ont épaulé, soutenu, encouragé et supporté tout au long de ma vie.

Thank you God for giving me the strength to surpass myself to get where I am today.

Introduction

Après le béton, l'acier est le matériau le plus utilisé pour les applications d'ingénierie, loin devant tous les autres métaux. Sa production mondiale est actuellement estimée à environ 1,8 milliards de tonnes et atteindra 2,8 milliards de tonnes d'ici 2050. Cette production nécessite une forte consommation d'énergie et entraîne l'émission de grandes quantités de CO_2. La production d'acier est à elle seule responsable de 33 % des émissions industrielles mondiales de gaz à effet de serre. Par conséquent, toute amélioration dans les méthodes de fabrication, d'utilisation ou de recyclage de l'acier aura des conséquences importantes sur son empreinte environnementale [1]. A sa propre échelle, ce travail de thèse contribuera à cet objectif, en participant à l'amélioration de la connaissance des aciers, notamment en permettant une maîtrise fine des procédés d'un produit déjà industriel.

La métallurgie des aciers au carbone offre une fascinante diversité de transformations de phases. Elle permet de fabriquer un très large spectre de microstructures multiphasées et donc d'atteindre des compromis mécaniques très variés entre résistance, ductilité et ténacité. Parmi les différentes possibilités, les aciers bainitiques ont suscité l'intérêt des producteurs d'acier. Ils sont aujourd'hui largement utilisés dans de nombreuses applications industrielles comme les pièces forgées dans l'automobile, les pièces embouties pour les liaisons au sol (bras de suspension) ou les pièces laminées pour les applications structurelles (rails). Ces dernières années, parmi les différents types d'aciers bainitiques, il est apparu que les microstructures Bainitique Sans Carbure (BSC) apportent des performances supérieures et sont de plus en plus recherchés.

Lorsqu'elles sont obtenues après des traitements isothermes (comme c'est le cas pour le recuit continu de produits plats), ces microstructures BSC présentent en effet de nombreux avantages : elles sont le plus souvent lamellaires, avec des tailles caractéristiques sub-micrométriques conduisant à une bonne résistance mécanique, une bonne ductilité et une bonne résistance à la fatigue [2]–[4]. De plus, ces microstructures contiennent une fraction élevée d'austénite résiduelle instable qui se transforme lors d'une sollicitation mécanique ultérieure à température ambiante et conduit à un éventuel effet TRIP (*TRansformation Induced Plasticity*) [2], [5] qui facilite les opérations d'emboutissage. Ce dernier processus d'écrouissage peut être bénéfique pour la résistance, la ductilité, la performance en fatigue et la résistance à l'endommagement de l'acier. Les mêmes avantages sont observés dans le cas des aciers obtenus par refroidissement continu (cas des opérations de forgeage ou de laminage) malgré une plus grande dispersion en taille et en morphologie des constituants microstructuraux [6], [7]. En comparaison avec la transformation BSC en condition isotherme, celle lors du refroidissement continu a reçu relativement peu d'attention.

C'est la raison pour laquelle ce travail de thèse a été financé par Ascometal (producteur d'acier, membre du groupe Swiss Steel). Il a été réalisé en collaboration entre l'Institut Jean Lamour (équipe Microstructures & Contraintes) basé à Nancy (France) et le CREAS, le centre de recherche d'Ascometal basé à Hagondange (France). Ce travail vise à mieux comprendre les mécanismes de transformation de phase bainitique sans carbure d'un acier industriel au cours d'un processus de forgeage, donc en conditions anisothermes.

Chapitre I

Le Chapitre I est essentiellement bibliographique et reprend quelques informations générales sur les bainites et leurs mécanismes de transformation après traitements isothermes, en nous limitant au cas des aciers bas carbone. Le domaine des aciers bainitiques est étudié depuis longtemps et de nombreux travaux de synthèse ont déjà été réalisés [2]. Ce Chapitre n'est donc pas destiné à être exhaustif, mais cherche à introduire les concepts de base et essentiels pour comprendre les transformation bainitiques et BSC qui sont au centre de ce travail. Nous retiendrons essentiellement que :

- Les microstructures de bainites formées sont complexes, ce qui peut expliquer le nombre relativement élevé de classifications possibles. Deux grands types de classifications sont en compétition ; celles basées sur les phases en présence et leurs distributions, et celles basées sur les microtextures.
- Une controverse persiste sur la nature fondamentale de la transformation bainitique et ses caractéristiques principales, comme le phénomène de transformation incomplète. Deux Ecoles de pensée proposent des explications concurrentes basées soit sur un mécanisme diffusif (comme une prolongation du domaine de la ferrite de Widmanstätten), soit sur des mécanismes sans diffusion (avec une grande proximité avec la martensite).
- Les transformations BSC sont très sensibles à la température. Pour les transformations en conditions isothermes, plus la température est basse, plus les microstructures BSC sont fines. Le phénomène de transformation incomplète impose aussi que l'austénite retenue sera plus enrichie en carbone. En conséquence, à basse température, la fraction d'austénite est faible mais l'austénite est très stable. Le comportement de l'acier ressemble alors à celui des aciers martensitiques revenus. À haute température, la fraction d'austénite est importante mais elle peut être instable, ce qui entraîne sa transformation martensitique partielle pendant le refroidissement final. Le comportement de l'acier ressemble alors à celui des aciers Dual-Phase ferrito-martensitique. Un optimum de propriétés mécanique existe entre la fraction et la stabilité de l'austénite retenue lorsqu'un effet TRIP efficace peut être obtenu.
- L'utilisation de traitements étagés (multistep) permet une première approche des transformations au refroidissement continu, mettant en évidence de nombreuses nouvelles questions par rapport aux expériences isothermes. Les transformations incomplètes (conditions de stasis), les tailles des microstructures, leurs microtextures et leurs contraintes internes dépendent toutes des températures de transformation. L'évolution de la température pendant la transformation affecte donc simultanément tous ces paramètres et permet d'atteindre des microstructures constituées vraisemblablement de plusieurs types de structures bainitiques.
- Pour les transformations en refroidissement continu, la vitesse de refroidissement a une forte influence sur la cinétique de transformation bainitique et les microstructures qui en résultent. Il reste aussi de nombreuses questions ouvertes sur les mécanismes de transformation (stades, cinétique, stasis, enrichissement, bilan carbone).

Chapitre II

Le matériau étudié et les méthodes de caractérisation associées sont présentés dans le Chapitre II. Dans ce Chapitre, nous décrirons d'abord comment l'alliage étudié a été produit et fabriqué par Ascometal, le partenaire industriel du projet, avant les expériences menées pendant la thèse. Puis, la procédure de Diffraction des Rayons X à Haute Energie (DRXHE) qui a été utilisée pour caractériser in situ les transformations de phase le long de différents traitements thermiques : maintiens isothermes, traitements étagés (paliers isothermes successifs) et refroidissements continus. Ces derniers schémas ont été conçus pour imiter les traitements thermiques rencontrés lors des opérations de forgeage industriel. La configuration expérimentale pour les expériences DRXHE sera détaillée ainsi que les procédures de dépouillement des diffractogrammes.
Dans la dernière partie du Chapitre, les techniques utilisées pour caractériser les microstructures à température ambiante seront présentées. Les microstructures formées après différents traitements thermiques lors des expériences de DRXHE seront analysées post mortem à l'aide de la microscopie électronique à balayage (MEB) couplée à la diffraction des électrons rétrodiffusés (EBSD) afin de mieux comprendre l'enchevêtrement complexe et progressif de ces microstructures multiphasées.

Des tests de dureté supplémentaires ont aussi été effectués pour évaluer les propriétés mécaniques de base des microstructures produites. Il est important pour le partenaire industriel d'identifier la sensibilité de la nuance aux vitesses de refroidissement et la qualité mécanique des microstructures obtenues après des traitements thermiques complexes.

Chapitre III

Dans le Chapitre III, nous présentons les résultats des expériences in situ réalisées par DRXHE pour étudier les transformations des BSC lors de traitements thermiques modèles ou représentatifs d'opérations industrielles. Ce type d'expérience permet d'acquérir les cinétiques précises de transformation des différentes phases issues de la décomposition de l'austénite mais aussi d'obtenir des connaissances importantes sur les compositions respectives des phases.

Transformations en conditions isothermes

La Figure 1 a) montre l'évolution de la fraction de bainite en fonction du temps lors de maintiens isothermes à différentes températures (300 °C, 350 °C, 400 °C, 450 °C et 475 °C). Les cinétiques de transformation obtenues lors des maintiens isothermes sont comparables à celles obtenues sur des aciers similaires étudiés dans la littérature, c'est-à-dire que plus la température est basse, plus la transformation est rapide et plus la fraction d'austénite en fin de maintien isotherme est élevée. Pour les transformations en dessous de M_S (ici la transformation à 300 °C), la transformation dépend de l'historique et des transformations précédentes (martensite).

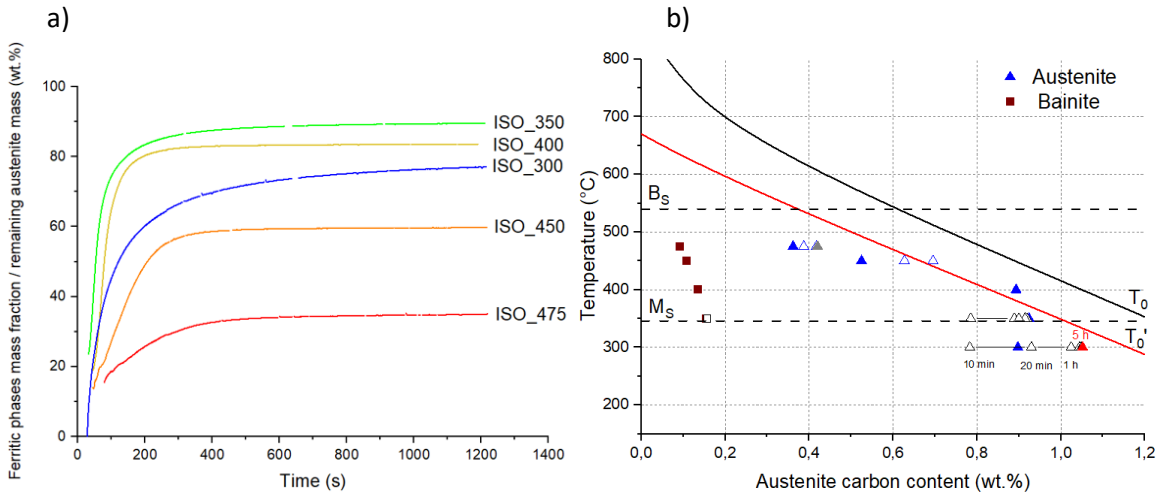

Figure 1 : a) Fraction massique normalisée des phases ferritiques en fonction du temps le long de maintiens isothermes (avec correction de la cinétique de transformation pour l'essai ISO_300 car la transformation bainitique se produit après une transformation martensitique partielle). b) Teneur en carbone dans la bainite (carrés) et dans l'austénite résiduelle pour des maintiens isothermes de 1200 s (triangles bleus) et des maintiens isothermes de 5 h (triangles vide) comparés aux lignes T_0 et T_0'.

Les compositions des phases ont été suivies de manière in situ grâce à la détermination du paramètre de maille de l'austénite et de la tétragonalité de la maille de la bainite. L'absence de dédoublement ou d'asymétrie des pics de la phase bainitique peut soumettre cette dernière détermination à controverse. Cependant, les mêmes conclusions sur les distributions de carbone auraient pu être tirées sans cette détermination par un simple bilan matière. Un de nos résultats majeurs est d'avoir prouvé sans conteste que la ferrite bainitique est toujours sursaturée en carbone, même pour des transformations à haute température. Nos expériences ne nous permettent cependant pas de préjuger de la distribution spatiale de ces atomes (solution solide, ségrégation sur les défauts). Ce résultat est essentiel pour le développement du modèle du Chapitre V. En effet, les atomes de carbone piégés dans la bainite ne sont pas disponibles pour l'enrichissement en austénite et limitent donc à leur tour la fraction possible d'austénite résiduelle. Les teneurs en carbone de la bainite mesurées en fonction de la température de transformation sont représentées par des carrés marron sur la Figure 1 b).

A la fin des maintiens isothermes, un fort enrichissement en carbone est aussi observé dans l'austénite. Les teneur en carbone de l'austénite à la fin du maintien (triangles sur la Figure 1 b)) ont été comparées à la ligne du critère d'arrêt T_0'. Les valeurs expérimentales sont proches de la ligne T_0', cependant, ce critère n'est pas respecté pour les transformations à haute température.

Des bilans carbone précis résolus dans le temps entre les phases ont été établis pour chaque traitement. La précision et la robustesse de notre approche nous ont permis d'identifier les conditions dans lesquelles une partie du carbone est également piégée sous forme de carbures de transition (à basse température de transformation). Ce dernier résultat a été confirmé par une analyse fine des diffractogrammes.

Transformation en condition de refroidissement étagé

Pour les expériences constituées de plusieurs maintiens isothermes, nous avons montré que la transformation bainitique peut redémarrer à basse température si la transformation n'est pas avancée à haute température. Le cas échéant, même si la transformation redémarre, la cinétique est également ralentie. La transformation bainitique ne respecte donc pas la règle d'additivité des transformations diffusives. Les conditions de stasis des transformations sont donc affectées par l'historique de la transformation. Un bilan carbone précis a été aussi proposé pour les expériences à deux et trois maintiens isothermes.

Transformation en condition de refroidissement continu

Les transformations bainitiques en refroidissement continu ont été étudiées pour trois vitesses de refroidissement : 0,1 °C/s, 0,3 °C/s et 0,5 °C/s. Nous avons dû développer une méthodologie originale pour déterminer de l'enrichissement en carbone de l'austénite basée une modélisation du coefficient de dilatation thermique de la maille. Cette méthode a été validée sur une expérience conçue pour imiter une condition de refroidissement continu à 0,3 °C/s, consistant en une succession de 7 courts paliers isothermes étagés. Cette nouvelle méthode est considérée comme plus fiable que celles précédemment suivies dans la littérature, basées sur la seule tétragonalité de la bainite.

Conformément à la littérature, les transformations bainitiques étudiées s'initient à haute températures (sur le dessus du nez bainitique) mais n'atteignent jamais de stasis stricto sensu. Les enrichissements moyens mesurés restent très en dessous du critère d'arrêt T_0' quel que soit la vitesse. Les différentes étapes de transformation décrites par Reisinger et al. [8] pendant les traitements de refroidissement continus ont également été observées, même si nous ne pouvons souscrire à leurs explications. Notre analyse de l'asymétrie du pic de diffraction de l'austénite soutient le fait que le carbone est réparti de manière homogène dans l'austénite au tout début de la transformation, mais le rebond cinétique observé (2^{nd} onset) ne peut pas être expliqué par le processus d'homogénéisation.

L'effet de la vitesse de refroidissement sur la microstructure finale conduit aussi à un résultat paradoxal. Plus le refroidissement est rapide, plus l'austénite est stabilisée. Ce résultat s'explique à la lumière des cinétiques de transformation et d'enrichissement ; notamment par l'effet inhibiteur des transformations à haute température observées aux faibles vitesses sur les cinétiques à basse température.

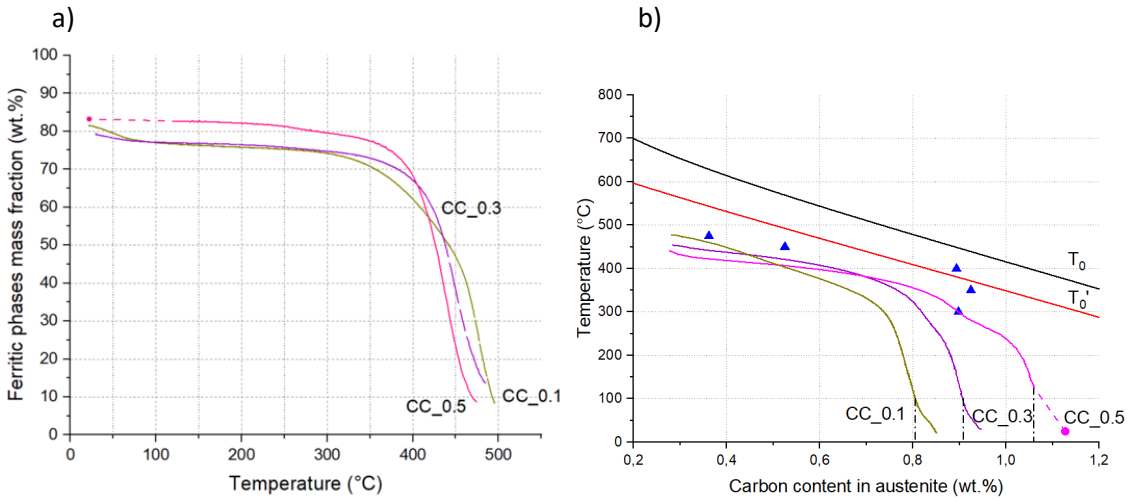

Figure 2 : a) Fraction massique des phases ferritiques en fonction de la température le long des expériences CC_0.1, CC_0.3 et CC_0.5, b) Évolution de la teneur en carbone de l'austénite pour les expériences de refroidissement continu par rapport aux lignes T_0 et T_0' et de la teneur en carbone dans l'austénite résiduelle pour les traitements isothermes (triangles bleus) présentés dans la Figure 1 b).

Chapitre IV

L'utilisation de la DRXHE ne permet cependant pas d'approfondir l'organisation hiérarchique et microtexturale particulière de ces microstructures BSC, ainsi que mesurer la taille respective des composants. C'est pourquoi les microstructures formées après les différents traitements thermiques ont été analysées de manière post mortem à l'aide de la Microscopie Electronique à Balayage (MEB) couplée à la diffraction des électrons rétrodiffusés (ESBD), techniques considérées comme la référence par de nombreux auteurs [9]–[14].

Transformations en conditions isothermes

Les microstructures obtenues après transformations à basses températures (à 300 °C, 350 °C et 400 °C) montrent une forte densité de joints de fortes désorientations (HAB : High Angle Boundaries) qui délimitent différents variants auto-accommodant à l'intérieur des paquets bainitiques. Ce type de microstructure peut être classé comme bainite inférieure en utilisant la classification microtexturale de Zajac [15].

Les microstructures obtenues après transformation à haute température (à 450 °C et 475 °C) montrent par contre une faible densité de HAB, mais une forte proportion de joints de faibles désorientations (LAB : Low Angle Boundaries), avec un seul variant par paquet bainitique. Ces microstructures peuvent être classées comme bainites supérieures en utilisant la classification de Zajac, même si elles contiennent une forte fraction d' îlots MA (Martensite-Austenite) qui perturbent cette analyse.

La Figure 3 montre les cartographies de figure de pole inverse de la phase ferritique réalisée par EBSD obtenues lors d'essais isothermes à 350 °C (Figure 3 a)) et 475°C (Figure 3 b)) respectivement.

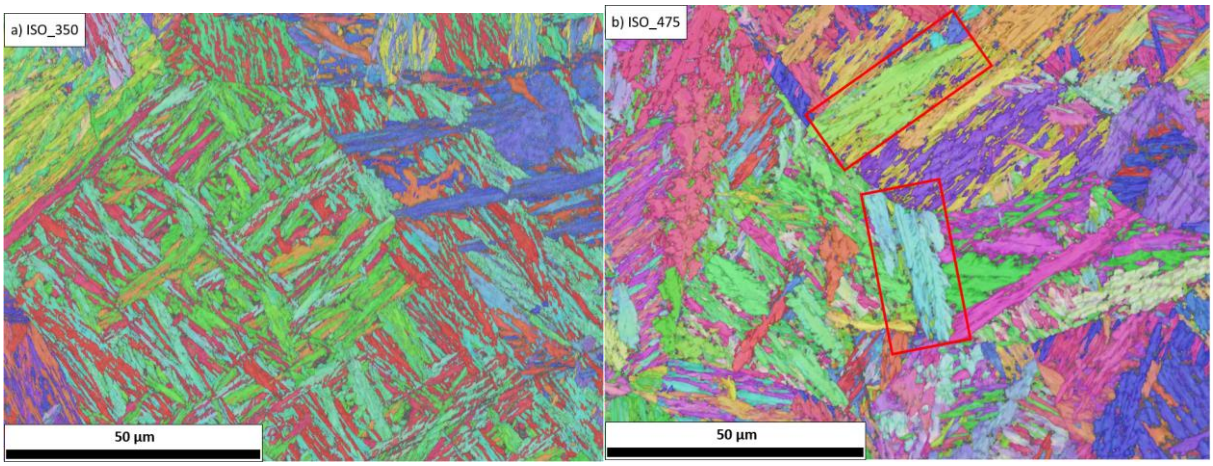

Figure 3 : Cartographie EBSD de l'indice de qualité et l'IPF des phases ferritiques après traitements isothermes à a) 350 °C et b) 475 °C. Les cadres rouges permettent d'identifier des paquets contenant un seul variant bainitique.

La taille des lattes bainitiques augmente avec la température de transformation en conditions isothermes, comme on peut le voir qualitativement sur la Figure 3. Cependant, l'évolution observée n'est pas aussi linéaire que le montre de Hell [14]. Nos résultats ont été comparés à des modèles de la littérature. La difficulté est apparue que les objets décrits dans la littérature sont souvent différents dans la pratique (épaisseur/volume, lattes/sous-unités). Ce travail nous a permis de montrer qu'il y a probablement un facteur 3 entre la taille des lattes mesurées et celle des sous-unités prédites.

En conséquence, un large éventail de microstructures peut être obtenu en fonction de la température en conditions isothermes, en termes de phases (carbure, bainite, austénite, martensite fraîche ou revenue), de composition mais aussi de tailles et de microtextures.

Transformation en condition de refroidissement étagé ou continu

Par comparaison, les microstructures obtenues après des traitements de refroidissement continu montrent une bien plus grande variabilité de tailles et de microtextures que celles obtenues après des traitements isothermes sur un même échantillon. Leurs tailles moyennes sont comparables aux bainites formées à des températures de transformation élevées et elles peuvent être classées comme bainite supérieure du point de vue cristallographique, même si elles contiennent une fraction significative de domaines fortement désorientés. Les classifications actuelles pour ces dernières microstructures formées progressivement à différentes températures montrent donc leurs limites (en particulier celle de Zajac). La Figure 4 montre par exemple une cartographie de figure de pole inverse de la phase ferritique réalisée par EBSD obtenue après un refroidissement continu à une vitesse de 0.3 °C/s.

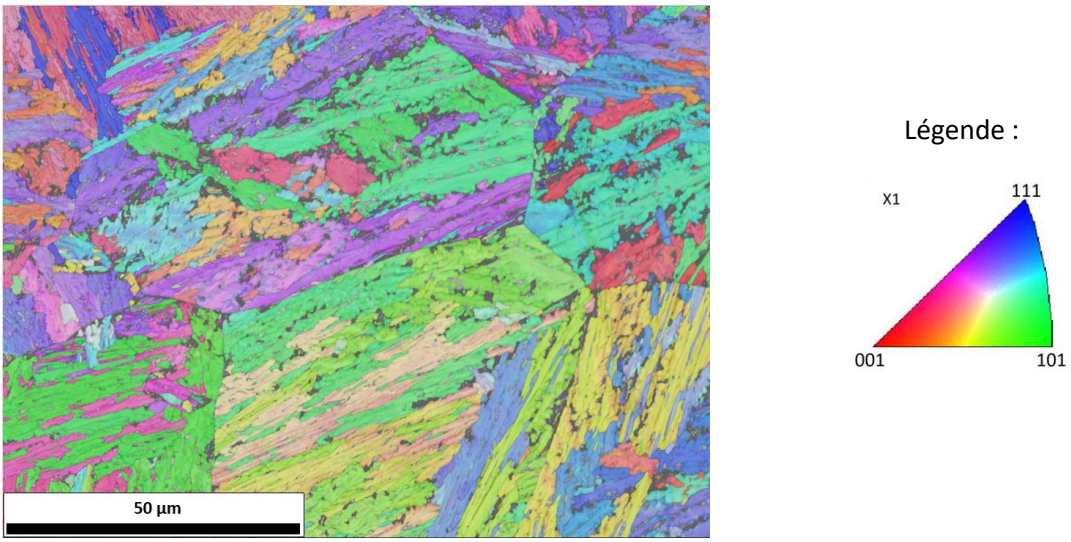

Figure 4 : Cartographie EBSD de l'indice de qualité et l'IPF des phases ferritiques après expérience avec refroidissement continu avec une vitesse de 0.3 °C/s.

Quelles que soit les conditions d'élaboration, les microstructures BSC sont fortement enchevêtrées confirmant une germination intergranulaire des paquets (pas seulement aux joints de grains austénitiques). Cette observation pourrait être le signe d'un processus autocatalytique pour la transformation de la bainite, processus autocatalytique est une composante importante du modèle développé dans le Chapitre V.

Propriétés mécaniques des BSC

La dureté des microstructures a été caractérisée, comme une première approche de leur propriétés mécaniques. Celle des échantillons produits en condition isotherme suit une évolution parabolique en fonction de la température, comme suggéré par Sugimoto et al. [16]. La dureté minimale est obtenue à 400°C environ. Le comportement en dessous de cette température est principalement contrôlé par un effet de taille de la bainite en l'absence de martensite fraîche (l'austénite résiduelle est stable). L'augmentation de la dureté aux plus hautes température s'explique par une augmentation de la fraction d'îlots MA et donc par une durcissement composite (austénite instable).

La dureté obtenue après un refroidissement continu à 0.3°C/s est plus faible qu'après un traitement isotherme à 400°C. Ce paradoxe s'explique car la microstructure en refroidissement continu est plus grossière et possède une austénite stable. En conséquence, elle bénéficie moins des mécanismes de durcissement discutés précédemment.

Chapitre V

Dans ce Chapitre, la cinétique de transformation de la bainite a été simulée en utilisant un modèle de la littérature, celui de Van Bohemen 2019 [17]. Ce modèle est basé sur une approche « sans diffusion » de la bainite, qui suppose que les lattes de ferrite bainitique se forment avec un mécanisme displacif et que leur taux de germination est le facteur limitant contrôlant la cinétique de transformation bainitique. L'originalité de ce modèle est d'introduire les effets de la stabilisation mécanique de l'austénite sur les dernières étapes de la transformation bainitique.

L'une des principales caractéristiques des expériences présentées au chapitre III est le phénomène de stasis observés lors des traitements de refroidissement isothermes. Le premier objectif de ce travail de simulation a été d'utiliser le modèle de [17] pour évaluer deux origines possibles de cette stagnation de la transformation de phase : la stabilisation mécanique de l'austénite, mais aussi son enrichissement par le carbone. Cette dernière origine n'est pas explicitement abordée dans la référence originale, où la plupart des aciers considérés ont une faible teneur en Si (donc propice à la précipitation des carbures). Toutefois, toutes les données nécessaires sont fournies pour modifier les paramètres du modèle en fonction de la composition en carbone de l'austénite. Outre l'étude de l'origine du stasis, l'objectif plus pratique de ce travail de simulation était également d'évaluer la capacité du modèle à prédire la cinétique de transformation bainite lors des traitements isothermes et de refroidissement continu.

On a constaté que les stabilisations mécaniques et chimiques ont un effet important et devraient être prises en compte afin d'obtenir une prévision précise de la cinétique et le stasis. Négliger la stabilisation mécanique entraîne des écarts importants. En ce qui concerne la stabilisation chimique, une connaissance précise de l'évolution de la composition du carbone en austénite est nécessaire. À une température de transformation plus basse, la cinétique de partitionnement du carbone tend à être plus lente que la cinétique de transformation globale de la bainite. Si cela est négligé, l'austénite se stabilise trop tôt par le carbone, et le modèle a alors tendance à sous-estimer la cinétique de transformation bainite et à prédire le stasis trop tôt. La solution provisoire que nous avons trouvée a été d'imposer dans les simulations l'évolution de la teneur en carbone austénitique dans l'austénite que nous avons mesurée par DRXHE in situ.

La Figure 5 a) montre ainsi les cinétiques de transformation bainitiques simulées (lignes continues) comparées aux cinétiques de transformation bainitiques obtenues expérimentalement par DRXHE (points) dans le cas du modèle ne prenant pas en compte la partition expérimentale du carbone. La Figure 5 b) montre la teneur en carbone de l'austénite en fin de maintien obtenues expérimentalement (carrés de couleurs) et par la modélisation (carrés noirs), ainsi que les courbes T_0 et T_0' (à 400 et 670 J/mol). Cette version du modèle arrête la transformation bainitique en accord avec le critère T_0' [2], avec une énergie élastique de 670 J/mol (au lieu de la valeur plus habituelle de 400 J/mol). Dans cette étude, nous avons délibérément choisi de ne pas rechercher un ajustement systématique des résultats expérimentaux au profit de la compréhension des effets relatifs des paramètres. C'est le cas, par exemple, du facteur autocatalytique, qui a été maintenu constant en fonction de la température.

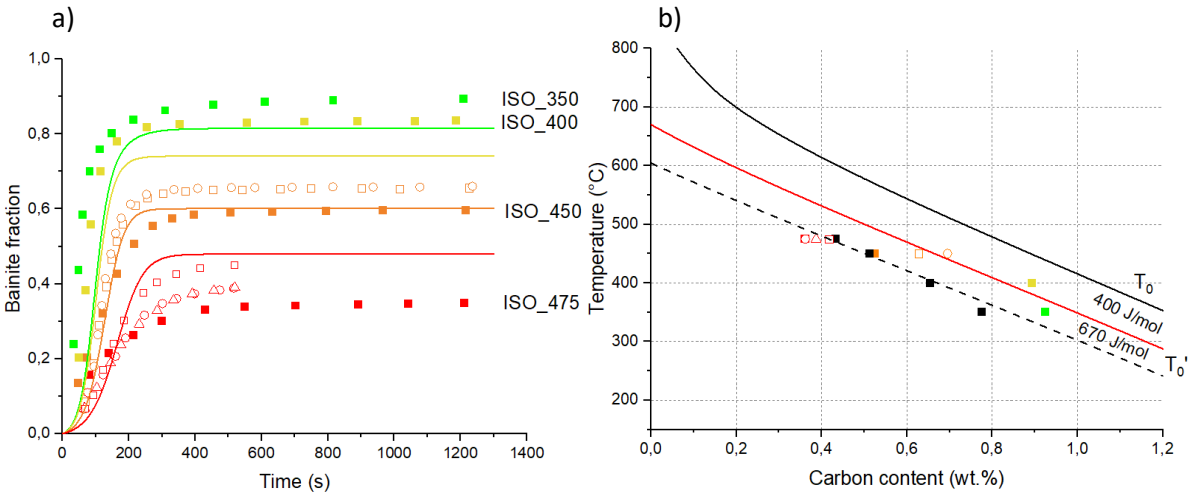

Figure 5 : a) Cinétique de transformation de la bainite obtenues par simulation (lignes continues) et les expériences DRXHE (points), lors de la transformation isotherme à 350 °C (vert), 400 °C (jaune), 450 °C (orange), 475 °C (rouge). b) Teneur en carbone dans l'austénite à la fin des maintiens isothermes, pour chaque température de transformation, selon l'expérience (carrés de couleur) ou la simulation (carrés noirs), ainsi que la courbe T_0 et les courbes T_0' avec une énergie de déformation élastique dans la ferrite de 400 J/mol ou 670 J/mol.

Une fois calibré sur des expériences isothermes, il a été possible d'utiliser le modèle pour simuler les cinétiques de la bainite pour des transformations anisothermes. Le modèle reproduit la tendance générale observée sans aucun ajustement supplémentaire. Cependant, il n'est pas capable de simuler correctement la sensibilité de la transformation aux vitesses de refroidissement. Nos expériences in situ révèlent en effet une tendance inattendue dans la gamme étudiée; plus le taux de refroidissement est élevé, plus la fraction d'austénite résiduelle stabilisée est importante. Nos expériences de traitement étagés du Chapitre III ont prouvé que la transformation bainitique est inhibée si une grande fraction de bainite est formée à haute température. Les mécanismes d'inhibition restent à établir et à modéliser. Ils pourraient être liés à des distributions locale du carbone dans l'austénite, aux processus de germination (effet de taille) ou à un processus de stabilisation mécanique. C'est la raison pour laquelle la version actuelle du modèle n'est pas capable jusqu'à présent de modéliser encore l'effet d'héritage propre à cette transformation.

Perspectives

Ce travail a donc permis d'identifier des pistes de travaux futurs :

- Approfondir les raisons pour lesquelles le critère de stasis conventionnel (T_0') n'est pas respecté à des températures de transformation élevées (sauf en modifiant l'énergie élastique). Ce comportement a également été observé dans d'autres études comme [18] mais reste mal compris. Cela pourrait signifier que la théorie diffusive (ou un mécanisme de *solute drag*) s'applique mieux à de telles températures, en gardant toutefois à l'esprit que nous avons clairement établi que le bainite est encore sursaturée en carbone à de telles températures. D'autres modèles basés sur des approches diffusives pourraient être testés dans ce cadre.
- Comprendre l'origine du mécanisme d'héritage dans le refroidissement continu est certainement l'un des défis les plus importants de l'avenir de cette étude. Différentes hypothèses ont été discutées dans les Chapitres III et V et devraient être évaluées de manière critique, soit par le biais d'expériences spécialisées (essais interrompus, effet de la taille de grains austénitique, …) et de méthodes de caractérisation avancées (EELS) ou en améliorant le modèle par la mise en œuvre d'effets supplémentaires de taille ou de stabilisation mécanique.
- Nous avons pu montrer que la ferrite bainitique reste sursaturée en carbone quel que soit le traitement (observé par d'autres auteurs [18]–[21]) et avons pu établir des bilans carbone parfaitement cohérents. Cependant, les pics de diffraction des phases ferritiques ne sont pas asymétriques, ce qui pose une question : La bainite est-elle vraiment quadratique ? Il n'est pas non plus certain que nos détermination englobe également les ségrégations sur les défauts [19], comme les dislocations ou les joints bainitiques [22]–[25]. Certaines expériences de tomographie par sonde atomique 3D (APT 3D) nous auraient permis d'avoir une idée plus précise de la distribution du carbone, comme l'ont fait [26]–[28].
- Notre méthode DRXHE permet de suivre la composition moyenne du carbone dans l'austénite mais montre ses limites lorsqu'il s'agit de la composition chimique locale. Nous avons mis en évidence que l'asymétrie des pics de diffraction de l'austénite révèle probablement une distribution hétérogène du carbone dans cette dernière. Les mesures des hétérogénéités de carbone à l'échelle du micron dans les îlots austénitiques (par exemple par la cartographie EELS en MET) pourrait apporter des informations précieuses pour mieux décrire l'hétérogénéité à une échelle statistiquement pertinente et pourrait aider à améliorer les modèles introduisant des échelles supplémentaires (distance de diffusion du carbone dans l'austénite par exemple).
- Dans le chapitre IV, nous avons montré qu'il est très difficile d'identifier les différentes phases ferritiques en présence (bainite/martensite), sur les cartographies EBSD. Certains auteurs tels que [13], [29], [30] s'intéressent à l'étude des structures bimodales mais leur méthodologie n'a pas été déployée dans le cadre de cette thèse.
- Un travail de normalisation devrait être conduit pour homogénéiser les pratiques de mesure de taille des bainites, en particulier les objets étudiés (épaisseur/volume, lattes/sous-unités) [31]–[35], afin de clarifier les conclusions de la littérature. Cette question est d'autant plus importante que la taille des éléments constituant les microstructures bainitiques est un élément clé des modèles.

Références :

[1] D. Raabe, C. C. Tasan, and E. A. Olivetti, “Strategies for improving the sustainability of structural metals,” *Nature*, vol. 575, no. 7781, pp. 64–74, 2019.

[2] H. K. D. H. Bhadeshia, *Bainite in steels: transformations, microstructure and properties*, 2. ed. London: IOM Communications, 2001.

[3] J. Tian, G. Xu, Z. Jiang, M. Zhou, H. Hu, and Q. Yuan, “Transformation Behavior of Bainite during Two-step Isothermal Process in an Ultrafine Bainite Steel,” *ISIJ Int.*, vol. 58, no. 10, pp. 1875–1882, Oct. 2018, doi: 10.2355/isijinternational.ISIJINT-2018-187.

[4] K. Sugimoto, A. Kanda, R. Kikuchi, S. Hashimoto, T. Kashima, and S. Ikeda, “Ductility and Formability of Newly Developed High Strength Low Alloy TRIP-aided Sheet Steels with Annealed Martensite Matrix.,” *ISIJ Int.*, vol. 42, no. 8, pp. 910–915, 2002, doi: 10.2355/isijinternational.42.910.

[5] A. Perlade, O. Bouaziz, and Q. Furnémont, “A physically based model for TRIP-aided carbon steels behaviour,” *Mater. Sci. Eng. A*, vol. 356, no. 1–2, pp. 145–152, Sep. 2003, doi: 10.1016/S0921-5093(03)00121-7.

[6] G. Mao, R. Cao, C. Cayron, X. Mao, R. Logé, and J. Chen, “Effect of cooling conditions on microstructures and mechanical behaviors of reheated low-carbon weld metals,” *Mater. Sci. Eng. A*, vol. 744, pp. 671–681, Jan. 2019, doi: 10.1016/j.msea.2018.12.035.

[7] J. Zhao *et al.*, “Transformation behavior and microstructure feature of large strain ausformed low-temperature bainite in a medium C - Si rich alloy steel,” *Mater. Sci. Eng. A*, vol. 682, pp. 527–534, Jan. 2017, doi: 10.1016/j.msea.2016.11.073.

[8] S. Reisinger *et al.*, “Strain energy contributions on the bainitic phase transformation in a CrMoV steel during continuous cooling,” *Mater. Des.*, vol. 155, pp. 475–484, Oct. 2018, doi: 10.1016/j.matdes.2018.06.014.

[9] H. Kitahara, R. Ueji, N. Tsuji, and Y. Minamino, “Crystallographic features of lath martensite in low-carbon steel,” *Acta Mater.*, vol. 54, no. 5, pp. 1279–1288, Mar. 2006, doi: 10.1016/j.actamat.2005.11.001.

[10] J. Mondal, K. Das, and S. Das, “Isothermal transformation kinetics, microstructure and mechanical properties of a carbide free bainitic steel,” *Mater. Charact.*, vol. 177, p. 111166, Jul. 2021, doi: 10.1016/j.matchar.2021.111166.

[11] K. Zhu, O. Bouaziz, C. Oberbillig, and M. Huang, “An approach to define the effective lath size controlling yield strength of bainite,” *Mater. Sci. Eng. A*, vol. 527, no. 24–25, pp. 6614–6619, Sep. 2010, doi: 10.1016/j.msea.2010.06.061.

[12] Gourgues A.-F., H. M. Flower, and T. C. Lindley, “Electron backscattering diffraction study of acicular ferrite, bainite, and martensite steel microstructures,” *Mater. Sci. Technol.*, vol. 16, no. 1, pp. 26–40, Jan. 2000, doi: 10.1179/026708300773002636.

[13] A. Navarro-López, J. Hidalgo, J. Sietsma, and M. J. Santofimia, “Characterization of bainitic/martensitic structures formed in isothermal treatments below the M s temperature,” *Mater. Charact.*, vol. 128, pp. 248–256, Jun. 2017, doi: 10.1016/j.matchar.2017.04.007.

[14] J.-C. Hell, “Aciers bainitiques sans carbure: caractérisations microstructurale multi-échelle et in situ de la transformation austénite-bainite et relations entre microstructure et comportement mécanique,” PhD Thesis, Metz, 2011.

[15] S. Zajac, V. Schwinn, and K. H. Tacke, “Characterisation and Quantification of Complex Bainitic Microstructures in High and Ultra-High Strength Linepipe Steels,” *Mater. Sci. Forum*, vol. 500–501, pp. 387–394, Nov. 2005, doi: 10.4028/www.scientific.net/MSF.500-501.387.

[16] K. Sugimoto, T. Iida, J. Sakaguchi, and T. Kashima, “Retained Austenite Characteristics and Tensile Properties in a TRIP Type Bainitic Sheet Steel.,” *ISIJ Int.*, vol. 40, no. 9, pp. 902–908, 2000, doi: 10.2355/isijinternational.40.902.

[17] S. M. C. van Bohemen, “Bainite growth retardation due to mechanical stabilisation of austenite,” *Materialia*, vol. 7, p. 100384, Sep. 2019, doi: 10.1016/j.mtla.2019.100384.

[18] L. Guo, H. K. D. H. Bhadeshia, H. Roelofs, and M. I. Lembke, “In situ synchrotron X-ray study of bainite transformation kinetics in a low-carbon Si-containing steel,” *Mater. Sci. Technol.*, vol. 33, no. 17, pp. 2147–2156, Nov. 2017, doi: 10.1080/02670836.2017.1353669.
[19] Y. Lu, H. Yu, and R. D. Sisson, “The effect of carbon content on the c/a ratio of as-quenched martensite in Fe-C alloys,” *Mater. Sci. Eng. A*, vol. 700, pp. 592–597, Jul. 2017, doi: 10.1016/j.msea.2017.05.094.
[20] Z. Nishiyama, *Martensitic transformation*. Elsevier, 2012.
[21] C. S. Roberts, “Effect of Carbon on the Volume Fractions and Lattice Parameters Of Retained Austenite and Martensite,” *JOM*, vol. 5, no. 2, pp. 203–204, Feb. 1953, doi: 10.1007/BF03397477.
[22] R. Rementeria *et al.*, “Quantitative assessment of carbon allocation anomalies in low temperature bainite,” *Acta Mater.*, vol. 133, pp. 333–345, Jul. 2017, doi: 10.1016/j.actamat.2017.05.048.
[23] R. Rementeria *et al.*, “Carbon concentration measurements by atom probe tomography in the ferritic phase of high-silicon steels,” *Acta Mater.*, vol. 125, pp. 359–368, Feb. 2017, doi: 10.1016/j.actamat.2016.12.013.
[24] S. Gaudez, “Kinetics and microstructural evolutions during the tempering of martensitic and nano-bainitic low alloyed steel: in situ experimental study and modelling,” PhD Thesis, Université de Lorraine, 2021.
[25] S. Gaudez, J. Teixeira, S. Denis, G. Geandier, and S. Y. P. Allain, “Martensite and nanobainite transformations in a low alloyed steel studied by in situ high energy synchrotron diffraction,” *Mater. Charact.*, vol. 185, p. 111740, Mar. 2022, doi: 10.1016/j.matchar.2022.111740.
[26] I. Pushkareva *et al.*, “The Influence of Vanadium Additions on Isothermally Formed Bainite Microstructures in Medium Carbon Steels Containing Retained Austenite,” *Metals*, vol. 10, no. 3, p. 392, Mar. 2020, doi: 10.3390/met10030392.
[27] F. G. Caballero, M. K. Miller, and C. Garcia-Mateo, “Carbon supersaturation of ferrite in a nanocrystalline bainitic steel,” *Acta Mater.*, vol. 58, no. 7, pp. 2338–2343, Apr. 2010, doi: 10.1016/j.actamat.2009.12.020.
[28] C. Garcia-Mateo *et al.*, “Low temperature bainitic ferrite: Evidence of carbon super-saturation and tetragonality,” *Acta Mater.*, vol. 91, pp. 162–173, Jun. 2015, doi: 10.1016/j.actamat.2015.03.018.
[29] E. P. Da Silva *et al.*, “Isothermal transformations in advanced high strength steels below martensite start temperature,” *Mater. Sci. Technol.*, vol. 31, no. 7, pp. 808–816, May 2015, doi: 10.1179/1743284714Y.0000000719.
[30] L. Qian, Z. Li, T. Wang, D. Li, F. Zhang, and J. Meng, “Roles of pre-formed martensite in below-Ms bainite formation, microstructure, strain partitioning and impact absorption energies of low-carbon bainitic steel,” *J. Mater. Sci. Technol.*, vol. 96, pp. 69–84, Jan. 2022, doi: 10.1016/j.jmst.2021.05.002.
[31] G. I. Rees, “Bainite transformation Part 1 Modified model,” vol. 8, p. 9, 1992.
[32] S. B. Singh and H. K. D. H. Bhadeshia, “Estimation of bainite plate-thickness in low-alloy steels,” *Mater. Sci. Eng. A*, vol. 245, no. 1, pp. 72–79, Apr. 1998, doi: 10.1016/S0921-5093(97)00701-6.
[33] N. A. Chester and H. K. D. H. Bhadeshia, “Mathematical Modelling of Bainite Transformation Kinetics,” *J. Phys. IV*, vol. 07, no. C5, pp. C5-41-C5-46, Nov. 1997, doi: 10.1051/jp4:1997506.
[34] S. M. C. van Bohemen, “Exploring the correlation between the austenite yield strength and the bainite lath thickness,” *Mater. Sci. Eng. A*, vol. 731, pp. 119–123, Jul. 2018, doi: 10.1016/j.msea.2018.06.041.
[35] Z. Yang, W. Xu, Z. Yang, C. Zhang, and S. van der Zwaag, “A 2D analysis of the competition between the equiaxed ferritic and the bainitic morphology based on a Gibbs Energy Balance approach,” *Acta Mater.*, vol. 105, pp. 317–327, Feb. 2016, doi: 10.1016/j.actamat.2015.12.040.

Contents

Introduction

After concrete, steel is the most widely used metal material for engineering applications. World production is currently estimated at around 1.8 billion tons and will reach 2.8 billion tons by 2050. This production requires a high energy consumption and leads to the emission of large quantities of CO_2. Steel production alone is responsible for 33 % of global industrial greenhouse gas emissions. Consequently, any improvement in the environmental footprint of steel manufacture, use or recycling will have significant consequences. At its own scale, this thesis work will contribute to this objective by helping to improve our knowledge of steel, in particular by allowing a careful control of its production processes and its scrapping ratio [1].

The metallurgy of carbon steels offers a fascinating diversity of phase transformations and consequently a very wide spectrum of multiphase microstructures and achievable mechanical compromise between strength, ductility and toughness. Among these different possibilities, bainitic steels have attracted the interest of steel producers. They are nowadays widely used in many industrial applications as forged parts in automotive/truck industry (crankshaft for instance, as shown in Figure 6), stamped parts for automotive drivelines (suspension arms) or rolled parts for structural applications (rails). In recent years, among the different type of bainitic steels, it appeared that Carbide-Free Bainite (CFB) microstructures bring superior performances and are more and more used.

Figure 6: Picture of a crankshaft taken from Ascometal's website [2].

When obtained after isothermal treatments (continuous annealing of flat products), these CFB microstructures have indeed many advantages: they are mostly lamellar with sub-micrometric characteristic sizes leading to a good mechanical strength, a good ductility and a good resistance to fatigue [3]–[5]. Moreover, they contain high fraction of unstable residual austenite that transforms during further mechanical solicitation at room temperature and that leads to a possible TRIP effect (TRansformation Induced Plasticity) [5], [6] favorable to further stamping operations.
The same benefits are observed in the case of steels obtained by continuous cooling (forging or rolling operations) despite a larger dispersion in size and morphology of constituting microstructure features [7], [8]. In comparison with that in isothermal transformation, the CFB

reaction during continuous cooling has however received relatively little attention in the literature as we will be shown in our state-of-art presented in Chapter I.
This is the reason why this thesis work has been funded by Ascometal (steel producer, member of Swiss Steel Group)**.** It has be conducted in collaboration between Institute Jean Lamour (Microstructures & Stresses team) based at Nancy and CREAS, the researcher center of Ascometal based at Hagondange and aims at a better understanding of the CFB phase transformation mechanisms of an industrial steel during a forging process.

The studied material and the associated characterization methods will be presented in Chapter II. From the experimental point of view, we have mainly conducted in situ High Energy X-Ray Diffraction (HEXRD) experiments to study phase transformation kinetics and phase compositions in condition as close as possible to the industrial practices (Chapter III). Both will be studied during isothermal holdings, multistep treatments and continuous cooling. We will pay particular attention to the mechanisms of carbon partition by establishing accurate time-resolved carbon balances between phases. The microstructures formed after different thermal treatments will be analyzed post mortem using Scanning Electron Microscopy (SEM) coupled with Electron Back-Scattered Diffraction (EBSD) (Chapter IV) to better understand the complex and progressive entanglement and refinement of such multiphased microstructures. It will help to identifying the sensitivity of the steel to the cooling rates and understanding the mechanical quality of the microstructures obtained after complex heat treatments. These experimental observations will then serve to develop, to calibrate and to assess a microstructure prediction model for this steel (Chapter V). At the end of this thesis, after a review of the conclusions obtained and the questions still opened, we will discuss some direct perspectives of this work.

References

[1] D. Raabe, C. C. Tasan, and E. A. Olivetti, “Strategies for improving the sustainability of structural metals,” *Nature*, vol. 575, no. 7781, pp. 64–74, 2019.

[2] “Accueil — Ascometal.” https://www.ascometal.com/ (accessed May 27, 2021).

[3] H. K. D. H. Bhadeshia, *Bainite in steels: transformations, microstructure and properties*, 2. ed. London: IOM Communications, 2001.

[4] J. Tian, G. Xu, Z. Jiang, M. Zhou, H. Hu, and Q. Yuan, “Transformation Behavior of Bainite during Two-step Isothermal Process in an Ultrafine Bainite Steel,” *ISIJ Int.*, vol. 58, no. 10, pp. 1875–1882, Oct. 2018, doi: 10.2355/isijinternational.ISIJINT-2018-187.

[5] K. Sugimoto, A. Kanda, R. Kikuchi, S. Hashimoto, T. Kashima, and S. Ikeda, “Ductility and Formability of Newly Developed High Strength Low Alloy TRIP-aided Sheet Steels with Annealed Martensite Matrix.,” *ISIJ Int.*, vol. 42, no. 8, pp. 910–915, 2002, doi: 10.2355/isijinternational.42.910.

[6] A. Perlade, O. Bouaziz, and Q. Furnémont, “A physically based model for TRIP-aided carbon steels behaviour,” *Mater. Sci. Eng. A*, vol. 356, no. 1–2, pp. 145–152, Sep. 2003, doi: 10.1016/S0921-5093(03)00121-7.

[7] J. Zhao *et al.*, “Transformation behavior and microstructure feature of large strain ausformed low-temperature bainite in a medium C - Si rich alloy steel,” *Mater. Sci. Eng. A*, vol. 682, pp. 527–534, Jan. 2017, doi: 10.1016/j.msea.2016.11.073.

[8] G. Mao, R. Cao, C. Cayron, X. Mao, R. Logé, and J. Chen, “Effect of cooling conditions on microstructures and mechanical behaviors of reheated low-carbon weld metals,” *Mater. Sci. Eng. A*, vol. 744, pp. 671–681, Jan. 2019, doi: 10.1016/j.msea.2018.12.035.

Chapter I: State of art

Introduction

In this brief bibliographic chapter, we will present some general information on bainite and their transformation mechanisms, restricted to the case of low carbon steels. We will first introduce the essential characteristics of these microstructures, of their known phase transformation kinetics during isothermal and continuous cooling treatments, as well as highlight the present-day scientific controversy on bainite formation mechanisms.

In a second part, the specificities of the Carbide-Free Bainitic microstructures will be detailed. We will discuss the influence of the holding temperature in isothermal conditions on the phase transformation process, on the resulting microstructures (microtextures and size) and finally on the resulting mechanical properties.

Finally, the very few works considering the formation of these microstructures during anisothermal treatments will be commented and critically assessed.

I. Generalities on bainitic transformation

I.1. Microstructure & classifications of Bainite morphologies

At the end of 1920, Davenport and Bain started studying isothermal decomposition of austenite in steels at temperatures comprised between the lower domain of the diffusive ferritic/pearlitic transformations and the beginning of the martensite transformation (starting below a critical temperature called M_S temperature for Martensite Start) [1]. Figure. I. 1 shows their original observation: a) pearlitic microstructure obtained at 720 °C, b) and c) two microstructures obtained after an isothermal transformation at 290 °C and 180 °C respectively and d) a martensitic microstructure obtained after a rapid quench. The lamellar microstructures made of ferrite and carbide and obtained in the intermediate temperature range were called “Bainite” in honor of Edgar C. Bain.

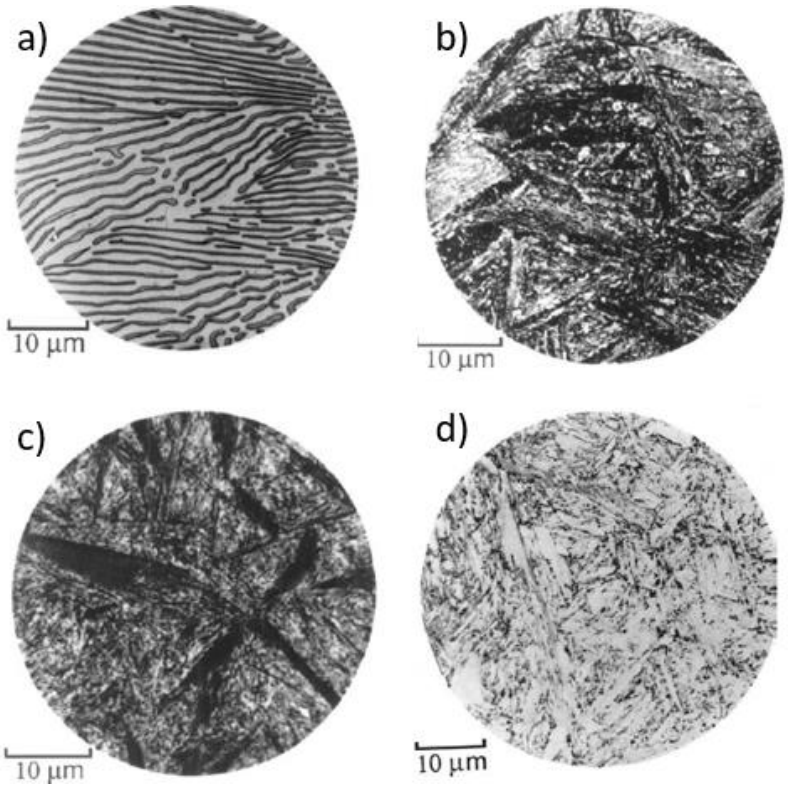

Figure. I. 1: Original micrographs from [2] obtained with a eutectoid steel: a) pearlite formed at 720 °C b) bainite obtained by isothermal transformation at 290 °C c) bainite obtained by isothermal transformation at 180 °C d) martensite.

Since these pioneer works, the definition of “Bainite” has been progressively clarified thanks to the progress in material science. Bainite is an aggregate of ferrite and second phases produced by the decomposition of austenite. As a consequence, like pearlite, it is not a stricto sensu phase in the thermodynamic sense. Ferrite often shows a lamellar or an acicular morphology, but not necessarily. In some cases, ferrite islands can be granular or globular [2]. The second phases can be of different natures (cementite or transition carbides, residual austenite or martensite) depending on the chemistry of the studied steel and on the thermal treatment. Bainite is thus a generic term comprising in fact many different microstructures with a wide range of mechanical properties.

It is in fact well admitted that in the case of acicular bainite obtained at low temperature, the second phases are more likely to be dispersed inside the acicular ferrite whereas at high temperature, the second phases are found in between ferritic structures. According to the classification of Takahashi and Bhadeshia [3] represented in Figure. I. 2, these latter microstructures correspond respectively to the so-called lower and upper bainites. S.A. Sajjadi and S.M. Zebarjad in 2007 [4] investigated for instance the isothermal transformation of austenite to bainite in high carbon steels. They conclude that upper and lower bainite C-curves intersect each other at approximately 325 °C, because lath-like upper bainite forms at temperatures between 475 °C and 250 °C and plate-like lower bainite transforms at temperatures between 375 °C and 250 °C.

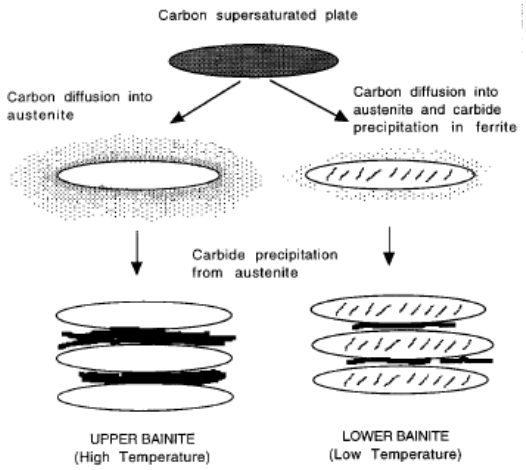

Figure. I. 2: Schematic formation of upper and lower bainites [2].

It must be mentioned that there are many classifications for bainitic microstructures, for instance Mehl (1939) [5], Aaronson (1969) [6], Ohmori (1971) [7], Bramfitt et Speer (1990) [8], Gourgues (2000) [9], Zajac (2005) [10], Furuhara (2006) [11], Takayama (2012) [12]. These classifications have recently been reviewed critically by Ben Haj Slama et al. [13] who show that they are not necessarily consistent, in particular the ones based on the analysis of the second phases and the ones based on microtextures.

I.2. Phase transformation kinetics

I.2.a. Time Temperature Transformation (TTT) and Continuous Cooling Transformation (CCT) diagrams

Contrary to the martensitic transformation, bainite follows a time-dependent transformation kinetics. It is thus possible to represent the progress of a bainitic transformation in a TTT (Time Temperature Transformation) diagram. Bainite as ferrite, pearlite or martensite can also be formed during continuous cooling (anisothermal). Figure. I. 3 shows the schematic representation of both TTT (Figure. I. 3 a)) and CCT (Continuous Cooling Transformation) (Figure. I. 3 b)) diagrams of a low carbon steel considering these latter transformations (taken from [2]).

In Figure. I. 3 a), the two C-curves correspond to two domains of phase transformations. At high temperatures, below the so-called Ae3 temperature, proeutectoid ferrite transformation can take

place, followed by a pearlitic transformation once the Hultgren criteria is reached [14]. Both phases transformations are reconstructive. The beginning of martensitic transformation is indicated by an horizontal line at M_S (Martensite Start) temperature. In between both preceding domains, bainite can form. Bainite transformation has two specificities: bainite can form only under a critical temperature often called T_h or B_S for Bainite Start temperature [2] and the beginning of the transformation shows a C-Shape which is characteristic of diffusional transformations. Contrary to ferrite and pearlite, bainite transformation is displacive as the martensite transformation meaning that bainite formation creates a relief at the free surface when occurring as shown by Ko et al. [15]. In the same way, the critical temperatures for the occurrence of the phase transformations can be defined in the CCT diagram shown Figure. I. 3 b).

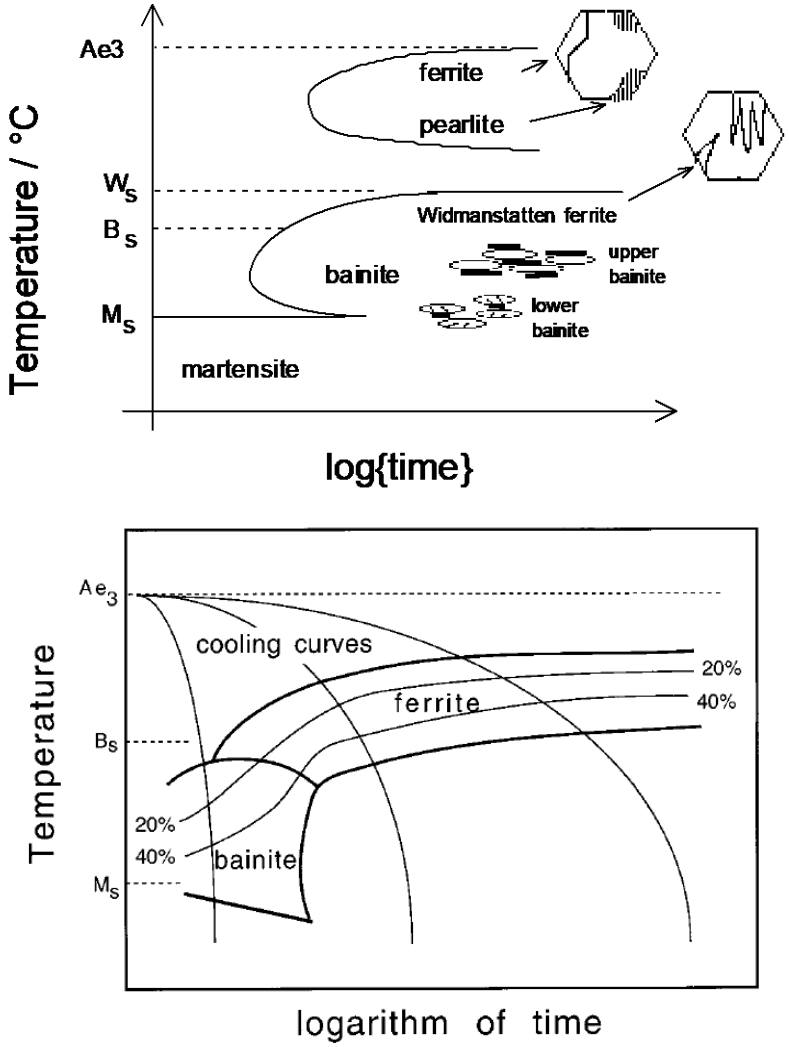

Figure. I. 3: Schematic representation of a) TTT diagram b) CCT diagram from [1] of a conventional steel after a full austenitic soaking.

I.2.b. Effect of the deformation in austenite

The bainitic transformation could also take place in a deformed austenite as in the case of forging. The bainitic reaction is then strongly affected by the residual strains as well as the possible internal stresses induced by the deformation process.

Figure. I. 4 shows for instance the TTT (dashed lines) and the CCT (solid lines) diagrams of a 30CrMnSiNi2 (0.28C-0.70si-1.08Mn-1.13Cr-1.93Ni) steel studied by Khlestov et al. [16] obtained from an undeformed austenite (index 1) and from a deformed austenite (25 % at 900 °C) (index 2). An acceleration of both ferrite-pearlitic and bainitic transformations due to the deformation under isothermal transformations is reported in the TTT diagram. 6 different cooling rates noted Vx in Figure. I. 4 were studied. The cooling rate noted V1 is the slowest rate, whereas the cooling rate V6 is the fastest cooling rate. The acceleration of the ferrite-pearlitic transformation from deformed austenite in the case of continuous cooling transformation is negligible. Moreover, the pearlite transformation is observed for low cooling rates for this steel due to the high stability of austenite. On the contrary, the bainite transformation from deformed austenite under continuous cooling treatment is significantly delayed.

The phase transformation kinetics are thus strongly affected by the deformation state of austenite and it is difficult to derive general rules from the numerous studies available in this field. The relative effect depends on the steel chemistry, the processing parameters and the deformation state. Some models exist but need to be extensively calibrated on each steel as the one of Van Bohemen [17].

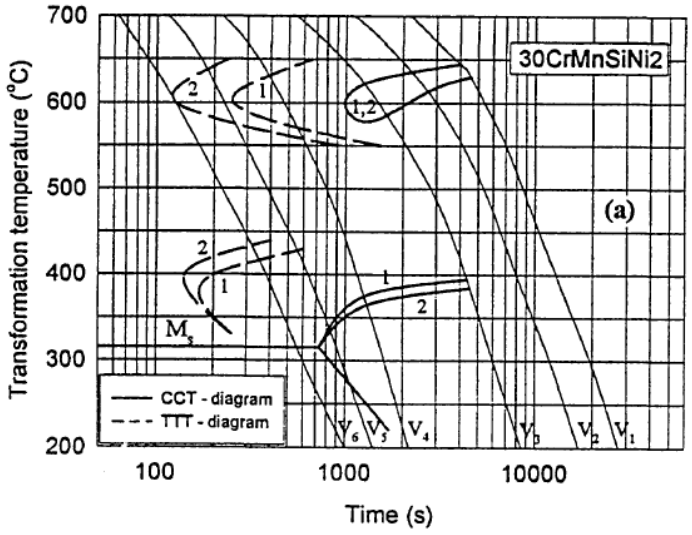

Figure. I. 4: TTT (dashed lines) and CCT (solid lines) diagrams for 30CrMnSiNi2 steel. 1-undeformed austenite ; 2-austenite deformed to 25 % at 900 °C from [16].

I.2.c. Transformations below M_S

Some authors as Kim et al. [18] have studied the time-dependent ferritic transformations during isothermal holdings below the M_S temperatures of different steels.

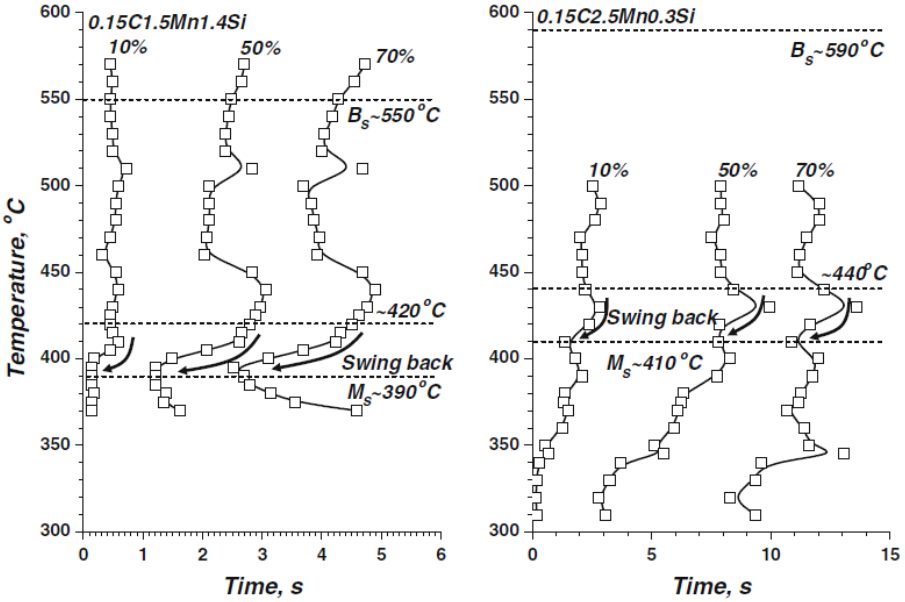

Figure. I. 5: TTT diagrams of the 0.15C-1.5Mn-1.4Si and 0.15C-2.5Mn-0.3Si steels from [18].

Figure. I. 5 shows the TTT curves of 0.15C-1.5Mn-1.4Si and 0.15C-2.5Mn-0.3Si steels obtained by these group of authors. Above M_S temperature, authors have observed a "swing back" of the transformation, characterized by an acceleration of the ferritic transformation about 30 °C above M_S. This phenomenon can be observed above and below M_S. For the 0.15C-1.5Mn-1.4Si steel the swing back phenomenon is observed only above M_S temperature, whereas for the 0.15C-2.5Mn-0.3Si steel the swing back phenomenon is observed above and below M_S temperature (above 350 °C). The authors do not decide as to the nature of the observed transformation (bainite or isothermal martensite) but many other studies [19] [20]–[23] consider that it is a bainitic transformation, accelerated by the presence of martensite (nucleation enhanced in the surrounding untransformed austenite).

I.3. Bainite transformation: controversy

Due to the diversity and the complexity of bainitic microstructures, a controversy on the mechanisms of bainite transformation still subsists, opposing at least two major theories [24]–[26]: the "diffusionless" theory established by Ko and Cotterel in 1952 [15] and supported by H. K. D. H. Bhadeshia [2] and the "diffusion-based" theory supported by H. Aaronson [25]. These theories have been translated into models for the bainite transformation kinetics during isothermal treatments based either on diffusional [27]–[29] or diffusionless approach [22], [30]–[34].

In "diffusionless" approaches, atomic rearrangements during bainite nucleation are supposed to occur without long-range atom diffusion and the interface ɣ/α is glissile as in martensitic transformation. However, while deemed impossible during their growth, the diffusion of interstitial atoms such as

carbon is thought possible after the formation of individual bainitic ferrite units. This is due to the relatively high temperatures at which the reaction takes place. Diffusional approaches assume on the contrary that the bainite growth rate is controlled by a diffusion mechanism at the sessile interface ɣ/α with a short-range diffusion of substitutional atoms at the interface ɣ/α [25] which control the transformation kinetics.

For "diffusionless" theory, bainite transformation has common features with martensite transformation. It is assumed that carbon atoms do not move during the formation of bainitic ferrite sub-units, which inherit the same carbon content as the parent austenite. Growth of bainite sheaves does not need diffusion as it proceeds by autocatalytic nucleation of ferritic units. Subsequently, the carbon, which is initially supersaturated inside the ferrite, can precipitate to form carbides or diffuse out to non-transformed austenite. Figure. I. 6 illustrates the sequence of the formation of bainitic ferrite sub-units according to Bhadeshia et al.'s point of view [2].

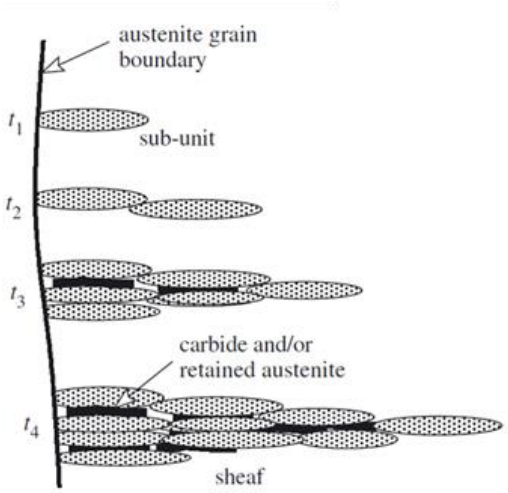

Figure. I. 6: Schematic representation of bainite formation according "diffusionless" approach [2].

According to the diffusion based theories, the growth of bainitic ferrite is driven by carbon diffusion [26]. Carbon is rejected from ferrite (partitioned) as soon has the ferrite unit is formed. At the ɣ/α interface, para-equililbrium (PE) is frequently assumed (e.g. [27], [35]): carbon partitions, whereas the other elements keep the same concentration on both sides of the interface. Quidort and Bréchet proposed a model based on a diffusional mechanism assuming paraequilibrium condition at the ɣ/α interface [36]. This model does not consider any effect of substitutional elements, except "indirectly" via their influence on local carbon activities. Precipitation of carbides (cementite, transition carbides) concomitant to the transformation have an impact on the global kinetic transformation. Indeed, the precipitation leads to a decrease in the carbon content of austenite and thus accelerate the kinetics [35].

In this thesis, we have chosen to implement a "diffusionless" model freely adapted from Van Bohemen [34] to describe the observed bainitic transformations. In Chapter V, more details will be given about this latter approach and the different derived models found in the literature.

II. CFB microstructures obtained after isothermal treatments

II.1. CFB microstructures

CFB microstructures are lath bainitic structures containing as second phases interlath retained austenite and martensite (often thus upper bainite according the conventional classifications). When obtained at low temperature, CFB microstructure can also contain few intralath carbides (lower bainite according the conventional classifications).

In such alloys, the carbide precipitation (cementite) is inhibited or delayed due to a judicious choice of the chemical composition, i.e. the typical addition of more than 1 % of Si or Al. These alloying elements thus contribute to the carbon enrichment of austenite during the bainitic transformation. In turn, carbon enrichment stabilizes austenite and thus leads to these microstructures consisting of bainitic ferrite and carbon enriched retained austenite.

In such microstructures, retained austenite is often found as thin films in between lamellar/acicular ferrite but also in coarse islands mixed up with fresh martensite (the so-called MA Martensite/Austenite islands). In the literature, the lamellar structures are sometimes called bainitic sheaves. According to few authors, these sheaves are themselves constituted with sub-units of ferrite ("diffusionless theory"), which are then the smallest units in such microstructure. Figure. I. 7 shows a typical SEM (Scanning Electron Microscope) micrograph of a CFB microstructure after etching from [37]. Bainitic ferrite appears in dark contrast and films of retained austenite and coarse MA islands appear in brighter contrast.

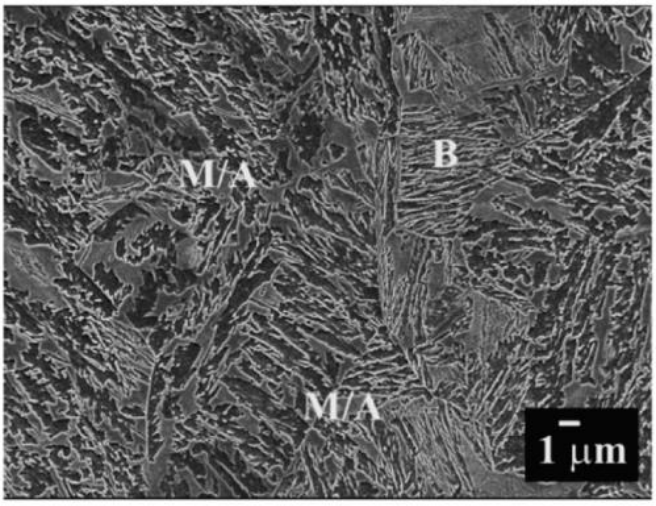

Figure. I. 7: SEM micrograph of a CFB microstructure after etching. Bainitic ferrite appears in dark contrast and films of retained austenite and coarse MA islands appear in light contrast [37].

Figure. I. 8 is a TEM (Transmission Electron Microscopy) micrograph of CFB microstructure (nanobainite in fact, which is a sub-class of high carbon CFB transformed at very low temperature) whose formation has been interrupted by quenching to visualize individually the bainitic sheaves and sub-units [2].

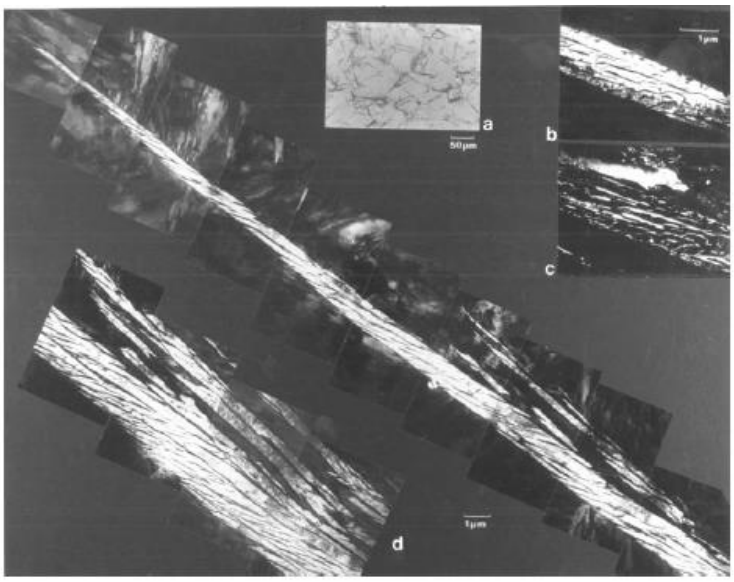

Figure. I. 8: Transmission Electron Micrograph of a sheaf of upper bainite in a partially transformed 0.43C-2Si-3Mn wt.% alloy: (a) light micrograph; (b,c) bright field and corresponding dark-field image of retained austenite between the sub-units ; (d) montage showing the structure of the sheaf [2].

The conventional classification of bainitic structures thus often considers CFB as upper bainite based on the intricate structure of their second phases. In this latter morphological description, the crystallographic dimension is missing. In fact, in many recent studies, thanks to the dissemination of EBSD (Electron Back-Scattered Diffraction) technique, bainitic structures and CFB microstructures in particular, have been analyzed extensively with regards to their microtextures (local orientation of ferritic units and the misorientation between them). In fact, it is well established that bainite transformation is displacive and that there exists an orientation relationship (OR) between the parent austenite and transformed bainitic units. Depending on the OR, ferrite can exhibit different orientations in a single former austenite grain. These different orientations are called variants.

As a single austenite grain does not transform into a single ferritic unit to minimize transformation strain, it appears that austenite grain after transformation shows an intricate and hierarchical organization of possible variants. This particular organization is represented schematically in Figure. I. 9 whereas Figure. I. 10 shows this organization in the Kikuchi Pattern Quality EBSD map taken from [38]. The smallest unit of this organization is the lath (constituted of very few sub-units if any). A lath corresponds to a single variant of parent austenite. The misorientation inside a given lath is limited and is due to residual geometrically necessary dislocations.

Neighboring laths from the same variant forms a sub-block and a block is made of low misoriented sub-blocks. By construction, blocks sharing the same habit planes are highly misoriented and form a packet. The Prior Austenite Grains (PAGs) are thus finally divided into a limited number of packets which show blocks with different habit planes.

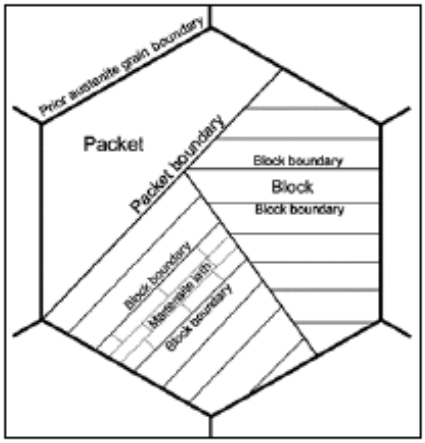

Figure. I. 9: Hierarchical and multi-scale organization of martensitic or bainitic laths in a prior austenite grain. The former prior austenitic grains, packets, blocks, sub-blocks and laths are defined in the text [39].

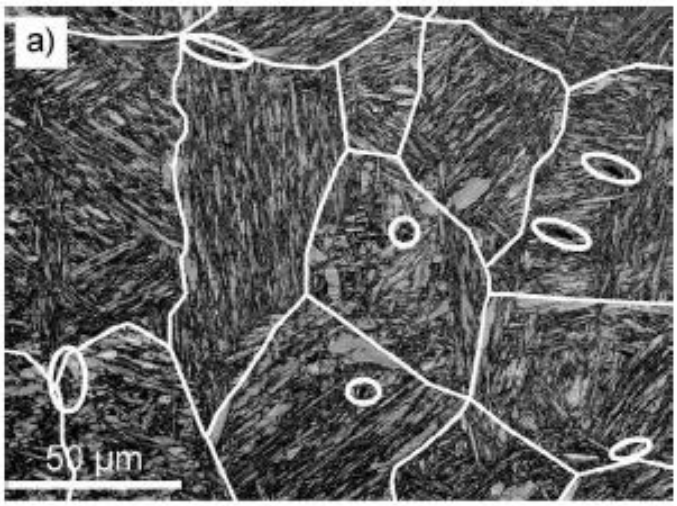

Figure. I. 10: Kikuchi Pattern Quality ESBD map (grey scale) of a 0.3C-2.5Mn-1.5Si-0.8Cr steel elaborated at M_S-50°C (austempering temperature). Prior austenitic grain boundaries have been highlighted (white lines) as well as some MA blocks (white circle), taken from [38].

The statistical occurrence of the misorientation angles can serve to establish the so called histograms of misorientations of a given map. This microtexture distribution can serve to classify bainitic microstructure as proposed by Zajac et al. [10]. The typical distributions serving to define the main classes of bainite are shown in Figure. I. 11. Lower bainite is characterized by a high density of highly misoriented grain boundaries (> 50 °) and few boundaries of low misorientation (< 20 °). Upper bainite is defined by a high proportion of low misorientation angles (< 20 °) and a low proportion of highly misoriented grain boundaries (> 50 °). Zajac et al. [10] describes the granular bainite with a random distribution of misorientation angles, however the distribution shows a broad peak for angles about 45 °.

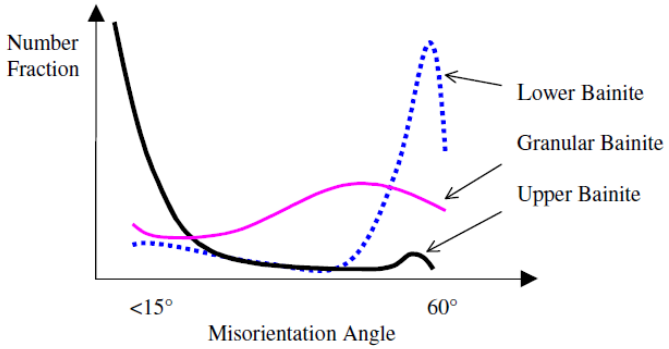

Figure. I. 11: Definition of the main classes of bainites based on the histogram of misorientations (distribution function of misorientation angles) after Zajac's [10].

From the microtextural point of view (Zajac's classification), both kind of lower and upper bainites have been reported [7]–[9] in CFB microstructures. In the upper range of transformation temperatures, bainite laths inside a packet are little disoriented (same variant) and in the lower range, bainite laths belongs to different variants (self-accommodating variants) regrouped into blocks and sub-blocks. Allain et al. [40] has for instance studied by ESBD the CFB microstructure obtained at 4 different temperatures with 0.3C-2.5Mn-1.5Si-0.08Cr steel (cf. Figure. I. 12). The corresponding histograms of misorientations have been plotted in Figure. I. 13. In ESBD maps, each blocks of variants appear in colors (IPF (Inverse Pole Figure) map of ferritic phases) and MA islands appear in dark contrast (not indexed by EBSD). At 450 °C, former PAGs contain very few different blocks and all the constituting laths seems to share almost the same orientation. On the contrary at 300 °C, within a PAG, self-accommodating blocks of variants (with alternated colors) can be identified easily, leading to a high proportion of 60 ° misorientation angles in the histogram. At 300 °C, the CFB is obviously a lower bainite from the microtexture point of view and at 450 °C, the CFB is more of upper type.

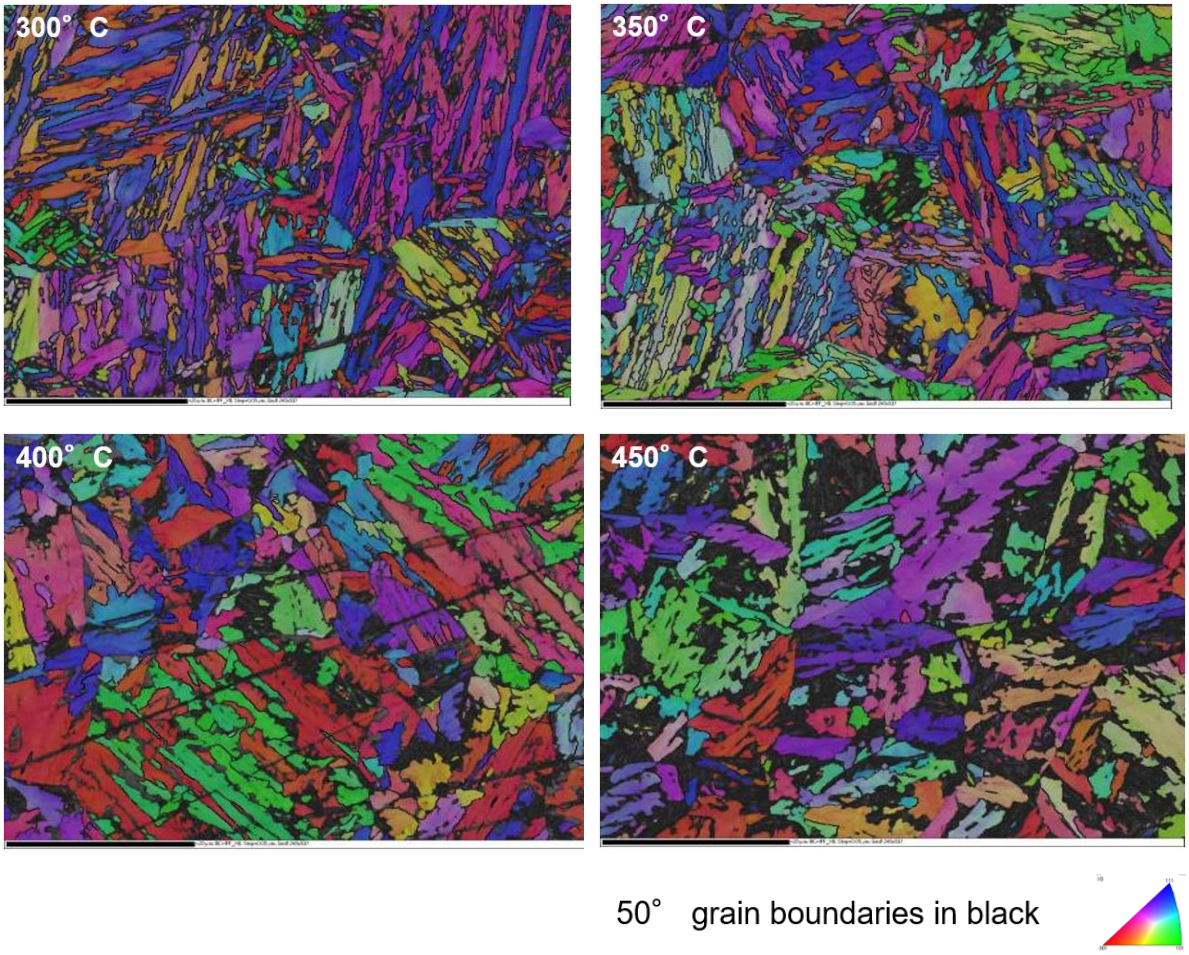

Figure. I. 12: ESBD maps (IPF representation of ferritic phases) of CFB microstructures obtained with a 0.3C-2.5Mn-1.5Si-0.08Cr steel at 4 different temperatures (scales are 20 µm).

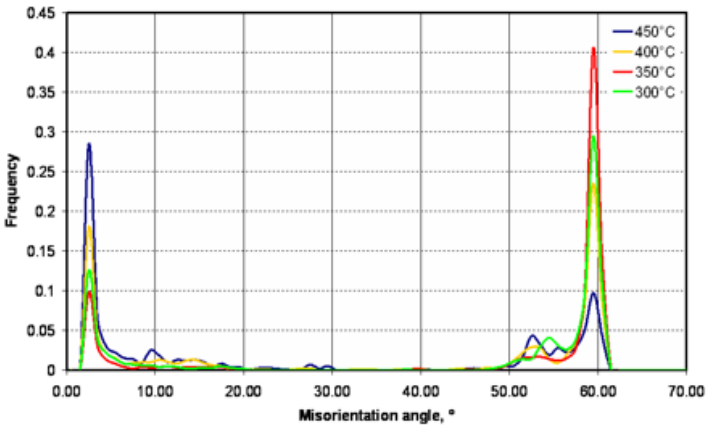

Figure. I. 13: Histograms of misorientations of the ESBD maps shown in Figure. I. 12.

II.2. CFB Transformation mechanisms along isothermal holdings

II.2.a. Incomplete transformation phenomenon and associated martensitic transformation

In the literature, CFB microstructures [2], [4], [41], [42] are often obtained during an isothermal holding, i.e. after a thermal schedule consisting first in a fully austenitic soaking followed by cooling with a sufficiently high rate to avoid the ferrite-pearlitic transformation and secondly in an isothermal stage (also called austempering or bainitizing stage) above the temperature B_S as the one drawn in Figure. I. 14. When ferrite laths appear in austenite grains, carbon is rejected from ferrite to enrich the austenite instead of precipitating. As mentioned above, this is made possible by Si and/or Al additions [43], [44], which delays carbide precipitation. This enrichment will help stabilizing retained austenite after final cooling [45].

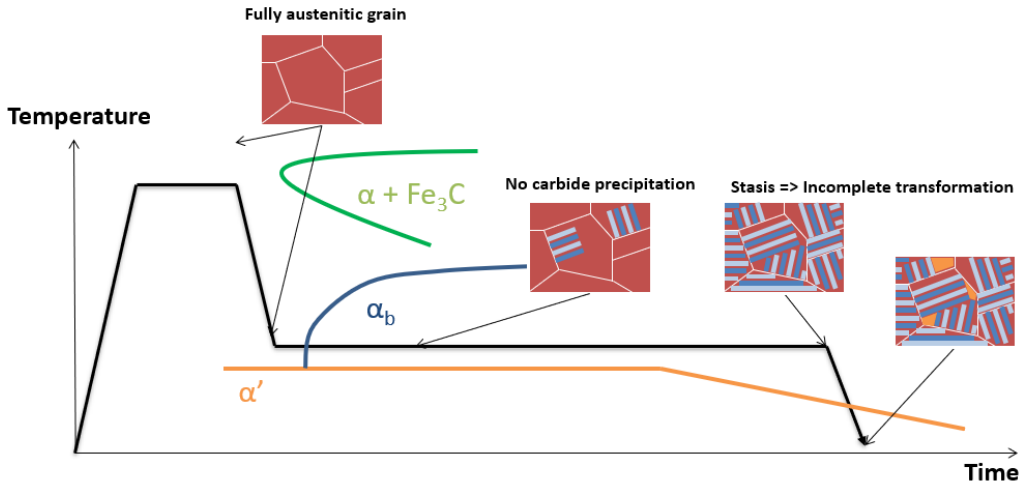

Figure. I. 14: Schematic thermal cycle to obtain CFB microstructures in relation with a typical TTT diagram (austenite decomposition).

The transformations kinetics strongly depends on the steel composition and the transformation temperatures [17], [31], [32], [37]. Given the large number of studies conducted on these isothermal transformations, it is impossible to be exhaustive and only a few representative examples will be discussed. Guo et al. [46] has for instance studied the bainitic transformations in a 0.22C-0.91Si-1.37Mn-0.06Ni-0.14Mo-1.54Cr-0.1Cu steel after a full austenitization at 1200 °C in the temperature range (370 °C / 490 °C). Figure. I. 15 shows the measured evolution of bainite volume fraction as a function of time during isothermal holding for different transformation temperatures. The fraction are measured in situ during High-Energy X-Ray Diffraction (HEXRD) experiments. In these experiments, the transformations do not show obvious incubation stages and the transformation rates increase when the transformation temperatures decrease. As a consequence, the times to reach of 50 % transformation decrease accordingly. An important characteristic of this CFB transformation is to be incomplete as it reaches a stasis (a plateau) before full completion, whatever the studied transformation temperature.

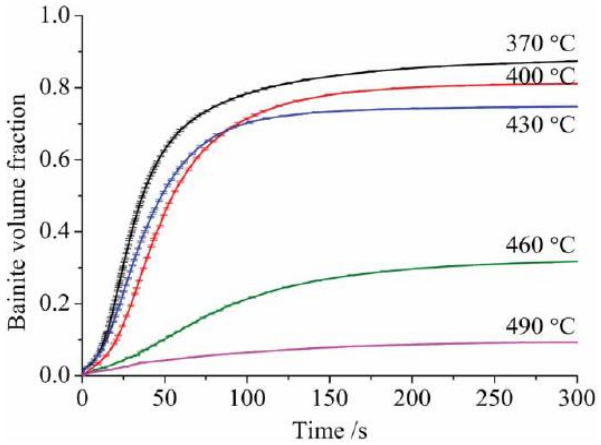

Figure. I. 15: Bainitic transformation kinetics in a 0.22C-0.91Si-1.37Mn-0.06Ni-0.14Mo-1.54Cr-0.1Cu steel during isothermal soakings, reproduced from [46].

According to "diffusional" approaches, the incomplete bainite transformation is due to solute drag effects: substitutional elements (like nickel, manganese) [25], [47] interact with the moving α/ɣ interface, slowing down its motion. Solute drag is also affecting the ferrite laths growth kinetics before the interruption, according to [36], [48]. In "diffusionless" approaches, the bainite transformation slows down when the carbon concentration in austenite exceeds some critical value. Indeed, the austenite gets progressively enriched by the carbon rejected by the ferrite. After a certain amount of transformation, the formation of ferrite without any change of carbon composition is no longer possible. This limit is reached when the Gibbs energy of both phases are equal (no more driving force for the transformation assuming a martensitic like nucleation). This thermodynamic criterion defines an upper-limit for austenite enrichment at a given transformation temperature. This thermodynamic analysis is represented in Figure. I. 16, considering possibly the strain energy in ferrite (with an elastic strain energy stored in ferrite equal to 400 J/mol in the classical displacive theory). The loci of these maximum enrichments as a function of the temperature are known as the T_0 and T_0' curves of the studied steel.

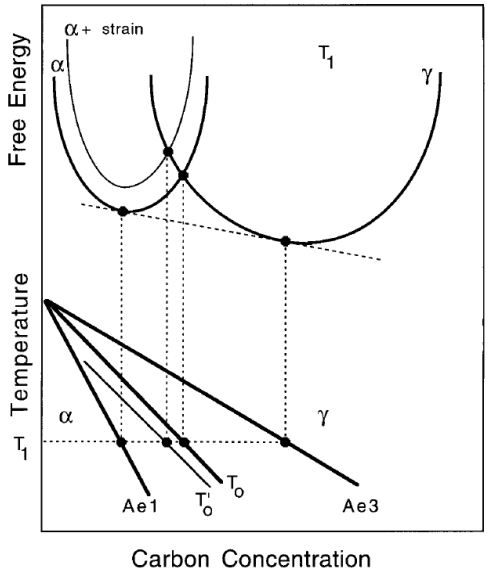

Figure. I. 16: Schematic construction of T_0 and T_0' curves [1].

When studying CFB transformations, it is fundamental to keep in mind that the transformed volumes at stasis depends on the transformation temperature. The lower the temperature, the higher the transformed volume when the transformation seems to stagnate, as shown in Figure. I. 15.

Whatever the possible explanations of the incomplete transformation phenomenon ("diffusionless" or "diffusion-based" approaches), the carbon enrichment in austenite is a function of the transformation temperature as a direct consequence. In fact, as carbon partitions between ferrite and austenite, the higher the fraction of bainite formed, the higher carbon content in austenite.
Guo et al. [46] using HEXRD have determined this progressive enrichment in austenite by monitoring the evolution of the lattice parameter of austenite. The results corresponding to the experiments in Figure. I. 15 are shown in Figure. I. 17 a). The enrichment kinetics follow more or less the ones observed on transformed fractions. As a rule of thumb, the lower the transformation temperature, the higher the enrichment at stasis as shown in Figure. I. 17 b) (except maybe at 370 °C as the transformation has not strictly reached a stasis). This Figure. I. 17 b) highlights also that in this case the T_0 criterion is not perfectly fulfilled. Similar results and conclusions are to be found in our first publication resulting from this thesis [23].

To understand the mechanisms behind this fundamental outcome on CFB transformation, the establishment of very precise carbon balances between phases is a necessity. For example, it requires quantifying the amount of carbon trapped in bainitic ferrite (solid solution, segregated on defects, …) and in possible carbides, as done for example [2], [49]. Confirming the work of Garcia-Mateo [50], [51], the recent works of Pushkareva et al. [52] coupling HEXRD and TEM-EELS have for instance shown that the carbon content trapped in bainite represents more than 30 % of the initial carbon content, meaning that this carbon content is lost to stabilize retained austenite. One of the major contributions of this thesis is to have been able to establish precise carbon balances between phases more systematically using HEXRD.

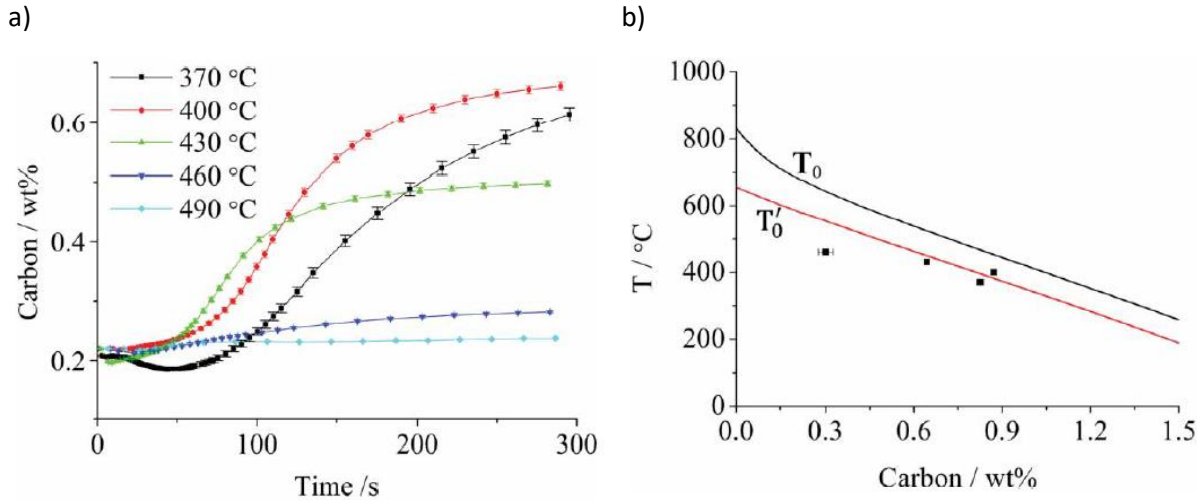

Figure. I. 17: a) Carbon content in austenite determined thanks to its lattice parameter as a function of the transformation time for the bainitic transformations shown in Figure. I. 15 ; b) chemical compositions of austenite at stasis for bainitic transformations shown in Figure. I. 17 a) compared to the T_0 and T_0' criterion defined in Figure. I. 16.

By affecting the carbon enrichment in austenite, the temperature dependent stasis controls also the final martensitic transformation when cooling down the sample to room temperature. If the carbon content in austenite is sufficient (i.e. the new M_S temperature is lower than room temperature), then all the austenite at the end of the isothermal holding will be stabilized down to room temperature. Otherwise, austenite can partially transform into martensite during final cooling, leading to the formation of MA islands. Hence, the lower is the transformation temperature, the higher the enrichment thus the lower the fraction of fresh martensite at room temperature, which could seem counterintuitive.

From the alloy design point of view, as already demonstrated, carbon, silicon and aluminum play a key role in the morphogenesis of these microstructures. It is in fact also the case of manganese, nickel and copper, which tend to stabilize also austenite and thus affect the incomplete transformation phenomenon [45]. Cr and Mo also play a less pregnant role on this mechanism but have a strong effect on kinetics [20], [53]–[55].

In this thesis, we will follow a HEXRD methodology very similar to that of Guo et al. [46] or Hell et al. [37], to investigate in situ transformation kinetics. The results of this experimental work will be mainly presented in Chapters III and V. The superiority of such technic compared to simple dilatometry or post-mortem observations will be discussed and demonstrated.

II.2.b. Size in CFB microstructures

The morphology and the size of the CFB microstructures obtained at stasis also strongly depends on the transformation temperature.

J-C Hell [37] carried out different isothermal holdings as represented in Figure. I. 18 a) on three steels C1 (0.1C-2.5Mn-1.5Si-0.8Cr); C2 (0.2C-2.5Mn-1.5Si-0.8Cr); C3 (0.3C-2.5Mn-1.5Si-0.8Cr). Figure. I. 18 b) shows the evolution of the mean thickness of bainitic laths as a function of the transformation temperature. These sizes have been estimated using EBSD maps with intercept method (with a critical disorientation angle of 5 °). For all studied steels, the average thickness obviously increases with the temperature.

a) b)

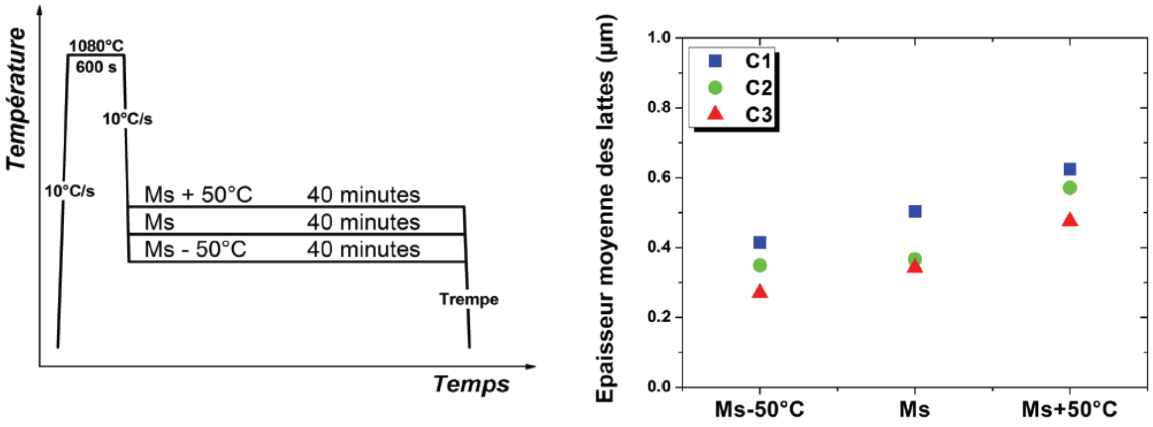

Figure. I. 18: a) Heat treatments performed by Hell [29], b) Average thickness I0 of ferrite bainitic laths (or martensite + « isothermal » phase at M_S -50°C) obtained with intercepts method with a critical angle 5° as a function of the transformation temperature [37].

This trend has also been observed by Tian et al. [41] when studying isothermal transformations above M_S and below M_S. Figure. I. 19 represents their heat treatments and the composition of the studied steel is (0.22C-1.8Si-2Mn-1Cr-0.23Mo).

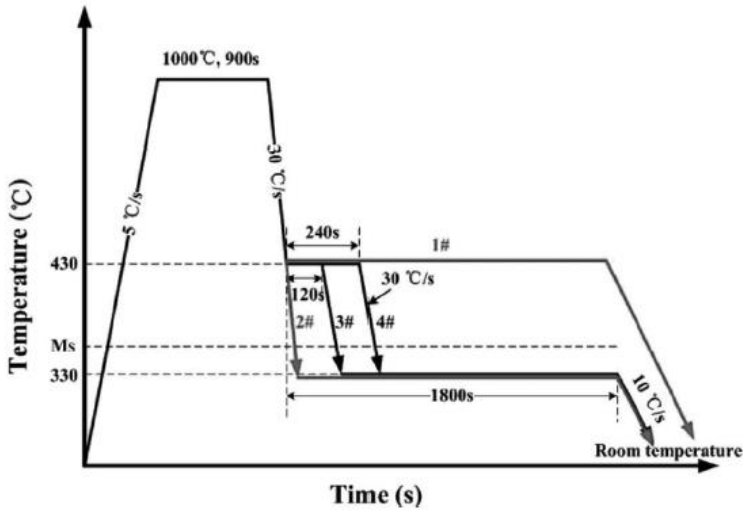

Figure. I. 19: Heat treatments applied by Tian et al. [41] on a (0.22C-1.8Si-2Mn-1Cr-0.23Mo) steel.

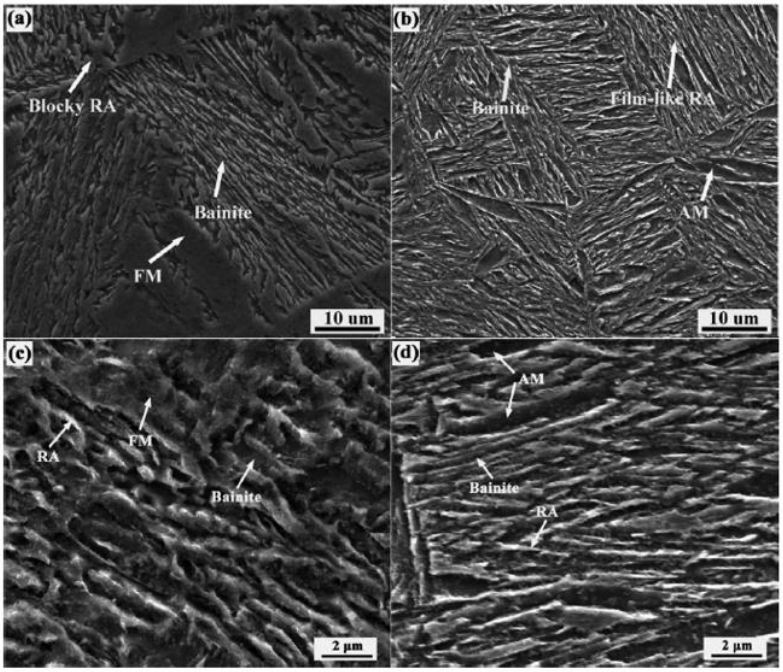

Figure. I. 20: SEM micrographs of the steels studied by [41]: (a) low and (c) high magnification of sample 1 austempered at 430°C for 30 min; (b) low and (d) high magnification of sample 2 austempered 330 °C for 30 min.

Figure. I. 20 shows the SEM micrographs of the microstructures after etching obtained by Tian et al. [41] at high and low magnifications; Sample 1 transformed at 430 °C for 30 min (above M_S) is composed mainly of fresh martensite (FM), bainite and blocky retained austenite (RA), whereas in sample 2, the microstructure is composed of annealed martensite, films of retained austenite and of course of bainite. Thanks to the high magnification SEM, the size of bainite measured for sample 1 is 757 nm, whereas it is 468 nm in sample 2 (transformed at 330 °C for 30 min). So, the bainite plates become finer when the sample is treated below M_S. That is to say, the lower the temperature, the finer the bainite as already shown by Hell [37].

The effect of holding temperature is also in agreement with Sugimoto's results in 2000 [58] as shown in Figure. I. 21. This figure presents the microstructures of a 0.2C-1.5Si-1.5Mn steel transformed at different temperatures observed by SEM after etching. As in prior Figure. I. 7, laths of bainite appears in dark contrast and the MA islands in clear contrast. The thickness of the laths obviously increases with temperature as well as the fraction of MA constituents as discussed in the previous section (incomplete reaction).

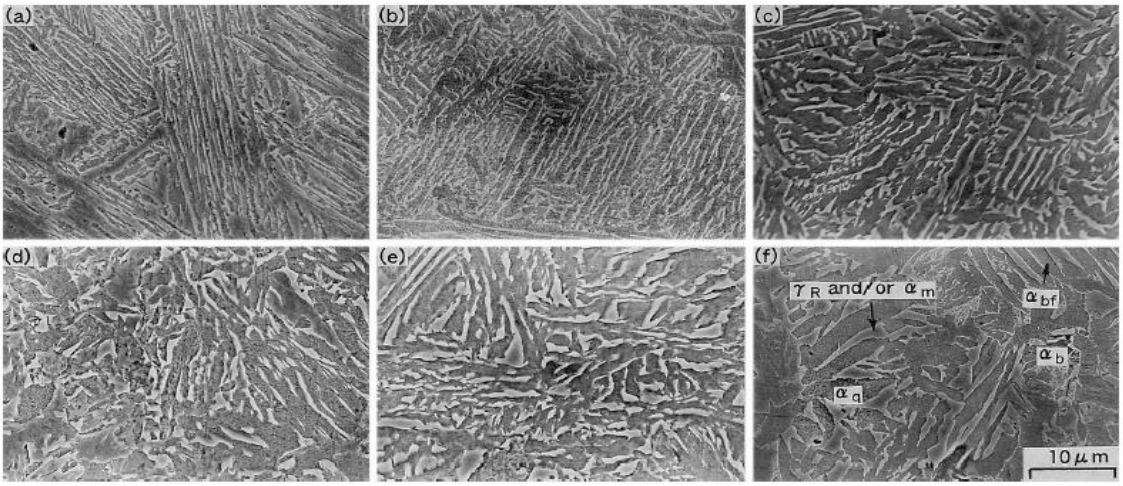

(a) 350℃, (b) 375℃, (c) 400℃, (d) 425℃,(e) 450℃, (f) 475℃

Figure. I. 21: SEM micrographs of a 0.2C-1.5Si-1.5Mn steel transformed at different temperatures (from 350 °C and 475 °C), reproduced from [58].

This refining effect of temperature is generally attributed to the increase in the strength of austenite with the decreasing temperature. As a consequence, it also depends of PAGs size [56], [57] and on the composition [59] The thickness of bainite plates are hence refined in carbon rich alloys.

This question being crucial in the tailoring of the microstructures and the mechanical properties of these steels, we shall come back to it in more details in Chapter IV, by presenting our own size measurements and by assessing critically existing models from the literature.

II.2.c. Main Conclusions

The transformation temperature has two main visible effects on the morphogenesis of CFB microstructures:

- The incomplete transformation phenomenon imposes that the lower the transformation temperature, the more enriched in carbon is the retained austenite. As a consequence, at low temperature, the fraction of austenite is low but the austenite is very stable. At high temperature, the fraction is large but austenite can be unstable, leading to a possible martensite transformation during final cooling. An optimum can then be found between the fraction and the stability of retained austenite.
- The lower the transformation temperature, the finer the CFB microstructures.

Both evolutions have a significant impact on the mechanical performance of the microstructure as explained in the following.

II.3. Structures properties relationship

Carbide-Free Bainite microstructure has many advantages compared to more conventional bainite:

- The very thin lamellar structure contributes to increase the yield stress as well as the fracture strain in particular when lath/blocks are highly misoriented from a crystallographic point of view (lower bainite according to Zajac's classification [10]).
- The absence of carbide significantly improves the damage resistance because in high strength bainitic steels, inter-lamellar precipitates of the second phases (like cementite) are known to be initiating sites for ductile failure [60].
- The thin films of inter-lath residual austenite and coarse residual austenite islands (often in MA islands) can transform during mechanical loading (strain-induced transformation of austenite into martensite) and promote in turn a potential TRIP effect (TRansformed-Induced Plasticity). TRIP effect is a dynamic work-hardening mechanism induced by the martensitic transformation of residual austenite during a mechanical loading. The progressive transformation of the ductile austenite in martensite with a high yield strength induces an increase in the macroscopic work hardening and so delays the necking condition. This is why the induced martensitic transformation contributes to increase steels formability [61]. As martensitic transformation is a displacive transformation, it also contributes to the macroscopic plastic deformation but this direct contribution to deformation is generally low. MA islands or strain induced martensite can however be detrimental to damage properties, since these phases are hard and brittle and represent potential sites of crack initiation [60]. Figure. I. 22 shows the tensile curves of a TRIP-assisted steel and a Dual phase steel with equivalent mechanical strength. It illustrates the possible gain in formability when an efficient TRIP effect is activated.

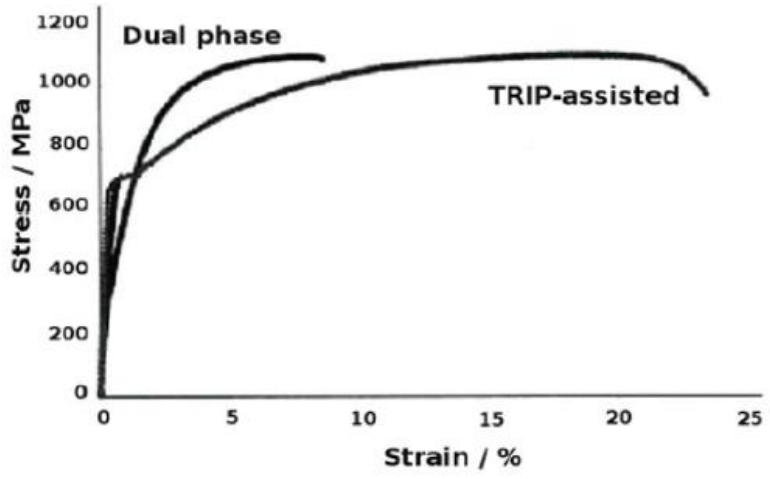

Figure. I. 22: Tensile curves of a TRIP-assisted steel and a Dual phase steel with equivalent mechanical strengths. Illustration of the gain in formability when an efficient TRIP effect is activated [62].

The strain induced transformation responsible for the TRIP effect depends on the stability of retained austenite and the contribution to hardening to the fraction of available austenite for the transformation (films are generally more stable than coarse islands, due their smaller sizes and often

to their higher carbon contents). As a consequence, the TRIP effect of CFB steels obtained after isothermal holding and their mechanical properties is highly sensitive to the transformation temperature. This relation between manufacturing parameters and properties has been studied systematically by Sugimoto et al. already in the late 1990's [58], [61], [63]. Figure. I. 23 shows for instance the evolution of the mechanical performances of seven steels as function of the transformation temperatures [63]. Their respective compositions are reported in Table 1. UTS stands for Ultimate Tensile Strength, Tel Tensile Elongation and RA Reduction of Area, related to the fracture strain. It appears that most studied steels present an optimized ductility at around 400 °C while their strength increases when the temperature decreases. For highly alloyed concepts (Mn rich), the steel can show a minimum in strength when the best formability is reached. The behavior of RA is more complex to analyze however. The observed trends of the literature have been summarized in Figure. I. 24.

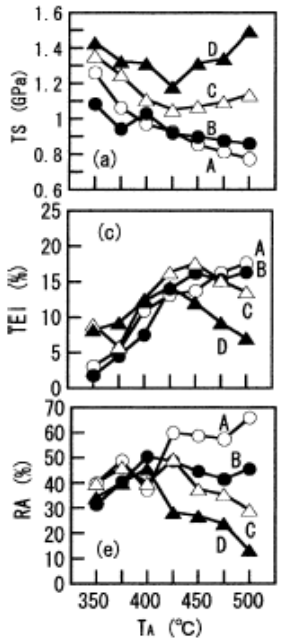

Figure. I. 23: Effect of the austempering temperature TA on the tensile behavior of CFB steels; Tensile strength (TS), Total Elongation (TEl) and Reduction of Area (RA), reproduced from [63].

Table 1: Chemical composition of steels studied by [63] and their respective calculated M_S temperatures.

Steel	C	Si	Mn	M_S (°C)
A	0.21	1.51	1.00	428
B	0.20	1.51	1.51	416
C	0.20	1.49	1.99	401
D	0.21	1.50	2.51	379

Figure. I. 24 shows that for low transformation temperatures, lower than 400 °C, the CFB microstructure behaves mostly like a "conventional" bainite, as the microstructure is made of a high

fraction of lamellar ferrite and a low fraction of very stable retained austenite (no TRIP effect). The laths at low transformation temperatures are fine and the microtextures highly misoriented (lower type bainite from the crystallographic point of view) [38]. If the temperature is lower than M_S, the resulting microstructure exhibits self-tempered martensite. As a consequence, the yield strength of the microstructure and the fracture toughness are high but the work-hardening is low. The obtained UTS and yield ratio are high (YS/UTS $\geqslant$ 0.7) and the formability is limited (good fracture strain however).

Then, for bainitizing temperature higher than 400 °C, the CFB microstructure behaves like a Dual Phase (YS/UTS = 0.5) steel. The microstructures contains a low fraction of bainitic ferrite, a high fraction of very unstable MA islands and possibly fresh high carbon martensite obtained during final cooling. The bainite structure is coarse (low proportion of highly misoriented boundaries). The retained austenite is too unstable and transformed rapidly during mechanical tests at room temperature and does not provide any efficient TRIP effect. As a consequence, the YS is low (controlled by the softest phase of the microstructure) and the work-hardening is enhanced by the sole composite effect (mixture of ferrite and martensite) [52]. The UTS is high due to the presence of fresh martensite (thermally-induced or strain-induced) and MA islands. The high mechanical contrasts between phases (bainite and MA) leads to a low resistance to damage (low fracture strain) [61], [63].

In an intermediate range of temperature, retained austenite can be sufficiently unstable to provide an efficient TRIP effect. This TRIP effect can contribute to enhance strength and ductility of the steel at the same time, resulting in the observed optimum.

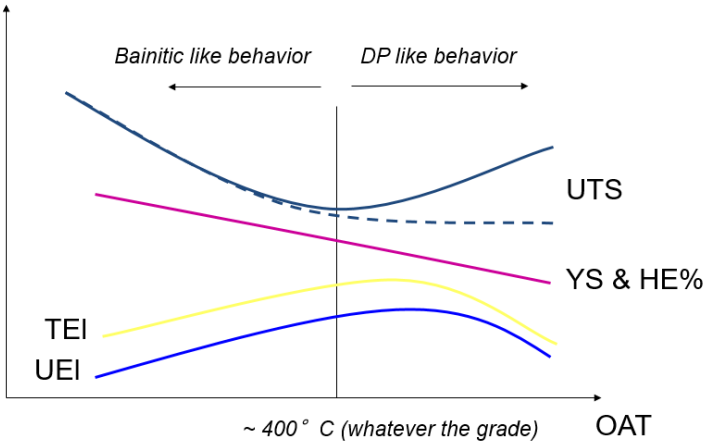

Figure. I. 24: Mechanical properties of CFB steels as a function of transformation temperatures (OAT = Overageing Temperature) in isothermal conditions – taken from [40]. Tensile strength (TS), Total Elongation (TEl), Uniform Elongation (UEl), Yield Strength (YS) and Hole Expansion (HE) related to the fracture strain.

III. Microstructures obtained after multistep holding sequences

CFB transformations can also be studied along step holding sequences (succession of isothermal holdings) which allow to better understand the morphogenesis of these microstructures, by deconvoluting nucleation and growth processes. These model cooling schedules are often seen as a preliminary stage in order to study continuous cooling sequences [41], [64], [65].

Wang et al. [65] have for instance studied the CFB transformation along the multistep heat treatments (succession of isothermal holdings at decreasing temperatures) represented in Figure. I. 25. The corresponding microstructures are also represented schematically. They have shown that such process permits to refine the microstructure and to control better the carbon enrichment in austenite by changing the size and stasis conditions all along the process. The microstructures obtained after the 2-step holding sequence, 3-step holding sequence and after the conventional 1-step treatment are shown in Figure. I. 26 (SEM observations after etching). The 2-step process leads to an interlaced organization of two bainitic structures (B_1, B_2) whereas the 3-step process leads to a interlaced organization of three components (B_1, B_2, B_3) obtained successively at different temperatures.

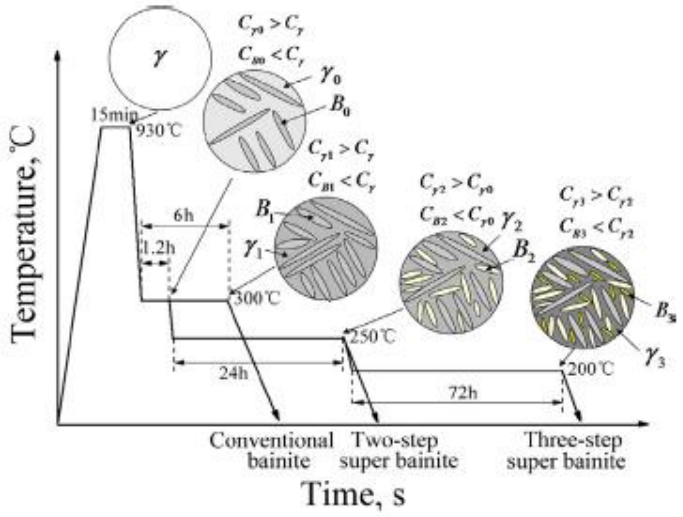

Figure. I. 25: Heat treatment cycles and resulting microstructures after multistep CFB transformations. (0.30C-1.46Si-1.97Mn-1.50Ni-0.30Cr-0.96Cu-0.25Mo steel), reproduced from [65].

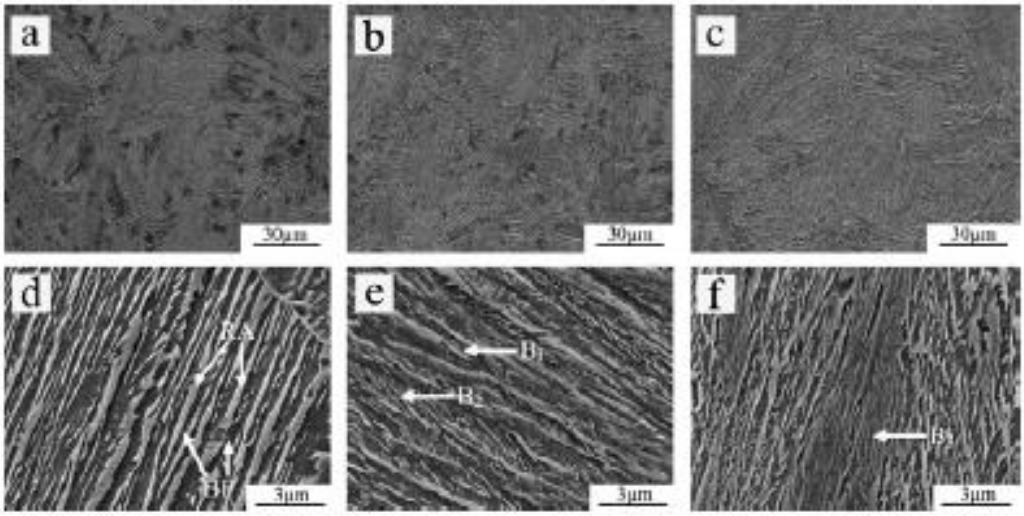

Figure. I. 26: SEM micrographs after etching at low and high magnification of the microstructures obtained at room temperature after the heat treatments depicted Figure. I. 25. (a, d) after isothermal bainitic transformation (b, e) after two-step bainitic transformation (c, f) three-step bainitic transformation [65].

As shown in Figure. I. 19, Tian et al. [41] also studied the bainite transformation along 2-step holding sequence and compared the obtained microstructures with the ones obtained after single step holding.

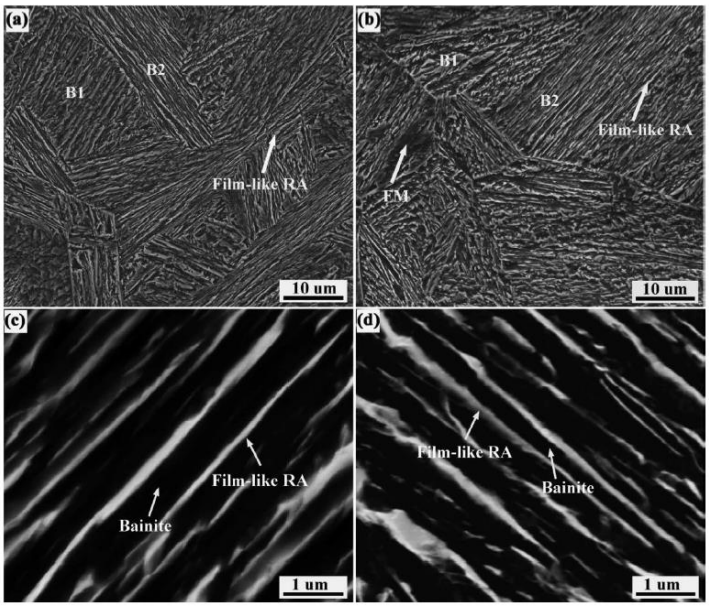

Figure. I. 27: SEM micrographs of the microstructures obtained after the two-step isothermal processes shown in Figure. I. 19: (a) and (c) sample 3 austempered at 430 °C for 2 min followed by 330°C for 28 min; (b) and (d) sample 4 austempered 430°C for 4 min followed by 330 °C for 26 min ; taken from [41].

Figure. I. 27 shows clearly a bimodal microstructure after the two-step transformation, in accordance with the observations of Wang et al. [65]. Interestingly, Tian et al. [41] have studied the effect of the duration of first bainitic transformation on the second one at lower temperature. Their study was conducted by dilatometry (the change of length of the sample is supposed to be proportional to the transformed fraction of bainite).

By doing so, they highlight that changing the first step duration affects the fraction of bainite formed during the first holding, the bainite transformation kinetics along the second step, as well as the final size distribution in the microstructure and the stability of retained austenite.

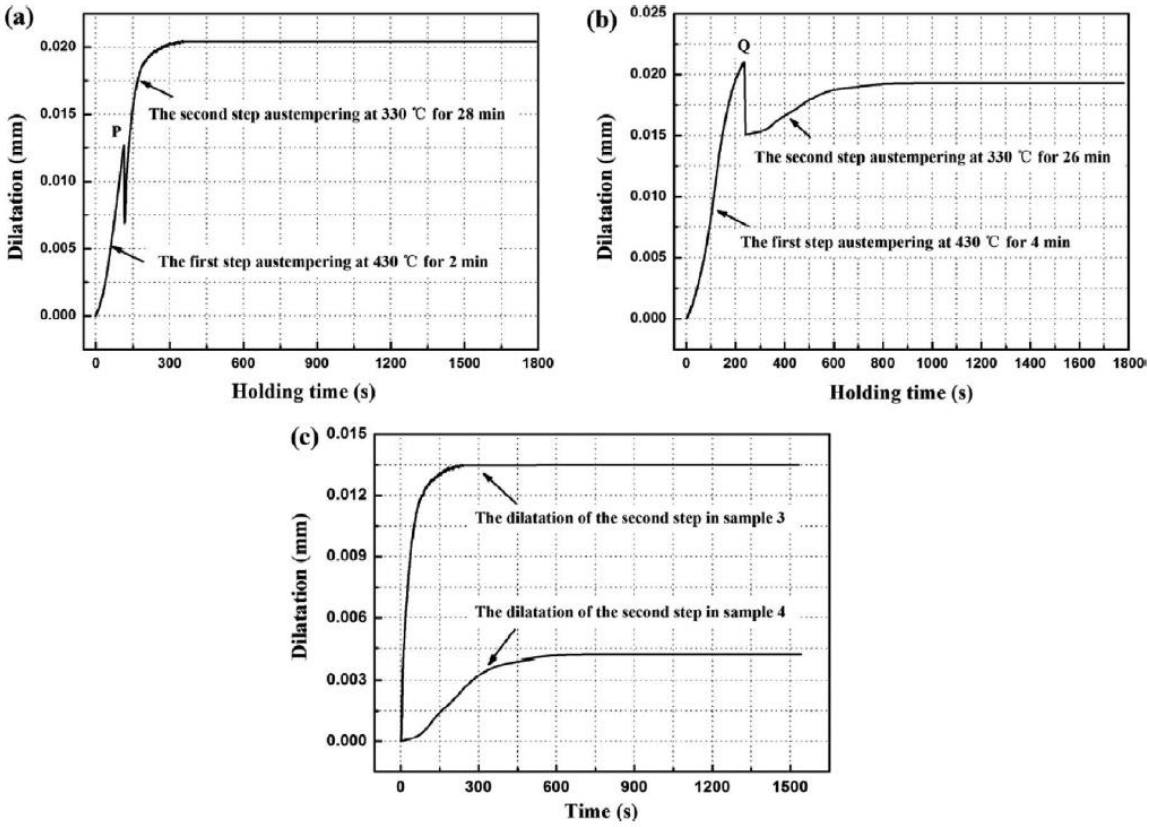

Figure. I. 28: Global kinetics obtained by dilatometry during the two-step bainite transformation for: (a) sample 3 austempered at 430 °C for 2 min followed by 330°C for 28 min; (b) sample 4 austempered 430°C for 4 min followed by 330 °C for 26 min ; (c) the dilatation in the second step of samples 3 and 4 taken from [41].

Figure. I. 28 shows the evolution of the sample dilatation as function of the holding time during two different two-step bainite transformations. Figure. I. 28 a) (sample3) corresponds to a heat treatment consisting in first step at 430 °C during 2 minutes followed by a second step at 330 °C during 28 minutes. Figure. I. 28 b) (Sample4) corresponds to a heat treatment consisting in a first step at 430 °C during 4 minutes followed by a second step at 330 °C during 26 minutes. In Figure. I. 28 a) , the dilatation reaches about 50 % of the maximal bainite fraction obtained during a classical isothermal treatment at the same temperature (430 °C), whereas in Figure. I. 28 b) the dilatation reaches about 95 % of the maximal bainite fraction obtained during an isothermal treatment at the same temperature. In both cases the transformation restart during the second step with different kinetics.

Figure. I. 28 c) shows the comparison of the dilatations as function of the time measured during the second step at 330 °C for the two discussed experiments (sample 3 and sample 4). The final fraction of bainite formed during the two-step treatments is obviously different (even if dilatometry only provide a relative result). As a consequence, it is reasonable to think that the final fraction of retained austenite

is also different. The final volume fraction of retained austenite and the carbon contents at room temperature after both experiments were measured by conventional X-Ray Diffraction (XRD). For the isothermal treatments at 430 °C and at 330 °C, the volume fractions of retained austenite are 7.9 % and 7.5 % with a carbon contents of 0.76 wt.% and 0.82 wt.% respectively. The carbon content of austenite is then higher for a lower transformation temperature (as already discussed in section II.2. a.). For the two-step treatments the volume fraction of retained austenite is equal to 12.7 % for sample 3 and 11.3 % for sample 4. The austenite carbon contents are equal to 0.90 wt.% for sample 3 and 0.92 wt.% for sample 4 respectively. Surprisingly, the volume fractions of retained austenite for the two-step treatments are higher than for a single isothermal treatments (even at 430 °C). Moreover, the austenite carbon contents are also higher. Those kinds of observations have been confirmed in our first paper derived from this thesis [23].

In [41], the authors compared a 1-step bainite transformation (transformation at 430 °C and 330 °C) with a two-step transformation (first step at 430 °C and the second step at 330 °C), and concluded that two-step transformation increases the mechanical performance of the steel, evaluated by the product between UTS and TEl. This is explained by a finer structure and an higher amount of film-like RA measured by X-Ray Diffraction (XRD). The film-like RA can significantly enhance the mechanical properties by the TRIP effect. Moreover, for two-step transformation, the shorter the first step, the better the mechanical properties improvement [64], [66], [67].

Other studies as [65] showed that three-stage treatments (heat treatment presented in Figure. I. 25) help reducing the amount of blocky austenite compared with two-stage treatment and compared with the single-stage treatment, as well as for martensite; but it is the inverse for the film-like austenite. After three-step transformation the volume fraction of bainite formed is higher than previous steps, austenite is then all the more transformed. All of this improve the mechanical properties.

As such multistep holding sequences have been seldom investigated, many questions remain about:

- In which conditions can a bainite transformation restart when changing the temperature? What are the rate-controlling mechanisms?
- Can the stasis criterion be described in the same way as during a single step holding?
- What is the related microstructural dispersion?
- Are the internal stresses at phase scale affected?

Some of these questions will be addressed in this work and will help to conduct our works on continuous cooling sequences.

IV. Continuous cooling sequences

Conventional bainite transformations along continuous cooling have been studied for years [20], [55], [68]–[74] as these thermal schedules are encountered in the production of thick plates, tubes, hot-rolled sheets or forged products. Such transformations are also observed in the HAZ (Heat Affected Zone) of welds [69] . As for isothermal holdings, all the mechanisms are not well understood, in particular why coarse granular structure can often be observed [75] instead of lamellar structures.

Among these studies, very few have been dedicated more specifically to CFB microstructures. Most of the works concerned the optimization of mechanical properties (tensile properties but also toughness) through the management of hot-rolling process parameters. The control of the cooling temperature, like the holding temperature for isothermal treatment, allows to identify CFB microstructures with bainitic, TRIP or DP-like mechanical behaviors. In these later studies, the morphogenesis are not necessarily detailed.

The mechanisms of formation and the performance of these microstructures are therefore even less known and little documented. We have, however, noted a strong research activity on these issues at present and some reference works has been published very recently [55], [71], [76]. We will detail their main findings in the following, starting by the main characteristics of the microstructures and following by the transformation processes. Our purpose is to show the limits of current knowledge on the subject and thus to define the scientific objectives and the problematic of this thesis.

IV.1. Characterization of the microstructures

Figure. I. 29 taken from [55] shows the CFB microstructures obtained after full austenitization and continuous cooling at 0.5 °C/s with two steels (Cr-free: 0.25C-1.83Si-2.02Mn-0.23Mo ; Cr-added: 0.22C-1.79Si-1.98Mn-1.00Cr-0.23Mo). This study published in 2017 reveals the wide diversity of microstructural constituents and the high degree of entanglement that can be observed under these conditions: coarse granular bainitic domains (GB) in addition to lath-like bainite (LB), polygon ferrite (PF), and martensite/austenite (M/A). The presence of PF means that the cooling rate was probably not sufficient to avoid the ferritic nose at high temperature. The coexistence of several bainite morphologies is on the other hand very interesting and to be put in connection with the observations during multistep holding sequences (B_1, B_2, B_3).

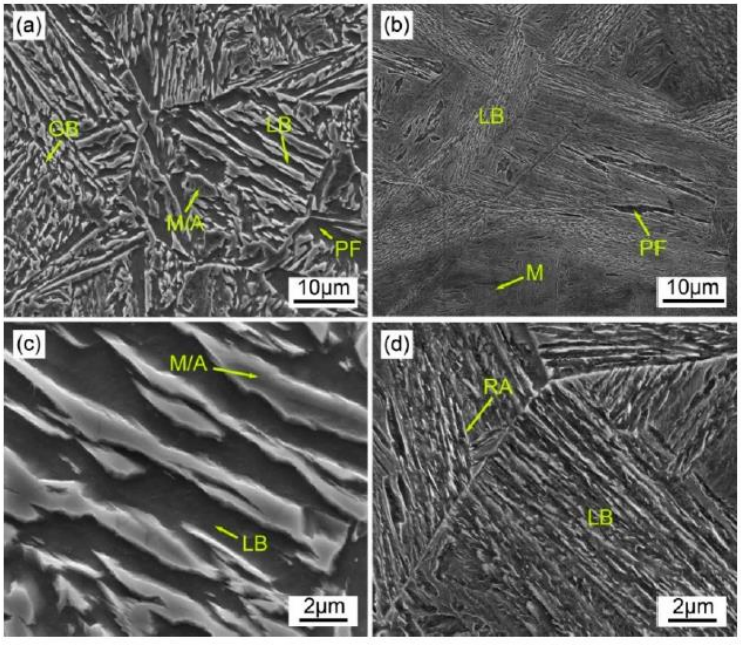

Figure. I. 29: SEM micrographs after etching of Cr-free and Cr-added steels after continuous cooling: (a,c) Cr-free steel; (b,d) Cr-added steel. Highlighted microstructure constituents: LB: lath-like bainite ; GB: granular bainite ; PF: polygonal ferrite ; M/A: martensite/austenite, reproduced from [55].

Others authors as Chen et al. [76] have studied the influence of the cooling rate on the microstructures obtained with a 0.25C-1.5Si-1.8Mn-0.23Mo-microalloyed steel. The alloys have been processed thermo-mechanically. The treatment consists in an austenitization stage at 1150 °C during 300 s followed by 40 % strain at 1050 °C and 60 % strain at 900 °C with a final cooling at different rates (between 0.05 °C/s to 10 °C/s). Figure. I. 30 shows the microstructures obtained after different cooling rates observed by SEM after nital 4 % etching.

- For low cooling rates (0.05 °C/s and 0.1 °C/s) the microstructures are mainly made of granular bainite (GB in Figure. I. 30 (a) and (b)), additional observations using optical microscope shows also a few amount of polygonal ferrite.
- For intermediate cooling rates (0.3 °C/s and 0.5 °C/s), the microstructures are mainly made of lath-like bainite (LB in Figure. I. 30 (c) and (d)).
- For high cooling rates (1 °C/s and 2 °C/s), the microstructures are mainly martensitic (M in Figure. I. 30 (e) and (f)).

They also observed that the morphology of bainite is strongly dependent to the cooling rate. This latter morphology plays an important role on the mechanical properties and an increase in hardness is observed when increasing the cooling rate. These authors have also analyzed the microstructure by SEM-EBSD to have a crystallographic description of the microstructures.

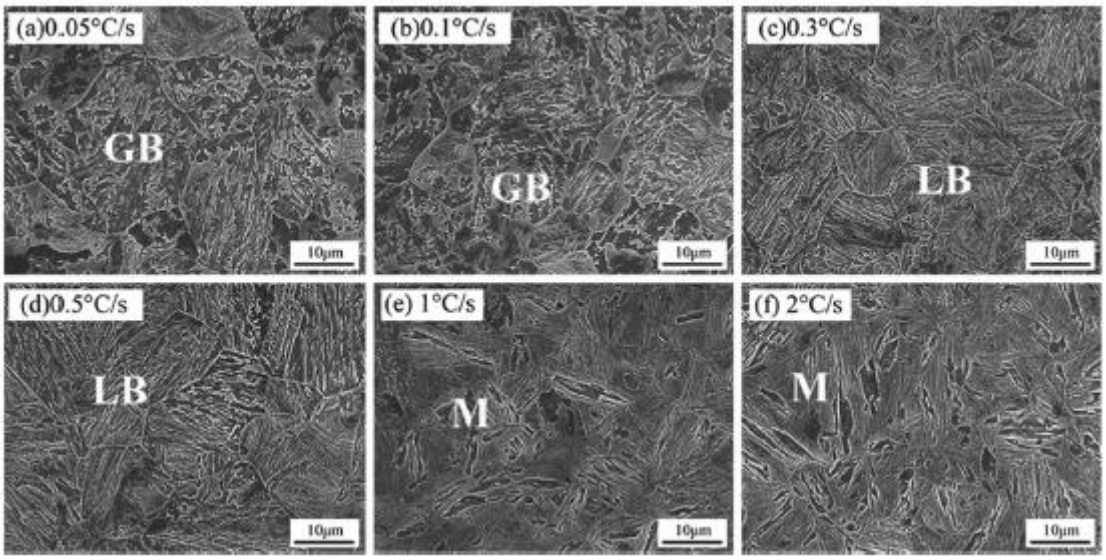

Figure. I. 30: Micrographs of the steel obtained after a nital 4 % etching observed by SEM with different cooling rates a) 0.05 °C/s ; b) 0.1 °C/s ; c) 0.13 °C/s ; d) 0.5 °C/s ; e) 1 °C/s ; b) 2 °C/s. GB: granular bainite ; LB: lath-like bainite ; M: martensite from [76].

Figure. I. 31 shows the EBSD maps obtained on the microstructures after 4 different cooling rates: 0.05 °C/s, 0.3 °C/s, 0.5 °C/s and 1 °C/s. Figure. I. 31 (a) to (d) show the Inverse Pole Figure maps of BCC phase (as bainitic ferrite and martensite). Figure. I. 31 (e) to (h) show the grain boundaries with misorientations between 2 ° and 15 ° in red and between 15 ° and 60 ° in black.

- At cooling rate of 0.05 °C/s (Figure. I. 31 (a) and (e)), the microstructure shows a granular morphology composed by large blocks of ferrite, which are separated by high angle grain boundaries with M/A islands.
- At cooling rate of 0.3 °C/s (Figure. I. 31 b) and f)), the microstructure is composed by packets of parallel laths (or plates) separated by high angle grain boundaries.
- At cooling rate of 0.5 °C/s (Figure. I. 31 (c) and (g)). The microstructure presents also a lath morphology but is finer than the one observed at 0.3 °C/s.
- At cooling rate of 1 °C/s (Figure. I. 31 (d) and (h), the microstructure is composed of martensite.

The fraction of retained austenite have been determined by XRD. The amount of retained austenite was shown to decrease with the increase in the cooling rate. The microstructure formed at low cooling rates thus contains a high proportion of blocky retained austenite (corresponding to M/A constituents). With the increase in the cooling rate, the proportion of M/A constituent decreases and the proportion of film-like austenite (more enriched in carbon) increases.

The histograms of misorientations presented in Figure. I. 31 (i) to (l) show that the proportion of High Angle Grain Boundaries (noted HAGBs) increases until 0.5 °C/s then decreases for higher cooling rates (formation of martensite). A high proportion of HAGBs can improve the toughness by preventing crack propagation.

The extensive study of Chen et al. [76] have shown the influence of cooling rates on:

- The phases formed during cooling. The higher the cooling rate, the lower the fraction of MA islands.
- The amount of retained austenite and their morphologies (blocky/films like and carbon content) and the impact on mechanical properties.
- The effect bainite morphologies and HAGBs proportion in the microstructure on mechanical properties. The higher the cooling rates, the higher the proportions of HAGBs (martensite and lower bainite).
- The increase in dislocation density in the BCC phase with the increase in the cooling rate.

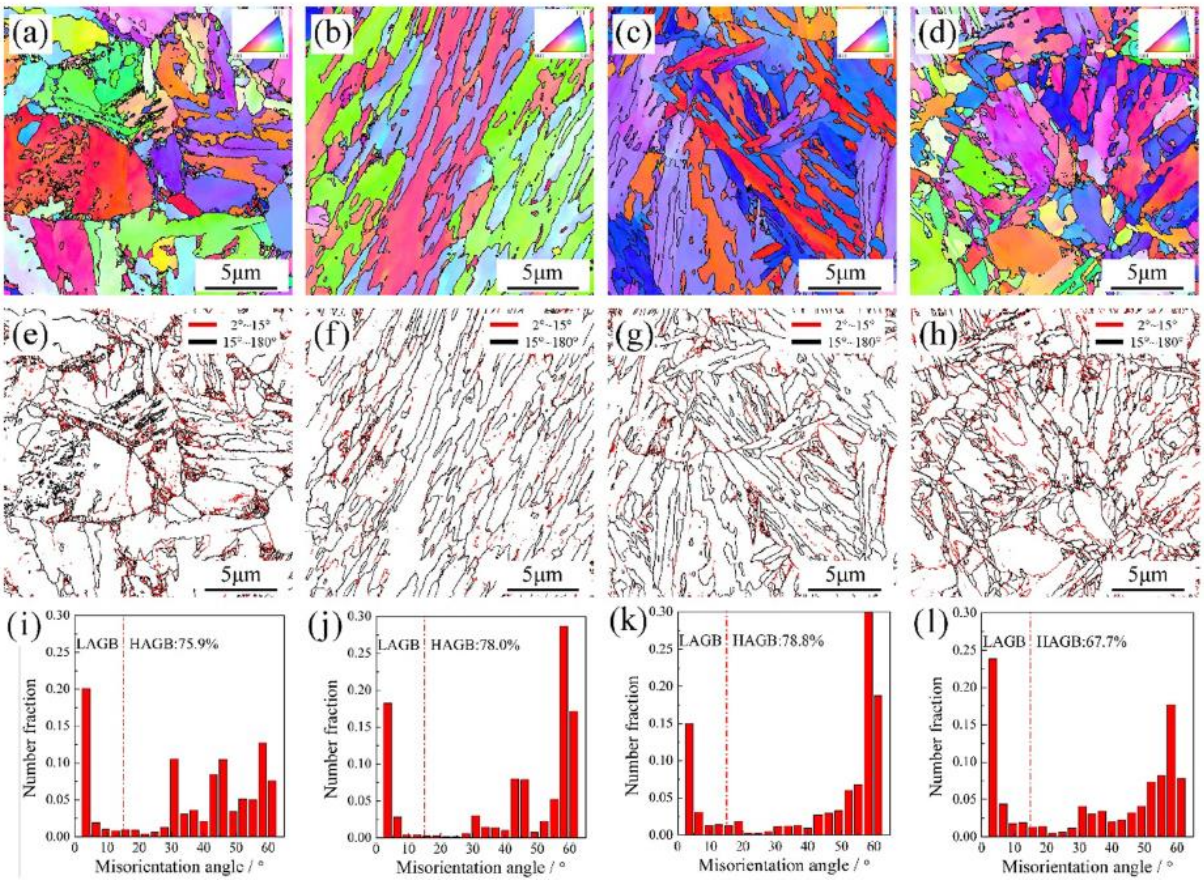

Figure. I. 31: EBSD Characterization of microstructures obtained at different cooling rates: 0.05 °C/s, 0.3 °C/s, 0.5 °C/s and 1 °C/s. (a)-(d) inverse pole figure ESBD maps ; (e)-(h) grain boundary ESBD maps ; (i)-(l) histogram of misorientations taken from [76].

IV.2. Kinetics and carbon partitioning

Reisinger et al. [71] have investigated the CFB transformation kinetics along continuous cooling schedules in a 0.28C-0.27Si-0.32Mn-0.43Cr-0.11Ni-2.82Mo-0.39V steel using High-Energy X-Ray Diffraction (HEXRD). We have also used this technique extensively in our study and the results will be presented in Chapter III.

Figure. I. 32 shows the evolution of the austenite (green) and bainite (red) mass fraction as function of temperature (in K) along continuous cooling treatments at 2 K/s (a)), 1 K/s (b)), 0.75 K/s (c)) and 0.43 K/s (d)). Along all cooling schedules, the fraction of bainite increases as a function of time when the temperature is decreasing, as during an isothermal holding with a global sigmoidal shape below B_S.

The authors have identified a systematic change in slope during the transformations. The temperature of this transition (2nd onset) depends on the cooling rate. This second stage of transformation is attributed to the carbon partitioning of austenite from the supersaturated bainite into coarse retained austenite islands. The mechanisms are still to be clarified. They also show that the fraction of the retained austenite at room temperature depends on the cooling rate and could present optimum (here at 0.75 K/s).

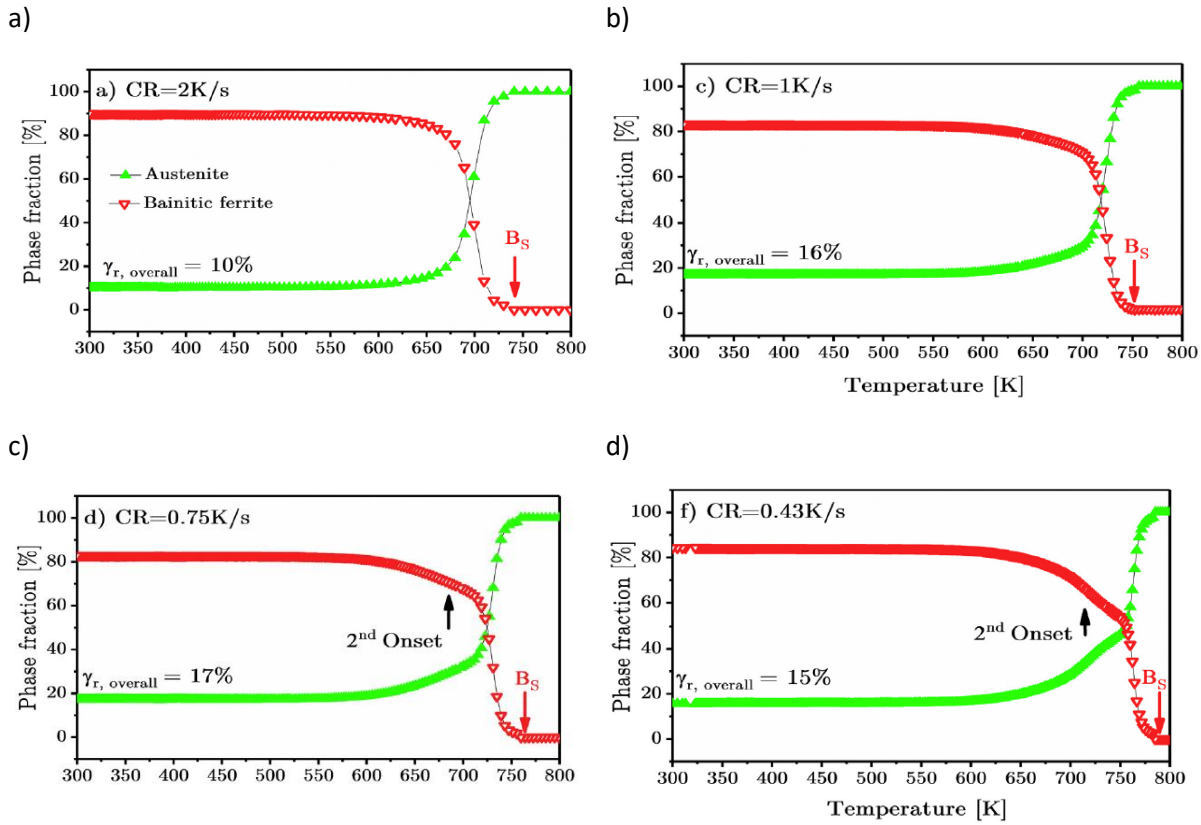

Figure. I. 32: Transformation kinetics of bainitic ferrite (red down triangles) and austenite (green up triangles) for continuous cooling experiments with a cooling rate of a) 2 K/s, b) 1 K/s, c) 0.75 K/s and d) 0.43 K/s.

Figure. I. 33 shows the evolution of carbon content in austenite as a function of the temperature and the FWHM (Full Width at Half Maximum) of the austenite (220) diffraction peak for two of the continuous cooling experiments presented above (2 K/s (Figure. I. 33 a) and 0.43 K/s (Figure. I. 33 b) respectively, reproduced from [71]).

The T_0' criterion with an additional elastic strain energy of 400 J/mol is represented in Figure. I. 33 by a dashed line. The author have chosen to represent also T_0' lines with an additional elastic strain energy of 950 J/mol for the slow cooling rate (0.43 K/s) and 1150 J/mol for the fast cooling rate (2 K/s).

The FWHM increases during bainite formation below the B_S temperature, then continues increasing at a much slower rate until a temperature of 600 K is reached, below which no significant evolution is noticed. In both experiments, the austenite carbon content increases with the decrease in the temperature during the bainite formation.

According to the authors, the carbon enrichment of austenite can be described by different stages. During the first stage, at high temperature, bainite starts to form below B_S. The austenite films are enriched by carbon partitioning but they are located between bainitic sub-units and represent a low fraction of the total austenite. As a consequence, the mean carbon content in austenite determined by HEXRD does not evolve.

During the second stage, carbon diffuses from the supersaturated bainitic ferrite into the remaining blocky austenite. This stage is short and presumably controlled by a modified T_0' criterion. For the experiment with a cooling rate of 0.43 K/s the austenite carbon enrichment seems to follow the T_0' line with an high elastic strain energy of 950 J/mol down to 725 K. For the experiment at 2 K/s, the

author claims surprisingly that the same situation applies with a modified energy of 1150 J/mol which is not obvious. In a third stage (starting at the 2nd onset), the modified T_0' criterion is no more verified and is accompanied by a long range diffusion of carbon into austenite islands. In their study, the local application of the T_0' criterion is difficult to believe, especially since it seems to be possible to verify itself throughout the processing in some cases and not at all in others (dependent on the cooling rate). On the other hand, they clearly show that the enrichment levels of austenite is highly sensitive to the cooling rate, as is the transformed fractions. However, in this study, the levels of carbon trapped in the bainite are not considered and discussed.

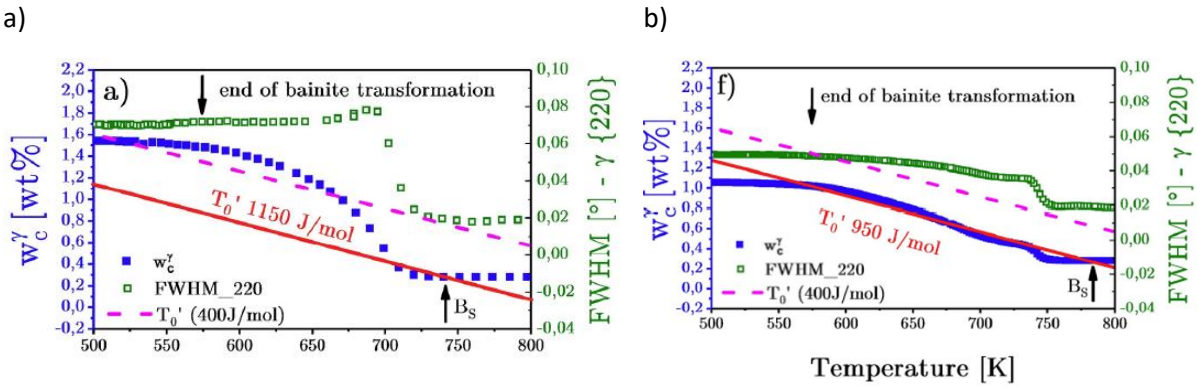

Figure. I. 33: Evolution of the austenite carbon content and FWHM of the (220) peak compared with the T_0' curve along a continuous cooling treatment with a cooling rate of a) 2 K/s and b) 0.43 K/s from [52].

The study and the understandings of anisothermal CFB transformations indeed present additional complexities compared to the isothermal CFB transformations. In fact, whatever the considered theory, transformation kinetics (nucleation/growth), thermodynamic conditions or kinetics explaining the "stasis", sizes and misorientations of microstructures, internal stresses on the phases scale are all dependent on the transformation temperatures. Modifying the temperature during the transformation will affect simultaneously all of those parameters.

Conclusion

The field of bainitic steels has been studied for a long time and a great deal of synthesis work has already been produced [2]. This bibliographical Chapter is therefore not intended to be exhaustive but to introduce the basic and essential concepts for understanding the bainite and Carbide-Free Bainite transformations, which are the heart of his work.

We will remember that:

- The bainite microstructures formed are complex, which may explain the relatively large number of attempts at proposing classifications. Two main type of classifications are in competition, those based on the phases and their morphologies, and those based on microtextures.
- A controversy persists on the fundamental nature of the bainitic transformation and its main feature, as the incomplete transformation phenomenon. Two schools of thought propose alternative explanations based either on diffusive or diffusionless mechanisms
- CFB transformations are highly sensitive to the transformation temperature. For isothermal transformations, the lower the transformation temperature, the finer the CFB microstructures. The incomplete transformation phenomenon imposes that the lower the transformation temperature, the more enriched in carbon is the retained austenite. As a consequence, at low temperature, the fraction of austenite is low but the austenite is very stable. The behavior of the steel is “bainitic”. At high temperature, the fraction is large but austenite can be unstable, leading to possible martensite transformation during final cooling. The behavior of the steel looks like the one of DP steels. An optimum can then be found between the fraction and the stability of retained austenite when an efficient TRIP effect can be tuned.
- The use of multistep processing allows a first approach to transformations in continuous cooling, highlighting many new questions compared to single-step experiments. The “stasis”, sizes and misorientations of microstructures, internal stresses are all dependent on the transformation temperatures. Modifying the temperature during the transformation affect simultaneously all of those parameters.
- For continuous cooling transformations, the cooling rate has a strong influence on the bainitic formation and the resulting microstructures. There are still many questions about transformation mechanisms (kinetics, stasis, enrichment, carbon balances). These questions will be addressed in part in this thesis work, but some complexities remain.

In this work, we will try to bring as factual as possible elements to contribute to the controversy about the nature of bainite. Our model will certainly be built on the basis of “diffusionless” theory, but these limits will be discussed, especially with regard to high temperatures in the bainitic nose. In the same way, we will systematically bring the elements to classify bainite without necessarily favoring a precise nomenclature.

References

[1] E. S. Davenport and E. C. Bain, “Transformation of austenite at constant subcritical temperatures,” *Metall. Mater. Trans. B*, vol. 1, no. 12, pp. 3503–3530, Dec. 1970, doi: 10.1007/BF03037892.

[2] H. K. D. H. Bhadeshia, *Bainite in steels: transformations, microstructure and properties*, 2. ed. London: IOM Communications, 2001.

[3] M. Takahashi, “Model for transition from upper to lovver bainite,” vol. 6, p. 12, 1990.

[4] S. A. Sajjadi and S. M. Zebarjad, “Isothermal transformation of austenite to bainite in high carbon steels,” *J. Mater. Process. Technol.*, vol. 189, no. 1–3, pp. 107–113, Jul. 2007, doi: 10.1016/j.jmatprotec.2007.01.011.

[5] R. Mehl, “Hardenability of alloy steels,” *ASM Met. Park OH*, vol. 1, 1939.

[6] H. Aaronson, “The mechanism of phase transformation in crystalline solids,” *Inst Met.*, vol. 270, 1969.

[7] Y. Ohmori, “The Crystallography of the Lower Bainite Transformation in a Plain Carbon Steel,” *Trans. Iron Steel Inst. Jpn.*, vol. 11, no. 2, pp. 95–101, 1971, doi: 10.2355/isijinternational1966.11.95.

[8] B. L. Bramfitt and J. G. Speer, “A perspective on the morphology of bainite,” *Metall. Trans. A*, vol. 21, no. 3, pp. 817–829, Mar. 1990, doi: 10.1007/BF02656565.

[9] Gourgues A.-F., H. M. Flower, and T. C. Lindley, “Electron backscattering diffraction study of acicular ferrite, bainite, and martensite steel microstructures,” *Mater. Sci. Technol.*, vol. 16, no. 1, pp. 26–40, Jan. 2000, doi: 10.1179/026708300773002636.

[10] S. Zajac, V. Schwinn, and K. H. Tacke, “Characterisation and Quantification of Complex Bainitic Microstructures in High and Ultra-High Strength Linepipe Steels,” *Mater. Sci. Forum*, vol. 500–501, pp. 387–394, Nov. 2005, doi: 10.4028/www.scientific.net/MSF.500-501.387.

[11] T. Furuhara, H. Kawata, S. Morito, and T. Maki, “Crystallography of upper bainite in Fe–Ni–C alloys,” *Mater. Sci. Eng. A*, vol. 431, no. 1–2, pp. 228–236, Sep. 2006, doi: 10.1016/j.msea.2006.06.032.

[12] N. Takayama, G. Miyamoto, and T. Furuhara, “Effects of transformation temperature on variant pairing of bainitic ferrite in low carbon steel,” *Acta Mater.*, vol. 60, no. 5, pp. 2387–2396, Mar. 2012, doi: 10.1016/j.actamat.2011.12.018.

[13] M. Ben Haj Slama, N. Gey, L. Germain, K. Zhu, and S. Allain, “Key Parameters to Promote Granularization of Lath-Like Bainite/Martensite in FeNiC Alloys during Isothermal Holding,” *Materials*, vol. 11, no. 10, p. 1808, Sep. 2018, doi: 10.3390/ma11101808.

[14] A. Hultgren, “Isothermal transformation of austenite,” *Trans. Am. Soc. Met.*, vol. 39, pp. 915–1005, 1947.

[15] T. Ko and S. Cottrell, “The formation of bainite,” *J. Iron Steel Inst.*, vol. 172, no. 3, p. 307, 1952.

[16] V. M. Khlestov, E. V. Konopleva, and H. J. Mcqueen, “Kinetics of Austenite Transformation During Thermomechanical Processes,” *Can. Metall. Q.*, vol. 37, no. 2, pp. 75–89, Apr. 1998, doi: 10.1179/cmq.1998.37.2.75.

[17] S. M. C. Van Bohemen, “Modeling Start Curves of Bainite Formation,” *Metall. Mater. Trans. A*, vol. 41, no. 2, pp. 285–296, Feb. 2010, doi: 10.1007/s11661-009-0106-9.

[18] D. H. Kim, J. G. Speer, H. S. Kim, and B. C. D. Cooman, “Observation of an Isothermal Transformation during Quenching and Partitioning Processing,” *Metall. Mater. Trans. A*, p. 13.

[19] M. Oka and H. Okamoto, “Swing back in kinetics nearM s in hypereutectoid steels,” *Metall. Trans. A*, vol. 19, no. 3, pp. 447–452, Mar. 1988, doi: 10.1007/BF02649258.

[20] F. Caballero *et al.*, “New advanced ultra high strength bainitic steels: ductility and formability (DUCTAFORM),” *Res. Fund Coal Steel*, 2013.

[21] A. Navarro-López, J. Sietsma, and M. J. Santofimia, “Effect of Prior Athermal Martensite on the Isothermal Transformation Kinetics Below M s in a Low-C High-Si Steel,” *Metall. Mater. Trans. A*, vol. 47, no. 3, pp. 1028–1039, Mar. 2016, doi: 10.1007/s11661-015-3285-6.

[22] A. M. Ravi, A. Navarro-López, J. Sietsma, and M. J. Santofimia, “Influence of martensite/austenite interfaces on bainite formation in low-alloy steels below M,” *Acta Mater.*, vol. 188, pp. 394–405, Apr. 2020, doi: 10.1016/j.actamat.2020.02.003.

[23] C. Rampelberg, S. Y. P. Allain, G. Geandier, J. Teixeira, F. Lebel, and T. Sourmail, “Carbide-Free Bainite Transformations Above and Below Martensite Start Temperature Investigated by In-Situ High-Energy X-Ray Diffraction,” *JOM*, vol. 73, no. 11, pp. 3181–3194, Nov. 2021, doi: 10.1007/s11837-021-04903-8.

[24] L. C. D. Fielding, “The Bainite Controversy,” *Mater. Sci. Technol.*, vol. 29, no. 4, pp. 383–399, Apr. 2013, doi: 10.1179/1743284712Y.0000000157.

[25] H. I. Aaronson, W. T. Reynolds, G. J. Shiflet, and G. Spanos, “Bainite viewed three different ways,” *Metall. Trans. A*, vol. 21, no. 6, pp. 1343–1380, Jun. 1990, doi: 10.1007/BF02672557.

[26] M. Hillert, “The Nature of Bainite.,” *ISIJ Int.*, vol. 35, no. 9, pp. 1134–1140, 1995, doi: 10.2355/isijinternational.35.1134.

[27] D. Quidort and Y. J. Brechet, “A model of isothermal and non isothermal transformation kinetics of bainite in 0.5% C steels,” *ISIJ Int.*, vol. 42, no. 9, pp. 1010–1017, 2002.

[28] W. W. Sun, H. S. Zurob, and C. R. Hutchinson, “Coupled solute drag and transformation stasis during ferrite formation in Fe-C-Mn-Mo,” *Acta Mater.*, vol. 139, pp. 62–74, Oct. 2017, doi: 10.1016/j.actamat.2017.08.010.

[29] Z. Yang, W. Xu, Z. Yang, C. Zhang, and S. van der Zwaag, “A 2D analysis of the competition between the equiaxed ferritic and the bainitic morphology based on a Gibbs Energy Balance approach,” *Acta Mater.*, vol. 105, pp. 317–327, Feb. 2016, doi: 10.1016/j.actamat.2015.12.040.

[30] A. M. Ravi, J. Sietsma, and M. J. Santofimia, “Exploring bainite formation kinetics distinguishing grain-boundary and autocatalytic nucleation in high and low-Si steels,” *Acta Mater.*, vol. 105, pp. 155–164, Feb. 2016, doi: 10.1016/j.actamat.2015.11.044.

[31] S. M. C. van Bohemen and J. Sietsma, “Modeling of isothermal bainite formation based on the nucleation kinetics,” *Int. J. Mater. Res.*, vol. 99, no. 7, pp. 739–747, Jul. 2008, doi: 10.3139/146.101695.

[32] H. Matsuda and H. K. D. H. Bhadeshia, “Kinetics of the bainite transformation,” *Proc. R. Soc. Lond. Ser. Math. Phys. Eng. Sci.*, vol. 460, no. 2046, pp. 1707–1722, Jun. 2004, doi: 10.1098/rspa.2003.1225.

[33] G. I. Rees, “Bainite transformation Part 1 Modified model,” vol. 8, p. 9, 1992.

[34] S. M. C. van Bohemen, “Bainite growth retardation due to mechanical stabilisation of austenite,” *Materialia*, vol. 7, p. 100384, Sep. 2019, doi: 10.1016/j.mtla.2019.100384.

[35] D. Quidort and Y. J. M. Brechet, “Isothermal growth kinetics of bainite in 0.5% C steels,” *Acta Mater.*, vol. 49, no. 20, pp. 4161–4170, 2001.

[36] D. Quidort and Y. Bréchet, “The role of carbon on the kinetics of bainite transformation in steels,” *Scr. Mater.*, vol. 47, no. 3, pp. 151–156, 2002.

[37] J.-C. Hell, “Aciers bainitiques sans carbure: caractérisations microstructurale multi-échelle et in situ de la transformation austénite-bainite et relations entre microstructure et comportement mécanique,” PhD Thesis, Metz, 2011.

[38] J.-C. Hell, M. Dehmas, S. Allain, J. M. Prado, A. Hazotte, and J.-P. Chateau, “Microstructure – Properties Relationships in Carbide-free Bainitic Steels,” *ISIJ Int.*, vol. 51, no. 10, pp. 1724–1732, 2011, doi: 10.2355/isijinternational.51.1724.

[39] H. Kitahara, R. Ueji, N. Tsuji, and Y. Minamino, “Crystallographic features of lath martensite in low-carbon steel,” *Acta Mater.*, vol. 54, no. 5, pp. 1279–1288, Mar. 2006, doi: 10.1016/j.actamat.2005.11.001.

[40] S. Allain, “Allain S., McMaster Workshop on Advanced High strength Steels (2010).”

[41] J. Tian, G. Xu, Z. Jiang, M. Zhou, H. Hu, and Q. Yuan, “Transformation Behavior of Bainite during Two-step Isothermal Process in an Ultrafine Bainite Steel,” *ISIJ Int.*, vol. 58, no. 10, pp. 1875–1882, Oct. 2018, doi: 10.2355/isijinternational.ISIJINT-2018-187.

[42] F. G. Caballero, S. Allain, J. Cornide, J. D. Puerta Velásquez, C. Garcia-Mateo, and M. K. Miller, "Design of cold rolled and continuous annealed carbide-free bainitic steels for automotive application," *Mater. Des.*, vol. 49, pp. 667–680, Aug. 2013, doi: 10.1016/j.matdes.2013.02.046.
[43] E. Kozeschnik and H. K. D. H. Bhadeshia, "Influence of silicon on cementite precipitation in steels," *Mater. Sci. Technol.*, vol. 24, no. 3, pp. 343–347, Mar. 2008, doi: 10.1179/174328408X275973.
[44] J. Tian, G. Xu, Z. Jiang, X. Wan, H. Hu, and Q. Yuan, "Transformation Behavior and Properties of Carbide-Free Bainite Steels with Different Si Contents," *Steel Res. Int.*, vol. 90, no. 3, p. 1800474, Mar. 2019, doi: 10.1002/srin.201800474.
[45] N. Fonstein, *Advanced high strength sheet steels*. Springer, 2015.
[46] L. Guo, H. K. D. H. Bhadeshia, H. Roelofs, and M. I. Lembke, "In situ synchrotron X-ray study of bainite transformation kinetics in a low-carbon Si-containing steel," *Mater. Sci. Technol.*, vol. 33, no. 17, pp. 2147–2156, Nov. 2017, doi: 10.1080/02670836.2017.1353669.
[47] W. T. Reynolds, S. K. Liu, F. Z. Li, S. Hartfield, and H. I. Aaronson, "An investigation of the generality of incomplete transformation to bainite in Fe-C-X alloys," *Metall. Trans. A*, vol. 21, no. 6, pp. 1479–1491, Jun. 1990, doi: 10.1007/BF02672563.
[48] G. R. Purdy and Y. J. M. Brechet, "A solute drag treatment of the effects of alloying elements on the rate of the proeutectoid ferrite transformation in steels," *Acta Metall. Mater.*, vol. 43, no. 10, pp. 3763–3774, Oct. 1995, doi: 10.1016/0956-7151(95)90160-4.
[49] F. G. Caballero, M. K. Miller, and C. Garcia-Mateo, "Carbon supersaturation of ferrite in a nanocrystalline bainitic steel," *Acta Mater.*, vol. 58, no. 7, pp. 2338–2343, Apr. 2010, doi: 10.1016/j.actamat.2009.12.020.
[50] C. Garcia-Mateo, F. G. Caballero, M. K. Miller, and J. A. Jimenez, "On measurement of carbon content in retained austenite in a nanostructured bainitic steel," *J. Mater. Sci.*, vol. 47, no. 2, pp. 1004–1010, Jan. 2012, doi: 10.1007/s10853-011-5880-2.
[51] C. Garcia-Mateo *et al.*, "Low temperature bainitic ferrite: Evidence of carbon super-saturation and tetragonality," *Acta Mater.*, vol. 91, pp. 162–173, Jun. 2015, doi: 10.1016/j.actamat.2015.03.018.
[52] I. Pushkareva *et al.*, "The Influence of Vanadium Additions on Isothermally Formed Bainite Microstructures in Medium Carbon Steels Containing Retained Austenite," *Metals*, vol. 10, no. 3, p. 392, Mar. 2020, doi: 10.3390/met10030392.
[53] T. Sourmail and V. Smanio, "Low temperature kinetics of bainite formation in high carbon steels," *Acta Mater.*, vol. 61, no. 7, pp. 2639–2648, Apr. 2013, doi: 10.1016/j.actamat.2013.01.044.
[54] V. Bordereau, "Relations quantitatives entre composition chimique, microstructure et propriétés mécaniques d'aciers bainitiques," PhD Thesis, Paris, ENMP, 2015.
[55] M. Zhou, G. Xu, J. Tian, H. Hu, and Q. Yuan, "Bainitic Transformation and Properties of Low Carbon Carbide-Free Bainitic Steels with Cr Addition," *Metals*, vol. 7, no. 7, p. 263, Jul. 2017, doi: 10.3390/met7070263.
[56] P. Abbaszadeh, S. Kheirandish, H. Saghafian, and M. hossein Goodarzy, "Effect of Austenitizing Temperature on Mechanical Properties of the Mixed Bainite - Martensite Microstructure in CrMoV Steel," *Mater. Res.*, vol. 21, no. 1, Nov. 2017, doi: 10.1590/1980-5373-mr-2017-0469.
[57] A. Kamada, N. Koshizuka, and T. Funakoshi, "Effect of Austenite Grain Size and C Content on the Substructure and Toughness of Tempered Martensite and Bainite," *Trans. Iron Steel Inst. Jpn.*, vol. 16, no. 8, pp. 407–416, Aug. 1976, doi: 10.2355/isijinternational1966.16.407.
[58] K. Sugimoto, J. Sakaguchi, T. Iida, and T. Kashima, "Stretch-flangeability of a High-strength TRIP Type Bainitic Sheet Steel.," *ISIJ Int.*, vol. 40, no. 9, pp. 920–926, 2000, doi: 10.2355/isijinternational.40.920.
[59] G. I. Rees and H. K. D. H. Bhadeshia, "Bainite transformation Part 1 Modified model," *Mater Sci Technol*, vol. 8, p. 965, 1992.
[60] A. Lambert-Perlade, "Rupture par clivage de microstructures d'aciers bainitiques obtenues en conditions de soudage," PhD Thesis, École Nationale Supérieure des Mines de Paris, 2001.
[61] K. Sugimoto, A. Kanda, R. Kikuchi, S. Hashimoto, T. Kashima, and S. Ikeda, "Ductility and Formability of Newly Developed High Strength Low Alloy TRIP-aided Sheet Steels with Annealed Martensite Matrix.," *ISIJ Int.*, vol. 42, no. 8, pp. 910–915, 2002, doi: 10.2355/isijinternational.42.910.

[62] F. Hassani and S. Yue, “Comparison of bainitic TRIP and dual phase microstructures,” in *41 st Mechanical Working and Steel Processing Conference*, 1999, pp. 493–498.
[63] K. Sugimoto, K. Nakano, S.-M. Song, and T. Kashima, “Retained austenite characteristics and stretch-flangeability of high-strength low-alloy TRIP type bainitic sheet steels,” *ISIJ Int.*, vol. 42, no. 4, pp. 450–455, 2002.
[64] K. Hase, C. Garcia-Mateo, and H. K. D. H. Bhadeshia, “Bimodal size-distribution of bainite plates,” *Mater. Sci. Eng. A*, vol. 438–440, pp. 145–148, Nov. 2006, doi: 10.1016/j.msea.2005.12.070.
[65] X. L. Wang, K. M. Wu, F. Hu, L. Yu, and X. L. Wan, “Multi-step isothermal bainitic transformation in medium-carbon steel,” *Scr. Mater.*, vol. 74, pp. 56–59, Mar. 2014, doi: 10.1016/j.scriptamat.2013.10.019.
[66] W. Lei, T. S. Wang, Z. Li, X. J. Zhang, Q. F. Wang, and F. C. Zhang, “A new process to fabricate ultrafine-grained low-carbon steel with high strength and high elongation,” *Mater. Sci. Eng. A*, vol. 528, no. 2, pp. 784–787, Dec. 2010, doi: 10.1016/j.msea.2010.09.072.
[67] J. Zhao, C. S. Hou, G. Zhao, T. Zhao, F. C. Zhang, and T. S. Wang, “Microstructures and Mechanical Properties of Bearing Steels Modified for Preparing Nanostructured Bainite,” *J. Mater. Eng. Perform.*, vol. 25, no. 10, pp. 4249–4255, Oct. 2016, doi: 10.1007/s11665-016-2289-8.
[68] J. Zhao *et al.*, “Transformation behavior and microstructure feature of large strain ausformed low-temperature bainite in a medium C - Si rich alloy steel,” *Mater. Sci. Eng. A*, vol. 682, pp. 527–534, Jan. 2017, doi: 10.1016/j.msea.2016.11.073.
[69] G. Mao, R. Cao, C. Cayron, X. Mao, R. Logé, and J. Chen, “Effect of cooling conditions on microstructures and mechanical behaviors of reheated low-carbon weld metals,” *Mater. Sci. Eng. A*, vol. 744, pp. 671–681, Jan. 2019, doi: 10.1016/j.msea.2018.12.035.
[70] F. G. Caballero, M. J. Santofimia, C. Capdevila, C. García-Mateo, and C. García de Andrés, “Design of Advanced Bainitic Steels by Optimisation of TTT Diagrams and T0 Curves,” *ISIJ Int.*, vol. 46, no. 10, pp. 1479–1488, 2006, doi: 10.2355/isijinternational.46.1479.
[71] S. Reisinger *et al.*, “Strain energy contributions on the bainitic phase transformation in a CrMoV steel during continuous cooling,” *Mater. Des.*, vol. 155, pp. 475–484, Oct. 2018, doi: 10.1016/j.matdes.2018.06.014.
[72] S. Allain and T. Iung, “Development of hot rolled copper/nickel alloyed TRIP steels with carbide-free bainitic matrix,” *Rev. Métallurgie*, vol. 105, no. 10, pp. 520–530, Oct. 2008, doi: 10.1051/metal:2008068.
[73] F. G. Caballero, C. GarcíA-Mateo, J. Chao, M. J. Santofimia, C. Capdevila, and C. G. de Andrés, “Effects of Morphology and Stability of Retained Austenite on the Ductility of TRIP-aided Bainitic Steels,” *ISIJ Int.*, vol. 48, no. 9, pp. 1256–1262, 2008, doi: 10.2355/isijinternational.48.1256.
[74] S. Hashimoto, S. Ikeda, K. Sugimoto, and S. Miyake, “Effects of Nb and Mo Addition to 0.2%C-1.5%Si-1.5%Mn Steel on Mechanical Properties of Hot Rolled TRIP-aided Steel Sheets,” *ISIJ Int.*, vol. 44, no. 9, pp. 1590–1598, 2004, doi: 10.2355/isijinternational.44.1590.
[75] M. B. H. Slama, “Étude multi-échelle et in situ des évolutions microstructurales en conditions isothermes d’aciers bainitiques en lattes,” PhD Thesis, Université de Lorraine, 2018.
[76] X. Chen, F. Wang, C. Li, and J. Zhang, “Dynamic continuous cooling transformation, microstructure and mechanical properties of medium-carbon carbide-free bainitic steel,” *High Temp. Mater. Process.*, vol. 39, no. 1, pp. 304–316, Jul. 2020, doi: 10.1515/htmp-2020-0051.

Chapter II: Materials and methods

Introduction

In this Chapter, we will describe first how the studied steel was produced and manufactured by Ascometal, the industrial partner of the project, prior to the experiments conducted during the PhD. In the second section, we will present the High-Energy X-Ray Diffraction (HEXRD) procedure which have been used to charaterize in situ its phase transformations along different imposed temperature cycles. The experimental configuration will be detailed as well the procedures to analyse the diffraction patterns. In the last section of the Chapter, the technics used to characterize the microstructures at room temperature will be presented. These latter examinations were conducted on the samples heat-treated during HEXRD experiments using Scanning Electron Microscopy (SEM) and the SEM coupled with Electron BackScattered Diffraction (EBSD). Additionnal hardness tests were performed also to evaluate the basic mechanical properties of the produced microstructures.

I. Materials

I. 1. Initial state and chemical composition of the studied industrial steel

The studied steel is produced commercially by Ascometal [1] as hot-rolled bar (⌀ 40 mm) and has for a base chemical composition 0.27C-1.5Mn-1.2Si-0.8Cr (wt.%) (called MC2). Other microalloying elements are also present but aren't communicated in this report for the sake of confidentiality. Nevertheless, they are not supposed to affect the results and the conclusions of this work. Two other steelswere investigated during the PhD but are not presented in this thesis.

The composition has been designed to produce carbide-free bainitic microstructures after forging operations. As explained in Chapter I, it must contain a significant carbon content to help stabilizing the austenite by partition during the bainitic transformation. Thanks to the addition of silicon, carbide precipitation is postponed during this latter transformation. Manganese and Chromium help to increase the hardenability of the steel and to avoid a possible proeutectoid ferritic transformation during the continuous cooling. Manganese content have a strong known effect also on the transformation stasis [2], [3] and on the T_0 curve.

Figure. II. 1 shows the Index Quality and Inverse Pole Figure maps of the ferritic phase on the microstructure of the commercial product (after hot-rolling at mid-radius of the bar) observed by SEM-EBSD. It seems to us appropriate to present this first result now so that the reader can appreciate the nature of the initial microstructure even if the elements for discussing in details this outcome will be presented later in Chapter II and in Chapter IV. The microstructure at the initial state is composed with coarse bainite plates (corresponding to a transformation at high temperatures) and some areas ressembling to Martensite-Austenite (MA) islands (islands with a dark contrast in the IQ map). HEXRD measurements at room temperature show that the fraction of austenite is about 15 wt.%. The estimated Prior Austenite Grain size is about 45 µm. The microstructure is thus already carbide-free bainite before the forging operation itself, which is not surpsinsing as the cooling schedule after hot rolling is quite similar to the one of forging.

This initial microstructure have been then heat treated to investigate its evolution along different thermal treatments mimicking industrial forging practices (or for knowledge building purposes) using

in situ and post mortem characterization methods. The effect of the forging strain has not be considered in the study as it occurs far above the non-recrystallization temperature of the alloy. Hence, the austenite microstructure is perfectly recrytallized before any phase transformation and the PAG morphology is hardly affected by the process.

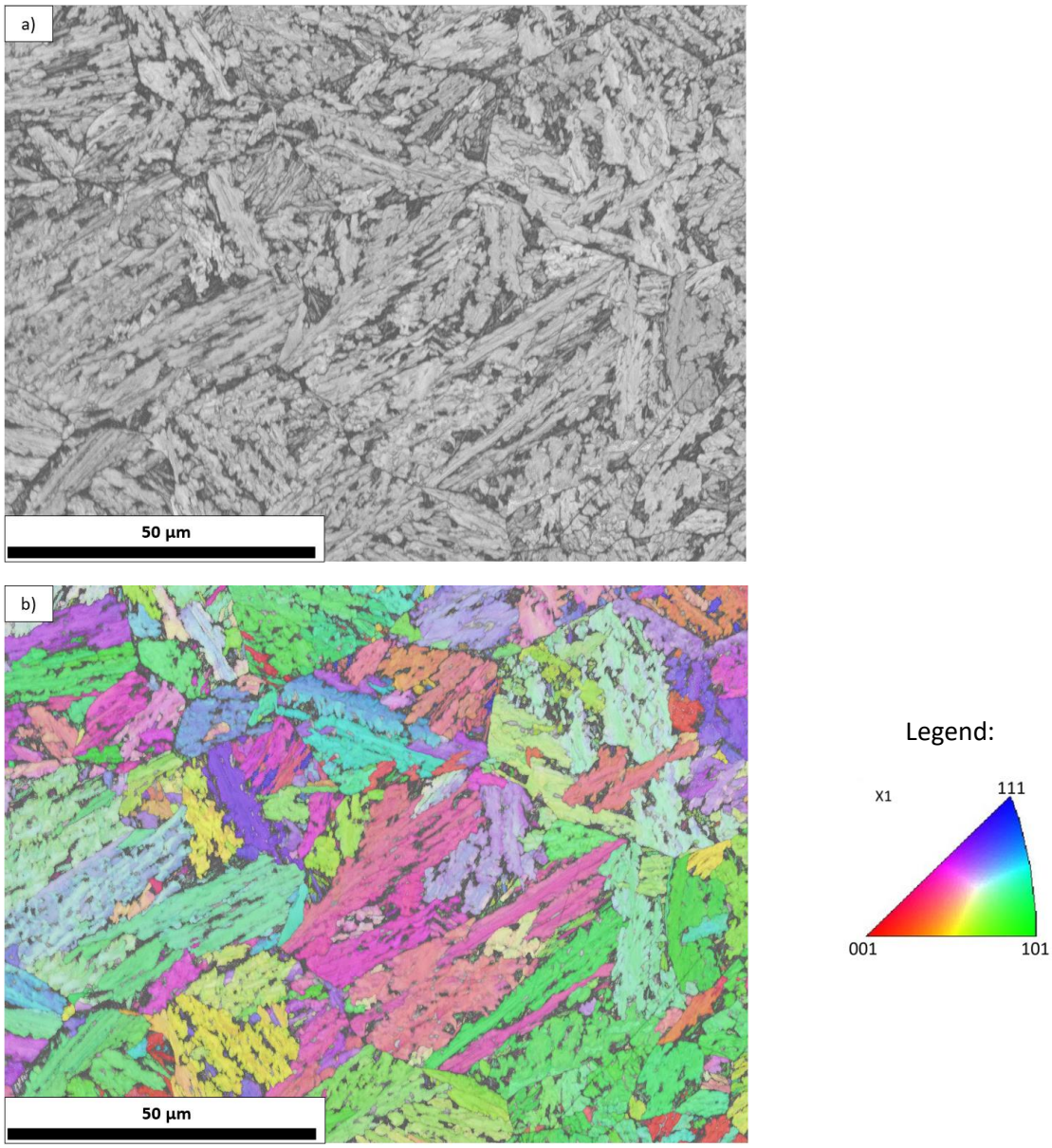

Figure. II. 1: Microstructure of the studied industrial steel after hot-rolling, prior to any forging operation observed by SEM-EBSD. a) IQ map (Index Quality map), b) corresponding IPF (Inverse Pole Figure) map of ferritic phases in the X direction.

II. In situ HEXRD experiments on synchrotron beamlines

The main in situ investigation method that was deployed during this thesis work consists of HEXRD experiments on synchrotron beamline. Such experiments consist in subjecting a steel sample to a thermal cycle using a controlled furnace (in this, case a dilatometer) while illuminating it with a monochromatic beam of high-energy photons. The diffraction patterns obtained from the bulk sample are then recorded by a 2D detector downstream of the sample.

II. 1. Sample Environment

II.1.a. Dilatometer set-up

The dilatometer used for the in situ experiments is a Bähr 805A/D located at DESY on PETRA III P07 line. It is equipped with an induction heating system located in a closed box under secondary vacuum (10^{-5} mbar) in order to limit oxidation phenomena during heating and at high temperature in the austenitic domain. Cooling is obtained by a helium or argon gas blowing system allowing to reach high cooling rates. The temperature is controlled by the mean of a thermocouple of type S welded at the middle of the cylindrical specimens (just above the incident synchrotron X-ray beam). The specimens of dimension 10 x 4 x 4 mm^3 were taken at mid-radius from rolled bars (⌀ 40 mm). The length variation is measured with alumina rods, this variation is transmitted to a LVDT (Linear Variable Differential Transformer) device. The heating chamber of the Bähr dilatometer is shown in Figure. II. 2.

It must be mentioned that different dilatometry tests were also realized at CREAS, the research center of Ascometal, to prepare our experiments off line. The two dilatometers are almost identical, except that the rod which is in silica at CREAS and in alumina at DESY. The second difference relies in the spire spacing which permits the incident beam and diffracted signal not to interact with the inductor. Except the experiments carried out at CREAS, the dilatometer signal has not been considered further to analyze phase transformations process, as it is less reliable than the HEXRD measurement.

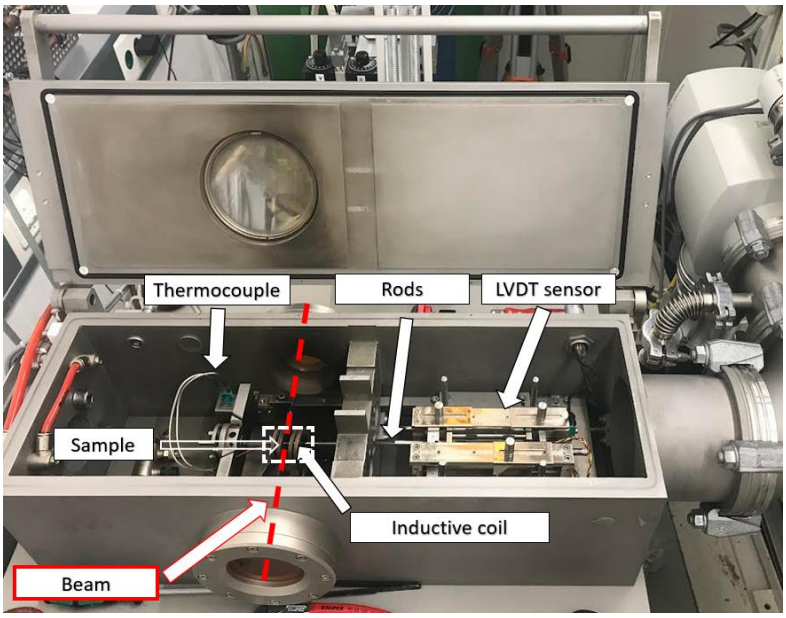

Figure. II. 2: Bähr dilatometer designed for in situ experiments at PETRA. The beam path is represented by a red dashed line.

Three types of heat treatments have been performed. They all starts with a full austenitization at high temperature followed by different cooling sequences:

- a single isothermal holding (single step experiment) followed by a rapid cooling down to room temperature
- a succession of isothermal holdings at different but decreasing temperatures (multistep experiments) followed by a rapid cooling down to room temperature
- a continuous cooling down to room temperature at a controlled and constant rate.

In the following, these cycles (temperature, time, cooling rate) will be briefly detailed below but the choice of the conditions will be justified on metallurgical basis only in the Chapter III.

II.1.b. Single step experiments

Figure. II. 3 shows the thermal schedules (temperature as a function of time) followed during single-step experiments. All these thermal treatments started with an austenitic soaking at 3 °C/s up to 1150 °C for 3 minutes. The reference time (t = 0) is set at the end of the austenitization stage. The transition between all the isothermal steps is performed at 50 °C/s. For such experiment, the isothermal holding temperatures are in a range between 300 °C and 475 °C and holding time is set up at 20 minutes. The experiments will be denoted as ISO_XXX with XXX corresponding to the temperature holding (XXX = 300, 350, 400, 450 or 475°C). Isothermal holdings are followed by a cooling down to room temperature (with a cooling rate of 50 °C/s). Other experiments were performed with longer holding times (5h at 300°C and 350°C respectively).

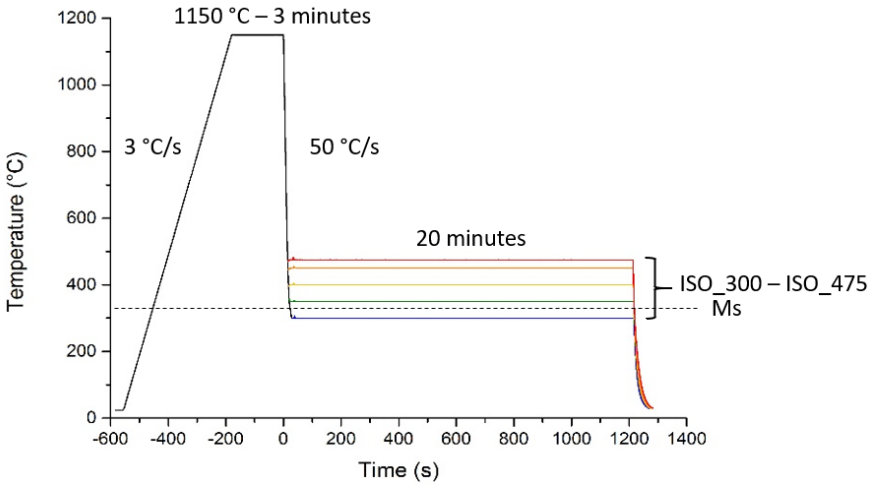

Figure. II. 3: Heat treatments performed on the studied steel to study in situ by HEXRD the bainitic transformations in isothermal conditions (ISO_300 to ISO_475 experiments according to the nomenclature described in the text).

II.1.c. Multistep experiments

Figure. II. 4 a) and b) show the thermal schedules followed to conduct two-step and three-step holding sequences respectively. The thermal treatments is composed by an austenitization at 1150 °C during 3 minutes. As for isothermal experiments, the reference time (t = 0) is set at the end of the austenitization stage.

The first two-step holding sequence is composed of steps at 400 °C and 300 °C respectively with a holding time of 1200 seconds for each step (pink). This condition is denoted as **2ST_L** corresponding to a two-step treatment with a **Long** duration time of the first step.

The second multistep is composed with two steps also, the first step with a holding time around 70 seconds and at 300 °C with a holding time of 1200 seconds. This treatment is denoted as **2ST_S** corresponding to a **Short** duration time of the first step.

For the first three-step holding sequence, the schedule presents steps at 475 °C, 400 °C and 300 °C with a holding time of 1200 seconds for each step (grey). This condition is later denoted as **3ST_L** corresponding to a three-step treatment with a **Long** duration time of the first step.

The second schedule presents three steps at 475 °C with a holding time of 114 seconds, 400 °C and 300 °C with a holding time of 1200 seconds for each step. This condition is later denoted as **3ST_S** corresponding to a three-step treatment with a **Short** duration time of the first step.

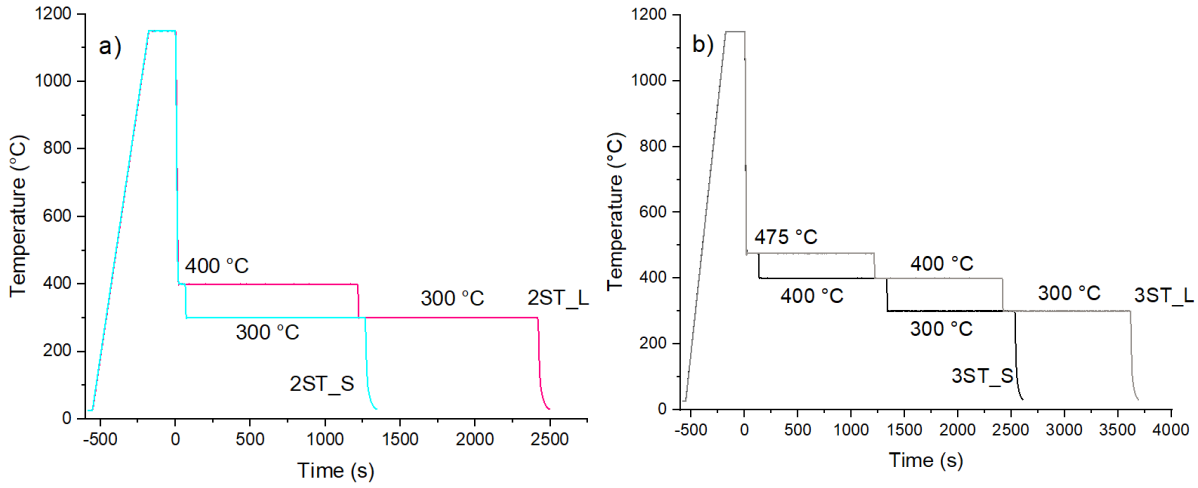

Figure. II. 4: Heat treatments for multistep experiments a) two-step experiments b) three-step experiments (named 2ST_L, 2ST_S, 3ST_L, 3ST_S experiments respectively according to the nomenclature described in the text).

II.1.d. Continuous cooling treatment at 0.3 °C/s and its associated equivalent multistep treatments

To mimic the air cooling sequence encountered during an industrial forging process, a thermal treatment with a reference cooling rate of 0.3 °C/s is simulated as represented in Figure. II. 5. To avoid the ferrite formation, a fast cooling down to 550 °C is performed before the slow cooling down to room temperature. This treatment is denoted as CC_0.3 in the following. Moreover, we performed a multistep experiment, which is a succession of 7 isothermal steps to mimic a continuous cooling condition at 0.3 °C/s named ST_0.3. Both thermal treatments are presented in Figure. II. 5 (the dark red curve for the ST_0.3 cooling sequences and the purple curve for the CC_0.3). This heat treatment is a step by step decomposition of a continuous cooling sequence with a mean cooling rate of 0.3 °C/s.

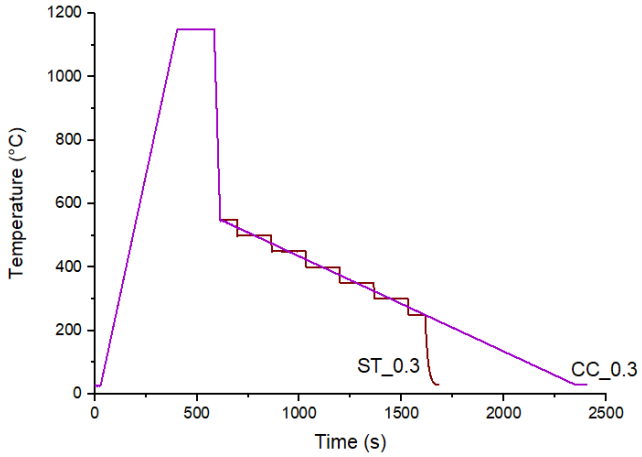

Figure. II. 5: Heat treatments for a continuous cooling with a cooling rate at 0.3 °C/s (purple) and an equivalent multistep (dark red) conditions (CC_0.3 and ST_0.3 experiments according to the nomenclature described in the text).

II.1.e. Thermal treatments conduced in continuous cooling with a cooling rate at 0.1 °C/s and 0.5 °C/s

The thermal schedule with a cooling rate at 0.3°C/s simulates the air cooling representative of the forging process (mean value). Two other cooling rates were also performed to simulate the cooling sequence at the center of a part (at 0.1 °C/s and named CC_0.1) and close to the surface of a part (0.5 °C/s and named CC_0.5) during air cooling. To avoid the ferrite formation, a fast cooling down to 550 °C is again performed before the slow cooling to room temperature. Figure. II. 6 shows the continuous cooling experiments conducted at 3 different cooling rates (0.1 °C/s, 0.3 °C/s and 0.5 °C/s).

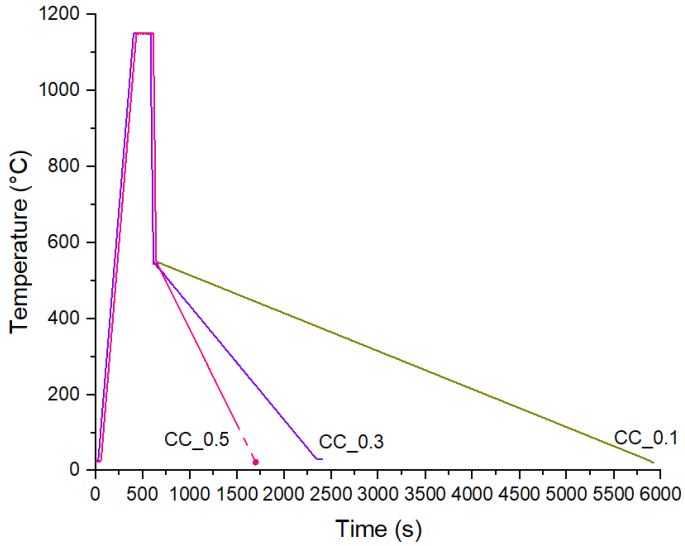

Figure. II. 6: Continuous cooling sequences with cooling rate of 0.1 °C/s, 0.3 °C/s and 0.5 °C/s (CC_0.1, CC_0.3 and CC_0.5 experiments according to the nomenclature described in the text).

We performed a total of 124 experiments, including 110 heat treatments on the three steels of the study and including in situ tensile tests and mapping of industrial parts, which will not be presented in this manuscript. The analysis of these data was conducted with the help of a master intern during 6 months (Fanta Kaba) and one industrial project at Mines Nancy (Clément Lintilhac, Mahel Voulhoux, Nicolas Liouville). All these experiments represent a total of about 6 Tera bytes of data. In this manuscript, we will present only 23 on the 38 experiments conducted on alloy MC2 in total.

II.2. High Energy X-Ray Diffraction

II.2.a. Experimental set-up

In situ High Energy X-Ray Diffraction Experiments (HEXRD) were realized at DESY (Deutsches Elektronen-Synchrotron) at Hamburg, Germany, on the P07 beamline in PETRA III. Two main campaigns have been organized in May 2019 and in May 2021 and were located to two different experimental hutches (EH3 and EH1) on the same line. Therefore, the two sets of experiments could not be conducted with exactly the same incident beam energy, but without affecting the quality of the results.

Figure. II. 7 a) shows a schematic representation of the experimental configuration for the synchrotron experiments in transmission from Gaudez [4]. The synchrotron X-Ray monochromatic beam (with a square section of 0.5 x 0.5 mm²) with a high energy (100 keV corresponding to a wavelength λ = 0.123984 or 87.1 keV corresponding to a wavelength λ = 0.142347 depending on the series of experiments) goes through the sample in a powder diffraction configuration. The cylindrical sample (Figure. II. 10) is heated with a Bähr dilatometer [5] presented in Figure. II. 2. As said before, the temperature is measured with a thermocouple welded at the middle of the cylindrical specimens. The high photon flux from synchrotron source and the large 2D detector (Perkin-Elmer) allows for collection of diffraction patterns at significant rates. Two acquisition rates have been used along a given cycle depending on the kinetics of the studied metallurgical mechanisms and to rationalize the quantity of experimental data: a slow rate (one image every 3 seconds) and a fast rate (one image every 0.1 seconds). Figure. II. 7 b) shows pictures of the experimental set-up on P07B-EH1 beamline at PETRA III. At the foreground, we can see the slits which serve to calibrate the beam, then the dilatometer in the second plane. Finally, the detector is located in the background.

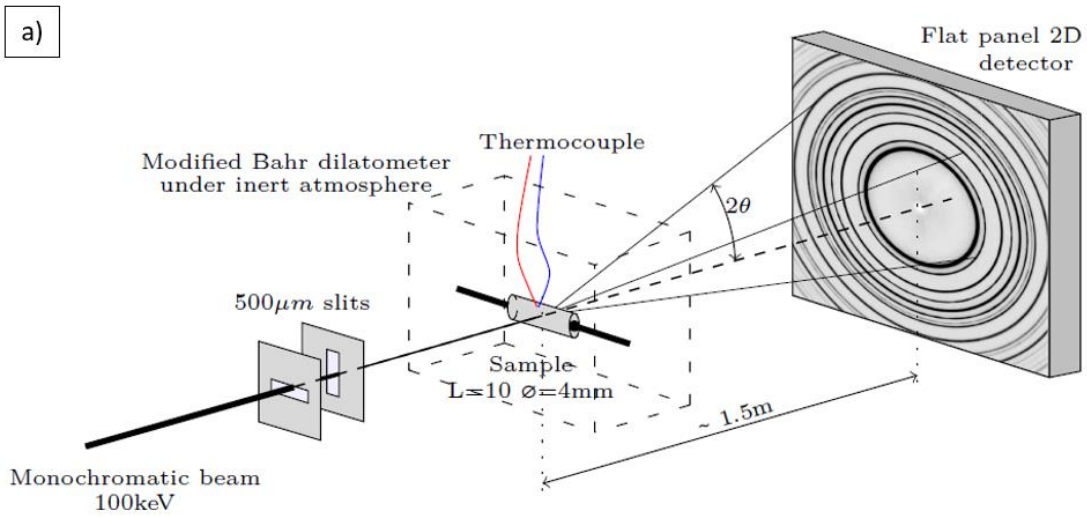

Figure. II. 7: a) Schematic representation of the configuration for synchrotron experiments from Gaudez [4] b) Picture of the experimental set-up on P07B-EH1 beamline at PETRA III.

II.2.b. Rietveld Analysis

II.2.b.1. Method

The two-dimensional X-Ray patterns obtained during the experiments (shown in Figure. II. 8 a)) consist in Debye-Scherrer rings if the condition of powder diffraction in transmission is respected. Each ring corresponds to a family of diffracting crystalline planes of a given phase. The diffraction Braggs law correlates the interreticular distance d, the diffraction angle θ (defined in Figure. II. 7 a)) and the incident beam wavelength λ (Eq. 1) as follows:

$$2d \sin\theta = n\lambda \qquad \textit{Eq. 1}$$

In practice, the intensity of the patterns were integrated circularly with the *PyFAI* python library [6] to obtain 1D diffractogram (integrated intensity as a function of the diffraction angle). Sample to detector distance and detector orthogonality to the beam had been calibrated using LaB6 powder (NIST 660a). Figure. II. 8 a) corresponds to an experimental 2D diffraction pattern showing mainly the two phases and Figure 8 b) to its associated 1D pattern after integration.

The 1D diffractograms (i.e. shown in Figure. II. 8 b)) were then analyzed following a Rietveld [7] refinement method using *FullProf* [8]. The diffracting plane families of the respective rings have been indicated for both phases. The Rietveld refinement is a mathematical procedure which consists in simulating a diffractogram using a crystallographic model and then in adjusting the mathematical parameters of that model so that the simulated diffractogram is as close as possible to the measured diffractogram. Pseudo-Voigt functions were used in our Rietveld refinements to represent diffraction peaks. The R-factor was used for each phase as the indicator of the quality of simulation [8], [9]. The mathematical parameters are then used to obtain information on the crystalline structure of the studied material. The Figure. II. 8 c) shows the result of such Rietveld procedure on the spectrum Figure. II. 8 b). The experimental and the simulated curves are respectively the red and black curves in Figure. II. 8 c), the blue curve corresponds to the differences between those two curves.

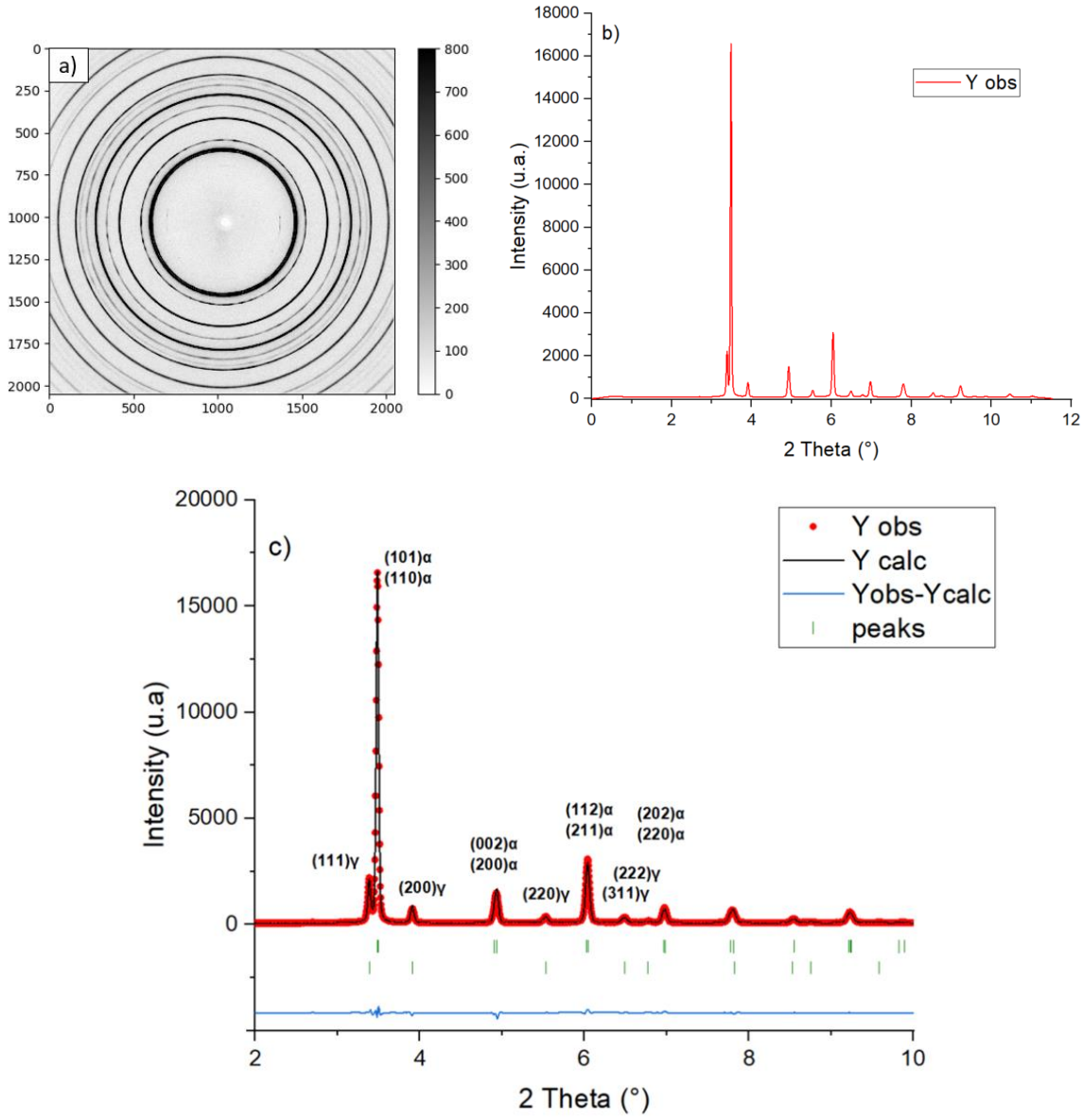

Figure. II. 8: a) Example of a 2D experimental diffraction pattern recorded on the detector ; b) associated 1D diffractogram after circular integration ; c) *Result of the* Rietveld refinement *procedure applied to the preceding diffractogram (red curve: experiment, black curve: simulated diffractogram, blue curve: difference between the red and the black curves; green segments: expected position of the diffraction peaks for both considered phases, centered-cubic and body centered phases). Miller's index of the diffraction planes are reported for the first main peaks.*

II.2.b.2. Phases in presence

As in [10]–[14], we have conducted our refinement considering two main phases: a cubic face centered (FCC) structure (Fm-3m) representing the austenite and a body-centered tetragonal (BCT) structure (I/4 mmm) representing all the body-centered cubic or close to cubic phases (ferrite, bainite and martensite). During the present experiments, it was not possible to discriminate bainite from martensite on the basis of their diffraction patterns. The measured mass fraction of BCT phase thus corresponds to the sum of bainite and martensite contributions. However, as they appear sequentially, their respective transformation kinetics can be identified uniquely by a metallurgical reasoning as discussed in Chapter III. It must be mentioned that the BCT structure systematically leads to a better adjustment than a BCC (Body-Centered Cubic) structure. This has already been observed in previous studies by some groups [10]–[14]. This justifies the use of a tetragonal unit cell to assess the carbon content in solid solution in bainitic ferrite (in absence of tempered martensite of course). Moreover, some peaks not corresponding to the two major phases were observed on some diffractograms at room temperature after heat treatment (Figure. III. 15 of Chapter III). These peaks were attributed to Epsilon carbides (which have a hexagonal space group structure P 6_3/mmc). The presence of such transition carbides have eventually been detected on the diffraction patterns depending on the transformation conditions (see Chapter III for more details). Nevertheless, as their fraction is limited (less than 1 wt.%), their quantification is impossible. As a consequence they haven't been considered further in the Rietveld procedure. When it will be necessary in the rest of the work, the diffraction patterns will be shown for qualitative discussions. It must be mentioned that the steel contains around 0.1 wt.% of sulfur. As a consequence, it contains a large fraction of MnS visible on micrographs and estimated at about 0.3 wt.% (± 1 wt.%) by HEXRD analysis, which also is highlighted by the diffractograms. Nevertheless, they have not been considered in the procedures since their main diffractions peaks do not overlap with the other important phases. A good example highlighting the presence of transition carbides and MnS will be given later in Figure. III. 15 of Chapter III and discussed in more detail.

II.2.b.3. Degrees of Freedom of the model

In the Rietveld process, many parameters considered as DOF (Degrees Of Freedom) have been introduced to describe mathematically the diffraction peaks and the background signal.

- 2 parameters to describe the background signal (linear behavior) and the SyCos parameter corresponding to a systematic 2θ shift in relation with the spherical aberrations related to the planeness of the detector compared to the sphere of Ewald.
- 6 and 7 parameters to describe the FCC and the BCT phases respectively (intensity, thermal scattering, shape of diffraction peak with a Pseudo-Voigt function, Full Width at Half Maximum (FWHM), lattice parameters). It must be mentioned that the FWHM is adjusted through only 2 parameters according to Cagliotti model [15].

In total, 16 parameters were adjusted on each diffractogram and this procedure was repeated either manually or in automated mode on each acquired diffractogram (typically 2500 per experiment). The mathematical uncertainties on each parameter is given by Fullprof [8]. In order to determine the

respective fraction of each phase, the chemical composition of the lattice is fixed. The absolute uncertainty on these fractions is typically of ± 1 wt.%. The relative uncertainties on the lattice parameters have been assessed with the calibrant around 2.10^{-4}.

II.2.b.4. Prior austenitic grain size issue

For all experiments, the mean Prior Austenitic Grain (PAG) size is around 74 ± 42 µm (and is large compared to the studied volume (500 x 500 x 4000 μm^3)). 4000 µm corresponds to the thickness of the sample.

As a consequence, the random powder diffraction condition is thus not met at high temperature when the alloy is fully austenitic. The Debye Scherrer rings are then discontinuous and exhibit many individual and intense spots as shown in Figure. II. 9 a). These spots affect the austenite peak shapes when calculating the 1D diffractograms as shown in Figure. II. 9 b). It is therefore impossible to characterize the evolution of the austenite phase with good accuracy from the high temperature and at the very beginning of the bainite transformation. These spots jeopardize not only the correct measurement of the phase fraction but also the austenite lattice parameters. The value becomes exploitable only after a certain amount of bainite transformation. The fraction of ferritic phase necessary to fractionate and disorient austenite grains was estimated around 15 wt.%, in order to make the Rietveld procedure really possible.

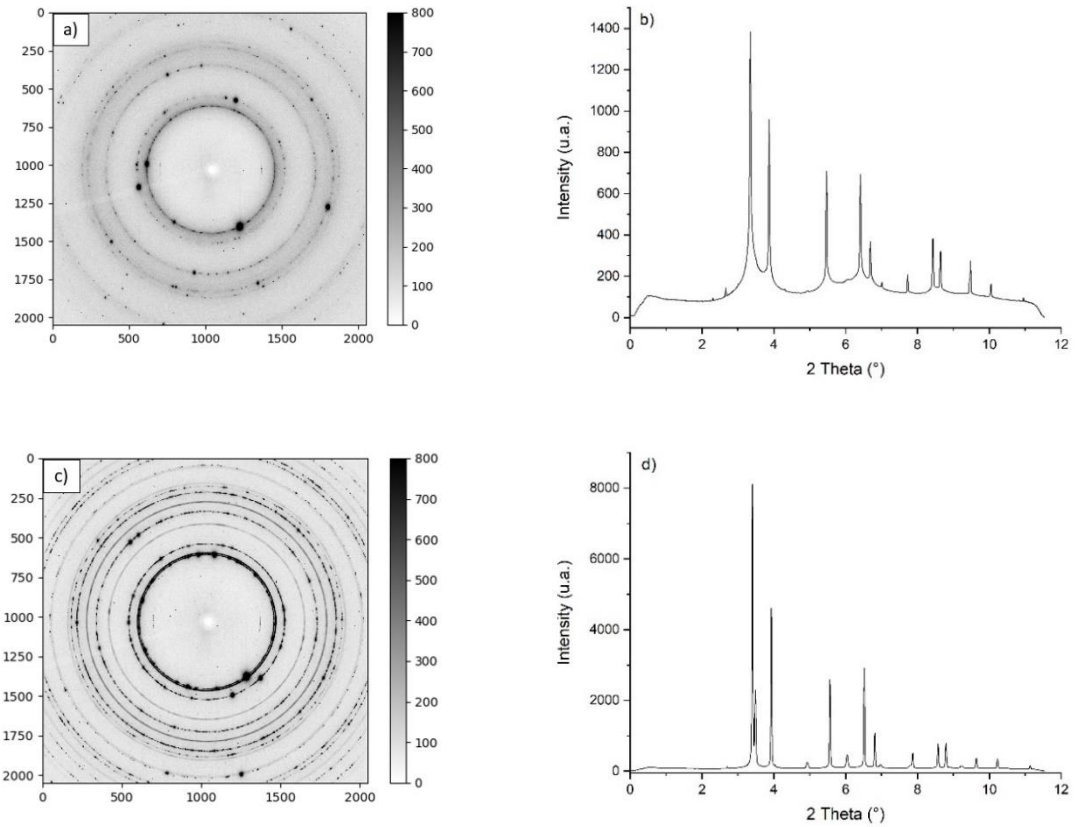

Figure. II. 9: 2D Image a) and 1D spectrum b) at the end of the austenitic soaking; 2D Image c) and 1D spectrum at the beginning of bainite formation, reproduced from [16].

Figure. II. 9 c) shows the two-dimensional image for the isothermal experiment at 400 °C after the formation of 20 wt.% bainite. The Debye Scherrer rings are still discontinuous and some spots are present and disturb the intensity. However, the position and the intensity of the peaks become insensitive to the apparition or the disappearance of single spots. At the stage shown in Figure. II. 9 d), it is considered that the determined values are meaningful and relevant. The R factor is slightly high (around 2.0) but decreases progressively afterward.

This issue related to our large austenitic grain sizes has greatly limited the analysis of early bainitic transformation. We could have avoided this by carrying out austenitization stage at a lower temperature (or with a pre-treatment of the material) but at the expense of industrial reality.

In this section, we have presented the in situ HEXRD experiments conducted to follow the evolution of the microstructures along different thermal treatments. The main results will be presented and discussed in Chapter III. In the next section, the methods to analyze the microstructures after the in situ trials will be presented.

III. Post mortem characterization methods

The microstructure characterization has been conducted on dilatometer samples after the in situ experiments, thus post mortem.

III.1. Characterization of microstructures

III.1.a. Sample preparation

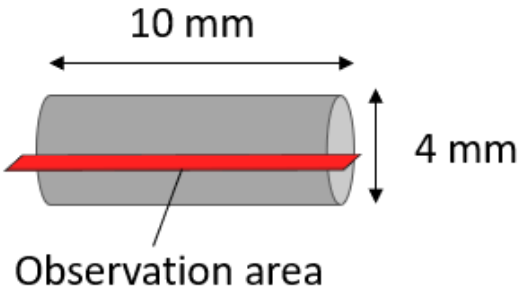

Figure. II. 10: Schematic representation of the cylindrical dilatometry sample and definition of the cutting plane.

The dilatometer cylindrical samples were cut after thermal treatments in the longitudinal direction along its axis as shown in Figure. II. 10. One half of the cut sample was then coated in a conductive carbon resin before automatic and manual polishing (with a progressive decrease in the grinding size). The final polishing operation consisted in a surface preparation with a suspension of diamond particles (3 µm and 1 µm sequentially) followed by an OPS colloidal silica solution dilute at 50 % with water for 10 minutes.

SEM-EBSD observations were performed at this preparation stage. In order to reveal the microstructures, etchings were further performed with a picral solution (20 to 30 seconds) or with a nital 2% solution (5 seconds). Microstructures were observed then by optical microscopy and by conventional Scanning Electron Microscopy. The measurements of PAGs were realized using software image J on about ten images with almost 25 to 65 PAG. The mean Prior Austenitic Grain Size (PAGS) is around 74 ± 42 µm as said above, based on the equivalent diameter of the grain.

III.1.b. Scanning Electron Microscopy (SEM)

The SEM observations were realized at IJL with a Gemini 500 Scanning Electron Microscope from Zeiss equipped with a SDD (Silicon Drift Detector) detector XMAX 80 (Oxford Instrument). The SEM micrographs were acquired with an acceleration voltage of 10 kV and a working distance around 4 mm. The Secondary Electron (SE) mode was used to observe the etched microstructures. The fractions of the phase revealed by their topologies after etching and their morphologies were estimated using software ImageJ.

III.1.c. Scanning Electron Microscopy coupling with Electron Back-Scattered Diffraction (SEM-EBSD)

III.1.c.1. Experimental configuration and conditions

During this thesis, SEM-EBSD was used to determine the type of bainitic microstructure (upper bainite, lower bainite, granular bainite) according to the cristallographic classifications of the literature, as well as the size distribution of bainitic ferrite laths. The results will be mainly presented in Chapter IV.

SEM-EBSD is a microstruture scanning technique for establishing local crytalline orientations at each point of an analyzed surface, and a consequence to establish possible phase maps. Figure. II. 11 shows the experimental configuration of the SEM-EBSD experiments after [17]. An electron beam is focused on the tilted sample. The back-scattered electrons can diffract according to Bragg's law with crystalline plane and form a series of two cones. Each pair of cones corresponds to a diffracting plane. The intersection of the diffraction cones with a fluorescent screen produces a set of lines, called pseudo-Kikuchi bands. The angles between these bands are characteristic of a given crystal structure. Each pair of parallel lines or band corresponds to a family of crystal planes and the interplanar distance of this family of planes is related to the width of the band. By knowing the crystalline structure of the studied phase, the measurement of the angles between the bands makes it possible to establish the crystallographic orientation of the analyzed zone.

The EBSD mappings were carried out at CREAS with a JEOL MEB-FEG JSM 7200F equipped with an ESPRIT EBSD acquisition system from Brüker. It has been operated with an acceleration voltage of 20kV, a working distance of 15 mm and a tilt angle of 70 °.

The acquisition software used on the JSM 7200F microscope is equipped with an automatic indexing after Hough transformation [18]. The average acquisition time per point is 40 points per second. Kikuchi lines are identified by geometric transformation of the image which is then processed by image analysis. The program extracts a Quality Index (QI) from the image, defined as the sum of the intensities of the strongest peaks in the transformed image. The local crystal orientation is determined by the different lines of the diffraction pattern, knowing the position (x, y, z) of the analysis point in the SEM and the crystal lattice. The search for the orientation of the crystal requires a criterion following a Confidence Index (CI between 0 and 1) calculated phase by phase from the ESPRIT software.

For all studied samples, four maps with different magnifications (x 1000 and x 2500) were realized. At the highest magnification (x 2500), three different areas were studied. The pixel size for the maps obtained at a magnification of x 1000 is equal to 0.1 µm and for the maps obtained at high magnification (x 2500) the pixel size is equal to 0.075 µm. In order to obtain optimal conditions between the scanning speed and the precision on the measurements, we used maps of 160 pixels × 120 pixels.

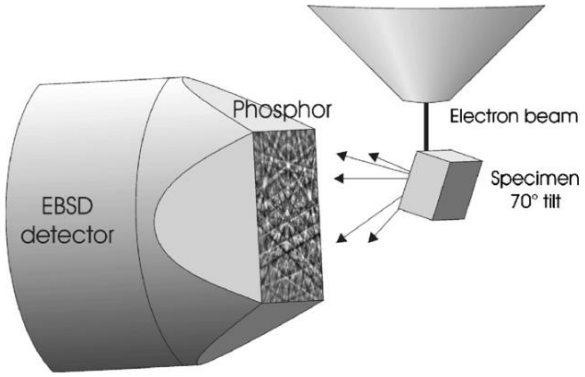

Figure. II. 11: Experimental configuration of the SEM-EBSD experiments [17].

III.1.c.2. Post-treatment of data

The EBSD maps were then analyzed using the HKL Channel 5 (Oxford) software.

On the maps, each pixel represents a single measure. When the quality of the Kikuchi diagram [18] is poor, the pixel is considered as a non-indexed point. The proportion of the non-indexed points for all analyzed maps was not more than 26 %, that is to say the indexation rates were higher than 70 %. The correction of some non-indexed points on the maps was realized for the isolated points and the pixels who are incorrectly indexed. Those later were pixels which have a very different orientation from their neighbors. Thus, these pixels are substituted by the average orientation of their five closest neighbors to obtain a cleaned map.

Figure. II. 12 shows an exemple of a cleaned IQ map (band constrast in grey level). Boundaries between pixels with a high misorientation (> 2°) are highlighted and their respective colors depends on the misorientation angle according to the legend. In a prior austenitic grain defined by a misorientation greater than 20 ° (in black), are present strongly disoriented boundaries in red > 50 °. From these maps, it is possible to draw the histograms of misorientations which are useful to classify the nature of the bainite according to the Zajac et al [15]. Figure. II. 13 show an exemple of such histogram established from the map in Figure. II. 12.

These maps can also serve to determine the characteristic size of the microstructure (an even the size distribution) providing the boundaries are well defined, i.e. a critical angle of misorientation is chosen to define the limits between different features in the microstructure. The classical “intercept” method with horizontal and vertical lines was used (100 lines per map). This analysis is conducted with different critical misorientation angle to define a boundaries. If the critical angle is low (case of laths), the probe lines will cross many boundaries and thus the corresponding microstructure size will be low. On the contrary, if the choose critical angle is high (up to 60°) (case of self-acommodating variants and PAG), the corresponding microstructure size will be larger. Hence, it is then possible to define a function relating the microstructure size to the critical angle chosen to define a boundary. The results of such analysis will be detailled in Chapter IV.

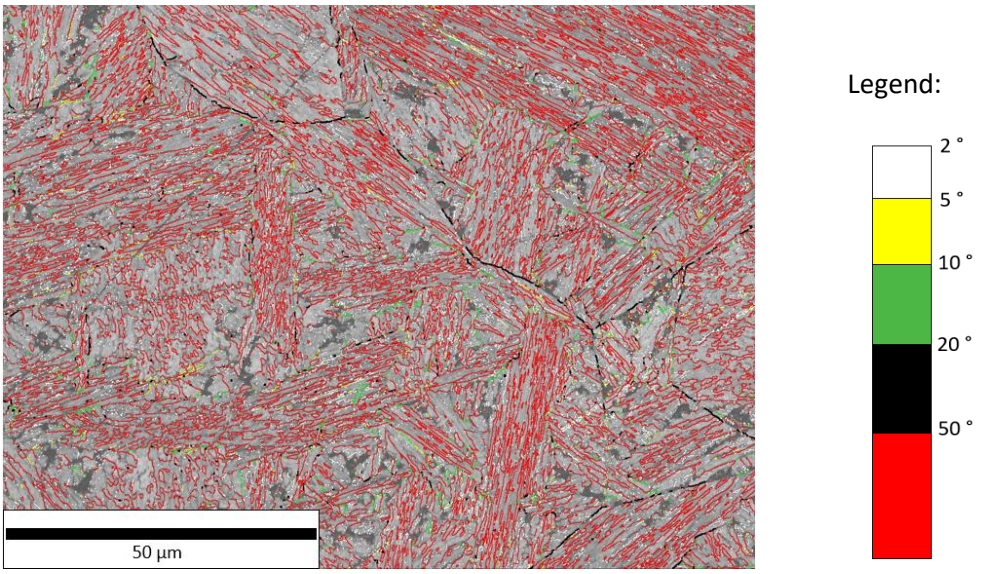

Figure. II. 12: Image Quality (grey level) and grain boundaries (misorientations according to the color code).

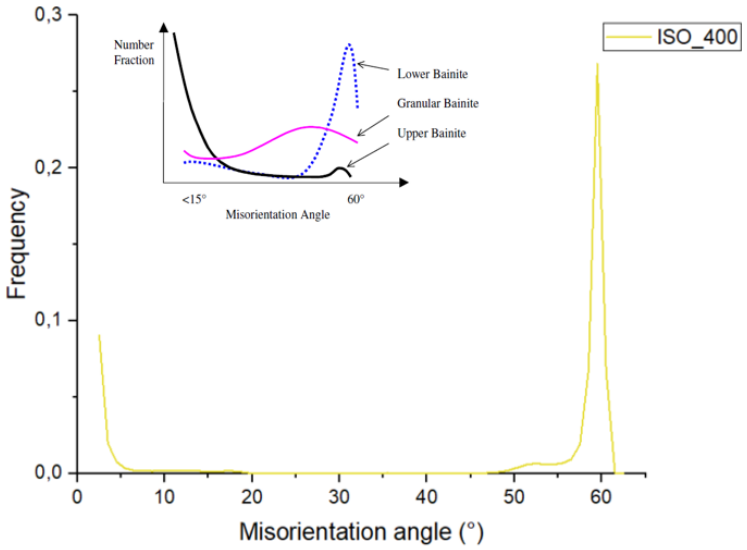

Figure. II. 13: Histogram of misorientations established on the map presented in Figure. II. 12 and definition of the main classes of bainite according to Zajac et al. [19].

III.2. Hardness

The mechanical properties of the samples were studied by Vickers hardness tests, using a Presi Durometer HZ 50-4. The indenter is a pyramid with a square diamond base; the two opposite faces make an angle of 136.0 ° ± 0.5 °.

For all conditions, we performed measurements using a loading of 0.1 kgf along straight lines (50 measurements with a spacing of 150 µm) in the transversal direction.

In this section, we have presented the post mortem technics of characterization and the different method of data analysis. These SEM-EBSD technics permit elucidate the morphology, the topology and the characteristic sizes of the bainitic microstructures formed after different thermal treatments while HEXRD could permit to have more reliable information on the phase fractions and on their respective compositions (carbon content). The main results of our SEM-EBSD study will be presented in Chapter IV.

Conclusion

In this Chapter, we have presented the different methods of characterization used in this PhD.

We have investigated the bainite formation using in situ High-energy X-Ray experiments on synchrotron beamlines. It allows to follow simultaneously the phase transformation kinetics and the evolution of lattice parameters of each phase. Those results will be presented in the next Chapter III.

The microstructures were analyzed by the SEM and the SEM-EBSD. The SEM micrographs were obtained after chemical etchings. It is possible to distinguish the different phases present on the microstructures by contrast between phases and to observe their morphologies. The SEM-EBSD technic permits to complete the analysis of the microstructure with a crystallographic description. The different microstructures formed after each thermal treatment were classified following Zajac's classification [19]. These results will be presented in Chapter IV.

References

[1] "Accueil — Ascometal." https://www.ascometal.com/ (accessed May 27, 2021).

[2] F. G. Caballero, M. J. Santofimia, C. García-Mateo, J. Chao, and C. G. de Andrés, "Theoretical design and advanced microstructure in super high strength steels," *Mater. Des.*, vol. 30, no. 6, pp. 2077–2083, Jun. 2009, doi: 10.1016/j.matdes.2008.08.042.

[3] F. G. Caballero *et al.*, "Novel high strength, high toughness carbide-free bainitic steels," *EUR*, no. 22450, 2007.

[4] S. Gaudez, "Kinetics and microstructural evolutions during the tempering of martensitic and nano-bainitic low alloyed steel: in situ experimental study and modelling," PhD Thesis, Université de Lorraine, 2021.

[5] J. W. Gibbs, C. Schlacher, A. Kamyabi-Gol, P. Mayr, and P. F. Mendez, "Cooling Curve Analysis as an Alternative to Dilatometry in Continuous Cooling Transformations," *Metall. Mater. Trans. A*, vol. 46, no. 1, pp. 148–155, Jan. 2015, doi: 10.1007/s11661-014-2603-8.

[6] G. Ashiotis *et al.*, "The fast azimuthal integration Python library: *pyFAI*," *J. Appl. Crystallogr.*, vol. 48, no. 2, pp. 510–519, Apr. 2015, doi: 10.1107/S1600576715004306.

[7] H. M. Rietveld, "A profile refinement method for nuclear and magnetic structures," *J. Appl. Crystallogr.*, vol. 2, no. 2, pp. 65–71, Jun. 1969, doi: 10.1107/S0021889869006558.

[8] J. Rodríguez-Carvajal, "Recent advances in magnetic structure determination by neutron powder diffraction," *Phys. B Condens. Matter*, vol. 192, no. 1–2, pp. 55–69, Oct. 1993, doi: 10.1016/0921-4526(93)90108-I.

[9] B. H. Toby, "*R* factors in Rietveld analysis: How good is good enough?," *Powder Diffr.*, vol. 21, no. 1, pp. 67–70, Mar. 2006, doi: 10.1154/1.2179804.

[10] C. N. Hulme-Smith, I. Lonardelli, A. C. Dippel, and H. K. D. H. Bhadeshia, "Experimental evidence for non-cubic bainitic ferrite," *Scr. Mater.*, vol. 69, no. 5, pp. 409–412, Sep. 2013, doi: 10.1016/j.scriptamat.2013.05.035.

[11] C. Garcia-Mateo *et al.*, "Low temperature bainitic ferrite: Evidence of carbon super-saturation and tetragonality," *Acta Mater.*, vol. 91, pp. 162–173, Jun. 2015, doi: 10.1016/j.actamat.2015.03.018.

[12] C. N. Hulme-Smith, M. J. Peet, I. Lonardelli, A. C. Dippel, and H. K. D. H. Bhadeshia, "Further evidence of tetragonality in bainitic ferrite," *Mater. Sci. Technol.*, vol. 31, no. 2, pp. 254–256, Jan. 2015, doi: 10.1179/1743284714Y.0000000691.

[13] H. K. D. H. Bhadeshia, "Carbon in cubic and tetragonal ferrite," *Philos. Mag.*, vol. 93, no. 28–30, pp. 3714–3725, Sep. 2013, doi: 10.1080/14786435.2013.775518.

[14] J. H. Jang, H. K. D. H. Bhadeshia, and D.-W. Suh, "Solubility of carbon in tetragonal ferrite in equilibrium with austenite," *Scr. Mater.*, vol. 68, no. 3–4, pp. 195–198, Feb. 2013, doi: 10.1016/j.scriptamat.2012.10.017.

[15] L. Lutterotti and P. Scardi, "Simultaneous structure and size–strain refinement by the Rietveld method," *J. Appl. Crystallogr.*, vol. 23, no. 4, pp. 246–252, Aug. 1990, doi: 10.1107/S0021889890002382.

[16] C. Rampelberg, S. Y. P. Allain, G. Geandier, J. Teixeira, F. Lebel, and T. Sourmail, "Carbide-Free Bainite Transformations Above and Below Martensite Start Temperature Investigated by In-Situ High-Energy X-Ray Diffraction," *JOM*, vol. 73, no. 11, pp. 3181–3194, Nov. 2021, doi: 10.1007/s11837-021-04903-8.

[17] A. Winkelmann, C. Trager-Cowan, F. Sweeney, A. P. Day, and P. Parbrook, "Many-beam dynamical simulation of electron backscatter diffraction patterns," *Ultramicroscopy*, vol. 107, no. 4–5, pp. 414–421, Apr. 2007, doi: 10.1016/j.ultramic.2006.10.006.

[18] "EBSD.com." https://www.ebsd.com/ebsd-explained/basics-of-automated-indexing (accessed May 20, 2022).

[19] S. Zajac, V. Schwinn, and K. H. Tacke, “Characterisation and Quantification of Complex Bainitic Microstructures in High and Ultra-High Strength Linepipe Steels,” *Mater. Sci. Forum*, vol. 500–501, pp. 387–394, Nov. 2005, doi: 10.4028/www.scientific.net/MSF.500-501.387.

[20] K. Zhu, O. Bouaziz, C. Oberbillig, and M. Huang, “An approach to define the effective lath size controlling yield strength of bainite,” *Mater. Sci. Eng. A*, vol. 527, no. 24–25, pp. 6614–6619, Sep. 2010, doi: 10.1016/j.msea.2010.06.061.

Chapter III: Phase transformations

Introduction

This Chapter presents the results of the in situ experiments conducted by High Energy X-Ray Diffraction (HEXRD) to study the CFB transformations along model heat treatments or along heat treatments representative of industrial operations. This type of experiments, as explained in Chapter I, makes it possible to acquire the transformation kinetics of the different phases resulting from the decomposition of the austenite but also to obtain important knowledge on the respective compositions of phases (in our study we have attributed the entire evolution of lattice parameter to the chemical evolution and have so neglected any the evolution of internal stresses).

In the following, the single-step experiments permitting to study bainitic transformations at constant temperature will be first presented as a reference case. These results will also be of prime importance to calibrate the model presented in Chapter V. It will be shown in particular how to obtain accurate carbon balances between phases. This methodology will then be developed to study the transformations under non-isothermal treatments. Two kinds of experiments are presented and discussed, namely sequences of isothermal holdings at different temperatures (multistep treatments) and continuous cooling schedules. These latter schedules have been designed to mimic the heat treatments encountered during industrial forging operations (excluding the strain effects as discussed in Chapter II).

I. Bainitic transformations during Isothermal heat treatments

I.1. TTT diagram and choice of the thermal cycle

In this section, five single-step experiments with transformation temperatures above and below M_S (Martensite Start temperature) will be presented and analyzed.

Temperature M_S of the alloy is about 350 °C (346 °C) as determined by prior dilatometer experiments. This value is consistent with the M_S calculated with Van Bohemen [1] and Barbier [2] equations (356 °C and 341 °C respectively). The highest studied transformation temperature (475 °C) was chosen below the temperature B_S (Bainite Start temperature), estimated around 540 °C using Van Bohemen's model [3].

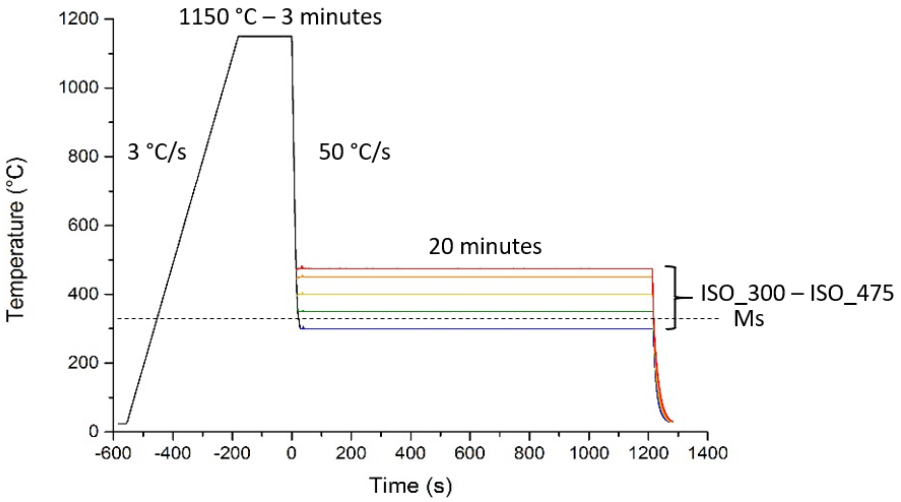

Figure. III. 1: Heat treatments performed to study by in situ HEXRD the bainitic transformations during isothermal holdings (ISO_300 to ISO_475 experiments according to the nomenclature described in the text).

Figure. III. 1 shows the experimental heat treatments conducted on the studied steel (temperature as a function of time). They consist in a full austenitic soaking at 1150 °C during 3 min followed by a rapid cooling stage to avoid any ferritic and pearlitic transformation before the bainitizing stage at constant temperature. Time 0 corresponds to the end of the austenitic soaking. The isothermal steps were chosen between 300 °C and 475 °C and the holding time is set up at 20 minutes. These conditions have been chosen on the basis of prior dilatometer experiments described below. The experiments will be denoted as ISO_XXX with XXX corresponding to the temperature holding (XXX = 300, 350, 400, 450 or 475). Isothermal holdings are followed by a rapid cooling stage down to room temperature at 50 °C/s.

Figure. III. 2 shows the TTT (Time Temperature Transformation) diagram of the studied steel (named MC2 by Ascometal). This diagram is obtained on the basis of dilatometry trials and has been provided by Ascometal at the beginning of the study. The dilatometry signal is normalized from 0 % to 100 % as it is not possible using this technique to appreciate the fraction of residual austenite if any (0 % corresponds to the beginning of the transformation, 100 % means that the "full" transformation is reached). The 2 %, 10 %, 50 %, 90 % and 98 % times of transformation are reported. Figure. III. 2 puts into evidence two main domains for austenite decomposition, namely the ferrite-pearlite one above 600 °C and the bainitic one below 500 °C and above 350 °C (M_S temperature of the alloy). The "C" shape of the bainitic domain is consistent with a theoretical B_S temperature close to 540 °C. The evolution of the dilatation as function of time for a given temperature permits to obtain different characteristic times of bainite transformation. In the studied range of temperatures, 1200 s seems sufficient to reach the stagnant stage for the bainitic transformations (100 % of normalized transformation).

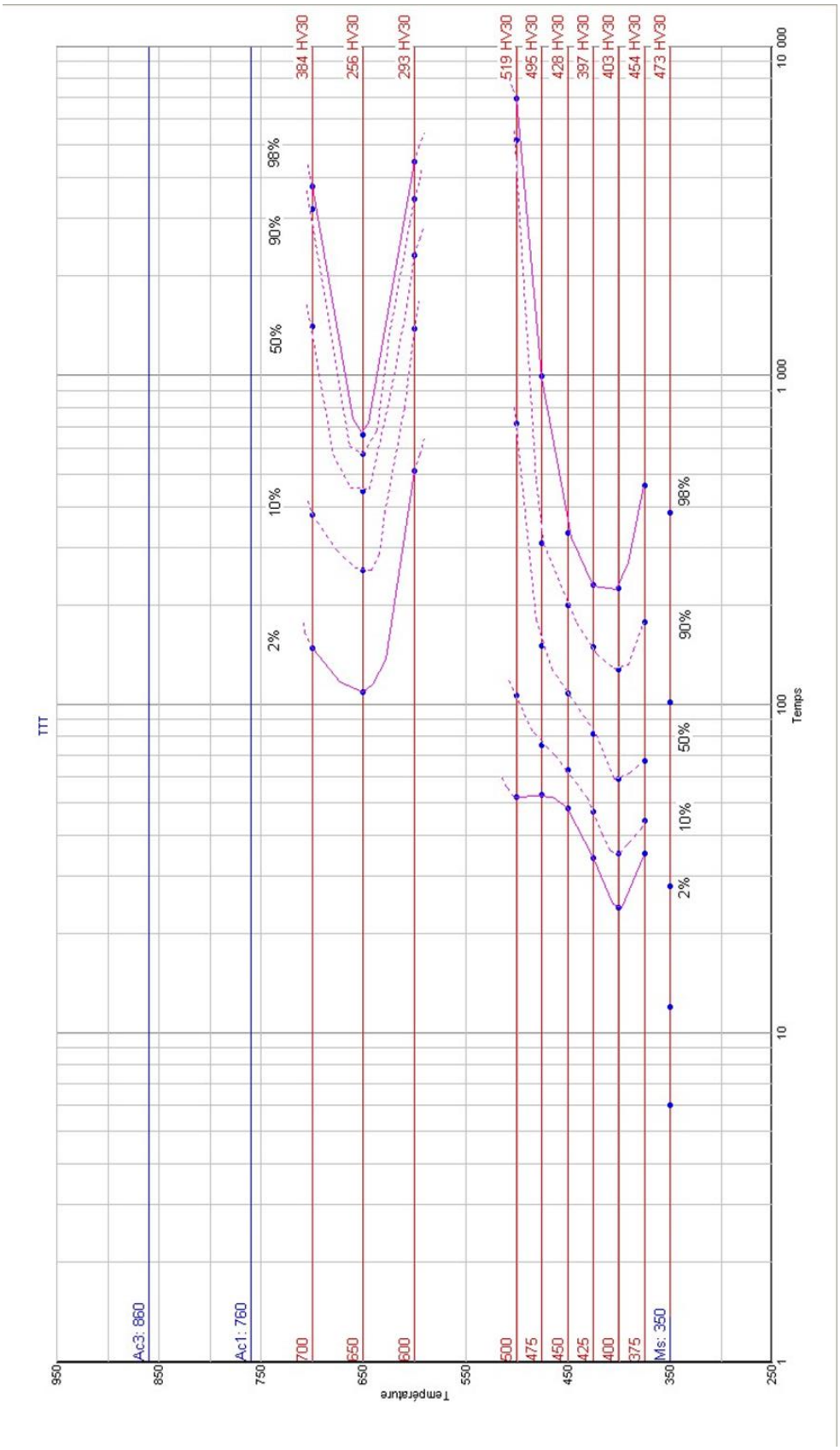

Figure. III. 2: TTT diagram of the studied steel provided by Ascometal at the beginning of the study to design in situ HEXRD experiments (based on dilatometer trials).

I.2. Kinetics of bainite and martensite transformations

I.2.a. Transformation kinetics during the holding stages

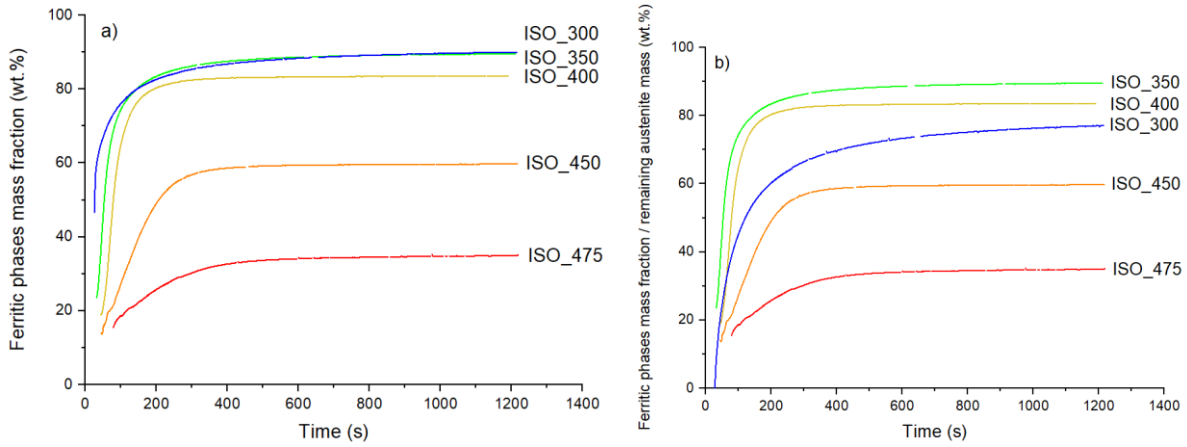

Figure. III. 3: a) Ferritic phases mass fraction as a function of time during isothermal holdings ; b) Normalized ferritic phases mass fraction as a function of time along isothermal holdings (The normalization procedure is explained in the text). Compared to Figure. III. 3 a), only ISO_300 experiment need to be corrected as bainitic transformation occurs after a partial martensitic transformation.

Figure. III. 3 a) shows the mass fraction of the ferritic phases as a function of time along isothermal holdings at different transformation temperatures between 300 °C and 475 °C measured by HEXRD. The mass fractions are the direct output of the Rietveld refinement procedure based on the absorption coefficients of atoms lattices. As explained in Chapter II, the nature of the ferritic phase cannot be decided on the sole basis of the diffraction patterns (imposed BCT structure). As a consequence, only metallurgical reasoning could decide if the studied transformation is ferritic, bainitic or martensitic. The mass fractions of the ferritic phases as a function of time are shown only for the duration of isothermal holding, excluding what could happen during the final cooling to room temperature for the moment. For isothermal holdings above M_S (350 °C and above), no proeutetoid ferrite transformation occurs during cooling and the studied transformation during the plateau is obviously bainitic. During the studied stages, bainite mass fraction increases as a function of time. Bainite transformation kinetics exhibits a sigmoidal curve and do not reach a full transformation. The maximum fraction of bainite formed decreases strongly at higher holding temperatures, which is consistent with the well-established incomplete transformation phenomenon discussed in Chapter I [4], [5]. The higher the temperature, the lower the initial transformation rate and the lower the transformed fraction when the plateau is reached. For experiment ISO_350, the slope of the curve at the end of the treatment remains significant meaning that the transformation is not strictly finished (the stasis is probably not reached). [6]

The isothermal transformation at 300 °C occurs below the M_S temperature. As consequence, the transformation during the plateau is preceded by a partial martensitic transformation. The kinetics of the ferritic phases transformations during ISO_300 experiment presented in Figure. III. 3 a) is thus the sum of two contributions; first, a martensitic transformation followed by a isothermal one. In order to compare the rate of this latter transformation only in austenite, kinetics have been normalized to consider only the transformation of austenite remaining after the martensitic transformation. The

measured fraction of martensite between M_S and 300 °C is f_M = 56 wt.%. The Koistinen-Marburger relation would have given around 61 wt.% [7].

The normalized mass fraction of the bainitic phase f_B is calculated as follows:

$$f_B = \frac{f_{M+B} - f_M}{f_A} \qquad \textit{Eq. 2}$$

where f_{M+B}, f_M and f_A are respectively the total mass fraction of BCT phases (data from Figure. III. 3 a)), the mass fraction of martensite before bainitic transformation and the mass fraction of austenite prior to the isothermal transformation. Figure. III. 3 b) shows the normalized kinetics for the different isothermal treatments as a function of time.

When comparing the normalized results, the rate of bainite transformation at 300 °C is far slower than the one obtained at 350 °C [5], [8]. There still a controversy about the nature of this time dependent transformation observed below M_S temperature [8]. The nature of the final product is claimed to be bainitic or martensitic. Some authors as Kim et al. [9] statute for instance that it is an athermal martensitic transformation. However, some authors as Van Bohemen et al. [10] consider that the final product as bainite. In this work, the isothermal transformation below M_S is also considered as a bainite transformation. Nevertheless, this bainitic nucleation is strongly affected by the prior martensitic transformation in the sense that it provides new nucleation sites for bainite, stimulating the autocatalytic nucleation processes at martensite/austenite interface as reported by Ravi et al. [11] for example. The accelerating effect of a prior martensitic transformation often observed in the literature is however not put in evidence in our experiment ISO_300 [11]. The bainite fraction reached at the end of experiment ISO_300 is 77 wt.%, lower than the fraction obtained at stasis for ISO_400. For experiment ISO_350, the stasis of the transformation is obviously not achieved as the slope remains significant at 1200 s.

The comparison of the time at 50 % and 90 % of transformation (noted t50% and t90% respectively) obtained in Figure. III. 2 (TTT diagram obtained by dilatometer trials) and the corresponding times obtained by HEXRD are reported in Figure. III. 4. The transformation rate have been recalculated considering a full transformation (100 %) when the stasis is reached. Globally, the HEXRD data are late at 50 % (about 20 s) and in advance at 90 % (also about 20 s) when compared to dilatometry. Nevertheless, the trends are similar. The observed differences are probably due to the heterogeneities of temperature generally observed along a dilatometry sample while the HEXRD measurements are more local, just below the control thermocouple. Nevertheless, HEXRD has a definite advantage because it allows an access to the austenite fraction at the end of transformation, a measure that can only be qualitative in dilatometry.

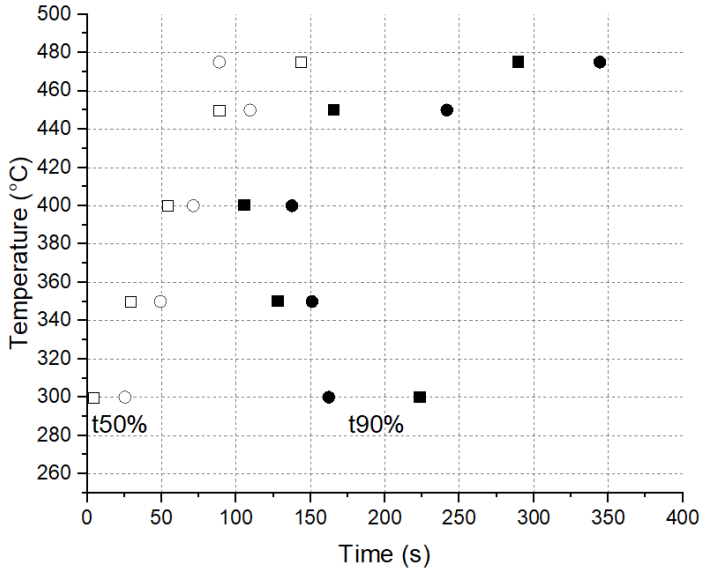

Figure. III. 4: Comparison between the times at 50% and 90% of bainitic transformation (empty and plain symbols respectively) obtained in dilatometry (squares, extracted from Figure. III. 2) and in HEXRD (circle).

I.2.b. Transformations during the final cooling stages

When cooling the samples down to room temperature, fresh martensite (FM) can be formed if austenite is not sufficiently stabilized by carbon partitioning. Figure. III. 5 shows the evolution of the ferritic phase fractions at the end of the 5 considered experiments (final cooling stage only) as a function of the temperature. For the experiments conducted at 475 °C and 450 °C, the fractions increase drastically during this last stage below 330 °C and 230 °C respectively. For the lower holding temperatures, the change is negligible (below the detection limit of HEXRD) meaning that the fraction of fresh martensite is lower than 1 wt.% in the final microstructure at room temperature. The austenite at the end of the bainitic stasis is more stable (lower M_S temperature and transformed fraction) when the holding temperature is low. This higher stability is explained in the literature by a higher carbon enrichment in austenite during the CFB transformation; this results will be confirmed in the following by our own investigations of the austenite lattice parameters.

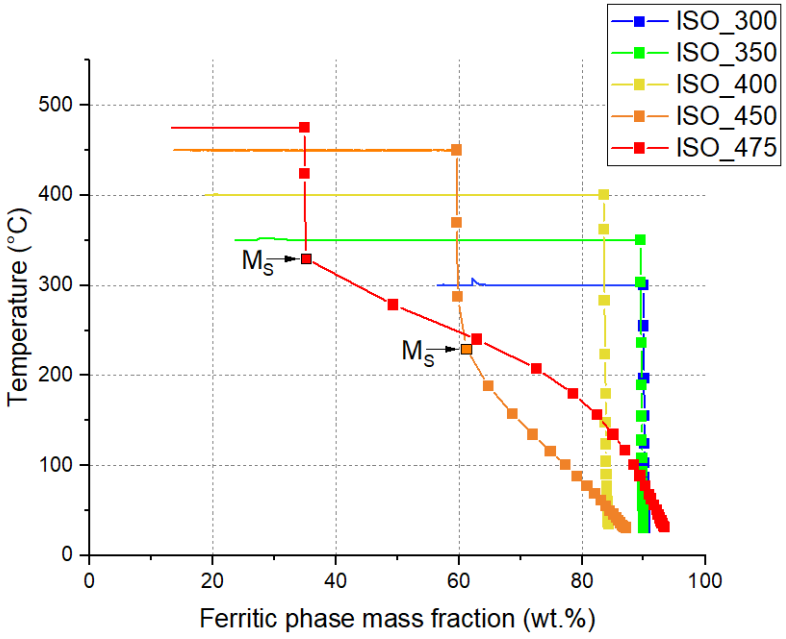

*Figure. III. 5: Evolution of the ferritic phase fractions during the final cooling of the 5 considered experiments (*Figure. III. 3*) as a function of the temperature.*

Table 2 shows the final phase composition of the microstructures after the 5 studied experiments as well as the experimental M_S temperatures of the austenite measured during the final cooling stages in Figure. III. 5. As discussed above, the fraction of bainite decreases with the holding temperature whereas the fraction of FM drastically increases at the expense of the fraction of austenite. The highest value of retained austenite fraction at room temperature is thus obtained after a transformation at 400 °C in the investigated conditions (ISO_400 experiments). These trends will be confirmed by direct microstructure observations at room temperature using SEM and EBSD and detailled in Chapter IV.

*Table 2: Phases fractions at room temperature after isothermal treatments measured by HEXRD and experimental M_S temperatures of austenite after the isothermal holdings as measured in Figure. III. 5: * associated martensitic transformation limited to 1 % max.*

Temperature (°C)	Bainite (wt.%)	Retained Austenite (wt.%)	Fresh martensite (wt.%)	Experimental M_S (°C)
350	90	10	0	155-128*
400	83	16	1	179-148*
450	60	13	27	230
475	35	7	58	330

I.2.c. Repeatability of the experiments in the higher temperature range

During this study, we have faced repeatability issues of the experiments at the highest holding temperatures.

For the sake of comparison, different results are reported in Figure. III. 6; namely the transformation kinetics obtained at 450 °C and 475 °C during single step experiments (presented already in Figure. III. 3), the kinetics of first holding stages at 450 °C of certain multistep experiments (not presented in this thesis), the first step at 475 °C of the three-step treatment (3ST_L presented in the next section) and additional experiments performed at 475 °C with an holding time of 500 seconds. The transformation kinetics obviously present significant differences, larger than the known precision of HEXRD measurements. For a same isothermal holding (450 °C or 475 °C), the kinetics are not equivalent in terms of initial rate and final fraction at stasis. In all the cases, the transformations reached the stasis however after 500 s. As a consequence, such repeatability issue cannot been detected by dilatometry.

The final fractions of bainite formed at stasis at 450 °C and at 475 °C can vary of 6 wt.% and 10 wt.% respectively in comparison with the reference isothermal treatments (ISO_450 and ISO_475). A direct consequence, is that the carbon enrichment in austenite can also vary significantly as a function of the experiments (it will be discussed later in Figure. III. 14). On the contrary, all the experiments conducted at temperatures lower than 400 °C have shown an excellent repeatability.

We have of course conducted additional investigations to understand the origin of this issue. Few hypothesis have been elaborated and assessed. It could be related to:

- a possible chemical heterogeneities in between the sample related to the sampling procedure which could affect the global kinetics. In that case, it is difficult to explain why the divergences are observed only at high temperatures.
- a possible chemical heterogeneities inside a given sample which could affect the local measurement of HEXRD. The EDS mapping as well as the microhardness cartography reveal that the scattering is not sufficient to explain the observed phenomenon.
- the temperature uncertainty related to the thermocouple precision (± 5 °C). A small difference of temperature can lead to high difference in terms of bainite mass fraction and austenite enrichment as the TTT nose is in fact flat close to the B_S (cf. Figure. III. 4). At lower temperature, a small error in the temperature does not affect much the kinetics.

To our best knowledge, the latter hypothesis seems the more relevant to explain the observed variability, i.e. the transformation kinetics are highly sensitive of the holding temperature in the upper transformation range and this sensitivity is reveals when confronted to all the sources of experimental scattering.

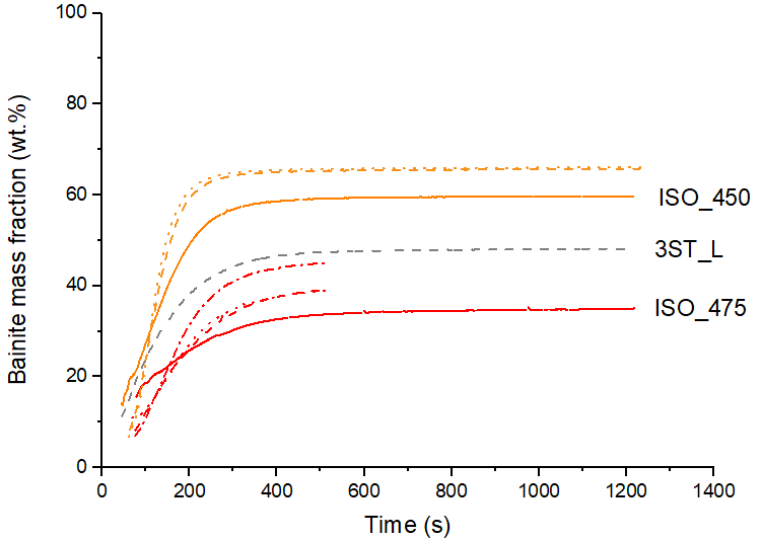

Figure. III. 6: Bainite transformation kinetics during isothermal holding at high temperatures (450 °C in orange and 475 °C in red) during ISO_450/ISO_475 experiments (continuous lines). Additional experiments and the first isothermal stages of multistep experiments (dot/dashed lines).

I.2.d. Behavior after longer isothermal holdings

As discussed above, at the end of the holding stages at 300 °C and 350 °C; the bainitic transformation hasn't presumably reach a stasis and the kinetics still present a significant slope after 1200 s (0.0020 wt.%/s)**.** In order to verify if a stasis can be reached after longer transformation plateau, in situ experiments have also been duplicated with far longer holding time, namely 18000 s instead of 1200 s (experiments named ISO_300_LT and ISO_350_LT). The transformation kinetics of the corresponding ISO_300_LT and ISO_350_LT experiments are reproduced in Figure. III. 7 and compared to the ISO_300 and ISO 350. Contrary to the experiments conducted above 450 °C, an excellent repeatability is obtained for the beginning of the transformation (up to 1200 s). It appears that the slope of kinetics at low temperature becomes negligible (less than 0.0010 wt.%/s) above 2000 s, meaning that a stasis seems to be reached also at low transformation temperatures. Nevertheless, this result depends on the choice of the criterion (as discussed in the article to Santajuana et al.[6]) for the end of the transformation. Even after 18000 s, the slope is weak but not strictly equal to zero but the studied variation falls into the resolution of the technic.

It must be mentioned that these latter transformation kinetics after long holding have been used to assessed the stasis and recalculate the 100 % transformation rate to build TTT diagram in HEXRD (cf. Figure. III. 4).

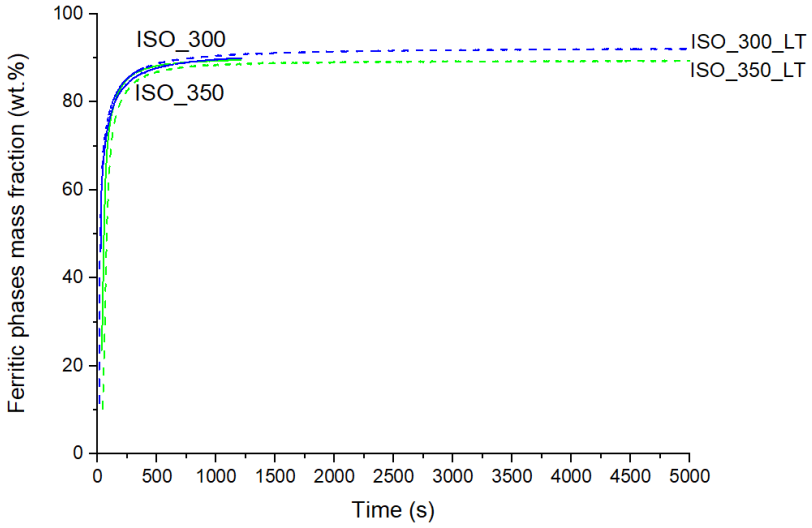

Figure. III. 7: a) Ferritic phase fractions as a function of time during long holding stages at 300 °C and 350 °C (dotted lines) (in situ ISO_300_LT and ISO_350_LT experiments respectively) compared to the results of ISO_300 and ISO_350 experiments (continuous lines).

I.2.e. Conclusions

The conducted in situ experiments have permitted to measure the bainite transformation kinetics of the studied steel at different temperatures. As expected from the literature review (cf. Chapter I), the transformation kinetics present a sigmoidal shape with a stasis level which depends on the transformation temperature. The lower the temperature is, the faster the initial transformation kinetics except maybe at 300 °C (even if the prior martensitic transformation is supposed to suppress the incubation stage) and the higher the transformed fraction at stasis. During the final cooling stage after holding, a martensite transformation is reported after the holdings at the highest temperatures, which is explained by a lower stability of the retained austenite. This result will confirmed in the next section by the direct determination of the carbon content in retained austenite at the end of the holdings.

The experiments highlighted the sensitivity of the transformation kinetics to the temperature in the upper bainitic range as the nose of the C-curve in the TTT diagram is flat meaning that a small temperature variation could lead to large differences in terms of kinetics and transformations at stasis. At lower temperatures the main difficulty is the detection of the stasis it-self.

As discussed in the literature review (Chapter I), carbon partitions from bainite to surrounded austenite during the carbide free bainitic transformation. The in situ investigation of the bainite transformation by HEXRD allows not only to measure the evolution of phase fractions but also to determine the carbon composition of the studied phases using the shapes, the widths and the positions of their diffraction peaks all along the isothermal holdings. In the following, we will consider first the determination of the carbon supersaturation of the bainite/martensite using the tetragonality of their crystalline lattice and then the determination of the carbon content in austenite using its lattice parameter. As a consequence very precise time-resolved carbon balances between the phases can be established which allows to analyze in turn the partitioning mechanisms and discuss the validity of certain stasis criteria of the literature.

I.3. Tetragonality and carbon supersaturation of the bainitic/martensitic phases

As explained in Chapter II, the c and a lattice parameters of the BCT ferritic phase were obtained from the Rietveld refinement. This measurement is not affected by the possible mechanisms affecting the widths of the diffractions peaks (related to defects or internal stresses) as the tetragonality is revealed only on certain diffraction peaks. In this study, we detect through the Rietveld analysis a specific enlargement of the certain peaks due to the degeneration outbreak of diffraction plane families affected by the c/a ratio ((200) and (002) are not equivalent in the {200} family whereas there is no distinction in the {111} family). As said in Chapter II, the quality of the Rietveld adjustment is also far better when considering a BCT phase than with a BCC phase (c/a = 1).

Even if this type of analysis has already been conducted with success by Guo et al. [4], such approach could remain controversial [12]–[16]. We must also recognize that we do not obverse any peak splitting which could prove unambiguously the presence of a tetragonal phase and the ferritic diffraction peaks remain irremediably symmetrical (cf. APPENDIX 1) whereas a skewness is expected in the presence of a tetragonal phase. Nevertheless, we will see later when establishing complete carbon balances between phase that the determination of the tetragonality and the associated carbon content in bainite is relevant.

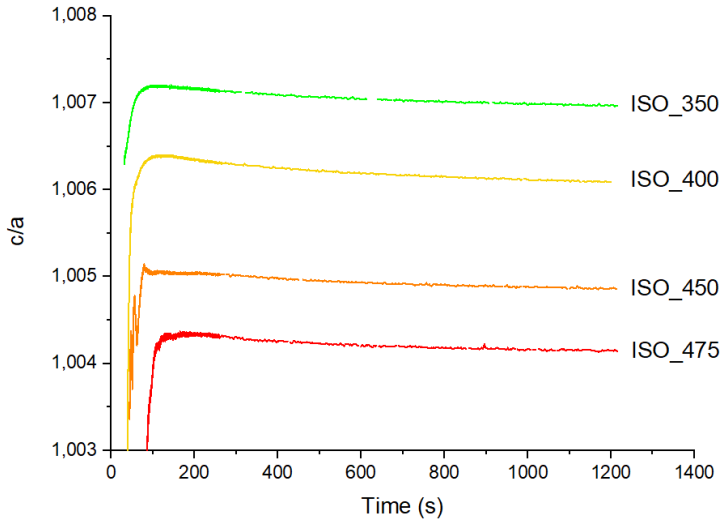

Figure. III. 8: Evolution of c/a ratio of the BCT ferritic phase during the studied isothermal holdings.

Having said that, Figure. III. 8 shows the evolution of c/a ratio as a function of the time during isothermal holdings at temperatures between 350 °C and 475 °C (without the final cooling stage). The experiment below 300 °C have been excluded as it is not possible to isolate convincingly the respective behaviors of bainite and martensite in the microstructure.

The evolutions of the c/a ratio show two successive behaviors: at the beginning of the bainite transformation, the c/a ratio increases rapidly during the very first 100 seconds. After reaching a maximum, it then decreases continuously while remaining above 1 (value corresponding to an ideal

body-centered cubic structure). The lower the holding temperature, the higher the c/a ratio at maximum and at the end of the holding stage.

The tetragonality of the ferritic phases is associated to the presence of carbon atoms in the body-centered lattice. According to the Zener ordering theory [17], the carbon atoms in solid solution in a ferritic lattice tend in fact to segregate collectively to certain octahedral sites and distort it. Due to the alignment of the carbon atoms, it is commonly admitted that a BCT structure is then obtained. The distortion of the lattice was shown to be proportional to the carbon content in solid solution. As in previous published works on bainitic and martensitic steels, the carbon content in bainite can be estimated on the basis of the tetragonality as followed (Eq. 3) [4], [18]–[21]**:**

$$\frac{c}{a} = 1 + 0.045\ x_C^{\alpha} \qquad \textit{Eq. 3}$$

where x_C^{α} is the concentration of carbon in wt.%. In the literature, it is not clear if this estimation of the carbon content also encompasses carbon clusters or carbon segregated at defects [19], such as dislocations or bainitic lath boundaries [22]–[24]. In other studies such as Lu et al. [19], the relationship between c/a ratio and bainite carbon content does not follow Eq. 3, but the relationship: $c/a = 1 + 0.031 x_C^{\alpha}$. This factor (0.031) seems to be linked with the carbon segregated into martensite and not the carbon in solid solution[1].

As a consequence, the estimated carbon content in bainite follows the trends illustrated in Figure. III. 9 if the linear (Eq. 3) applies. For the four isothermal experiments above M_S, the carbon content first increases rapidly and decreases smoothly after about 100 s. The rapid increase must not be interpreted as the fraction of bainite is low and the uncertainty about the tetragonality measurement is too high. However, the trends after 100 s are more relevant. Indeed, these c/a ratio are high and the behaviors can be interpreted easily in the frame of the diffusionless theory of bainitic transformation presented in Chapter I. At the beginning of transformation, supersaturated bainite nucleate with a carbon content equal to the prior austenite. During the transformation process, the c/a ratio decreases due to carbon partitioning between bainite and austenite. Figure. III. 9 shows the evolution of the estimated carbon content in the ferritic phase as a function of the time (after 100 s) for the 4 in situ experiments carried out above 350 °C.

It also appears that the lower the transformation temperature is, the higher the carbon content in bainite (from around 0.09 wt.% at 450 °C up to around 0.15 wt.% at 350 °C at the end of the experiments). These high values are consistent with the values reported in the literature in similar alloys and were used to support the diffusionless theories [12], [13].

[1] Moreover, it must be mentioned that the recent works of Maugis et al**.** [25] show that the distortion due to Zener's ordering could also lead to an orthorhombic lattice under a compressive stress state (tetragonal in tension) [25], [26]. It could explain why an even better agreement can be obtained with an orthorhombic lattice to model diffraction peaks [12].

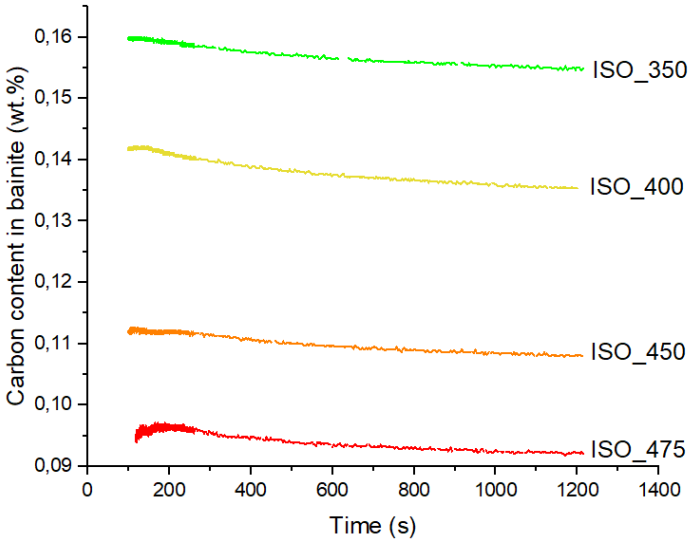

Figure. III. 9: Estimated carbon content in bainite using its measured tetragonality by HEXRD as a function of the time (after 100 s) for the 4 in situ experiments carried out above 350 °C.

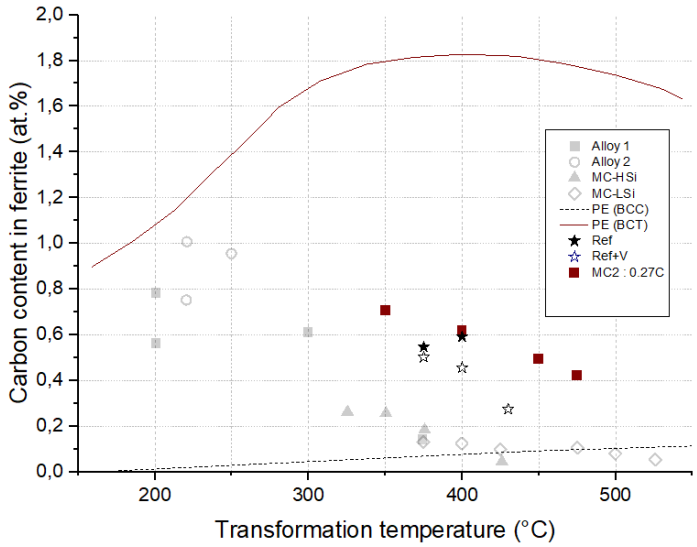

Figure. III. 10: Carbon contents determined by HEXRD in the bainitic ferrite at the end of isothermal holdings in the studied steel as a function of the transformation temperatures (red squares). Our values are compared to measurements by APT (Atom Probe Tomography) in similar alloys from [14] and by EELS (Electron Energy Loss Spectroscopy) from [27].

Ours results have been compared to recent works of literature [14], [27]**.** Figure. III. 10 shows the carbon content in bainitic ferrite (at.%) at the end of the isothermal holdings for 4 considered experiments. The carbon contents in bainitic ferrite obtained by APT (Atom Probe Tomography) measurements in different steels taken from [14] are represented by grey and white symbols and the ones obtained by EELS (Electron Energy Loss Spectroscopy) measurements in two steels taken from [27] are represented with blue stars. These measurements of carbon content in bainite are compared to the para-equilibrium (PE) lines between the body-centred tetragonal ferrite and austenite (PE BCT), and between the body-centred cubic ferrite and austenite (PE BCT) for Fe-C system [16]. At low temperature, the carbon content in bainite seems to be closer to the PE (BCT) line, bainite presents thus a BCT structure. If the holding temperature increases, the carbon content in bainite decreases

and is closer to the PE (BCC) line. The calculation of the para-equilibrium (PE) lines are obtained by Jang et al. [16] using the TCFE6.2 Thermocalc database on a Fe-C system.

As already discussed, these values are high compared to the carbon solubility in BCC phase and support according to [28] the diffusionless theory of bainitic transformation. These results for all the isothermal experiments plead in favor of a bainite formed at low temperature following the lower bainite description of Bhadeshia [15]. Carbon remains trapped in bainite at low temperature since the diffusion of carbon is slow at low temperature. CFB obtained after isothermal annealing is thus highly supersaturated in carbon and its carbon content depends on the transformation temperature.

In conclusion, our analysis of the tetragonality of the bainitic phase obtained along isothermal treatments reveals that this phase is probably highly supersaturated in carbon and its carbon content depends on the transformation temperature. The values found in bainite are as high as 0.15 wt.% of carbon for the ISO_350 experiment meaning that almost one half of the nominal carbon could remain trapped in bainite (solid solution and more probably segregated on defects). This result will be confirmed when establishing carbon balances between phases. The next sections will be hence dedicated to the study of carbon enrichment in austenite monitored in situ during our HEXRD experiments.

I.4. Austenite lattice parameter and carbon partitioning

Figure. III. 11 represents the austenite lattice parameters measured in situ by HEXRD as a function of the time along isothermal holdings at temperatures between 300 °C and 475 °C (the cooling section is not represented). The initial values differ as the lattice parameter of austenite increases with temperature due to the sole thermal expansion. At the onset of isothermal holding, the austenite is in fact assumed to contain the nominal carbon composition of the studied steel.

For all studied isothermal holdings, the evolution of austenite lattice parameters show a sigmoidal shape. At low temperatures (300 °C/350 °C), the austenite lattice parameter does not show any saturation regime at the end of the experiment (even after 1200 s). This is consistent with the transformation kinetics observed at the same temperatures and discussed in the previous section. The transformations still continue during the whole experiments without reaching a real stasis. When analysis the ISO_300_LT and ISO_350_LT experiments a saturation is observed at longer time (about 3600 s). For the ISO_300_LT experiment, the austenite lattice parameter increases to reach a plateau around 9000 seconds. This indicates a lower enrichment after 1h of treatment visible in Figure. III. 14. For the sake of clarity, the values obtained at the end of the long holding stages will be discussed later on. On the contrary, for ISO_400, ISO_450 and ISO_475 experiments, a stasis is observed. The higher the transformation temperature, the lower the increase in the austenite lattice parameter is at the end of the holding.

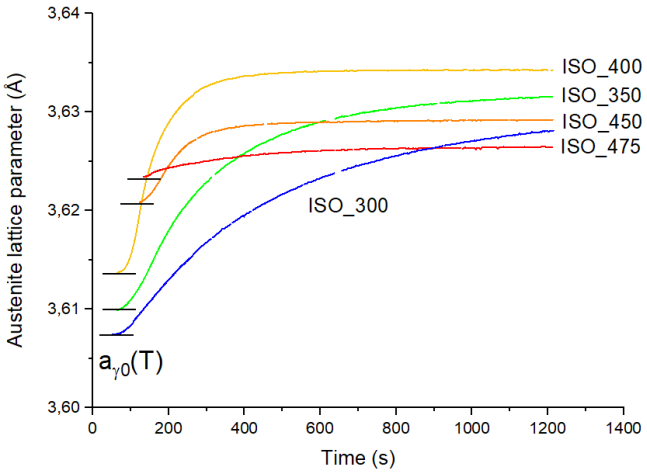

Figure. III. 11: Evolution of the austenite lattice parameter as a function of time for the 5 isothermal experiments.

The variation of the austenite lattice parameter can be related quantitatively to the carbon enrichment in austenite under certain hypothesis. Assuming the variation of the parameter is solely due to the carbon enrichment of austenite, and thus neglecting any evolution in the hydrostatic internal stress of the phase due to the displacive transformation, the carbon content in retained austenite can be determined using the empirical (but commonly admitted) equation proposed by Dyson and Holmes (Eq. 4) [29]:

$$x_C^\gamma = x_C^0 + \frac{a_\gamma - a_{\gamma 0}(T)}{0.033} \qquad \textit{Eq. 4}$$

where x_C^γ and x_C^0 are the carbon contents in retained austenite and the nominal composition respectively (given in wt.%), a_γ and $a_{\gamma 0}(T)$ are the austenite lattice parameter of the carbon-enriched retained austenite and the austenite lattice parameter reference before bainite transformation starts respectively (both given in Å). This last parameter depends on the transformation temperature as shown in Figure. III. 11. The procedure to evaluate the local composition in austenite is very common and has been exploited extensively in previous works from the literature [4], [24], [30], [31].

Nevertheless, it has been clearly demonstrated by Pushkareva et al. [27] that it corresponds to a mean value whereas the carbon is not necessarily homogeneously distributed throughout the austenite. The films of retained austenite are often more enriched than blocky austenite as discussed in Chapter I. The austenite carbon content measured by HEXRD is a mean value taking into account the film-like austenite carbon-rich and blocky austenite carbon-poor, and is closer to these last values. Some authors [4], [22], [23], [32] have succeeded in monitoring the heterogeneity of carbon content taking into consideration two austenite phases in the Rietveld refinement procedure. Our analysis conducted with a single austenite phase is not able to reveal this underlying complexity. This issue will be discussed at the end of this Chapter III when discussing continuous cooling experiments and in Chapter V.

The study of Pushkareva et al. [27] coupling HEXRD and EELS on alloys similar to the studied steel confirms nevertheless the validity of HEXRD compared to direct carbon measurement. It sustains also in turn the hypothesis that the hydrostatic stresses do not play a major role in the evolution of the

lattice parameter of austenite during the bainitic transformation (EELS is not sensitive to the stress state). It must be mentioned that it is not the case if the bainitic transformation is preceded by a martensitic transformation, as is it the case of Q&P steels [33], [34]. As a consequence, the results from ISO_300 must be considered with care, having in mind a possible contribution of the hydrostatic stress relaxation in the evolution of the lattice parameter during the bainitic transformation. This latter contribution is difficult to assess due to the large austenitic grain sizes.

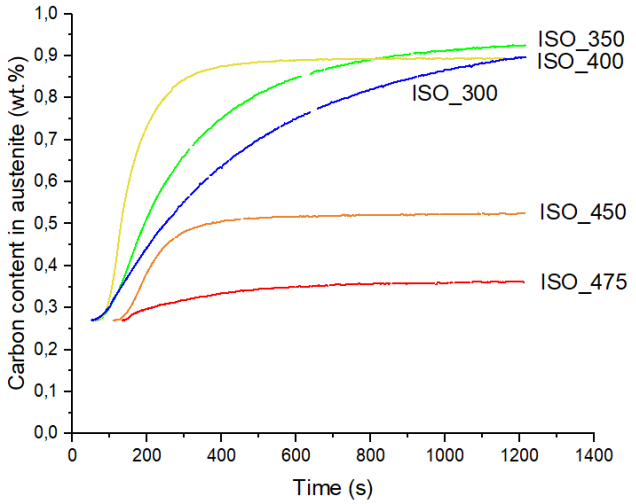

Figure. III. 12: Evolution of the carbon content in retained austenite as a function of the time during the isothermal holdings between 300 °C and 450 °C, determined using Eq. 4 (nominal carbon content 0.27 wt.%).

Figure. III. 12 shows the evolution of the mean carbon content in austenite determined according to the procedure described above. As expected, the carbon content increases in all cases following sigmodal curves, i.e. with a rapid initial enrichment starting from the nominal carbon content (0.27 wt.%) then followed by a plateau (except at low temperatures).

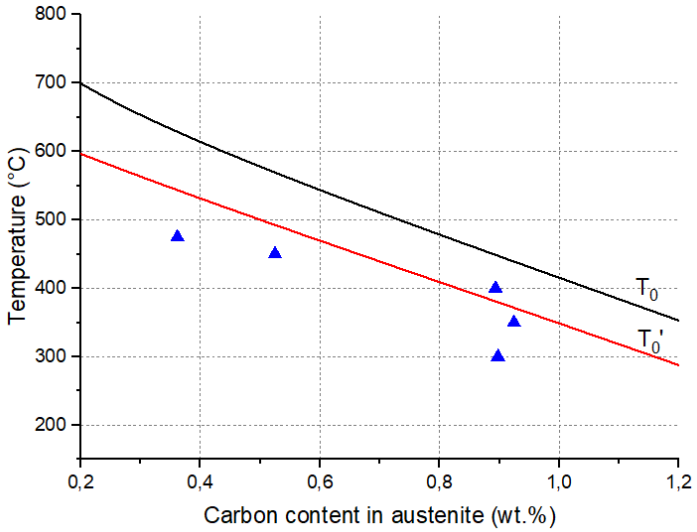

Figure. III. 13: Carbon content in retained austenite at the end of 1200 s isothermal treatments (blue triangles) compared with T_0 and T_0' lines (calculated on the basis of the nominal composition).

Figure. III. 13 shows the carbon content in retained austenite at the end of the isothermal holdings of the 5 in situ experiments as a function of the temperature (blue triangles). These values are compared

with the T_0 and T_0' lines calculated with *Thermocalc* software and TCFE9 database (red and black continuous lines). The T_0' line also takes into account an additional elastic strain energy of 400 J/mol in the ferrite in accordance with the "diffusionless" theory of Bhadeshia [13].

Experimental results are close to the T_0' line only at the lower transformation temperatures (ISO_400 and ISO_350 experiments). For the latter, the transformation was shown to not have reached the stasis (transformation time is too short). This is all the more true for the experiment conducted at 300 °C (ISO_300). The values obtained at 300 °C and 350 °C after 1200 s are thus necessarily low compared to the value expected at stasis. To complete the analysis, the results obtained during the long holding experiments (ISO_300_LT and ISO_350_LT) have thus been reported in Figure. III. 14. This latter figure is similar to Figure. III. 13 with the additional values obtained gathered during these longer experiments (hollow triangles) as a function of the transformation time (10 min, 20 min, 1 h, 5 h). It contains also the data relative the carbon content in bainite determined at the end of isothermal treatments (brown squares) and the one for the ISO_350_LT (hollow brown square).

For the isothermal holding at 350 °C, at the end of the 5 h of holding, the final austenite carbon content is identical to the one determined after 20 min of isothermal holding within the experimental accuracy. For the isothermal holding at 300 °C, the austenite carbon content continue to increase after 20 min of holding. The austenite carbon content determined at the end of the 5 h treatment is closer to the T_0' line. It must be mentioned also the bainite carbon content at the end of the 5 h holding at 350 °C is identical to the ones determined at the end of the 1200 s holding treatment.

On the contrary, at high temperatures (ISO_450 and ISO_475 experiments) the values are far from the T_0' line even if the kinetics show a clear stasis (cf. Figure. III. 3 a)). Such discrepancy between experiments and T_0' line at high temperatures has also been reported by some groups [4], [28], [35].

This result should be mitigated at the light of the known scattering of our experiments at these temperatures. Figure. III. 14 shows the austenite carbon content at the end of the additional experiments at 450 °C and 475 °C presented in Figure. III. 6. For transformations at 450 °C and 475 °C, a large variability in the carbon enrichments are observed. For transformations at 475 °C, the minimal austenite carbon content measured is equal to 0.36 wt.% and the maximal is 0.42 wt.%. For transformations at 450 °C, the minimal austenite carbon content measured is equal to 0.53 wt.% and the maximal is 0.70 wt.%. These difference can be explained as presented by the assumptions made in Section I.2.c.. For certain experiments at 450 °C, the T_0' can be satisfied but it is never the case at 475 °C. The T_0' criterion seems thus to be validated at low temperature but is less verified in the upper range of temperatures.

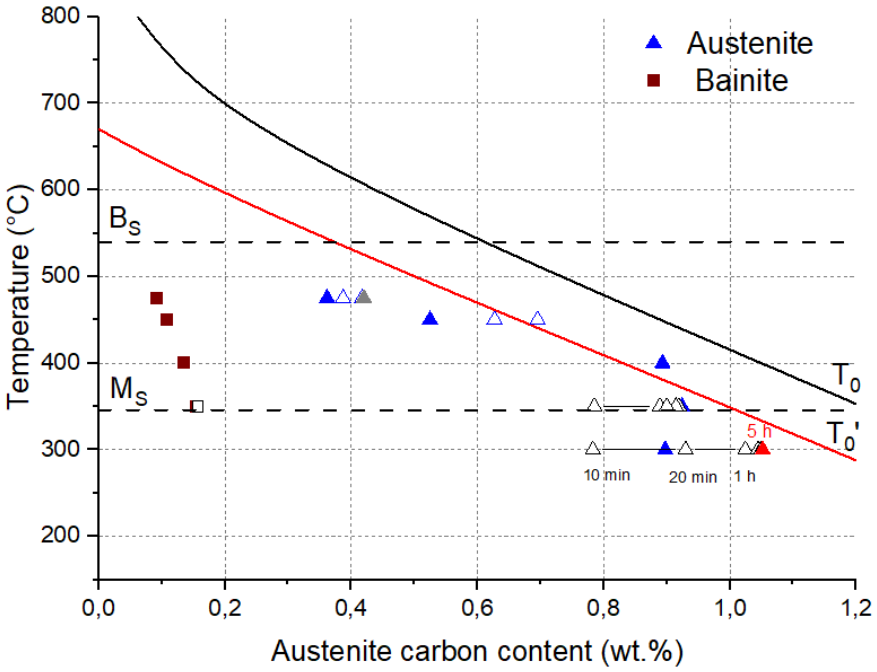

Figure. III. 14: Carbon content in bainite (squares) and in retained austenite for 1200 s isothermal holdings (blue triangles) and 5 h isothermal holdings (hollow triangles) compared with T_0 and T_0' lines.

The evolution of the austenite lattice parameter have been analyzed as the proof of the carbon partitioning between bainite and austenite during the bainitic transformation. This carbon enrichment thus provides a straightforward explanation for the observed stabilization of retained austenite when decreasing the transformation temperature. As discussed above, a martensitic transformation can be observed during the final cooling after the transformation at the highest temperatures and the measured M_S temperatures increase with the transformation temperatures (cf. Table 3). The carbon contents determined in austenite at the end of the holdings was used to calculate the M_S temperatures with the formulae of Van Bohemen [1] and Barbier [2]. These calculations have been summarized in Table 3. A good agreement is found between the observed and calculated M_S temperatures which supports again the determination of the mean carbon content in austenite by HEXRD.

Table 3: Austenite carbon content determined by HEXRD; the M_S calculated using [1] and [2], and the experimental M_S temperatures of austenite at the end of the isothermal holding measured in Figure. III. 5.

Transformation temperature (°C)	Austenite carbon content (wt.%) x_C^γ	calculated M_S (°C) [1]	calculated M_S (°C) [2]	Experimental M_S (°C)
350	0.92	140	136	155-128
400	0.89	148	143	179-148
450	0.52	257	249	230
475	0.36	317	306	330

In conclusion, our analysis of the austenite lattice parameters permits to determine the austenite carbon enrichments along isothermal transformations. The austenite carbon contents at the end of isothermal holdings were compared to the T_0 and T_0' criteria from diffusionless theory. For low

temperature transformations as 350 °C and 300 °C the T_0' criterion is satisfied for long duration time experiments (noted ISO_350_LT and ISO_300_LT), even if for isothermal transformation at 350 °C there is no enrichment after 1200 seconds of holdings. Divergences at T_0' criteria have been observed for high temperature transformations as 475 °C.

In the two last sections, we have investigated independently the carbon content in bainite using the observed tetragonality of the phase and the carbon content in retained austenite using its lattice parameter. In the next section, both measurements will be exploited together to establish carbon balances between the phases and to check their consistency.

I.5. Carbon mass balance at the end of the isothermal holdings

Table 4 summarizes the phase fractions and carbon contents at the end of isothermal experiments (before final cooling). The first column contains the temperature of isothermal holdings. The second and the fourth columns contain the bainite mass fraction f_B (wt.%) and the austenite mass fraction f_A (wt.%) determined by Rietveld refinement respectively at the end of the holding. The third column shows the x_C^α in wt.% corresponding to the carbon content in bainite obtained thanks to the tetragonality ratio c/a at the end of the isothermal holding using (Eq. 2).

For the isothermal transformation at 300 °C (ISO_300), the total fraction of the ferritic phases at the end of the holding is reported in the second column of Table 4.The carbon content of the ferritic phases has also been estimated on the basis of the phase tetragonality but the value is surely difficult to interpret correctly in the presence of a mixture of tempered martensite and bainite. Moreover, for this particular experiment, we have clearly demonstrate that the bainitic transformation is far from having reached a stasis after 1200 s.

Table 4: Phase fractions and carbon contents measured by HEXRD at the end of holdings, the estimated ΔC by a simple carbon mass balance.

Transformation temperature (°C)	Bainite mass fraction (wt.%) f_B	Bainite carbon content (wt.%) x_C^α	Austenite mass fraction (wt.%) f_A	Austenite carbon content (wt.%) x_C^γ	$x_C^\alpha f_B + x_C^\gamma f_A$	ΔC
300	f_{M+B} = 90	0.15	10	0.90	0.22	0.05
350	90	0.15	10	0.92	0.24	0.03
400	84	0.14	16	0.89	0.26	0.01
450	60	0.11	40	0.52	0.27	0.00
475	35	0.09	65	0.36	0.27	0.00

The mathematical error in the Rietveld procedure for the determination of the phase fractions is ± 1 wt.%. On the contrary the relative error on the measurement of the austenite lattice parameter is low (2.10^{-4}). The errors made on the tetragonality are more difficult to evaluate as it could depend on the way in which the width of diffraction peaks is modeled.

Nevertheless, the high degree of confidence on the phase fraction and lattice parameter of austenite leads to the same conclusion that a significant part of the carbon content remains in fact trapped in bainite. The order of magnitude of the carbon content out of austenite is calculated with (Eq. 5) would

have given similar values between 0.2 wt.% and 0.1 wt.%. These values are indubitably higher than the values expected in a BCC phase after a transformation under paraequilibrium.

$$\text{Carbon content out of austenite} = \frac{x_C^0 - x_C^\gamma f_A}{1 - f_A} \quad \textit{Eq. 5}$$

Hence, considering that the determinations in both phases are reliable, it possible to estimate the total carbon content trapped in both phases as follows (sixth column of Table 4) calculated with (Eq. 6):

$$\text{Carbon content trapped in both phases} = x_C^\alpha f_B + x_C^\gamma f_A \quad \textit{Eq. 6}$$

This latter value should correspond to the nominal carbon content of the alloy C_0 (0.27 wt.%). Obviously, except at high temperatures (450 °C and 475 °C), the balance sheet doesn't close perfectly and a carbon deficit is observed. The last column of Table 4 contains the carbon deficit, ΔC, deduced from the carbon mass balance as followed:

$$x_C^0 = x_C^\alpha f_B + x_C^\gamma f_A + \Delta C \quad \textit{Eq. 7}$$

The very low residual fraction of carbon ΔC represents the carbon missing in solid solution in bainite and in austenite. The values found are weak (max. 10 % of the nominal carbon content) and decrease with increasing transformation temperatures. Above 400 °C, the values are negligible considering the precision of the measurement. If solid solution is set aside, the other possible mechanisms able to trap carbon are numerous: segregations on dislocations, segregations on lath/blocks/packet boundaries, local enrichment in austenite or precipitation of carbides. In the literature, it is not well established whether the carbon segregated on defects also contributes to the obvious tetragonality observed on the bainitic phase [22], [36].

The presence of carbides is the better explanation found to explain the ΔC values at low transformation temperatures (mainly at low temperatures as 300 °C and 350 °C). The ΔC values for ISO_300_LT and ISO_350_LT are identical to the ones determined for ISO_300 and ISO_350 experiments. In fact, carbides can also be directly evidenced by SEM observations (cf. Figure. IV. 1) and by looking carefully at diffractograms at the end of the studied thermal treatments as shown in Figure. III. 15.

At 300 °C and 350 °C, the transition carbides mass fraction is estimated less than 1 wt.% using a manual refinement (the uncertainty in phase fraction obtained by the Rietveld refinement is ± 1 wt.%), value that is consistent with the one obtained by the carbon mass balance. In the Rietveld refinement procedure, only austenite and bainite are considered. As a consequence, it is not possible to decide if the whole ΔC value can be explained by these carbides. Nevertheless, the fraction of precipitates remains very low (far below the experimental resolution) and doesn't affect the fraction measured above.

The presence of the weak peaks at 3.1 ° and 4.4 ° (brown boxes) can be unambiguously attributed to the presence of transition carbides (eta or epsilon) in the microstructure [37], [38]. These peaks are far weaker that the ones corresponding the main phases (austenite / bainite). The peaks at 2.8 °, 3.9 ° and 4.7 ° correspond to the MnS (cyan boxes). It must be mentioned that the steel contains around 0.1 wt.%

of sulfur. As a consequence, it contains a large fraction of MnS which is well highlighted on the diffractograms. Even if the studied steel contains a large fraction of MnS visible on micrographs and estimated at about 0.3 wt.% (± 1 wt.%) by HEXRD analysis, the mean Mn composition in the matrix is not affected (no effect on M_S and T_0 lines). On the diffraction patterns, there is no overlapping peaks between MnS, transition carbides and cementite.

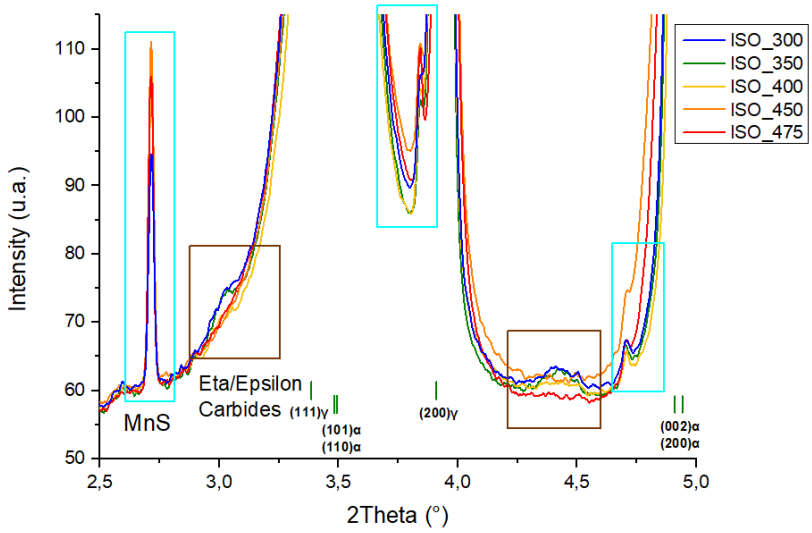

Figure. III. 15: Diffractograms at the end of the 5 studied thermal treatments, the weak peaks at 3.1 ° and 4.4 ° (brown boxes) correspond to transition carbides and cyan boxes correspond to MnS precipitates respectively.

I.6. Conclusion

Bainite transformations were investigated by in situ High energy X-Ray diffraction above and below the M_S temperature of the alloy. These experiments have permitted to determine with a good accuracy the bainite kinetics transformation along isothermal treatments. The composition of phases are tracked thanks to the austenite lattice parameter and the tetragonality of bainite lattice. At the end of isothermal holdings, a carbon enrichment is observed in austenite despite high carbon content trapped in bainite (in particular for low temperatures up to 0.15 wt.%). The austenite carbon content at the end of the holding was compared to the diffusionless stasis criterion (T_0' line). The experimental values are close to the T_0' line however this criterion is not respected for high temperature transformations. For low temperature transformation as 300 °C, the stasis criteria is respected for a long holding time (5 hour holding). For transformations above M_S, a precise carbon mass balance is proposed highlighting carbide formation at the lowest temperatures, which is confirmed by our SEM observations (presented in next Chapter IV) and by the careful observations of the diffractograms.

In the next section, we will present the evolution of ferritic phases kinetics along multistep holding sequences which are a succession of isothermal holdings at decreasing temperatures.

II. Bainitic transformations during successive isothermal holding at different temperatures

Before analyzing the transformations during continuous cooling, intermediate scenarios must be presented. The proposed experiments consist in studying the bainitic transformations during successive isothermal holdings at different temperatures. Such cooling schedules are rarely considered in the literature but the recent work of Tian et al. and Wang et al. [39], [40] show their strong interest. They permit for instance to verify if a bainitic transformation can restart at a lower temperature once a stasis is reached at a given temperature or to investigate how a partial transformation bainitic microstructure affects further kinetics. The present section will focus on these important fundamental questions. The produced microstructures show also a higher complexity as they are made with a mixture of bainitic structures obtained at different temperatures with thus different sizes and microtextures.

II.1. Investigated multistep holding sequences

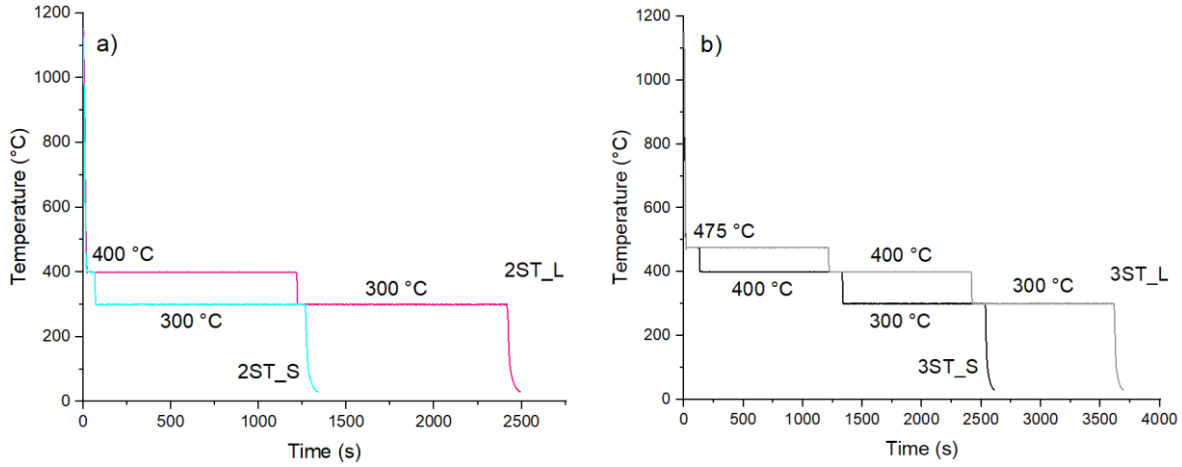

Figure. III. 16: Heat treatments for multistep holding sequences a) two-step holding sequences b) three-step holding sequences.

Figure. III. 16 a) and b) show the evolution of the temperature as function of the time in two-step and three-step holding sequences respectively as disclosed already in Chapter II. The thermal treatments were composed by an austenitization at 1150 °C during 3 minutes in all treatments. As for isothermal experiments, the reference time (t = 0) is set at the end of the austenitization stage. The two-step holding sequence were composed by two steps at 400 °C and 300 °C with a holding time of 1200 seconds for each steps (pink). This condition will be later denoted as 2ST_L corresponding to a two-step treatment with a long duration time of the first step. The second multistep is composed with two steps also, the first step during which the stasis is not reached with a holding time around 70 seconds (chosen using dilatometric trial to reach about 50 wt.% of bainite before the transformation at 300 °C) and at 300 °C with a holding time of 1200 seconds. This treatment will be denoted by 2ST_S corresponding to a short duration time of the first step. For the three-step holding sequences, the schedules present three steps at 475 °C, 400 °C and 300 °C with a holding time of 1200 seconds for

each step (grey). This condition will be later denoted as 3ST_L corresponding to a three-step treatment with a long duration time of the first step. The second presents three steps at 475 °C with a holding time of 114 seconds (chosen using dilatometric trial to reach about 50 wt.% of bainite before the transformation at 400 °C), 400 °C and 300 °C with a holding time of 1200 seconds for each step. This condition will be later denoted as 3ST_S corresponding to a three-step treatment with a short duration time of the first step.

II.2. Two-step holding sequences

II.2.a. 2ST_L experiment

Schedule 2ST_L presents two successive steps at 400 °C and 300 °C during 1200 seconds each.

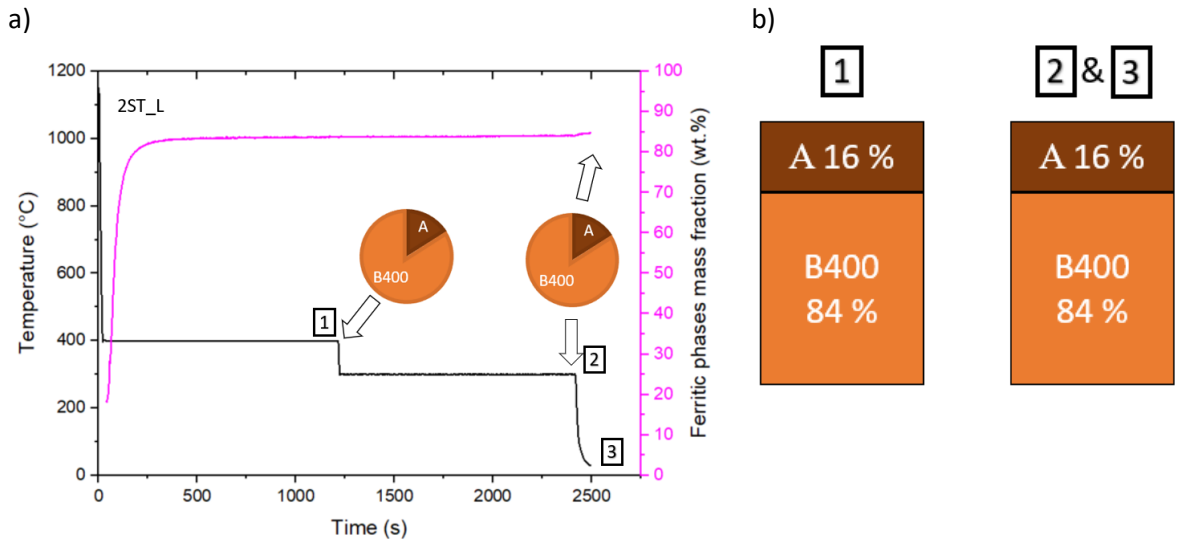

Figure. III. 17: a) Temperature and ferritic phase fraction as function of time for experiment 2ST_L. Pie charts illustrate the composition of microstructure at different times (numbered in the figure). b) Summary of the microstructure compositions (in wt.%) before and after the bainitic transformation at 300 °C (at the end of the first step (#1), at the end of the second step (#2), and after the final cooling at room temperature (#3)). A = Austenite and BXXX = Bainite obtained at XXX °C.

Figure. III. 17 a) shows the evolution of the temperature and ferritic phases mass fraction as a function of time for the considered experiment. During the first step at 400 °C, the transformation is obviously bainitic as in the case of the ISO_400 experiment. The fraction of bainite progressively follows exactly the same evolution as the isothermal transformation at the same temperature (cf. previous Figure. III. 3). This is also true for the tetragonality and the austenite lattice parameter of austenite, thus for the carbon balance between phases.

At the end of the first step (#1), the mass bainite fraction is 84 wt.% as in a purely isothermal ISO_400 treatment, where the stasis was reached. During the second step at 300 °C, the transformation does not restart. The maximal bainite fraction at the end of the second stage (84 wt.%) (#2) is lower than the maximal value obtained in isothermal transformation at 300 °C (experiment ISO_300). After the final cooling to room temperature, there is no formation of fresh martensite (less than 1 wt.%) (#3) as in the case of experiment ISO_400. The microstructure compositions at the transition between isothermal steps and before final cooling are represented schematically in Figure. III. 17 b) to ease the understanding of the transformation sequence (all phases lower than 1 wt.% will not be represented on these representations).

Austenite carbon content at the end of the first step at 400 °C is 0.86 wt.%, value which is close to value given by the T_0' line as shown previously during single isothermal holding at the same temperature (0.89 wt.%). The carbon content in retained austenite at the end of second step at 300 °C does not evolve significantly (0.87 wt.%). The value is also close to the carbon content measured in isothermal treatment at the same temperature (0.90 wt.% for experiment ISO_300) but is lower than the one expected at stasis (1.05 wt.% for experiment ISO_300_LT).

II.2.b. 2ST_S Experiment

Contrary to the prior schedule, experiment 2ST_S schedule was designed to avoid the stasis to be reached during the first step. A reduced holding time of 70 seconds was thus chosen using dilatometric trial to reach about 50 wt.% of bainite before the transformation at 300 °C. The step at 300 °C was kept with a holding time of 1200 seconds. The temperature schedule is represented in Figure. III. 16.

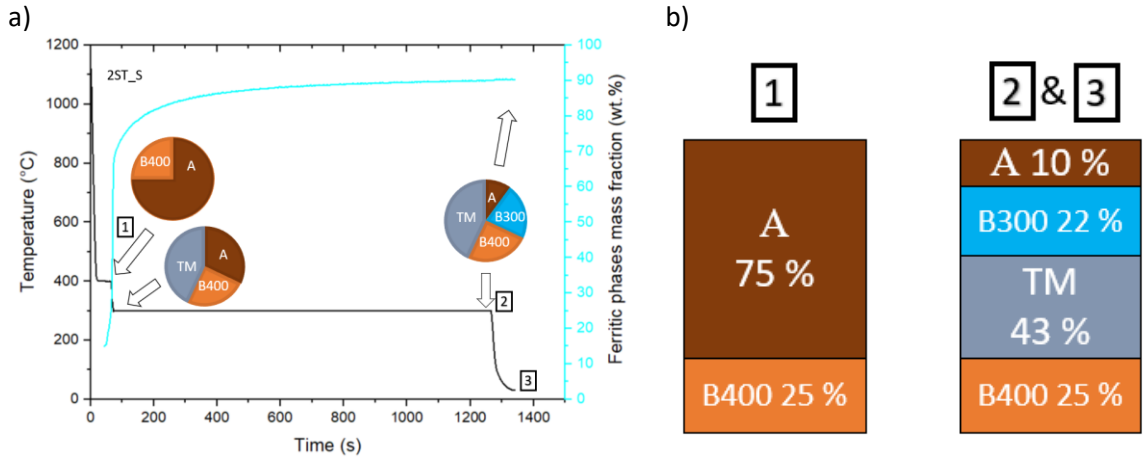

Figure. III. 18: a) Temperature and ferritic phase fraction as function of the time for experiment 2ST_S. Pie charts illustrate the composition of the microstructures at different important times. b) Summary of the microstructures compositions (in wt.%) before and after the bainitic transformation at 300 °C (at the end of the first step (#1), at the end of the second step (#2), and after the final cooling at room temperature (#3)). A = Austenite, TM = Tempered Martensite and BXXX = Bainite obtained at XXX °C.

Figure. III. 18 a) shows the evolution of the temperature and ferritic phases mass fraction as a function of time for experiment 2ST_S. During the first step at 400 °C, the transformation is obviously again bainitic as in experiment ISO_400. The bainite mass fraction follows the same evolution as shown previously for an isothermal transformation (cf. Figure. III. 3). At the end of the first step, the bainite mass fraction is 25 wt.% and the stasis is obviously not reached (#1). Unfortunately, this latter fraction was lower than expected (far less than 50 wt.%).

During the transition between 400 °C and 300 °C, the fraction of the ferritic phases increases suddenly below 340 °C, close to the nominal M_S temperature of the alloy. This transformation looks like in terms of kinetics to a martensitic transformation. This is not surprising in the sense that after only 25 wt.% of bainitic transformation, the carbon enrichment of retained austenite is insufficient. All these factors

led us to conclude that the transformation observed is martensitic. The transformation is partial but significant (about 43 wt.%).

The ferritic phase transformation restarts during the second step at 300 °C but with a lower rate than at 400 °C. As in the case of the ISO_300 experiment, this time-dependent transformation is attributed to a bainitic transformation. The fraction transformed at 300 °C is 22 wt.% after 1200 s (the stasis is not reached as in experiment ISO_300) (#2) and no transformation is observed during the final cooling (#3). The total transformed fraction is 90 wt.% at the end of second holding. This value is the same as the one obtained at the end of experiment ISO_300 (contrary to previous experiment 2ST_L). Figure. III. 18 b) summarizes the microstructure composition before and after the final step at 300 °C. It contains 25 wt.% of bainite obtained at 400 °C; 43 wt.% of fresh martensite obtained between 400 °C and 300 °C and furthered tempered at 300 °C; 22 wt.% of bainite obtained at 300 °C and 10 wt.% of retained austenite.

II.2.c. Discussion: carbon balances

These investigations of the transformations along multistep holding sequences offer the advantage, contrary to the continuous cooling scheme, to isolate each progress of the bainitic transformation at a known and fixed temperature. As a consequence, the reference lattice parameters of the phases doesn't change due to the thermal expansion during a given step (as along a single isothermal holding). As consequence, the direct determination of the carbon enrichment in austenite is possible without any additional hypothesis, hence using again Eq. 4.

The carbon enrichments in retained austenite all along the transformation sequences have been determined but are not presented here in a spirit of synthesis. The values obtained at the end of the holdings at 300 °C for the two-step experiments (pink and cyan squares) have been compared in Figure. III. 19 to the values of previous Figure. III. 13. The final carbon content in both conditions are close to the ones measured in ISO_400 and ISO_300 conditions, consistent with the observed kinetics. A higher deviation from the T_0' line is observed for experiment 2ST_L as the stasis is not reached at 300 °C after 1200 s as in experiment ISO_300.

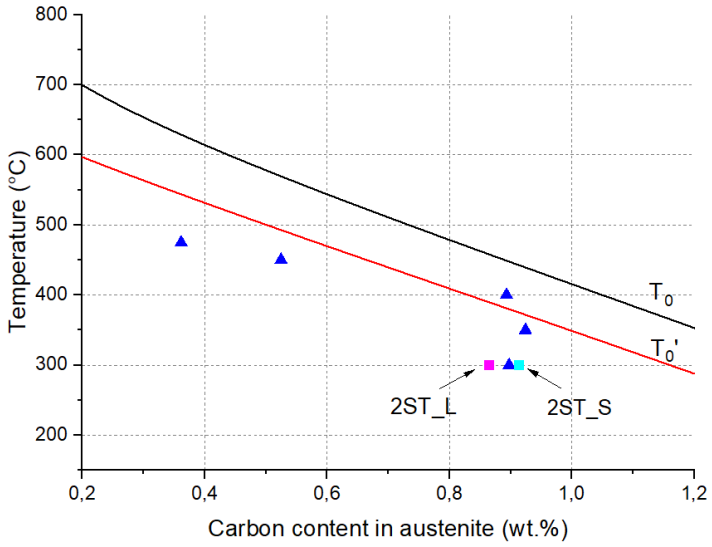

Figure. III. 19: Austenite carbon contents for 1200 s isothermal experiments (blue triangles), experiments 2ST_L and 2ST_S (squares) compared with T_0 and T_0' lines.

Table 5 is a summary of austenite fractions and austenite carbon contents at the end of the last step at 300 °C for the 2ST_L and 2ST_S cooling sequences. As presented before, transformed austenite mass fraction depend on the schedule. A higher fraction of retained austenite is measured at the end of treatment 2ST_L, even if the austenite carbon content at the end of the final step is very close for both two-step treatments. The martensite/bainite carbon contents at the end of the step at 300 °C were determined using the evolution of the c/a ratio. In both conditions (2ST_L and 2ST_S) carbon stays trapped in martensite/bainite and are estimated to 0.13 wt.% and 0.15 wt.%, respectively. Those values are close to the one measured for the isothermal treatment ISO_400 (0.14 wt.%) and ISO_300 treatment (0.15 wt.%). The calculation of the carbon mass balance in both two-step holding sequences (ΔC = 0.03 and 0.04 respectively) predicts the presence of a small amount of carbides, presence which have been confirmed on the final diffractograms at room temperature (shown in APPENDIX 2). Hence, the carbon balances in the two-step microstructures depend on the transformation history, and not on the sole last transformation step.

Table 5: Fractions and compositions of the phases determined by HEXRD experiments ISO_300 and ISO_400 and at the end of the 300 °C step for the two-step holding sequences (2ST_S & 2ST_L). The carbon balance is established as in the previous section.

Experiment	Austenite mass fraction (wt.%)	Austenite carbon content (wt.%)	Bainite/Martensite mass fraction (wt.%)	Bainite carbon content (wt.%)	$x_C^\alpha f_B + x_C^\gamma f_A$	ΔC
ISO_300	10	0.90	90	0.15	0.22	0.05
ISO_400	16	0.89	84	0.14	0.26	0.01
2ST_L	16	0.87	84	0.13	0.24	0.03
2ST_S	10	0.91	90	0.15	0.23	0.04

These experiments highlight that a bainite transformation can restart at a lower temperature if the bainite fraction is not enough advanced. In the studied cases, if the transformation has reached the stasis at 400 °C, it does not restart at lower temperature even is the transformation is “theoretically possible” at 300 °C. Moreover, these experiments permit to claim that the bainite transformation does not respect the additivity rule for diffusive transformations (not only in terms of phase fractions but also of carbon balance between phases), i.e. that it does depend on the transformation history and not only the sole transformation temperature. As a consequence, it cannot been described correctly by a simple Scheil’s additivity rule [41], [42].

II.3. Three-step holding sequences

II.3.a. 3ST_L experiment

The three-step experiments permit to investigate other combinations of transformation temperatures, in particular including an initial step at 475 °C which induces a bainitic transformation more representative of the first bainite formed during continuous cooling scheme. Schedule 3ST_L consists in three holding steps at 475 °, 400 °C and 300 °C respectively with the same holding time of 1200 seconds.

a) b)

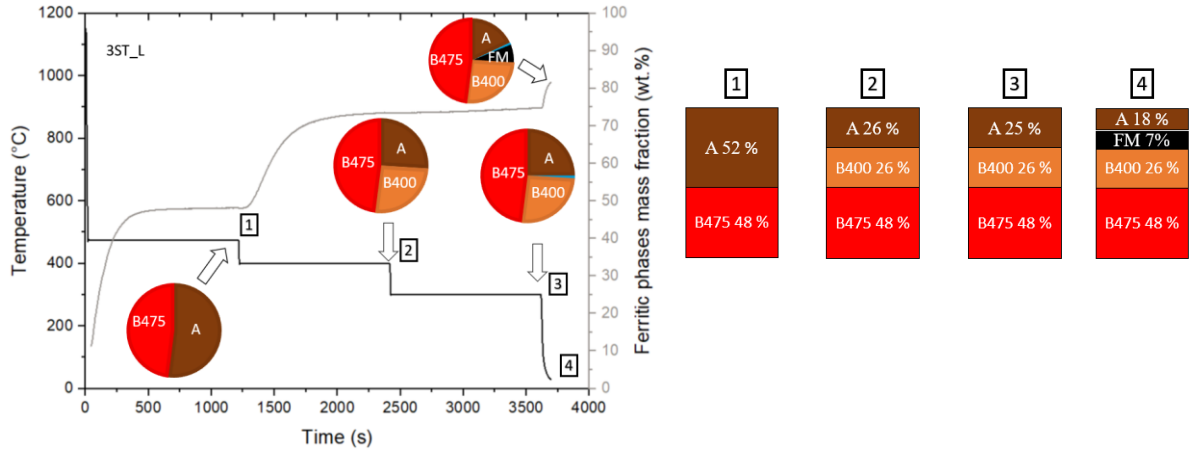

Figure. III. 20: Temperature and ferritic phasse fraction as function of the time for experiment 3ST_L. Pie charts illustrate the composition of the microstructures at different important times. b) Summary of the microstructures compositions (in wt.%) at the end of each steps and after the final cooling to room temperature (numbered from #1 to #4). A = Austenite, BXXX = Bainite obtained at XXX °C and FM= fresh martensite.

Figure. III. 20 a) shows the temperature and the ferritic phases mass fraction as a function of the time during experiment 3ST_L. During the first step at 475 °C, the transformation is obviously bainitic as for experiment ISO_475 (Figure. III. 6). The transformation reaches a stasis and the maximal fraction after about 500 s is equal to 48 wt.% (#1). The comparison between the kinetics of experiments 3ST_L and ISO_475 shows significant differences which have already been discussed in the first section of this Chapter (cf. Figure. III. 6).

During the second step at 400 °C, the bainitic transformation restarts as no martensitic transformation is expected. The transformation reaches almost then a new stasis and 26 wt.% of bainite formed from the 52 wt.% of remaining austenite. The total fraction of bainite (48 + 26 = 74 wt.%) (#2) is significantly lower than the one obtained at stasis during experiment ISO_400 (83 wt.%). The rate of the transformation during the second step is also far slower than the one observed during a single-step. The new stasis is hardly reached after 1200 s whereas it takes less than 500 s to reach it along a single step. The prior transformation at 475 °C thus prevents the transformation to reach the stasis condition expected at 400 °C and affects the transformation kinetics.

During the last step at 300 °C, the transformation does not restart as in the case of experiment 2ST_L, less than 1 wt.% of bainite is formed despite a larger fraction of retained austenite (25 wt.% instead of 16 wt.% (#3)).

During the final cooling, a new transformation is observed which is obviously of martensitic nature. the transformed fraction is equal to 7 wt.%. The remaining austenite at the end of the last step at 300 °C is thus unstable. The final microstructure thus contains 48 wt.% of bainite obtained at 475 °C, 26 wt.% of bainite obtained at 400 °C and 18 wt.% of retained austenite and 7 wt.% of fresh martensite (#4). Figure. III. 20 b) summaries the microstructure compositions at the end of each isothermal holdings. During each step the austenite is progressively enriched in carbon even if some carbon stays trapped in bainite and martensite (about 0.11wt.% after the tetragonality of the lattice). The enrichment of austenite takes place mostly during the first step at 475 °C (0.42 wt.%). The carbon partitioning continues during the bainite transformation along the second step at 400 °C up to 0.70 wt.%. The obtained value at the end of the step is far lower than the one obtained during experiment ISO_400 (0.89 wt.%). As no bainitic transformation takes place during the last step, the carbon content hardly evolves and remains far from the T_0' line at 300 °C. As the value is low just before final cooling, it is not surprising to observe a significant martensitic transformation.

II.3.b. 3ST_S experiment

Contrary to the prior schedule, experiment 3ST_S schedule was designed to avoid the stasis to be reached during the first step. A reduced holding time of 114 seconds was thus chosen for the first isothermal holding at 475 °C. This last schedule 3ST_S presents three steps at 475 °C, 400 °C and 300 °C with a holding time of 1200 seconds for the last two steps. The temperature schedule is represented in Figure. III. 16.

a)

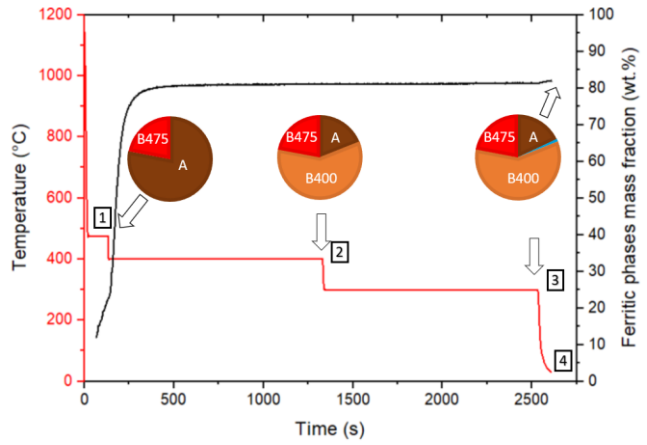

b)

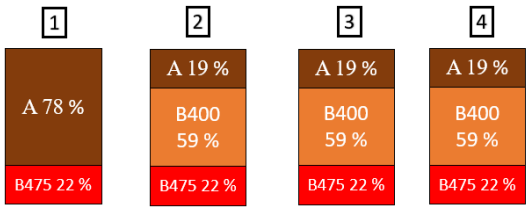

Figure. III. 21: Temperature and ferritic phase fraction as function of the time for experiment 3ST_S. Pie charts illustrate the composition of microstructure at different important times. b) Summary of the microstructures compositions (in wt.%) at the end of each steps and after the final cooling to room temperature (numbered from #1 to #4). A = Austenite and BXXX = Bainite obtained at XXX °C.

Figure. III. 21 a) shows the evolution of the ferritic phase mass fraction as a function of the time for experiment 3ST_S. During the three holding stages, the transformation is bainitic and no martensitic transformation occurs during the intermediate and final cooling stage.

During the first step at 475 °C, the bainite mass fraction increases and follows the kinetics observed in experiment ISO_475 within the limits of the repeatability issue discussed above. At the end of this first

step (#1), 22 wt.% of bainite is formed (0.28 wt.%C in austenite far from the composition of the austenite at T_0'). The slight change in the slope of the transformation kinetics is observed around 120 s, this change in slope is associated with the beginning of the second step. During the second step at 400 °C, the transformation thus continues rapidly, 59 wt.% of bainite forms (austenite carbon content reaches 0.93 wt.%) (#2). During the last step at 300 °C, the bainite transformation is inhibited as in experiment 3TS_L and less than 1 wt.% of bainite forms (#3). Finally, the microstructure at the end of the last step and at room temperature (#4) is composed by 22 wt.% of bainite formed at 475 °C, 59 wt.% of bainite formed at 400 °C and 19 wt.% of retained austenite (Figure. III. 21 b)).

II.3.c. Discussion: carbon balances

As in the previous cases, the austenite is again progressively enriched in carbon and some carbon is trapped in bainite (0.13 wt.%). The enrichment of austenite takes place here mostly during the second step at 400 °C (0.93 wt.%). This is the reason why the carbon content in austenite at the end of experiment 3ST_S is close to the value obtained during experiment ISO_400. It explains also why no martensitic transformation is observed during the final cooling stage. This value is also close to the stasis value reported at 300 °C after 1200 s but far from the one obtained after 5 h (ISO_300_LT). This austenite carbon content at the end of the last step of experiment 3ST_S (black square) is compared to values obtained for isothermal transformations and to the T_0' line in Figure. III. 22. The austenite carbon content at the end of the last step of the 3ST_L experiment (grey square) was compared to the austenite carbon content obtained at after the single-step isothermal holdings in Figure. III. 22.

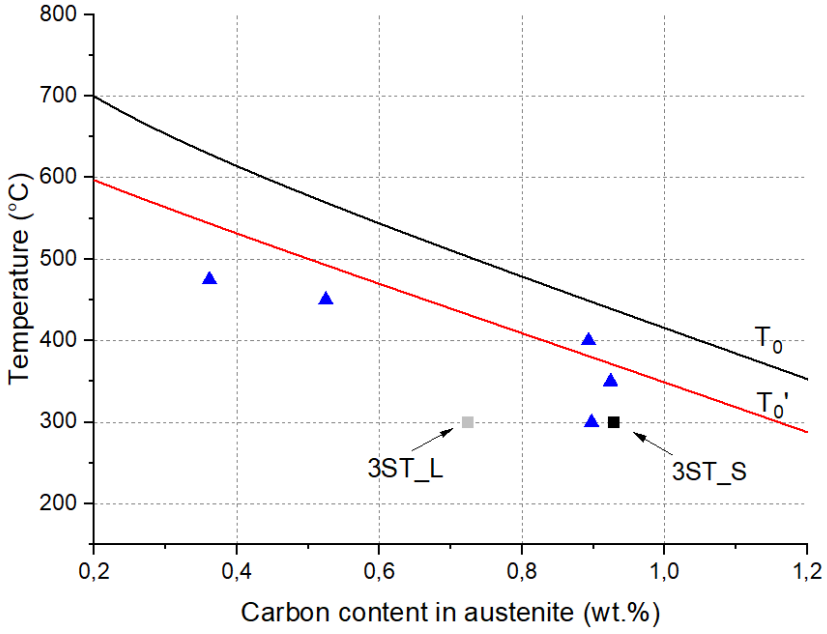

Figure. III. 22: Austenite carbon contents for 1200 s isothermal experiments (blue triangles), experiments 3ST_L and 3ST_S (squares) compared with T_0 and T_0' lines.

Table 6 shows the final phase fractions and the final carbon compositions of austenite and bainite/martensite at the end of the last step at 300 °C. A carbon mass balance was calculated at the end of each step in 3ST_L and 3ST_S conditions. At room temperature, there is no deficit of carbon (ΔC = 0) within the accuracy of the technic, consequently no carbide precipitation is visible on diffractograms (cf. APPENDIX 3). This result is consistent with the fact that most of the transformation occurs in both cases at high temperatures, temperatures at which no carbide during single-step isothermal holding was reported.

Table 6: Mass fractions and carbon contents of the constituting phases measured by HEXRD at the end of the last step of three-step holding sequences.

Experiment	Austenite mass fraction (wt.%)	Austenite carbon content (wt.%)	Martensite/ Bainite mass fraction (wt.%)	Martensite/Bainite carbon content (wt.%)	$x_C^\alpha f_B + x_C^\gamma f_A$	ΔC
3ST_L	25	0.72	75	0.11	0.27	0.00
3ST_S	19	0.93	81	0.13	0.28	-0.01

In all multistep experiments, the slope of the kinetics during the second step is lower for a given transformed fraction. As bainite is formed from an austenite less enriched in carbon, the driving force for the transformation should has been higher. As a consequence, the reduced transformation rate must be attributed to the fact that fewer nucleation sites are available.
Surprisingly, the transformation does not restart during the last step at 300 °C. Hence, this result proves that the transformation rate depends not only on the temperature and the transformed fraction but also on the prior transformation conditions. Theses experiments also highlight that a bainite transformation can restart if the temperature change even if it has previously reached a stasis. Moreover, the stasis conditions seem to depend also on the history of the transformation and not solely on the transformation temperature.
These experiments highlight that a bainite transformation can restart at a lower temperature if the bainite fraction is low. The bainite transformation thus does not respect the additivity rule as observed by Hasan et al. [43].

II.4. Conclusions on multistep holdings

The multistep experiments have been carried to investigate more in details the carbide-free bainitic transformations in the studied alloy at successive temperatures. They have been designed to study the transformations at low temperatures from different states, after partial martensitic/bainitic transformations or transformations already at stasis. Depending on the experience, it is difficult to obtain an obvious criterion for determining whether or not the transformation can resume. It seems that the transformed fraction, independently if a stasis is reached, is a good indicator: below 50 wt.% it restarts systematically (ISO_300, 2ST_S, 3ST_L, 3ST_S), above 70 wt.% it doesn't restart (2ST_L, 3ST_L). Even if the transformation restarts, the kinetics at a given temperature is also lowered. The

stasis conditions of the transformations are affected by the history of the transformation. A large transformation at 475 °C, prevent the transformation at 400 °C to reach the stasis conditions, resulting in a lower stability of retained austenite and in a higher fraction of martensite. On the contrary, a partial bainitic transformation at 475 °C doesn't affect the behavior expected at 400 °C. In this latter case, the martensitic transformation is avoided.

Hence, these experiments prove unambiguously that the bainitic transformation doesn't follow the additivity rule encountered in purely diffusive transformations, i.e. the transformation rate doesn't only depend of the temperature and the already transformed fraction.

Moreover, the calculation of the carbon mass balance by (Eq. 7) in both two-step holding sequences (ΔC = 0.03 and 0.04 respectively) predicts the presence of a small amount of carbides, presence which have been confirmed on the diffractograms (shown in APPENDIX 2). For three-step holding sequences the carbon mass balance predicts the absence of carbide (shown in APPENDIX 3). The formation of carbides hence depends on the thermal treatments. The higher the transformed fractions at high temperature, the lower the carbide fraction is.

III. Continuous cooling

III.1. Continuous cooling with a cooling rate at 0.3°C/s and the associated multistep holding sequence

In this section, our investigations of the continuous cooling treatments representative of the industrial forging practices will be presented. Our reference treatment consists in the thermal schedule represented in Figure. III. 23 (a full austenitization at 1150 °C during 3 minutes followed by a rapid cooling down to 550 °C and a continuous cooling at 0.3 °C/s). This latter is called CC_0.3 (purple curve in Figure. III. 23). Additionally, a multistep experiment which consists in a succession of 7 isothermal steps to mimic a continuous cooling condition at 0.3 °C/s named ST_0.3 (dark red curve in Figure. III. 23) was also studied. This latter "twin" trial was designed to study more easily the evolution of the lattice parameter of austenite, i.e. to unconvolute the effect of the carbon enrichment and the thermal contraction of the lattice. In fact, the determination of the reference non-enriched stress-free lattice parameter of austenite at a given temperature is not straightforward and will require additional hypothesis to post-treat continuous cooling schemes.

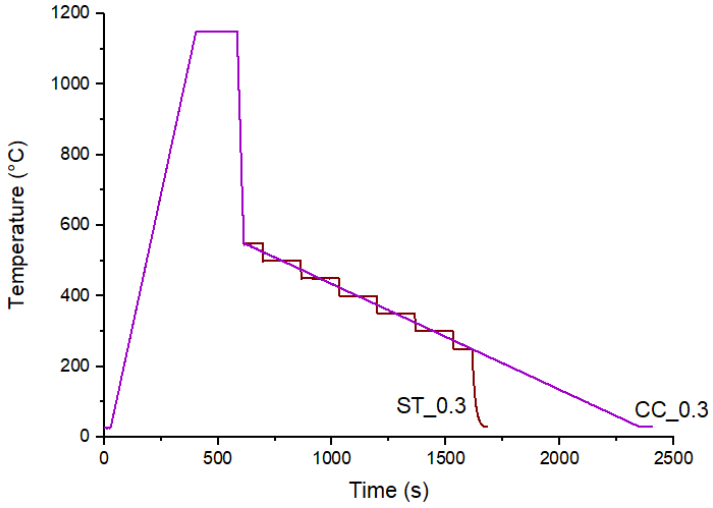

Figure. III. 23: Studied heat treatment representative of a forging condition with a constant cooling rate at 0.3 °C/s below 550 °C (purple) and multistep experiment ST_0.3 (dark red) with a mean cooling rate at 0.3 °C/s below 550 °C.

III.1.a. Kinetics of bainite and martensite transformations

Figure. III. 24 shows the evolution of ferritic phases mass fraction as a function of the time (Figure. III. 24 a)) and as function of the temperature (Figure. III. 24 b)) obtained by HEXRD along cooling sequences ST_0.3 (dark red) and CC_0.3 (purple) respectively. The reference time (t = 0) is fixed by convention at the end of the austenitic soaking for both experiments.

During both experiments, the ferritic phases mass fraction increases. The kinetics curves do not start at 0 wt.% as the quantification is made possible only above about 10 to 15 wt.% due to large prior austenitic grain size. It is this not possible to quantify transformation kinetic during the two first steps

at high transformation temperatures (550 °C and 500 °C) for cooling sequence ST_0.3 as shown in Figure. III. 24 b). In the case of experiment CC_0.3, the transformation seems to start above 500 °C and 38 wt.% of bainite is already transformed at 450 °C.

The kinetics of transformation show globally a sigmoid shape, but a slight bump is observed at low temperatures (below 150 °C for both experiments, after 1025 s for experiment ST_0.3 and 1600 s for experiment CC_0.3). It is believed that this latter increase is due to a final martensitic transformation (about 2 wt.% for CC_0.3 and 4 wt.% for ST_0.3 experiments respectively) whereas the rest of the transformation is of bainitic nature, in accordance with the experiments detailed above. Most of the transformation takes in fact place above the nominal M_S of the alloy (above 350 °C). As in previous treatments, the bainite mass fraction does not reach a maximum value of 100 wt.% of transformation. Kinetics in both conditions are in fact very closed, except maybe at high temperature. The difference could be related to the high sensitivity of the transformation kinetics to the high temperatures. The holding sequences ST_0.3 is thus capable to simulate with good agreement the CC cooling experiment in terms of transformed fractions (global kinetics, incomplete transformation, final martensitic transformation).

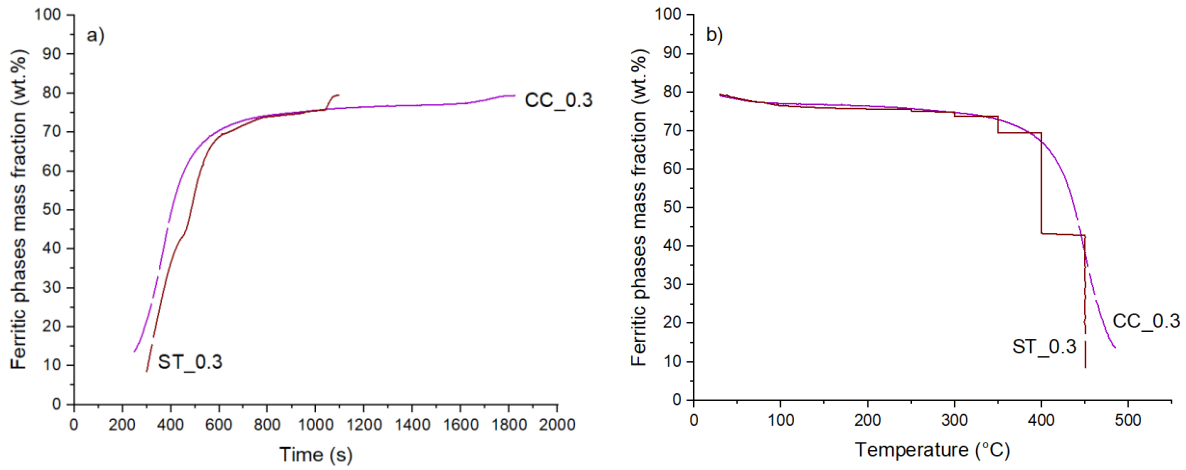

Figure. III. 24: a) Ferritic phases mass fraction as function of time b) Ferritic phases mass fraction as function of the temperature during experiments ST_0.3 and CC_0.3.

III.1.b. Evolution of lattice parameters and carbon content in phases

As for the previous experiments, the tetragonality of the ferritic phase lattices have been extracted from the Rietveld analysis all along the treatments. Figure. III. 25 shows its evolution as function of the time during experiments ST_0.3 and CC_0.3 respectively as well as the transformation fraction for the sake of comparison.

In the case of experiment ST_0.3 (shown in Figure. III. 25 a)), the c/a ratio increases significantly during the step at 450 °C before a slight decrease (as for ISO_450 experiment). The c/a ratio continues to increase more progressively then during the steps at 400 °C and 350 °C. Along the two last steps at low temperatures (300 °C and 250 °C) the c/a ratio tends to stabilize at 1.0053 despite the progress of the transformation (2 wt.%) and the decrease in the transformation temperature. The slight decrease at

the end is attributed to the martensitic transformation, which affect the stability of the measurement. The c/a ratio during experiment CC_0.3 increases continuously along the cooling up to a plateau at 1.0053. It starts to increase at the beginning of the transformation (above 450 °C). During the final cooling at room temperature the c/a ratio also decreases again in relation with the final martensitic transformation.

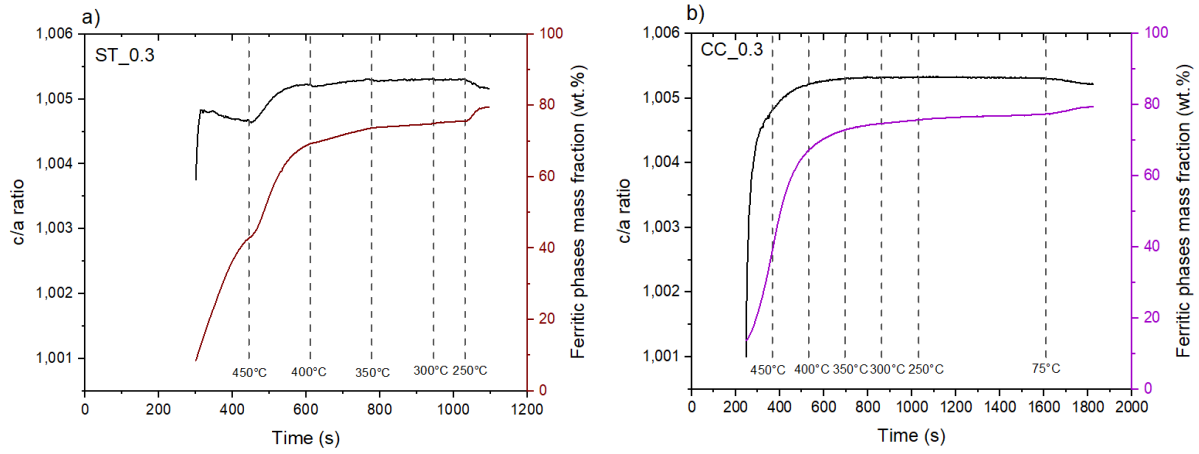

Figure. III. 25: Evolution of c/a ratio (black) and ferritic phases mass fraction as a function of time during a) experiment ST_0.3 (dark red) b) experiment CC_0.3 (purple).

The derived carbon content in bainite at the end of each step of cooling sequence ST_0.3 (determined at each time presented by dashes in Figure. III. 25 a)) and at identical temperatures for cooling sequence CC_0.3 are represented in Figure. III. 26 by dark red and purple squares respectively**.** The estimated carbon content in bainite increases between the step at 450 °C and the step at 400 °C, then tend to stabilize along the cooling. Behaviors in both cases are close (0.12 wt.%), and compared to the isothermal treatments the carbon content in bainite for ST_0.3 and CC_0.3 are comparable to the bainite carbon content measured for experiment ISO_450. The attention of the reader must be drawn on the fact that the values provided by a such methodology, as for the previous steps must be handled with care as bainite appears progressively. As a consequence, the measurement of the tetragonality is certainly done on a large variety of bainitic states with different degrees on partitioning.

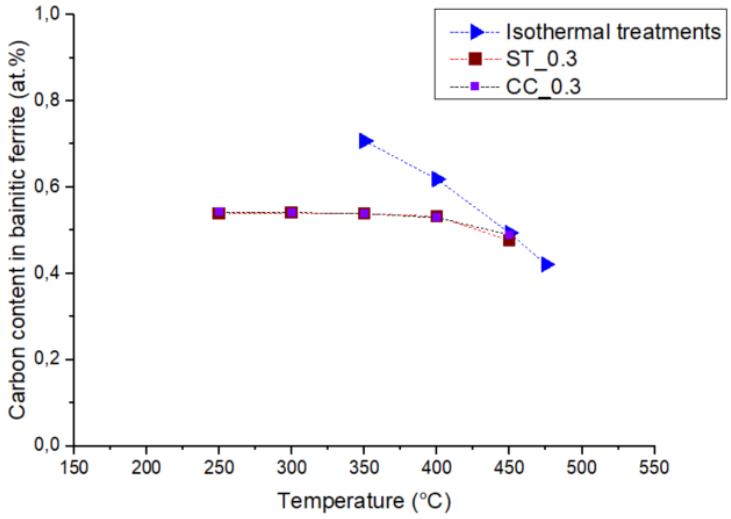

Figure. III. 26: Carbon content in bainitic ferrite determined HEXRD as function of the temperature after 1200 s isothermal transformations (blue triangles), along experiments ST_0.3 (red squares) and CC_0.3 (purple squares).

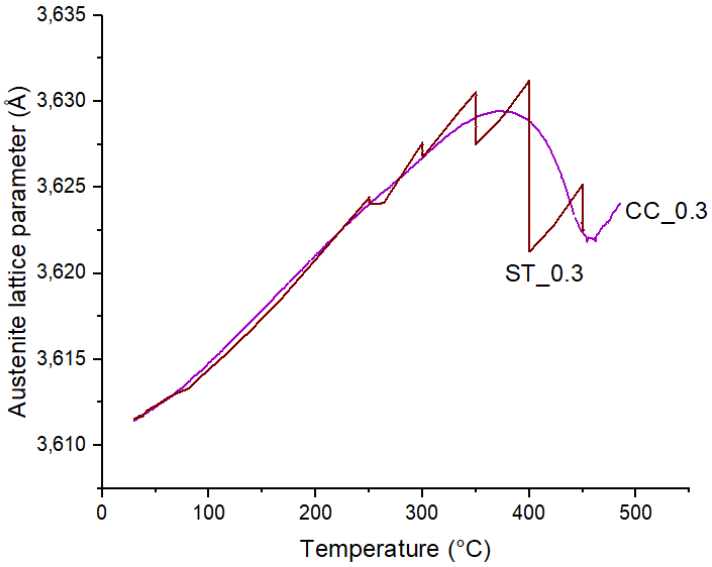

Figure. III. 27: Evolution of the austenite lattice parameter as a function of temperature during treatment ST_0.3 (dark red curve) and treatment CC_0.3 (purple curve).

Figure. III. 27 shows the evolution of austenite lattice parameter as function of temperature along ST_0.3 and CC_0.3 cooling sequences. As explained above, the measurement is not possible at high temperature (large austenite grain issue). For experiment ST_0.3, the measurements are possible below 450 °C. The austenite lattice parameter increases during the holding of each step and decreases during the temperature transitions. The increases are due to the relative carbon enrichment in austenite and the decreases to the pure thermal contraction of the lattice. During such schedule, as for previous two- and three-step experiments, it is possible to determine with precision the carbon content in austenite all along the schedule above 250 ° C. The final martensitic transformation below 100 °C is accompanied by a slight dilatation of the lattice due presumably to unrelaxed internal stresses. The austenite lattice parameter measured along experiment CC_0.3 follows globally the same

evolution. In that case, the measurement is possible below 500 °C, it first increases due to the carbon enrichment and finally decrease to reach the same value as for experiment ST_0.3. The final martensitic transformation seems also to affect the final slope. The difficulty to analyze such experiment comes from the fact that the carbon enrichment in austenite cannot be assessed in a relative way at constant temperature. The evolution of the parameter is the convolution of two phenomena, the time-dependent carbon enrichment and the thermal contraction due to the progressive temperature change.

In their recent works, Reisinger et al. [44] have avoided the issue by calculating the carbon in austenite on the basis of a carbon balance provided the carbon content in bainite is known. They have used in that case the absolute value of the lattice parameter of the ferritic phase (not the tetragonality) to make their measurements. We believe that this methodology is not reliable as the position of the sample is not known a priori even if the set-up is perfectly aligned and calibrated. Moreover, the use of an empirical equation based on the tetragonal lattice is curious when the data are analyzed with a cubic lattice (c/a = 1).

As a consequence, we have developed our own methodology to determine the progressive carbon enrichment in austenite. To do so, we use an extrapolation of the austenite lattice parameter at low temperature which accounts from the sole thermal contraction. At a given temperature, the difference between the experimental measurement and our extrapolation is thus due to the relative carbon enrichment. This method requires an accurate and absolute description of the evolution of the austenite lattice parameter. To our best knowledge, the best extrapolation is provided by the empirical model of Van Bohemen [45] (Eq. 8) which proposes a temperature dependent CTE (Coefficient of Thermal Expansion):

$$\alpha^{\gamma}(T) = B^{\gamma}\left(1 - e^{-\frac{T}{\theta^{\gamma}}}\right) \qquad \textit{Eq. 8}$$

with B^{γ} the value of the CTE at high temperature and θ^{γ} a critical temperature, two parameters which have been calibrated for austenite on highly alloyed steels (with low M_S temperatures) by Van Bohemen. In the present work, the proposed formalism was used for austenite and recalibrated based on HEXRD measurements (experiments on small austenitic grains – not presented in this thesis). The best fit has been obtained with B^{γ} = 2.52 × 10^{-5} K^{-1} and θ^{γ} = 250 K. The absolute evolution of the lattice has then been calibrated to fit the experiment at 500 °C.

The results of the procedure are sensitive to the choice of the parameters. Figure. III. 28 a) shows for instance the experimental and the possible extrapolations of the non-enriched austenite lattice parameter as a function of the temperature for 3 different B^{γ} values (2.4, 2.5 and 2.6 × 10^{-5} K^{-1} respectively). The corresponding carbon contents estimated in austenite with our procedure are plotted in Figure. III. 28 b) for the three B^{γ} values. The recorded variation at room temperature is about 0.1 wt.%. in practice, the determination of B^{γ} is relatively accurate and the error generated by our method is smaller than this variation.

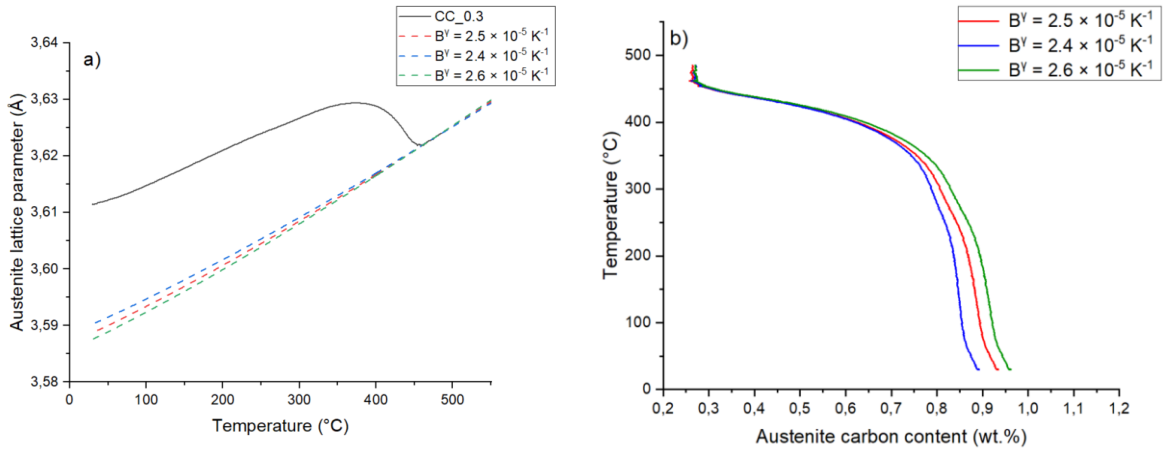

Figure. III. 28: a) Evolution of the austenite lattice parameter along experiment CC_0.3. Dashes curves represent the evolution of non-enriched austenite lattice parameter calculated with (Eq. 8) for 3 parameters B^{γ} b) Influence of parameter B^{γ} on the evolution of austenite carbon content determined in austenite.

Figure. III. 29 shows the carbon contents in retained austenite at the end of each step of cooling sequence ST_0.3 (dark red squares) and along experiment CC_0.3 treatment (purple curve) determined with the new procedure explained above. The values measured at the end of the isothermal treatments after 1200 s (blue triangles) have also been reported for the sake of comparison, as well as the T_0 and T_0' lines.

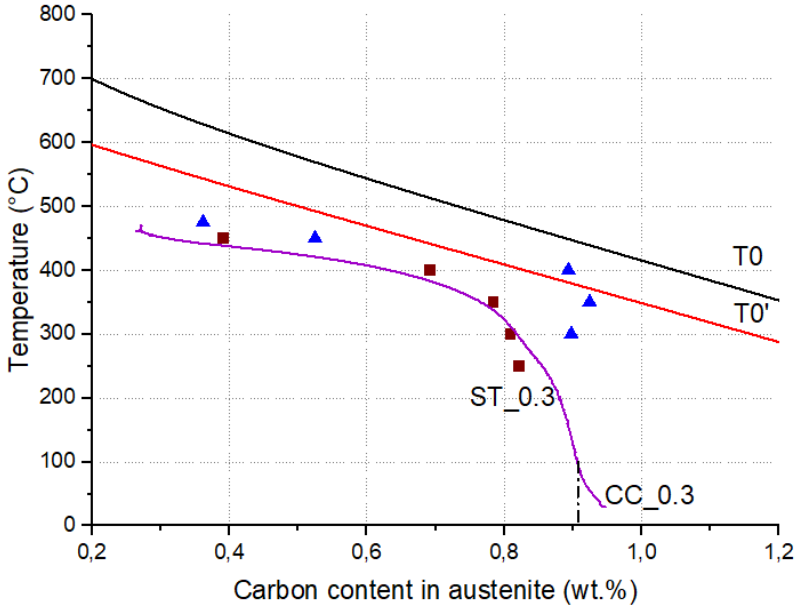

Figure. III. 29: Carbon contents in retained austenite for 1200 s isothermal experiments (blue triangles), ST_0.3 (dark red squares) and CC_0.3 conditions (purple line) with T_0 and T_0' lines.

During both non-isothermal CC_0.3 and ST_0.3 treatments, the measured austenite carbon increases all along the transformation. The values are quite similar which justifies a posteriori the proposed method of determination above 250 °C. Below, as the cooling is rapid in experiment ST_0.3, the sole observed transformation is the martensitic one around 100 °C. The carbon content at the end of the 250 °C holding is 0.82 wt.%. For experiment CC_0.3, the transformation continues below 250 °C and the carbon enrichment is significant. Below 100 °C, an increase in the lattice parameter is observed

which must not been attributed to a carbon enrichment but more likely to a final martensitic transformation (effect of transformation stress state). As a consequence, the last increase must not been considered. The carbon content at the end of the experiment is thus estimated around 0.90 wt.%. In fact, when now compared to the final enrichments reached after single isothermal holdings, both CC_0.3 and ST_0.3 non-isothermal treatments lead to an enrichment which are far lower than the ones measured at stasis. The final enrichments are similar to the one observed at 400 °C but with large transformations below this temperature.

III.1.c. Discussion

III.1.c.1. Carbon heterogeneities in austenite ?

When having a closer look to the enrichment kinetics, it appears that it doesn't start when the transformation itself begins. Figure. III. 31 shows that the enrichment, whatever the hypothesis made for the analysis, is negligible down to about 450 °C. As said before, at this temperature, the transformed fraction is about 40 wt.% and the carbon content in bainite is already high. If a global partitioning would have taken place, the carbon content would have been close to 0.38 wt.% calculated with a simple carbon mass balance shown in Eq. 9:

$$x_C^{\gamma} = \frac{x_C^0 - x_C^{\alpha} f_B}{1 - f_B} \qquad \textit{Eq. 9}$$

This stagnant stage has already been put into evidence by Reisinger et al. [44] during continuous cooling experiments. Its duration is estimated at 150 s in the studied case. Such stages can be observed during isothermal holdings at 450 °C and 475 °C (the enrichment starts when the transformed fraction is about 30 - 40 wt.%) even if it is more difficult to put them into evidence as they are shorter.

This stage was attributed by Reisinger et al. [44] to the enrichment of film-like retained austenite in between the first formed bainite sheaves, leaving most of retained austenite not enriched (blocky austenite). Their conclusions was sustained their analysis of the diffracting crystallite sizes of retained austenite while saying at the same time that the FWHM of the diffracting peaks is affected by the coexistence of two kinds of austenite in the microstructure with different lattice parameters. As a consequence, even if the proposed mechanism is convincing, the proposed reasoning is not conclusive.

To our opinion, a better proof of these heterogeneities in carbon distributions can be found in the analysis of the asymmetry of the austenite diffraction peaks. Such analysis has already been used by Allain et al. [38] in Q&P steel to put into evidence the existence of transitory carbon gradients in retained austenite. Figure. III. 30 shows the diffraction peaks corresponding to the [220] reflection of austenite measured at different times before and during the bainitic transformation (black lines) (intensity as function of θ). As the mean lattice parameter evolves due to the carbon enrichment and the temperature evolution, the peaks have been centered at the origin (maximum value at 0 ° - the adjustment has been made manually). The red lines correspond to the data plotted as a function of -θ. If the peak is symmetric, the black and the red curves must be superimposed. If not, it means that the peak is asymmetric. This behavior of this peak has been chosen as an example; the same behaviors are reported on all the other peaks. Additionally, Figure. III. 31 shows the evolution of the mean carbon

content in austenite and the bainite/martensite fraction as function of the temperature for the studied experiments. The squares correspond to the times at which the peaks have been drawn, numbered from 1 to 6 in Figure. III. 30.

The [220] diffraction peak at high temperature, prior to any transformation (#1), is almost symmetrical and becomes asymmetrical as soon as the transformation is initiated (#2). The left profile of the peak is more extended than the right one, even if the mean position of the peak (at maximum) has not changed. It is interpreted as an heterogenous enrichment of austenite (a low fraction of austenite is presumably enriched in carbon, thus with a larger lattice parameter). The degree of asymmetry continues to increase (#3 & #4) as the transformation proceeds with a maximum at 410 °C (#4). At 300 °C (#5), the mean parameter has continued to increase but the asymmetry has completely been resorbed. It is likely that the austenite is homogenously enriched in carbon and it remains homogenous down to room temperature (#6).

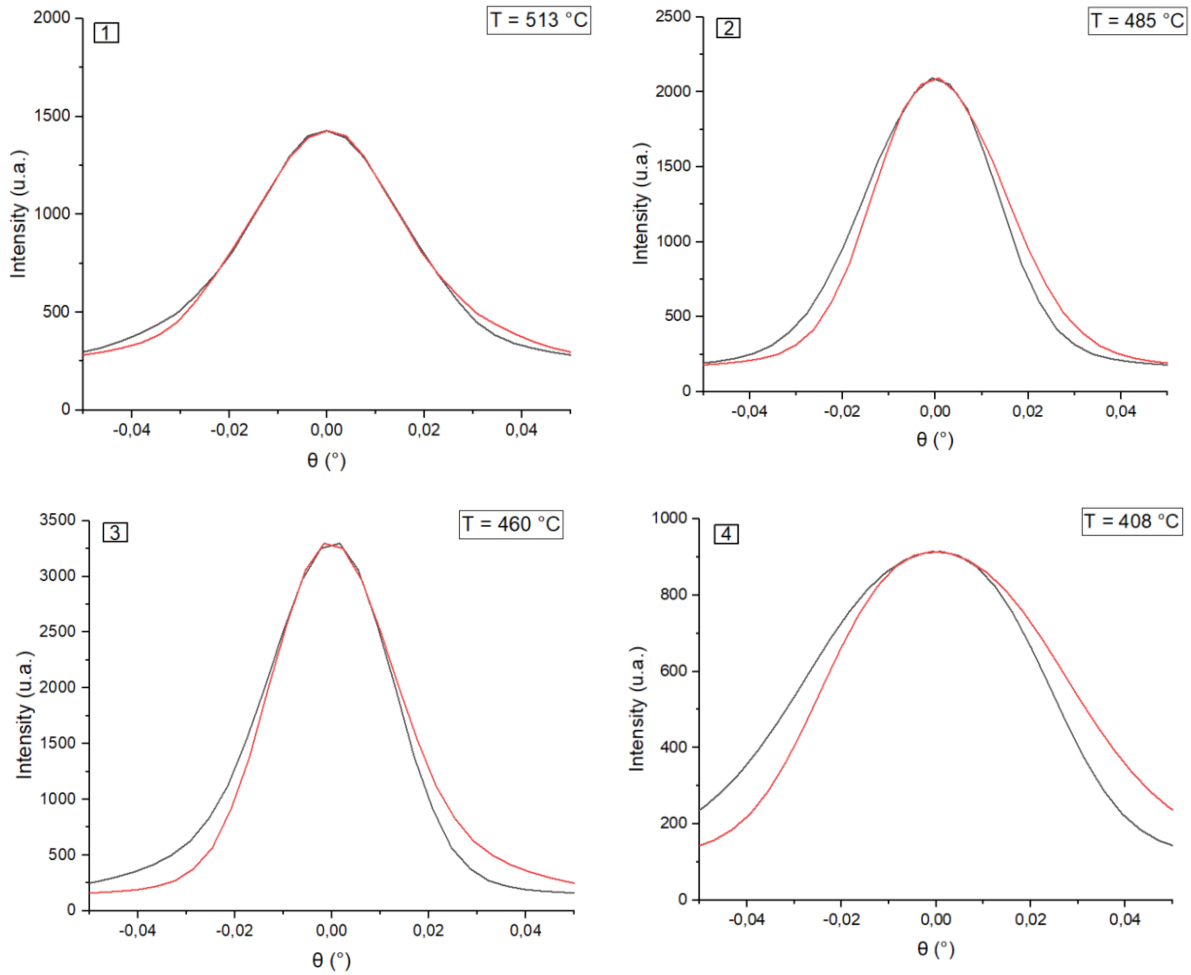

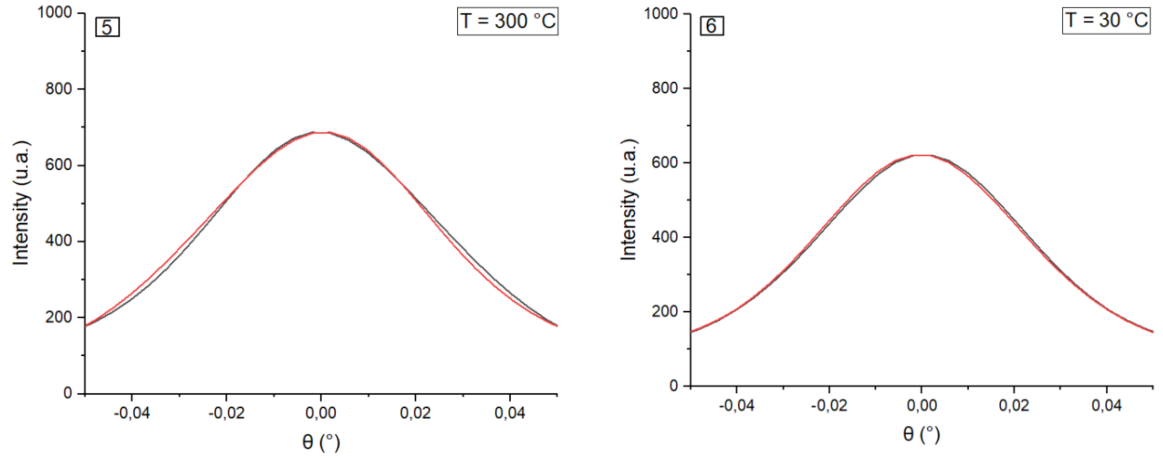

Figure. III. 30: Diffraction peaks of the [220] reflection of austenite measured at different times (numbered from #1 to #6) (black lines) as function of ϑ and same values plotted as a function of -ϑ (red lines). The peaks have been centered manually at 0 ° to compare their respective left and right profiles.

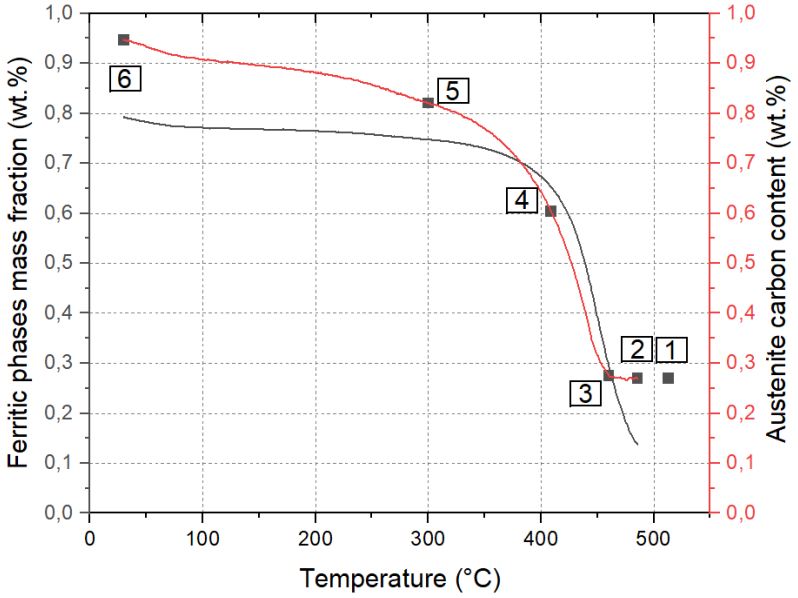

Figure. III. 31: Evolution of ferritic phases mass fraction and austenite carbon content as a function of temperature along experiment CC_0.3. The squares with numbers correspond to the time at which the peaks have been drawn in Figure. III. 30.

Studies to interpret the diffraction spectrum of austenite with two austenitic phases and different levels of enrichment have in fact similar objectives [4], [6], [24], [32], [38], [46]–[48]. In our case, the enrichment differentials being low, this latter approach could not be conducted and we preferred to qualitatively analyze the asymmetry of the austenite peak.

Following the conclusions of Reisinger et al. [44], we also conclude that the mean carbon content in austenite determined using a single lattice parameter is not able to capture the underlying complexity of the enrichment. The deduced carbon enrichments are probably representative of the mean behavior of coarse austenite islands, rather than the behavior of austenite films. Nevertheless, the evolution of the asymmetry of diffraction peak sustains that the carbon is rather homogenously distributed before the end of the transformation. The conclusions also apply surely in the case of isothermal holdings.

III.1.c.2. Second onset of transformation ?

A slight change in the curvature of the transformation curve is also observed at about 300 °C on the transformation kinetics and is visible on the evolution of the austenite lattice parameter of experiment CC_0.3 (cf. Figure. III. 31 and Figure. III. 27). This weak event looks like the second onset of the bainitic transformation highlighted by Reisinger et al. [44] and is also observed on the enrichment kinetics. This phenomenon will be revealed more clearly when studying the transformation at an even lower cooling rate (0.1 °C/s presented in the next section). This transition was also observed by Gupta et al. [49]. It was associated to the precipitation of cementite in austenite permitting the transformation to restart. Nevertheless, our own experiments invalidate this hypothesis. In fact, no carbides was formed during experiments ST_0.3 and CC_0.3 according to the observation of 1D diffractograms all along the experiments (the ones at the end of the treatments are shown in Figure. III. 32). This is also the conclusion of Reisinger et al. [44]. In their paper, this last group of authors claims that it is related to the long range diffusion of carbon and the enrichment of blocky austenite (called stage III in their paper). Our observation of peak asymmetry does not support this conclusion as the observed austenite peaks at 300 °C are already symmetric, meaning that the carbon homogenization is already over.

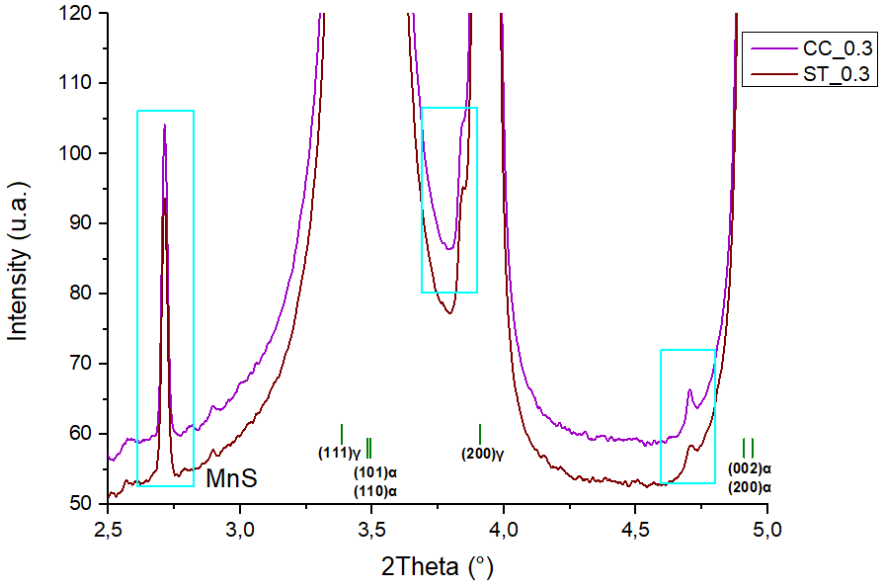

Figure. III. 32: Diffractograms at the end of experiments CC_0.3 (purple) and ST_0.3 (dark red). The cyan boxes indicate diffraction peaks corresponding to MnS precipitates. The presence of carbides would have been revealed by additional diffraction peaks as in Figure. III. 15.

III.1.d. Conclusion

In conclusion, multistep experiment ST_0.3 is a first approach of the continuous cooling schedules. Along this schedule, apart from the problems of measurement in the presence of large austenitic grains, the transformation takes place mostly at high temperature (above 400 °C) accounting for the mean cooling rate. As observed previously in two-step experiments, the transformations at lower temperatures are then limited which jeopardize the possibility to enrich sufficiently the austenite in carbon and to stabilize it down to room temperature. The enrichment after the last step at 250 °C is far from the T_0' line. As a consequence, a final martensitic transformation is observed below 100 °C during the final rapid cooling. As most of the microstructure is formed above 400 °C, it doesn't contain any carbide and the mean carbon content in bainite is low (It is not possible to distinguish the bainites formed at different temperatures).

Continuous cooling experiment CC_0.3 shows exactly the same trends in terms of transformed fraction, carbon content in bainite and presence of carbides. Our methodology to determine the carbon enrichment in austenite has been validated on the values found for ST_0.3. This enrichment is progressive but never reaches the T_0' line. The careful analysis of the concomitant transformation and carbon partitioning reveals that at high temperature, the mean carbon enrichment in austenite is delayed when compared to the transformation kinetics. This delay is thought to be due to the specific carbon enrichment of film-like retained austenite which doesn't represent a significant fraction of the austenite. As a consequence, the diffraction peaks become asymmetric while the mean position of the peaks doesn't evolve much. During experiment CC_0.3, a slight change in the transformation kinetics is also observed around 300 °C as in Reisinger et al.'s works [44], but our analysis reveals that is cannot be related to the precipitation of cementite or transition carbides. Its origin is not clear as it cannot neither be due to the carbon homogenization, yet over at this temperature.

III.2. Continuous cooling with a cooling rate at 0.1 °C/s, 0.3 °C/s and 0.5 °C/s

A continuous cooling at 0.3 °C/s below 550 °C was considered to simulate the mean cooling condition encountered during air cooling of a forging process. Two other experiments were conducted to simulate the cooling behaviors at the center of large parts and close the surface during air cooling (0.1 °C/s named CC_0.1 and 0.5 °C/s named CC_0.5 respectively). Figure. III. 33 shows the heat treatments in continuous cooling conditions for three experiments with different cooling rates 0.1 °C/s, 0.3 °C/s and 0.5 °C/s below 550 °C.

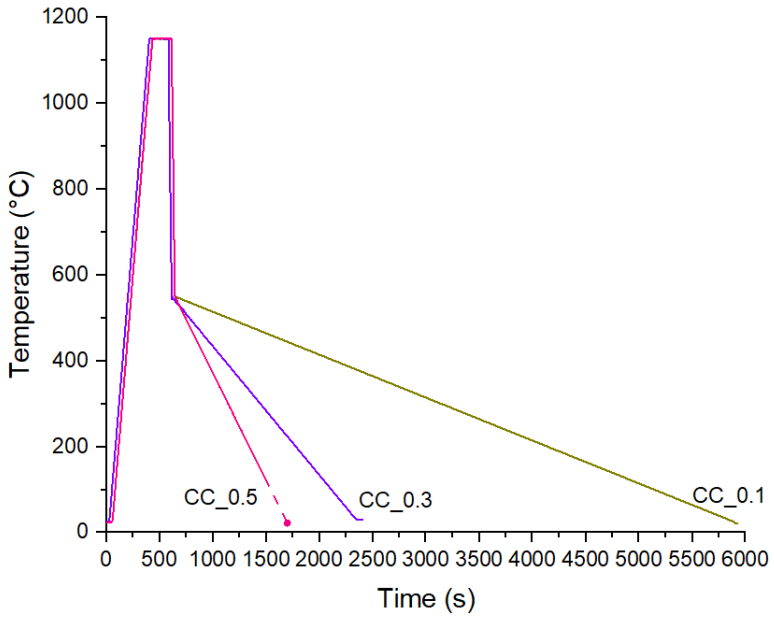

Figure. III. 33: Studied heat treatments representative of forging conditions with different cooling rates of 0.1 °C/s, 0.3 °C/s and 0.5 °C/s below 550 °C (austenitization 3 min at 1150 °C followed by a rapid cooling at 50 °C/s).

Figure. III. 34 shows the evolution of ferritic phase mass fraction as a function of time (Figure. III. 34 a)) and the temperature (Figure. III. 34 b)) during the slow cooling sequences of experiments CC_0.1, CC_0.3 and CC_0.5. The measured kinetics are similar to the one obtained at 0.3 °C/s and already discussed above and must be interpreted in the same way (bainite above 100 °C and martensite below 100 °C).

For the three experiments, the transformations started slightly above 500 °C but it is difficult to be definitive due to large austenitic grain size issue.

In the upper temperature range, the initial transformation rate as function of the time depends on the cooling rate. The higher the cooling rate, the higher the rate is. Nevertheless, things reverse if we talk about the transformed fraction at a given temperature. At 450 °C, the transformed fractions are 46 wt.%, 38 wt.% 22 wt.% and at 0.1°C/s, 0.3 °C/s and 0.5 °C/s respectively. The transformation rates as a function of the temperature are quite similar for the three experiments and the kinetics seems to be just shifted to the low temperatures when the cooling rate increases.

The transformation curves show a first slow down after 40 wt.%, 60 wt.% and 70 wt.% at 0.1 °C/s, 0.3 °C/s and 0.5 °C/s respectively. The curves thus cross in Figure. III. 34 b) above 400 °C. A second change of slope is clearly observed at about 350 °C at 0.1 °C/s while a weak burst is observed at 300 °C

for experiments at 0.3 °C/s and 0.5 °C/s. The final bainite fraction above 100 °C is higher for the CC_0.5 than CC_0.1 and CC_0.3 experiments.

At the end of the transformation (below 100 °C), no change in slope is observed for the CC_0.5 condition, it is not the case for CC_0.3 and CC_0.1. This change in slope is attributed to the formation of fresh martensite. Those results are consistent with the conclusions already presented for the multistep holding sequences (3ST). In fact, if too large fraction of bainite is formed above 450 °C, the transformations at lower temperature are difficult and the kinetics are reduced. As a consequence, austenite is less stabilized and a final martensitic transformation can occur.

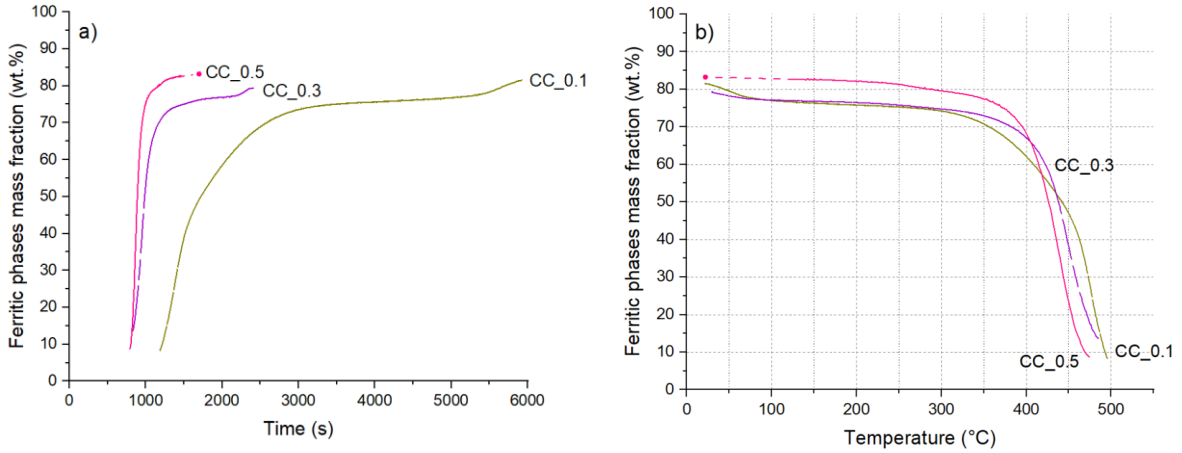

Figure. III. 34: a) Ferritic phases mass fraction as function of the time and b) Ferritic phases mass fraction as function of temperature along CC_0.1, CC_0.3 and CC_0.5 experiments.

Figure. III. 35 shows the evolution of the austenite carbon content along the three continuous cooling sequences (lines) determined with the method validated previously, blue triangles correspond to the carbon content at the end of 1200 s isothermal holdings (presented in Figure. III. 13) compared to the T_0' line.

Along all cooling sequences, the carbon content in austenite increases and the kinetics of enrichment are dependent to the cooling rate while following the same stages reported at 0.3 °C/s. All the curves shows a stagnant stage. As the transformation progresses as function of the temperature decreases with the cooling rate, the significant enrichment starts at lower temperature at 0.5 °C/s. In accordance with the transformation rates, the final enrichment before the martensitic transformation increases with the cooling rate on the contrary. The observed changes in the transformation kinetics are concomitant with changes in the enrichment kinetics (at 400 °C and 300 °C respectively). As at 0.3°C/s the final martensitic transformations are accompanied with an increase in the austenite lattice parameter that must not be interpreted as a carbon enrichment (internal stresses). As a consequence, the final carbon content in austenite are 0.80 wt.%, 0.90 wt.% and 1.05 wt.% after cooling at 0.1 °C/s, 0.3 °C/s and 0.5 °C/s respectively.

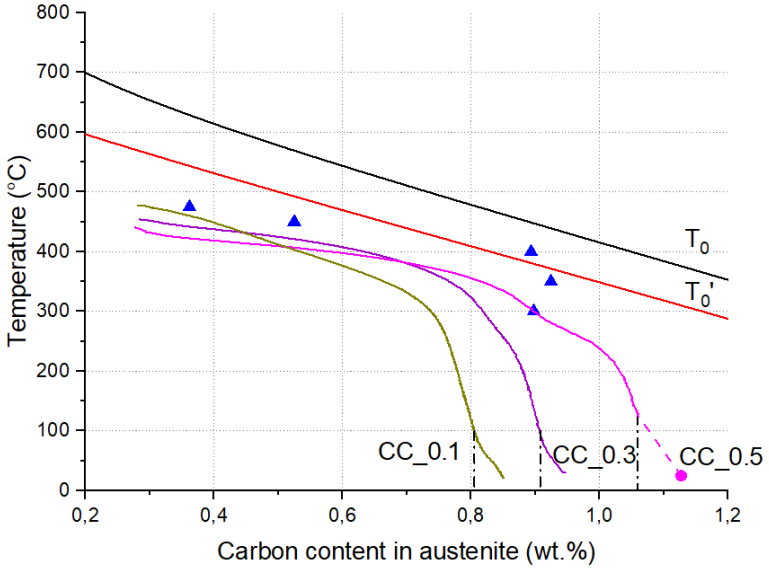

Figure. III. 35: Evolution of the austenite carbon content for the continuous cooling experiments compared to the T_0 and T_0' lines and the carbon content in retained austenite for isothermal treatments (blue triangles) presented in Figure. III. 13.

III.2.a. Discussion: Carbon balance after continuous coolings

The carbon balances has been established using Eq. 7. The observations of the diffractograms along the cooling schedules reveal the absence of significant carbide precipitation. The equation was thus used to estimate the total carbon trapped in bainite (solid solution and segregation). However, the estimated carbon content calculated with (Eq. 3) using the c/a ratio of the ferritic phases at room temperature gives the same value. Table 7 summarizes the phase fractions and carbon contents after the formation of fresh martensite for continuous cooling experiments, respectively. The first column contains the names of the experiments. The second and the fourth columns contain the bainite mass fraction f_B (wt.%) and the austenite mass fraction f_A (wt.%) determined by Rietveld refinement respectively. The third column shows the bainite carbon content x_C^α in wt.% calculated with the mass balance. The fourth column shows the austenite carbon content x_C^γ in wt.% corresponding to the carbon content in austenite. In Table 7, the fraction of fresh martensite f_{FM} (wt.%) is presented corresponding to the fraction of the ferritic phase formed below 100 °C.

Table 7: Phase fractions and carbon contents measured by HEXRD for the continuous cooling experiments at room temperature.

Heat treatments	Bainite mass fraction (wt.%) f_B	Bainite carbon content (wt.%) x_C^α	Austenite mass fraction (wt.%) f_A	Austenite carbon content (wt.%) x_C^γ	Fresh martensite mass fraction (wt.%) f_{FM}
CC_0.1	78	0.12	18	0.8	4
CC_0.3	77	0.08	21	0.9	2
CC_0.5	83	0.11	17	1.05	<1

The bainite mass fraction and the austenite mass fraction are similar in experiments CC_0.3 and CC_0.1, however, transformation and enrichment kinetics are significantly different. The austenite carbon

content is higher in the case of CC_0.3 than CC_0.1 cooling sequences. For experiment CC_0.5, the bainite mass fraction is higher than the bainite mass fraction measured for slow cooling rates experiments. The carbon content in austenite for CC_0.5 experiment is also higher (lower austenite mass fraction). The austenite is thus more stable for a high cooling rate. For all continuous cooling conditions, carbon contents trapped in bainite are almost equivalent (0.11- 0.12 wt.%) in all continuous cooling conditions.

Reisinger et al. [44] showed also that the carbon content in austenite is higher for the fast cooling rate (2 K/s) than the slow cooling rate (0.43 K/s). The fraction of retained austenite for the continuous cooling at 2 K/s is also lower. Our results are in agreement with their study. For the continuous cooling with a high cooling rate (0.5 °C/s), the fraction of bainite and the austenite carbon content are higher than the continuous cooling condition with a slow cooling rate (0.1 °C/s). The obtained result is quite paradoxical from the applicative point of view. We could have expect that a slow cooling rate encountered in the central region of a heat treated part would have led to a microstructure containing more bainite and less MA islands (thus presumably less brittle). The obtained result is counterintuitive and relies on the fact that a large fraction of bainite is formed at high temperature could prevent a further transformation at low temperature and prevent the austenite enrichment. The mechanisms behind this outcome are not clearly established in this work and this is the reason why this particular experimental result will be difficult to simulate in Chapter V.

III.2.b. Discussion

As shown in Figure. III. 34, the transformation rates as a function of the temperature along the continuous cooling at three cooling rates (0.1 °C/s, 0.3 °C/s and 0.5 °C/s) are quite similar for the three experiments. Therefore, the kinetics seems to be just shifted to the low temperatures when the cooling rates increase. As observed by Reisinger et al. [44] the kinetics of bainite formation show different curvatures. The transformation kinetics show a first slow down at about 450 °C for the continuous cooling experiment with a cooling rate of 0.1 °C/s after 40 wt.%. For the continuous cooling experiment with a cooling rate at 0.3 °C/s, a first slowdown is observed at about 400 °C, after 60 wt.% of bainite formed. For the continuous cooling experiment with a cooling rate at 0.5 °C/s a first slowdown is observed after 70 wt.% of bainite formed at about 400 °C. This first slowdown has been observed by Reisinger et al. [44] (stage I in their paper) and was attributed to the enrichment of film-like retained austenite in between the first formed bainite sheaves, leaving most of retained austenite enriched (blocky austenite).

For the continuous cooling experiment with a cooling rate at 0.3 °C/s and 0.5 °C/s, a slight change in the curvature of the transformation curve is observed at about 300 °C on the transformation kinetics, comparable to the second onset of the bainitic transformation highlighted by Reisinger et al. [44]. This event is also visible on the austenite enrichment kinetics and is related to the long range diffusion of carbon and the enrichment of blocky austenite (called stage III in their paper). A second change of slope is clearly observed at about 350 °C in the transformation rate at 0.1 °C/s, however the mechanism related to this second onset need still to be determined.

Conclusions

We have developed a robust methodology to analyze the CFB transformations by in situ High-Energy X-Ray Diffraction along complex thermal schedules. These experiments have permitted to determine bainite kinetics of transformation with a good accuracy (superior to the dilatometry) and to establish carbon mass balance between the phases. The precision of these balances is sufficient to identify the thermal treatments leading to carbide precipitation. Our original method to determine the carbon enrichment in austenite during continuous cooling has also been validated using a multistep twin.

The main scientific results of this chapter are the following:

- We have confirmed that bainitic ferrite is highly supersaturated in carbon whatever the studied conditions. This supersaturation depends on the transformation sequences and deprives austenite from a large source of carbon.
- The austenite carbon contents at the end of the holdings were compared with the displacive criterion T0' line. The experimental values are close to the T0' line, however, this criterion is not respected for high temperature transformations. For transformations in multistep, the stasis conditions are affected by the history of the transformation.
- Studied bainitic transformations are subject to strong inheritance effect and do not respect the additivity rule. In the case of anisothermal treatments, bainitic transformation can occur at low temperature only if the transformation is not enough advanced at high temperature. The transformation kinetics depend on the transformation history.
- The different stages on bainite kinetics during continuous cooling treatments described by Reisinger et al. [44] were also observed even we cannot subscribe to their explanations. Our analysis of diffraction peak asymmetry supports the fact that carbon is homogeneously distributed in austenite at the very beginning of the transformation but the second onset cannot be explained by the process of homogenization so far.
- The effect of the cooling rate on the final microstructure leads to a paradoxical result. The faster the cooling, the more austenite is stabilized. This result is explained in the light of transformation and enrichment kinetics, in particular by the inhibitory effect of transformations at high temperatures.

In order to go farther in the understanding of such transformations, the characterization of the different microstructures using SEM and SEM coupling with EBSD will be presented in the next Chapter.

References

[1] S. M. C. van Bohemen, “Bainite and martensite start temperature calculated with exponential carbon dependence,” *Mater. Sci. Technol.*, vol. 28, no. 4, pp. 487–495, Apr. 2012, doi: 10.1179/1743284711Y.0000000097.

[2] D. Barbier, “Extension of the Martensite Transformation Temperature Relation to Larger Alloying Elements and Contents: Extension of the Martensite Transformation Temperature Relation …,” *Adv. Eng. Mater.*, vol. 16, no. 1, pp. 122–127, Jan. 2014, doi: 10.1002/adem.201300116.

[3] S. M. C. van Bohemen, “Bainite and martensite start temperature calculated with exponential carbon dependence,” *Mater. Sci. Technol.*, vol. 28, no. 4, pp. 487–495, Apr. 2012, doi: 10.1179/1743284711Y.0000000097.

[4] L. Guo, H. K. D. H. Bhadeshia, H. Roelofs, and M. I. Lembke, “In situ synchrotron X-ray study of bainite transformation kinetics in a low-carbon Si-containing steel,” *Mater. Sci. Technol.*, vol. 33, no. 17, pp. 2147–2156, Nov. 2017, doi: 10.1080/02670836.2017.1353669.

[5] A. Navarro-López, J. Hidalgo, J. Sietsma, and M. J. Santofimia, “Characterization of bainitic/martensitic structures formed in isothermal treatments below the M s temperature,” *Mater. Charact.*, vol. 128, pp. 248–256, Jun. 2017, doi: 10.1016/j.matchar.2017.04.007.

[6] Santajuana *et al.*, “Quantitative Assessment of the Time to End Bainitic Transformation,” *Metals*, vol. 9, no. 9, p. 925, Aug. 2019, doi: 10.3390/met9090925.

[7] D. Forgeoux, “Application des structures bainitiques par transformation isotherme et d’un traitement de surface adapté aux vis à haute résistance,” Theses, Université de Technologie de Belfort-Montbeliard, 2016. [Online]. Available: https://tel.archives-ouvertes.fr/tel-01872749

[8] A. Navarro-López, J. Sietsma, and M. J. Santofimia, “Effect of Prior Athermal Martensite on the Isothermal Transformation Kinetics Below M s in a Low-C High-Si Steel,” *Metall. Mater. Trans. A*, vol. 47, no. 3, pp. 1028–1039, Mar. 2016, doi: 10.1007/s11661-015-3285-6.

[9] D. Kim, S.-J. Lee, and B. C. De Cooman, “Microstructure of Low C Steel Isothermally Transformed in the M S to M f Temperature Range,” *Metall. Mater. Trans. A*, vol. 43, no. 13, pp. 4967–4983, Dec. 2012, doi: 10.1007/s11661-012-1338-7.

[10] S. M. C. van Bohemen, M. J. Santofimia, and J. Sietsma, “Experimental evidence for bainite formation below Ms in Fe–0.66C,” *Scr. Mater.*, vol. 58, no. 6, pp. 488–491, Mar. 2008, doi: 10.1016/j.scriptamat.2007.10.045.

[11] A. M. Ravi, A. Navarro-López, J. Sietsma, and M. J. Santofimia, “Influence of martensite/austenite interfaces on bainite formation in low-alloy steels below M,” *Acta Mater.*, vol. 188, pp. 394–405, Apr. 2020, doi: 10.1016/j.actamat.2020.02.003.

[12] C. N. Hulme-Smith, I. Lonardelli, A. C. Dippel, and H. K. D. H. Bhadeshia, “Experimental evidence for non-cubic bainitic ferrite,” *Scr. Mater.*, vol. 69, no. 5, pp. 409–412, Sep. 2013, doi: 10.1016/j.scriptamat.2013.05.035.

[13] C. N. Hulme-Smith, M. J. Peet, I. Lonardelli, A. C. Dippel, and H. K. D. H. Bhadeshia, “Further evidence of tetragonality in bainitic ferrite,” *Mater. Sci. Technol.*, vol. 31, no. 2, pp. 254–256, Jan. 2015, doi: 10.1179/1743284714Y.0000000691.

[14] C. Garcia-Mateo *et al.*, “Low temperature bainitic ferrite: Evidence of carbon super-saturation and tetragonality,” *Acta Mater.*, vol. 91, pp. 162–173, Jun. 2015, doi: 10.1016/j.actamat.2015.03.018.

[15] H. K. D. H. Bhadeshia, *Bainite in steels: transformations, microstructure and properties*, 2. ed. London: IOM Communications, 2001.

[16] J. H. Jang, H. K. D. H. Bhadeshia, and D.-W. Suh, “Solubility of carbon in tetragonal ferrite in equilibrium with austenite,” *Scr. Mater.*, vol. 68, no. 3–4, pp. 195–198, Feb. 2013, doi: 10.1016/j.scriptamat.2012.10.017.

[17] C. Zener, “Kinetics of the decomposition of austenite,” *Trans Aime*, vol. 167, pp. 550–595, 1946.

[18] J. W. Christian, “Tetragonal Martensites in Ferrous Alloys — A Critique,” *Mater. Trans. JIM*, vol. 33, no. 3, pp. 208–214, 1992, doi: 10.2320/matertrans1989.33.208.

[19] Y. Lu, H. Yu, and R. D. Sisson, "The effect of carbon content on the c/a ratio of as-quenched martensite in Fe-C alloys," *Mater. Sci. Eng. A*, vol. 700, pp. 592–597, Jul. 2017, doi: 10.1016/j.msea.2017.05.094.
[20] Z. Nishiyama, *Martensitic transformation*. Elsevier, 2012.
[21] C. S. Roberts, "Effect of Carbon on the Volume Fractions and Lattice Parameters Of Retained Austenite and Martensite," *JOM*, vol. 5, no. 2, pp. 203–204, Feb. 1953, doi: 10.1007/BF03397477.
[22] R. Rementeria *et al.*, "Quantitative assessment of carbon allocation anomalies in low temperature bainite," *Acta Mater.*, vol. 133, pp. 333–345, Jul. 2017, doi: 10.1016/j.actamat.2017.05.048.
[23] R. Rementeria *et al.*, "Carbon concentration measurements by atom probe tomography in the ferritic phase of high-silicon steels," *Acta Mater.*, vol. 125, pp. 359–368, Feb. 2017, doi: 10.1016/j.actamat.2016.12.013.
[24] S. Gaudez, "Kinetics and microstructural evolutions during the tempering of martensitic and nano-bainitic low alloyed steel: in situ experimental study and modelling," PhD Thesis, Université de Lorraine, 2021.
[25] P. Maugis, D. Connétable, and P. Eyméoud, "Stability of Zener order in martensite: an atomistic evidence," *Scr. Mater.*, vol. 194, p. 113632, Mar. 2021, doi: 10.1016/j.scriptamat.2020.113632.
[26] P. Maugis, "Nonlinear elastic behavior of iron-carbon alloys at the nanoscale," *Comput. Mater. Sci.*, vol. 159, pp. 460–469, Mar. 2019, doi: 10.1016/j.commatsci.2018.12.024.
[27] I. Pushkareva *et al.*, "The Influence of Vanadium Additions on Isothermally Formed Bainite Microstructures in Medium Carbon Steels Containing Retained Austenite," *Metals*, vol. 10, no. 3, p. 392, Mar. 2020, doi: 10.3390/met10030392.
[28] R. Ranjan and S. B. Singh, "Isothermal bainite transformation in low-alloy steels: Mechanism of transformation," *Acta Mater.*, vol. 202, pp. 302–316, Jan. 2021, doi: 10.1016/j.actamat.2020.10.048.
[29] D. J. DYSON, "Effect of Alloying Additions on the Lattice Parameter of Austenite," *J Iron Steel Inst*, vol. 208, pp. 469–474, 1970.
[30] P. Jacques *et al.*, "Bainite transformation of low carbon Mn–Si TRIP-assisted multiphase steels: influence of silicon content on cementite precipitation and austenite retention," *Mater. Sci. Eng. A*, vol. 273–275, no. 0, pp. 475–479, Dec. 1999, doi: 10.1016/S0921-5093(99)00331-7.
[31] C. Garcia-Mateo, F. G. Caballero, M. K. Miller, and J. A. Jimenez, "On measurement of carbon content in retained austenite in a nanostructured bainitic steel," *J. Mater. Sci.*, vol. 47, no. 2, pp. 1004–1010, Jan. 2012, doi: 10.1007/s10853-011-5880-2.
[32] S. S. Babu *et al.*, "In-situ observations of lattice parameter fluctuations in austenite and transformation to bainite," *Metall. Mater. Trans. A*, vol. 36, no. 12, pp. 3281–3289, 2005.
[33] S. Allain, G. Geandier, J.-C. Hell, M. Soler, F. Danoix, and M. Gouné, "Effects of Q&P Processing Conditions on Austenite Carbon Enrichment Studied by In Situ High-Energy X-ray Diffraction Experiments," *Metals*, vol. 7, no. 7, p. 232, Jun. 2017, doi: 10.3390/met7070232.
[34] S. Y. P. Allain *et al.*, "Internal stresses and carbon enrichment in austenite of Quenching and Partitioning steels from high energy X-ray diffraction experiments," *Mater. Sci. Eng. A*, vol. 710, pp. 245–250, Jan. 2018, doi: 10.1016/j.msea.2017.10.105.
[35] H.-D. Wu, G. Miyamoto, Z.-G. Yang, C. Zhang, H. Chen, and T. Furuhara, "Incomplete bainite transformation in Fe-Si-C alloys," *Acta Mater.*, vol. 133, pp. 1–9, Jul. 2017, doi: 10.1016/j.actamat.2017.05.017.
[36] F. G. Caballero, M. K. Miller, and C. Garcia-Mateo, "Carbon supersaturation of ferrite in a nanocrystalline bainitic steel," *Acta Mater.*, vol. 58, no. 7, pp. 2338–2343, Apr. 2010, doi: 10.1016/j.actamat.2009.12.020.
[37] S. Allain *et al.*, "In Situ Investigation of the Iron Carbide Precipitation Process in a Fe-C-Mn-Si Q&P Steel," *Materials*, vol. 11, no. 7, p. 1087, Jun. 2018, doi: 10.3390/ma11071087.
[38] S. Y. P. Allain, S. Gaudez, G. Geandier, F. Danoix, M. Soler, and M. Goune, "Carbon heterogeneities in austenite during Quenching & Partitioning (Q&P) process revealed by in situ High Energy X-Ray Diffraction (HEXRD) experiments," *Scr. Mater.*, vol. 181, pp. 108–114, May 2020, doi: 10.1016/j.scriptamat.2020.02.022.

[39] J. Tian, G. Xu, Z. Jiang, M. Zhou, H. Hu, and Q. Yuan, "Transformation Behavior of Bainite during Two-step Isothermal Process in an Ultrafine Bainite Steel," *ISIJ Int.*, vol. 58, no. 10, pp. 1875–1882, Oct. 2018, doi: 10.2355/isijinternational.ISIJINT-2018-187.

[40] X. L. Wang, K. M. Wu, F. Hu, L. Yu, and X. L. Wan, "Multi-step isothermal bainitic transformation in medium-carbon steel," *Scr. Mater.*, vol. 74, pp. 56–59, Mar. 2014, doi: 10.1016/j.scriptamat.2013.10.019.

[41] X. Chen, N. Xiao, D. Li, G. Li, and G. Sun, "The finite element analysis of austenite decomposition during continuous cooling in 22MnB5 steel," *Model. Simul. Mater. Sci. Eng.*, vol. 22, no. 6, p. 065005, Sep. 2014, doi: 10.1088/0965-0393/22/6/065005.

[42] P. R. Woodard, S. Chandrasekar, and H. T. Y. Yang, "Analysis of temperature and microstructure in the quenching of steel cylinders," *Metall. Mater. Trans. B*, vol. 30, no. 4, p. 815, Aug. 1999, doi: 10.1007/s11663-999-0043-4.

[43] S. M. Hasan, S. Kumar, D. Chakrabarti, and S. B. Singh, "Understanding the effect of prior bainite/martensite on the formation of carbide-free bainite," *Philos. Mag.*, vol. 100, no. 7, pp. 797–821, Apr. 2020, doi: 10.1080/14786435.2020.1712486.

[44] S. Reisinger *et al.*, "Strain energy contributions on the bainitic phase transformation in a CrMoV steel during continuous cooling," *Mater. Des.*, vol. 155, pp. 475–484, Oct. 2018, doi: 10.1016/j.matdes.2018.06.014.

[45] S. M. C. van Bohemen, "The nonlinear lattice expansion of iron alloys in the range 100–1600K," *Scr. Mater.*, vol. 69, no. 4, pp. 315–318, Aug. 2013, doi: 10.1016/j.scriptamat.2013.05.009.

[46] A. S. Podder, I. Lonardelli, A. Molinari, and H. K. D. H. Bhadeshia, "Thermal stability of retained austenite in bainitic steel: an *in situ* study," *Proc. R. Soc. Math. Phys. Eng. Sci.*, vol. 467, no. 2135, pp. 3141–3156, Nov. 2011, doi: 10.1098/rspa.2011.0212.

[47] X. C. Xiong, B. Chen, M. X. Huang, J. F. Wang, and L. Wang, "The effect of morphology on the stability of retained austenite in a quenched and partitioned steel," *Scr. Mater.*, vol. 68, no. 5, pp. 321–324, Mar. 2013, doi: 10.1016/j.scriptamat.2012.11.003.

[48] H. J. Stone, M. J. Peet, H. K. D. H. Bhadeshia, P. J. Withers, S. S. Babu, and E. D. Specht, "Synchrotron X-ray studies of austenite and bainitic ferrite," *Proc. R. Soc. Math. Phys. Eng. Sci.*, vol. 464, no. 2092, pp. 1009–1027, Apr. 2008, doi: 10.1098/rspa.2007.0201.

[49] C. Gupta, G. K. Dey, J. K. Chakravartty, D. Srivastav, and S. Banerjee, "A study of bainite transformation in a new CrMoV steel under continuous cooling conditions," *Scr. Mater.*, vol. 53, no. 5, pp. 559–564, Sep. 2005, doi: 10.1016/j.scriptamat.2005.04.031.

Appendix

APPENDIX 1: Diffraction peaks of the (002) and (200) reflections of the ferritic phase

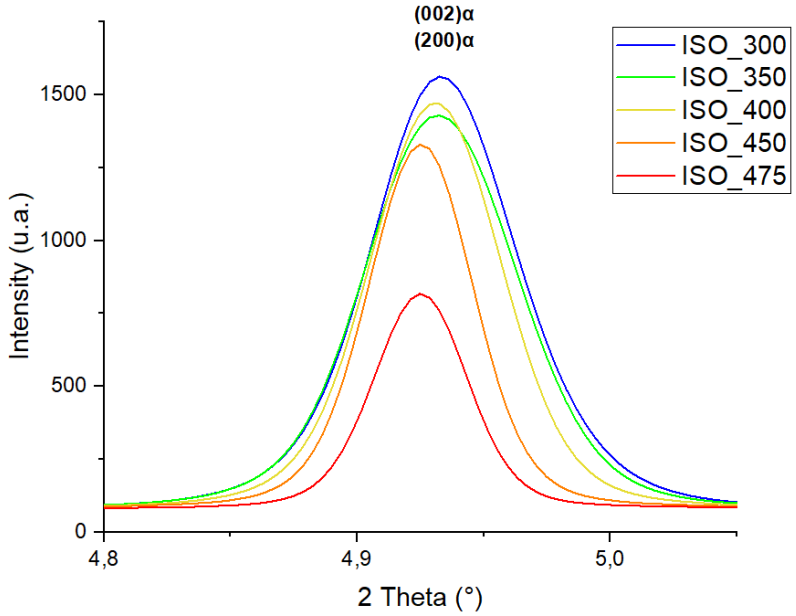

Figure. III. 36: Diffraction peaks of the (002) and (200) reflections of the ferritic phase at room temperature for isothermal experiments.

APPENDIX 2: Diffractograms after two-step holding sequences

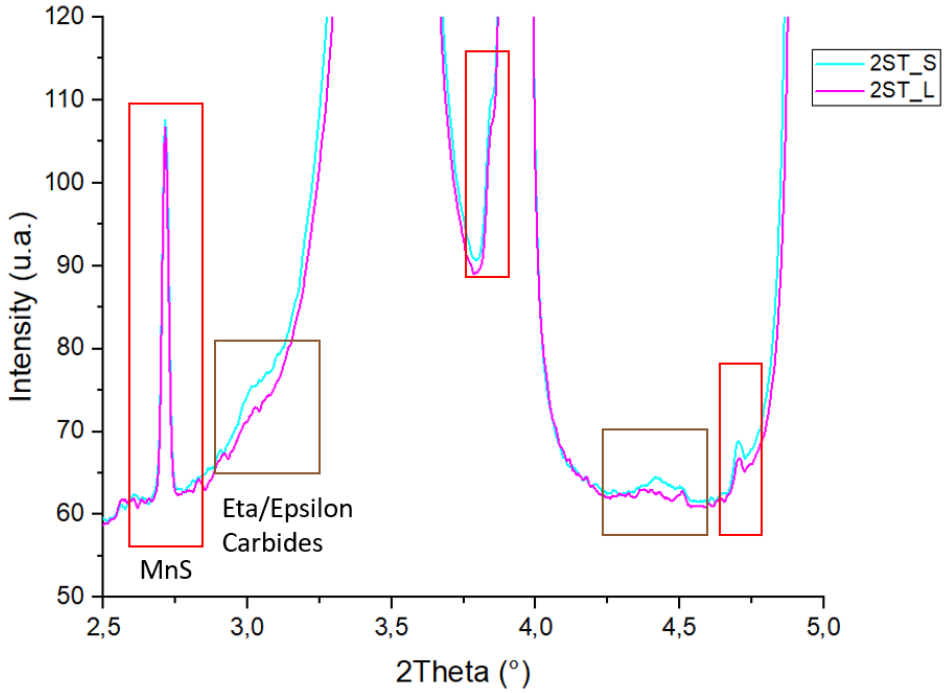

Figure. III. 37: Diffractograms at the end of the thermal treatments for treatments 2ST. The weak peaks at 3.1° and 4.4° (brown boxes) correspond to Eta-Epsilon carbides and (red boxes) correspond to MnS precipitates

Figure. III. 37 shows the diffractograms obtained at room temperature for the 2ST_L and 2ST_S conditions. The presence of the weak peaks at 3.1° and 4.4° (brown boxes) can be unambiguously attributed to the presence of transition carbides (eta or epsilon) in the microstructure. These peaks are far weaker that the one corresponding the main phases (austenite / bainite) which prevents using a conventional Rietveld procedure. The peaks at 2.8°, 3.9° and 4.7° correspond to the MnS (red boxes).

APPENDIX 3: Diffractograms after three-step holding sequences

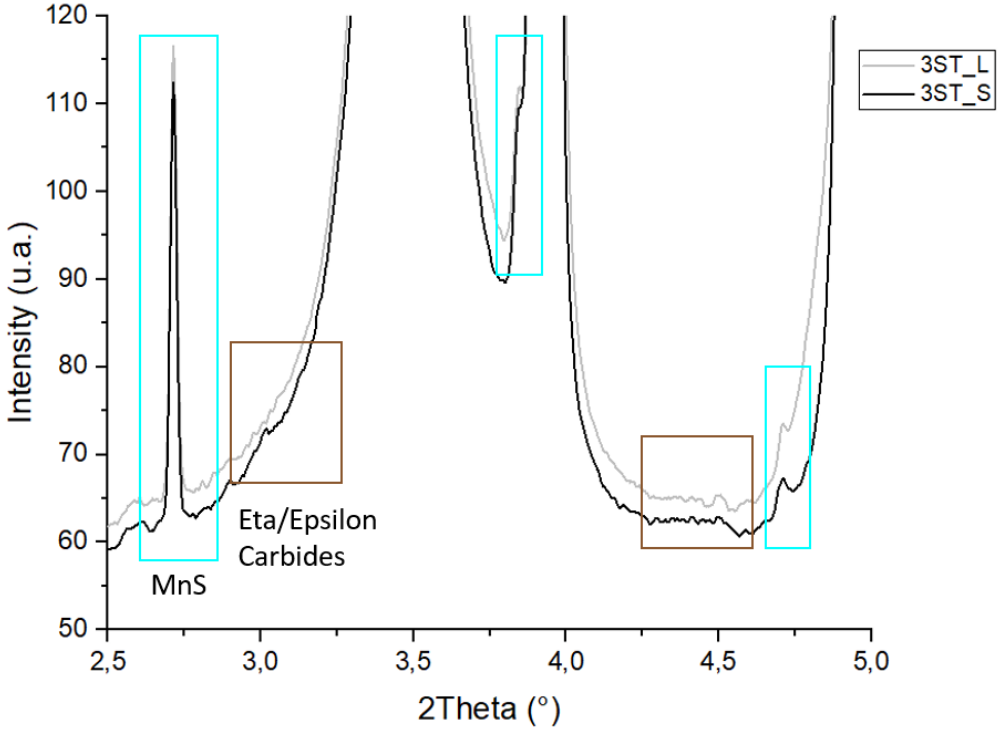

Figure. III. 38: Diffractograms at the end of the thermal treatments for 3ST_L and 3ST_S treatments

Figure. III. 38 shows the diffractograms obtained at room temperature for the 3ST_L and 3ST_S conditions. The characteristic peaks of Eta-Epsilon carbides are not present in the diffractograms.

Chapter IV: Microstructural characterizations and microtextures using SEM and SEM-EBSD

Introduction

As presented in Chapter I, CFB steels exhibit multiphased microstructures made of intricated ferrite, retained austenite and tempered/fresh martensite. By the mean of HEXRD, it was shown in Chapter III how bainite transformation kinetics depends on the thermal paths and on the carbon partition between the different constituting phases. The use of HEXRD however does not allow to investigate further the particular hierarchical and microtextural organization of these microstructures as well as the respective size of the components. All these complimentary features are necessary to understand better the phase transformation mechanisms and from a more practical point of view to build a consistent physically-based model. As in Kitahara et al. [1], Mondal et al. [2], Navarro-Lopez et al. [3], Ben Haj Slama et al. [4], Zhu et al. [5], Gourgues et al. [6] SEM-EBSD technique was considered as the relevant techniques to perform such investigations.

As a reminder, Chapter I shows that CFB microstructures obtained after isothermal treatments are lath bainitic structures containing as second phases interlath retained austenite and martensite. When obtained at low temperatures, CFB can also contain few intralath carbides. The conventional classification of bainitic structures thus often consider CFB as upper bainite. Nevertheless, from the microtextural point of view (Zajac classification) both kind of lower and upper are often observed [7]–[9], i.e. in the upper range of transformation temperature, bainite laths inside a packet are little disoriented (same variant) and in the lower range, bainite laths belongs to different variants (self-accommodating variants [10], [11]) regrouped into blocks and sub-blocks. It is also well established that the lath thickness decreases with the temperature. As a consequence, a broad kind of microstructures can be obtained as a function of the transformation temperature, with varying phase fraction, composition but also size and microtexture. In comparison with that in isothermal transformations, the CFB reaction during continuous cooling has however received relatively little attention in the literature. These first results shows that CFB microstructures formed in that conditions show a far larger distribution in size and morphology of ferrite laths [12], [13].

Our study aims at a better understanding of the CFB phase transformations mechanisms in non-isothermal treatments by a systematic comparison between the microstructures obtained after isothermal and continuous cooling treatments and by clarifying the successive mechanisms explaining the progressive establishment of the microstructure and the resulting large dispersion of microstructure feature. In order to achieve these objectives, the microstructures of the HEXRD samples have been characterized by SEM-EBSD post mortem after the different in situ thermal treatments, i.e. the isothermal holding (ISO_300, ISO_350, ISO_400, ISO_450 and ISO_475), the multistep holding sequences (2ST_L, 2ST_S, 3ST_L and 3ST_S) and the continuous cooling sequence (CC_0.3)**.** The results will be presented in this Chapter following this order, as the microstructures present an increasing complexity.

I. Characterization of microstructures obtained after isothermal holdings

This section will present the systematic characterization of the microstructures of the samples after in situ HEXRD isothermal experiments. These results will be discussed then at the light of the literature.

I.1. Microstructural characterization by SEM

The microstructures of the samples after in situ isothermal experiments have been first observed by Scanning Electron Microscopy (SEM) after nital 2 % etching. Microstructures are composed with tempered martensite (TM) (for the treatment at 300 °C below the M_S temperature of the alloy), bainitic ferrite (B), retained austenite (A) and fresh martensite (FM).

The etching is sensitive to the carbon content of the phases. The lower the carbon content, the more etched is the phase. Bainite and tempered martensite are thus appearing in dark contrast whereas austenite and martensite are hardly etched. Martensite shows a weak roughness and austenite remains completely flat. The interlath retained austenite is enriched in carbon and stabilized at room temperature. The retained austenite appears as a discontinuous films. At low temperatures (300 °C and 350 °C), as expected (cf. Figure. III. 15), some carbides appear also in bright contrast in bainitic laths or in tempered martensite in Figure. IV. 1 a) and Figure. IV. 1 c).

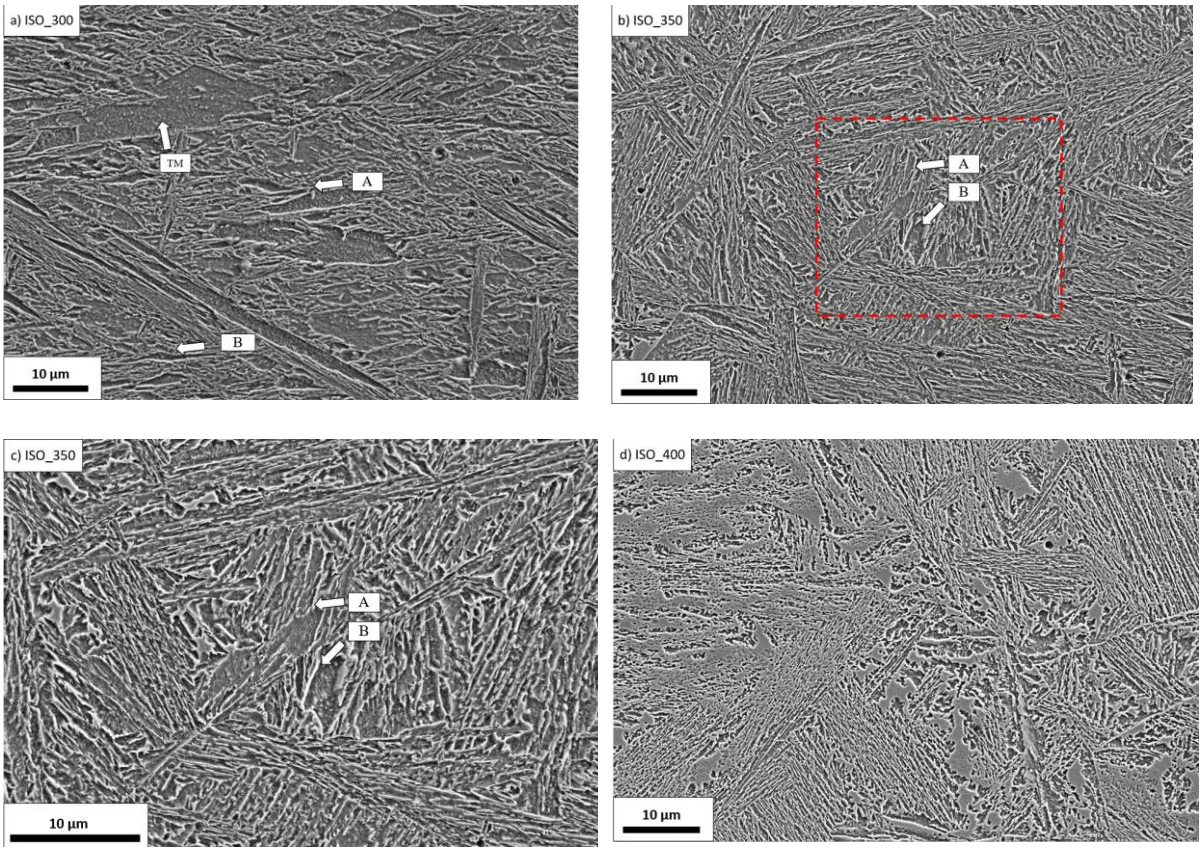

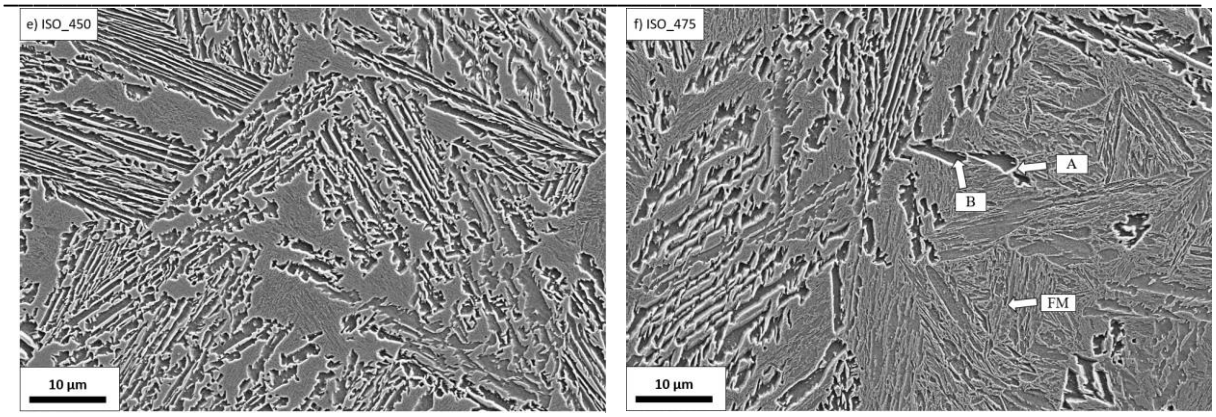

Figure. IV. 1: SEM micrographs after nital etching 2% of the studied steel after isothermal experiments at a) 300 °C, b) 350 °C with the red box corresponding to the enlargement presented in Figure. IV. 1 c), c) Enlargement of the 350 °C, d) 400 °C, e) 450 °C, f) 475 °C . When possible, the microstructure components (A = Austenite, B = Bainite , FM = Fresh martensite) are indicated by white arrows.

Due to the sensitivity of the etching, it is difficult to have a quantitative description of each phase but few main trends can be highlighted.

When cooling the samples down to room temperature, fresh martensite (FM) can be formed if austenite is not sufficiently stabilized by carbon partitioning. The fresh martensite found in MA islands appears in light contrast in microstructures. In Figure. IV. 1, a highest proportion of fresh martensite is found in ISO_475 experiment (FM label in Figure. IV. 1 f)). The fraction of FM drastically increases with the holding temperature, at the expense of the fraction of austenite (Table 2). As a reminder, the highest value of retained austenite fraction at room temperature is obtained after a transformation at 400 °C. For isothermal transformations at 400 °C and below, the fresh martensite fraction formed at the end of the thermal treatment is low (close to zero wt.%). Those observations are consistent with the HEXRD results shown in Chapter III and summarized in Table 2.

The SEM characterization after etching shows the lath morphology and the presence of the different phases in the microstructure, but the lath structure is hardly revealed making difficult the quantitative and systematic measurement of the bainite laths sizes. To overcome this limitation, SEM coupling with Electron Back Scattering Diffraction (EBSD) was used instead.

I.2. Microstructural and microtexture characterizations by SEM-EBSD

I.2.a. Preliminary discussion

Our EBSD study has faced the same difficulty already encountered when analyzing HEXRD results and related to the large Prior Austenitic Grain (PAG). After the austenitization at 1150 °C, the austenite grain size is around 74 ± 42 µm. A compromise must in fact be found between the magnification (to observe a statically relevant number of PAG of a single map), the probe size (to resolve the smallest features of the hierarchical microstructure, retained austenite films and laths) and the experiment durations (to avoid experimental artefacts).

Figure. IV. 2 shows for instance the Image Quality (IQ) and the Inverse Pole Figure (IPF) maps of the retained austenite for the ISO_400 experiment at x 2500 magnification. In Figure. IV. 2, the light grey areas are associated to the bainitic phase, the austenite appears in colors as discontinuous films between bainitic laths (cf APPENDIX 4). The colors represent the local orientation of the phase

according to standard triangle in the Figure. IV. 2. The film-like retained austenite which has the same crystalline orientation belongs to the same Prior Austenite Grain (PAG).

For all isothermal treatments, the measured fractions of austenite by EBSD were lower than 5 %, far below the measurements by HEXRD. At this magnification it is difficult to reveal correctly austenite. Moreover, even if the PAG boundaries can be deduced from the residual austenite orientation, the statistical of observations of different PAGs is not possible at this scale. The following observations will be carried out at a lower magnification (x 1000) in order to gain a statistically relevant knowledge about bainitic lath structure but leaving aside the possibility to have a precise characterization of the austenite.

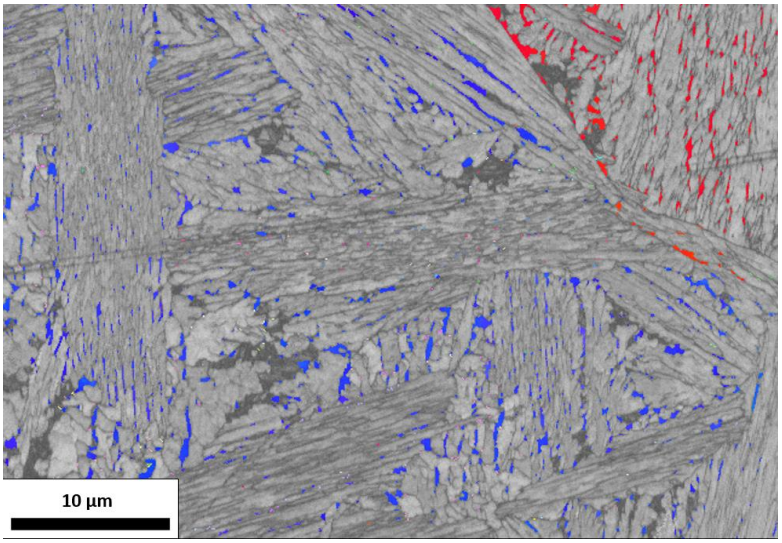

Figure. IV. 2: IQ and IPF maps in direction X of austenite for experiment ISO_400 at high magnification (x2500) with only two incomplete PAG.

I.2.b. Results

ESBD maps presented in Figure. IV. 3 and Figure. IV. 4 correspond to the samples annealed between 300 °C and 475 °C. They have been obtained at medium magnification (x 1000) with a probe size of 0.1 µm. The area of the maps is 120.3 µm x 90.2 µm.

Table 2 shows the final composition of the microstructures deduced by HEXRD and the fraction of indexed phases by EBSD respectively BCC and FCC phases corresponding to the ferritic phases and the austenite, respectively. The zero solution corresponding to the non-indexed fraction. The last column contains the indexing rate.

Table 8: Phases fractions at room temperature for isothermal experiments measured by HEXRD and by EBSD. The last column contains the fraction of indexation.

	HEXRD			**EBSD**			**EBSD**
Temperature (°C)	Bainite (wt.%)	Retained Austenite (wt.%)	Fresh martensite (wt.%)	Ferritic phases (BCC) (%)	Retained Austenite (FCC) (%)	Zero solution (%)	Indexing rate (%)
300	34	10	TM = 56	75	2	23	77
350	90	10	0	83	4	13	87
400	83	16	1	83	5	12	88
450	60	13	27	73	1	26	74
475	35	7	58	80	3	17	83

Figure. IV. 3 shows the Image Quality (IQ) and the maps of boundaries with certain misorientation angles. The IQ contrast corresponds to the quality of the Hough pattern matching. The brighter value means that the software is confident in the crystalline indexation. In turn, it means that a “bright” phase contains less crystalline defects than a “dark” phase.

The angular misorientations of boundaries are defined by different colors in maps. Low angle boundaries (LAB) < 10 ° are represented in white for angle > 2 ° and yellow for angle > 5 °. The intermediate angle boundaries > 10 ° to 20 ° are represented in green. High angle boundaries (HAB) < 60 ° (maximal misorientation angle for a cubic symmetry) are represented in black > 20 ° and in red for angle > 50 °. These latter high misorientations (> 50 °) are characteristic of packet boundaries and block boundaries separating self-accommodating variants [9].

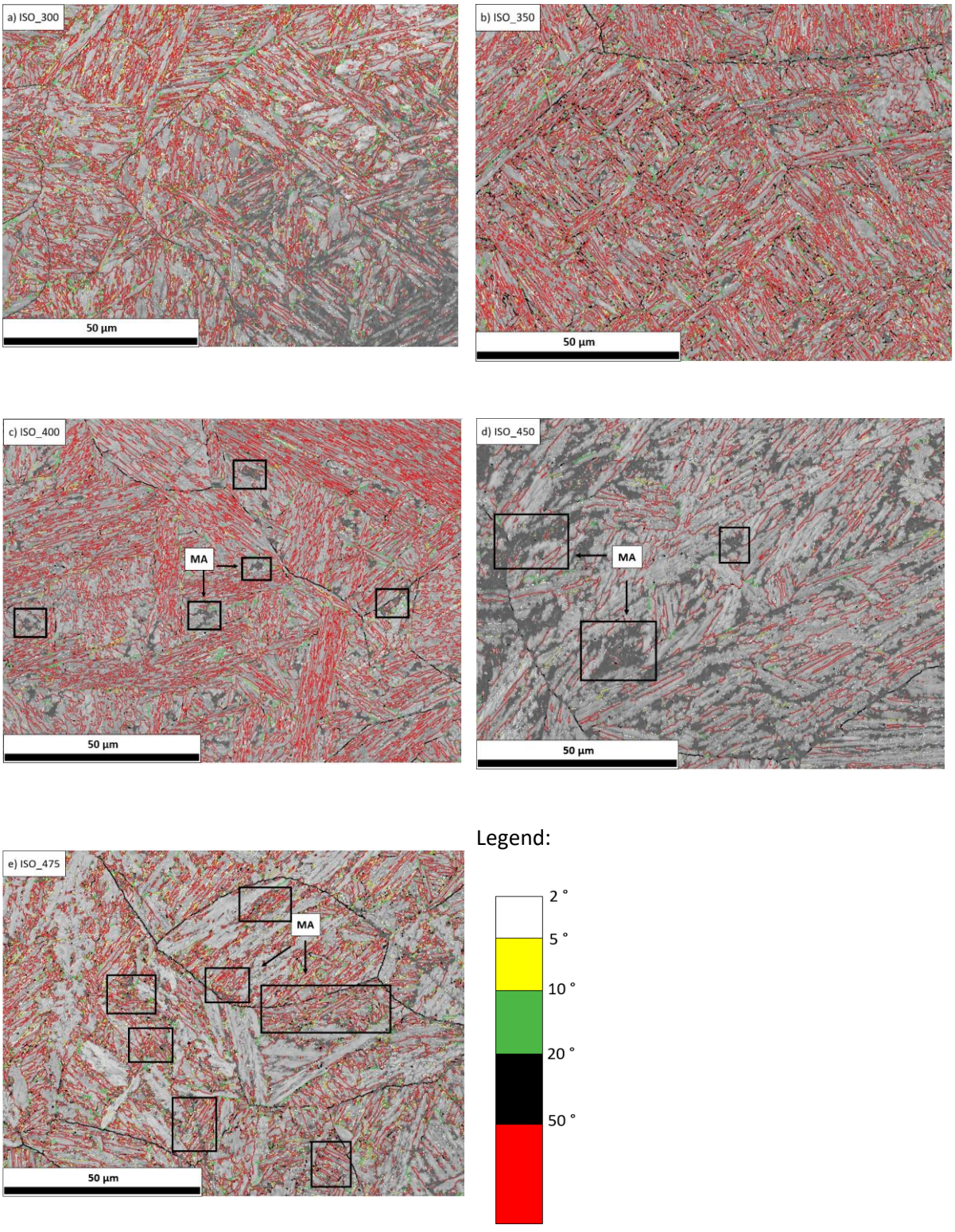

Figure. IV. 3: Image Quality and misoriented boundaries after the 1200 s isothermal holdings at a) 300 °C, b) 350 °C, c) 400 °C, d) 450 °C, e) 475 °C.

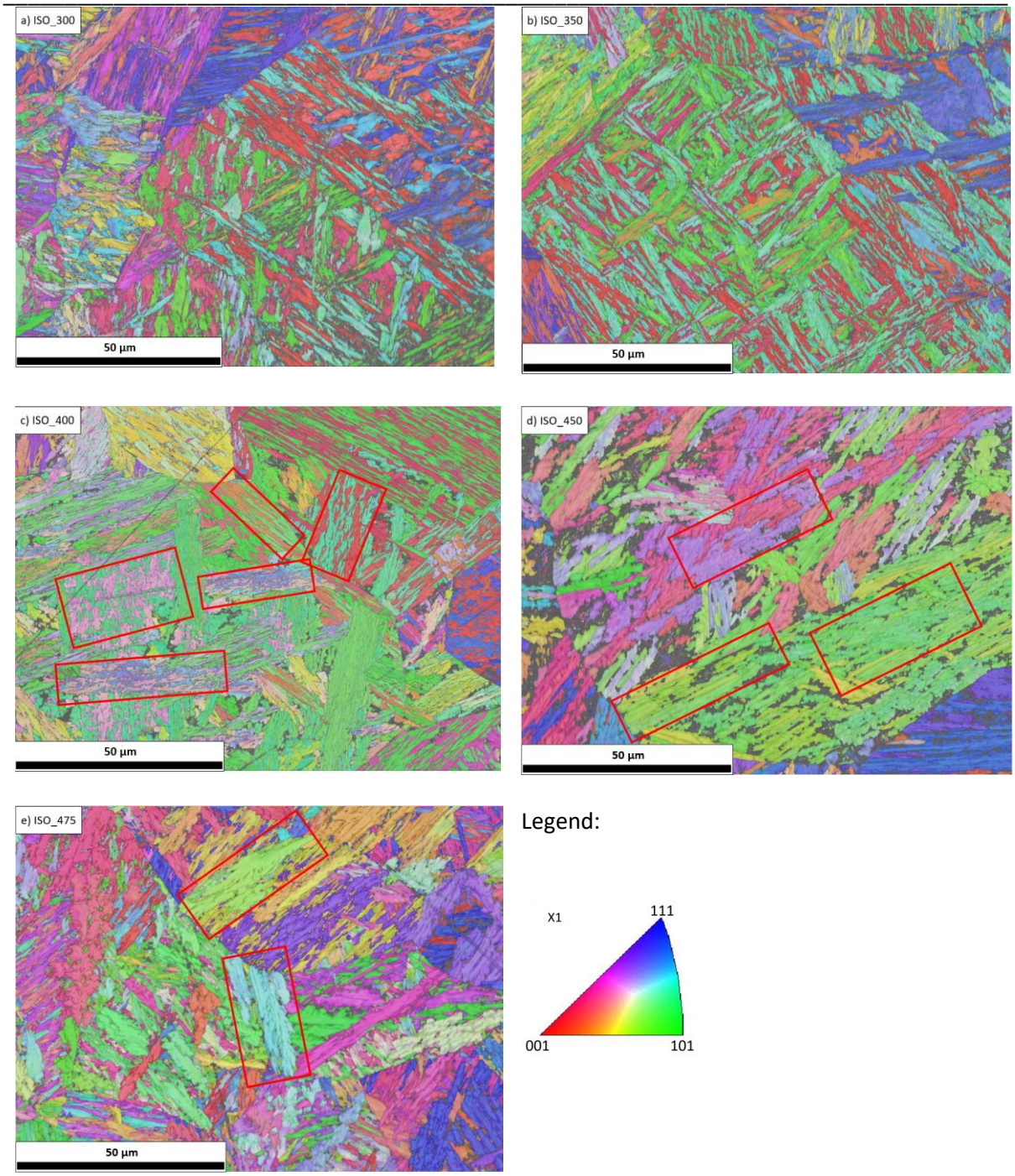

Figure. IV. 4: Superimposed Image Quality and Inverse Pole Figure maps of ferritic phases *after the 1200 s isothermal holdings* at a) 300 °C, b) 350 °C, c) 400 °C, d) 450 °C, e) 475 °C.

Figure. IV. 4 shows the superimposed Image Quality (IQ) and Inverse Pole Figure (IPF) maps of ferritic phases for 1200 s isothermal treatments. The non-indexed area are represented in grey. The larger grain size did not permit to observed full PAGs even at x 1000.

The interpretation of such maps is not straight forward and must be conducted at the light of Chapter III:

- After the treatment at 350 °C, the microstructure only contains bainite and austenite (almost no FM). The IQ contrast Figure. IV. 3 b) is rather uniform in the lath structure but the density of high angle boundaries (HAB) (red lines) is high. This is confirmed by Figure. IV. 4 b) showing that the laths are organized in very small blocks (and thus packets) containing in general two variants (probably self-accommodating). The length of the packet (long direction of the laths) is far lower than the PAG. Some packets have surely nucleated inside the PAG, supporting the autocatalytic nature of the bainitic transformation. Inside almost all PAGs, at least three habit planes can be observed. The bainitic laths are thus highly intricated.
- After the treatment at 300 °C, Figure. IV. 4 a) map looks like the microstructure observed after the treatment at 350 °C (Figure. IV. 4 b)) from the microtexture point of view. Figure. IV. 3 a) present however many large laths with a bright IQ contrast. These large laths correspond in fact to the tempered martensite which appears prior to the bainitic transformation. The bainite thus corresponds to the domains with a higher density of HAB. This comparison shows that distinguishing martensite and low temperature bainite is almost impossible as both shows almost the same size and share similar Orientation Relationship (OR). It must be mentioned that less HAB have been highlighted on the bottom right of the map has due to a lower acquisition quality (artefact).
- After the treatment at 400 °C, the packets of self-accommodating blocks of laths are far larger than at 350 °C and they often occupy the full width of the PAGs (cf. Figure. IV. 4 c). At this temperature (and below), the thickness of the blocks is often restricted to the thickness of a single lath. At this magnification and with this probe size, austenite cannot be detected systematically (between the laths as shown in Figure. IV. 2 for instance). Figure. IV. 4 e) reveals now clearly some islands with a dark IQ contrast. These islands, often located at PAG boundary but not systematically, are the so-called MA (Martensite-Austenite) islands made of fresh martensite and austenite. They corresponds to the last domains transformed at low temperature during the final cooling (less enriched and thus less stable austenite). The carbon content in these domains is high meaning that the fresh martensite appears at low temperature and contains a high density of defects. This high density of defects explains why it is nearly impossible to resolve these domains by EBSD.
- After the treatment at 450 °C, the microstructure presents as expected a high fraction of MA islands (27 wt.% is expected by HEXRD) with a dark IQ contrast as revealed by Figure. IV. 3 d) and the microtexture is now intermediate between an upper and lower type bainite (according to Zajac's classification) as revealed by Figure. IV. 4 d). In fact the packet still contains self-accommodating blocks separated with HAB but the thickness of the blocks is far higher than at 400 °C (many laths in thickness) as the red/purple ones at the center of the map. Some packets with a single Bain orientation can also be observed (green one on the bottom right). These analysis will be sustained in the following by a more systematic analysis of the sizes and the histograms of misorientations.
- After the treatment at 475 °C, Figure. IV. 4 e) looks like the microstructure observed after the treatment at 450 °C (Figure. IV. 4 d)) from the microtexture point of view or to the initial microstructure before forging (cf. Figure. II. 1). Packets of laths look large and contain often a single variant from the crystallographic point of view (highlighted with red boxes). However, such first impression must be mitigated when comparing Figure. IV. 3 d) and Figure. IV. 3 e). Microstructure after annealing at 475 °C seems to contains two phases, i.e. large laths with a

bright IQ contrast embedded in sub-domains with a high density of HAB. The large laths corresponds in fact to the bainitic lath whose fraction is limited at this temperature (about 35 wt.% according to Table 1) and the others domains to fresh-martensite. In that case, the MA islands have been indexed as the carbon enrichment in austenite is far lower than at 400 °C and the martensitic transformation occurs during final cooling at higher temperature (at about 330 °C). The fresh martensite thus contains less austenite and less defects and can be indexed by EBSD. As a consequence, the microstructure could looks finer in Figure. IV. 4 e) but it is related to the presence of high fraction of fresh martensite (in Figure. IV. 4 d)). It must be mentioned that the difference in IQ contrast between bainite and low carbon fresh martensite is not sufficient to distinguish both constituents.

The qualitative analysis of the EBSD maps after the isothermal treatments reveals the complexity of such microstructures, mainly related to the concomitant presence of martensite under different forms (tempered/fresh) which shares the same crystallographic and morphogenesis than bainite. In order to go farther, the distribution of misorientations and the size of the structures will be determined quantitatively and discussed.

I.2.c. Histograms of misorientations

The statistical analysis of the misorientations in Figure. IV. 3 permits to calculate the so-called histograms of misorientation angles of the maps. These distributions serve to classify bainitic microstructures as proposed by Zajac et al. [14] as explained in Chapter II. The results of this analysis for our five experiments are presented in Figure. IV. 5.

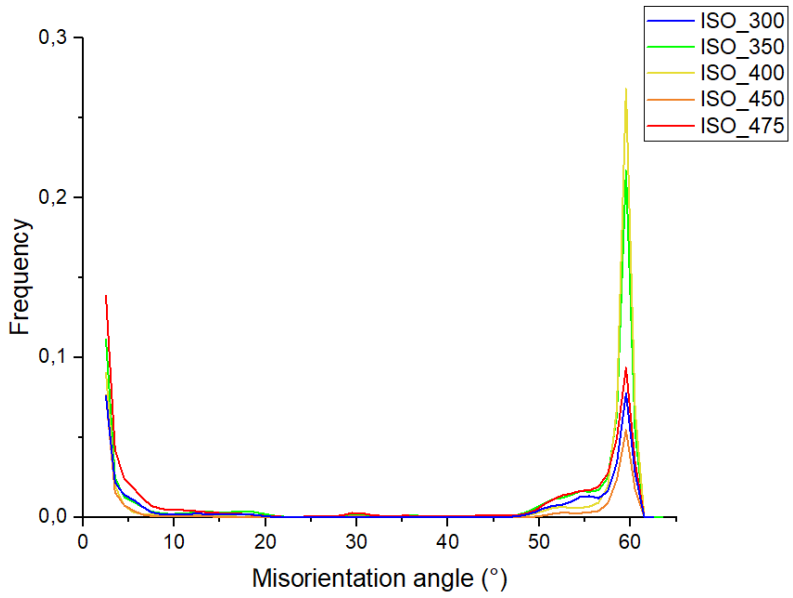

Figure. IV. 5: Histograms of misorientations measured in Figure. IV. 3 (microstructures studied after 1200 s isothermal holdings).

The microstructures obtained after isothermal schedules at low temperatures above M_S (350 °C and 400 °C) present a high density of high misorientation angles around 60 °. In the Zajac' classification such bainite can be classified as lower bainite [2], [15], [16]. This result is not impacted by the presence of fresh martensite which is not indexed (MA islands appearing in dark IQ contrast but without revealing HAB).

The microstructures obtained at high transformation temperatures (450 °C and 475 °C) microstructures are composed of a mixture of bainitic ferrite and fresh martensite. In literature, martensite was shown to have a distribution of misorientation angles comparable to the one of lower bainite [6]. It is hence difficult to uncouple the contribution of bainite and martensite. However, peaks at high misorientation angles for both temperatures is lower than for low temperature transformations (especially at 50 °). Bainite formed at high temperatures can thus be considered as a mixture between lower and upper bainite using Zajac's classification [17], [18]. This is confirmed by the presence of packets with a single variant of bainite at 450 °C. At 475 °C, the fraction of upper structure is probably higher as the laths of bainite (large lath revealed by the IQ maps) contains more systematically a single variant.

For the treatment at 300 °C, i.e. below the M_S temperature, the presence of tempered martensite make again the analysis less obvious. Some authors as Mondal et al. [2], Navarro-Lopez et al. [3] and Da Silva et al [19] have studied the CFB microstructures formed below M_S. Mondal et al. [2] establish that the microstructure formed below M_S can be classified as upper bainite. On the contrary, Da Silva et al. [19] claim that the microstructure formed below M_S can be classified as lower bainite, similar to the bainite formed above M_S. For experiment ISO_300, the peak at high misorientation angles is a bit lower than for low temperature transformations 350 °C and 400 °C (Figure. IV. 5). For microstructures composed of a mixture of bainite and martensite as the microstructure formed at 475 °C, it is impossible to identify upper bainitic domains on the IQ map and the distribution in misorientation angles does not show an increase at low angle (as it would be the case of an upper bainite even if partially hindered by the presence of martensite).

I.2.d. Measurement of characteristic sizes

I.2.d.1. Choice of the measuring strategy

The bainite lath sizes can be measured with different experimental techniques as SEM (Scanning Electron Microscopy) after etching [20], by EBSD [5], [8], [9], [20], [21] or by TEM (Transmission Electron Microscopy) [2]. The latter does not offer the sufficient statistic and tends to put more into evidence the low angle boundaries vs. high angle boundaries. The quantitative studies of microstructures after etching suffered from bias inherent to the etching itself (repeatability, interpretation, …). As a consequence, EBSD was chosen to conduct these measurements in a reliable and statistical way. The choice of this technique requires in return to define a crystallographic criterion (critical misorientation angle) to define the interface between two constitutive objects (for example two laths). This choice is the key to compare the results from different studies.

In practice, the measurement of the characteristic sizes was realized with the intercept method (horizontal and vertical lines) using the software CHANNEL 5. The EBSD maps have been analyzed with different critical misorientation angles.

Figure. IV. 6 shows an example of the horizontal intercept method with a critical angle of 50 ° applied to the microstructure after the isothermal treatment at 400 °C. When the analyzing line crosses a boundary of the microstructure with the sufficient critical angle, the color of the analyzing line changes (blue and yellow segments). Some domains have not been indexed at the limits of the image (red segments). The measurement was realized on four maps per experiment, one map at low magnification (x 1000) and three maps at high magnification (x 2500) on different areas of the sample. The grains smaller than 0.15 µm were eliminated. It is difficult to discriminate the martensite contribution in MA islands which are partially non indexed as discussed above (except for condition ISO_475). This is the reason why we have used high magnification maps to decrease the proportion of MA islands present in the analyzed area (statistical issue). However, the comparison of the line intercept grain size measurements shows that the measurement is not enough affected by the magnification used (cf. Figure. IV. 7).

For experiment ISO_475, the high fraction of fresh martensite (58 wt.%) does not permit to make the same automatic post-treatment of the maps. A manual measurement of sizes using the intercept method was realized on the IQ and misoriented grain boundaries maps presented in Figure. IV. 3 e). The measured sizes is then attributed to the mean line intercept measurement with a critical misorientation angle upper to 20 ° reported in Figure. IV. 8.

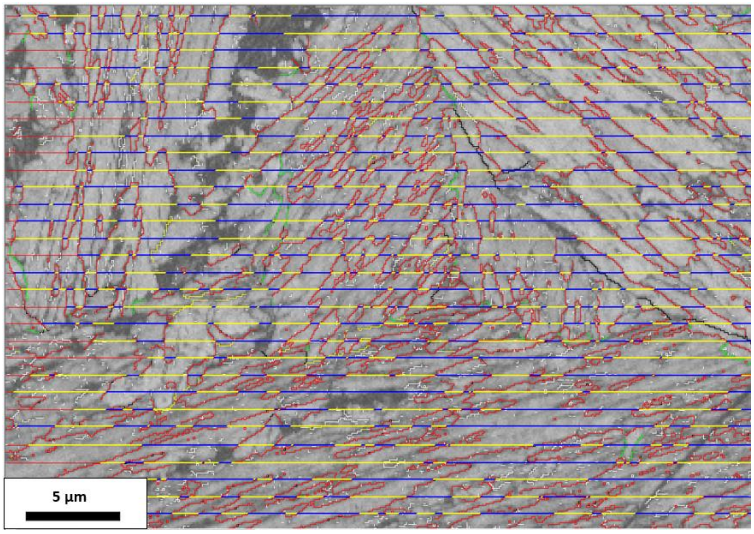

Figure. IV. 6: Illustration of the horizontal intercept method with a critical angle of 50 ° for the isothermal experiment at 400 °C.

I.2.d.2. Results

Figure. IV. 7 shows the mean horizontal (squares) and vertical (circles) line intercept grain sizes as function of the critical angle misorientation for experiment ISO_400. The yellow line represents the mean line intercept grain size between the horizontal and vertical measurements for the magnification at x 1000. The line intercept grain size increases with the critical misorientation angle whatever the studied areas, the direction of the intercept lines and the magnification. At a given critical misorientation angle, a difference is observed between the horizontal and the vertical measurement. This difference is due to the spatial orientation of bainite structure. Moreover, a dispersion in the mean

line intercept grain sizes is observed for all measurements. This measurement dispersion was observed for the other experiments obtained after isothermal treatments. For the sake of comparison, we have thus chosen to present the mean line intercept grain size at a same magnification (x 1000) for all experiments obtained after an isothermal heat treatment. The error bars on the average sizes measured at x 1000 magnification correspond to the standard deviation of the average of each size measurement in horizontal and vertical for each misorientation angle.

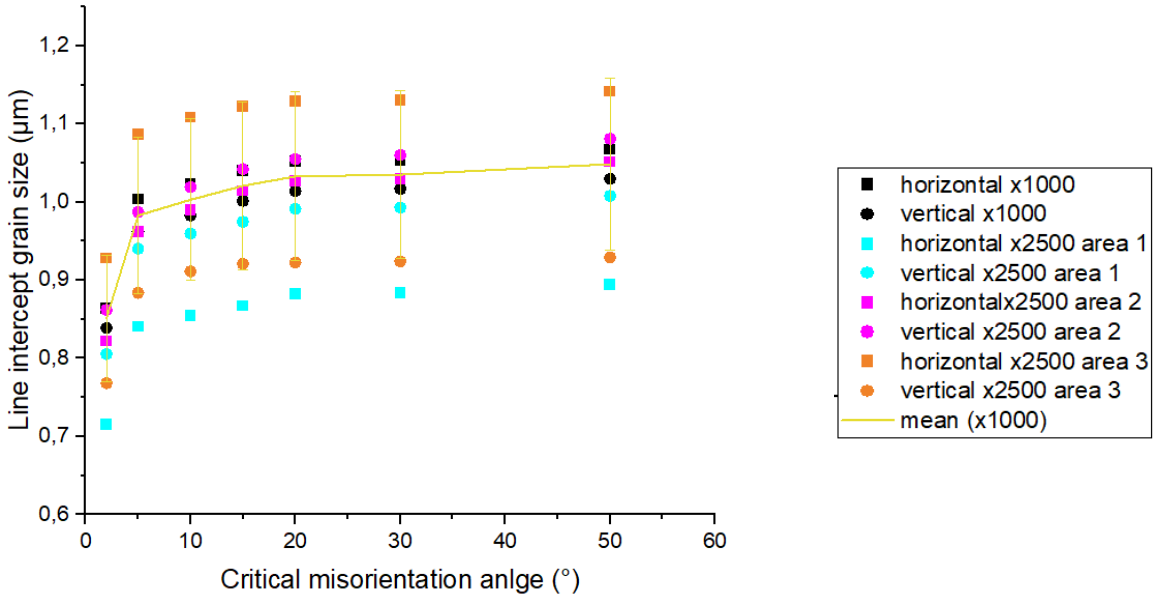

Figure. IV. 7: Horizontal (squares) and vertical (circles) line intercept grain size as a function of critical misorientation angle on four maps with the magnification x 1000 and x 2500 for the ISO_400 experiment.

The distance between two boundaries as a function of the considered critical angle are plotted in Figure. IV. 8 [5] for the 5 studied experiments. The distance between two boundaries increases with the angle [9], [15] as the density of low angle boundaries is far higher than the one of high angle boundaries. The lowest size corresponds to the laths (low critical angle of misorientation) and the highest size to the blocks/packets (high critical angle of misorientation). Above 350 °C, the lower the temperature, the lower the size for a given critical angle. The distribution of sizes of the microstructure obtained at 300 °C does not follow the same trend. The sizes between two HAB is higher than in the microstructure obtained at 400 °C or at 350 °C. This has to do with the presence of large laths of tempered martensite in the microstructure (appeared above 300 °C). Here again, the presence of a mixture of tempered martensite and bainite make the analysis more difficult.

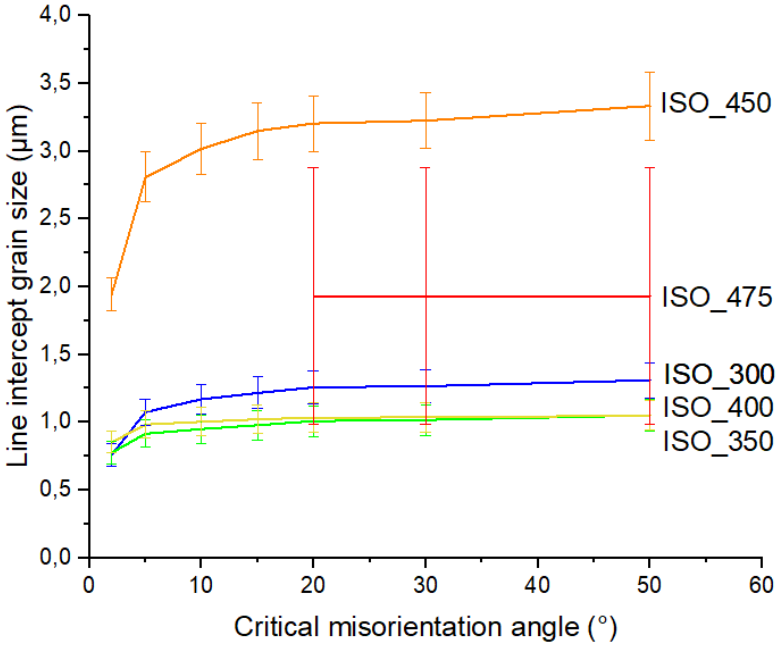

Figure. IV. 8: Line intercept grain size as a function of critical misorientation angle.

In the literature, a critical angle of 5 ° is often arbitrarily choose to determine the size of the laths, this value is sufficiently high with respect to EBSD angular resolution and to encompass all the laths with considering possible variant misoriented at 5 °. This conventional choice will be followed in the rest of this work.

Zhu et al. [5] have also shown that the intercept distance must be corrected to assess to the true lath thickness considering stereological concepts. The stereological factor accounts for two corrections, the intercept line cross bainite lath with an random angle (stereological effects), and the random 2D cut effect associated with the observation of 3D entity [15]. The thickness of bainite lath (l_0) obtained using the 5 ° critical angle to define the boundaries can be calculated as (Eq. 10)**:**

$$l_0 = 0.32l' \qquad \textit{Eq. 10}$$

With l' corresponding to the mean intercept length.

The true bainite laths thickness (l_0) as a function of the temperature for the experiments obtained after 1200 s isothermal holdings is reported in

Table 9. For the annealing temperatures between 350 °C and 450 °C (noted ISO_350 and ISO_450 respectively), the size increases with the temperature. The size measured manually for ISO_475 (about 1.9 µm before correction) is a little bit lower than ISO_450 condition but with a large uncertainty, as shown in Figure. IV. 8. These sizes measurement will be compared with results from the literature [8] in Figure. IV. 9, in the next section.

Table 9: Bainite laths thickness (l_0) measured by EBSD (with critical angle of 5 °) for each isothermal treatment.

Temperature (°C)	Bainite laths thickness l_0 (µm)
300	0,31
350	0,25
400	0,30
450	0,87
475	0,62

I.2.d.3. Discussion and comparison with the literature

Figure. IV. 9 shows the true bainite laths thickness (l_0) as a function temperature of isothermal holdings compared with the sizes measured by Hell [8] with the same methodology on three alloys noted C1 (0.1C-1.5Si-0.8Cr-2.5Mn), C2 (0.2C-1.5Si-0.8Cr-2.5Mn) and C3 (0.3C-1.5Si-0.8Cr-2.5Mn) respectively.

Hell demonstrates that the size of bainite laths increases with the temperature and follow a clear linear trend whatever the composition. The sizes measured on the studied alloy are in the same magnitude than the ones measured by Hell (except for the ISO_450) but the linear trend cannot be obviously confirmed.

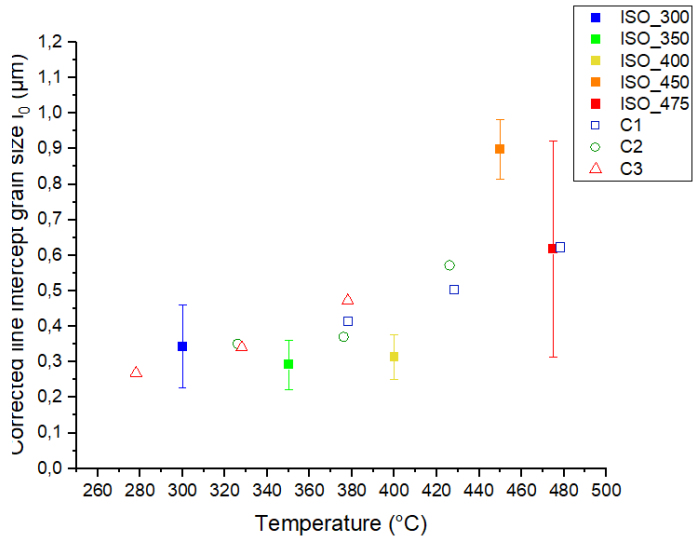

Figure. IV. 9: True bainite lath thickness as a function of temperature of the isothermal annealing isothermal treatment compared the three steels of [8].

In order to clarify this situation, our findings have been also compared to empirical models found in the literature. Figure. IV. 10 shows the comparison between the bainite lath thicknesses measured by EBSD on the studied steel with the results of these different models:

- Chester et al. [22] have determined a linear relation of the sub-unit width in (µm) with the temperature presented based on experimental measurements of the bainite sub-unit width on 6 steels from Chang [23], the sub-unit width can be calculated by (Eq. 11):

$$u_w = 0.001077T - 0.2681 \quad \textit{Eq. 11}$$

Where u_w is the sub-unit, T is the temperature in °C.

The evolution of the sub-unit width with the temperature calculated using the Eq. 11 was reported by the blue curve in Figure. IV. 10.

- Based on the evolution of bainite plate thickness with the isothermal transformation temperature obtained by experimental measurements by Chang et al. [23], Garcia-Mateo et al. [24], Cota et al. [25] and Soliman et al. [26], Van Bohemen [27] develops a model to describe the evolution of bainite lath thickness as function of temperature. The bainite lath thickness can be calculated as (Eq. 12):

$$t = \frac{K}{(\sigma_y^\gamma - \sigma_{lim})} \quad \textit{Eq. 12}$$

Where K is a constant (2 µm.MPa), σ_y^γ the austenite yield strength (cf. Eq. 44), σ_{lim} the lower limit strength estimated with (Eq. 13).

$$\sigma_{lim} = 66.6 + 140x_C - 1.1x_{Mn} + 1.8x_{Si} + 2.6x_{Cr} + 7.7x_{Mo} - 0.8x_{Ni} + 1.5x_{Al} + 2.2x_{Co} + \frac{4.9}{\sqrt{d^\gamma}} \quad \textit{Eq. 13}$$

The lower limit strength (noted σ_{lim}) is estimated by an empirical equation taking into account the alloy composition and the average prior austenite grain size. The austenite yield strength (noted σ_y^γ) is calculated by a polynomial function of the austenite yield strength at room temperature and the temperature. Based on previous studies from Ivrine et al. [28], Van Bohemen [27] optimizes the calculation of the austenite yield strength at room temperature by an empirical equation dependent to the alloy composition and the average prior austenite grain size. The estimation of the evolution of bainite plate thickness for the studied steel was estimated using the Eq. 12 proposed by Van Bohemen and presented in Figure. IV. 10 by the pink curve. The evolution of bainite lath thickness is non-linear as function of temperature (parabolic shape).

- Other authors as Yang et al. [29] develop a model capable to describe bainite plate thickness combining the influence of the temperature, the chemical free energy change ($\Delta G^{\gamma\to\alpha}$) and the strength of austenite (σ_y^γ) given by (Eq. 14):

$$t = f\left(T, \sigma_y^\gamma, \Delta G^{\gamma\to\alpha}\right) = 222 + 0.01242 \times T + 0.01785 \times \Delta G^{\gamma\to\alpha} - 0.5323 \times \sigma_y^\gamma \quad \textit{Eq. 14}$$

The model shows a linear evolution of the bainite plate thickness as function of temperature. The evolution of the bainite plate thickness with the temperature calculated using the model of Yang et al. [29] was represented by the orange curve in Figure. IV. 10.

- Others authors as Rees and Bhadeshia [30] and Singh et al. [31] have studied the evolution of bainite plate thickness as function of temperature using a neural network [30], [31]. The bainite plate thickness is describe as a function of austenite strength, the driving force for nucleation of bainitic ferrite and the transformation temperature. The black curve in Figure. IV. 10 shows the evolution of bainite plate thickness as a function of temperature determined by Rees and Bhadeshia [30] on the Fe-Mn-Si-C steel. The purple curve in Figure. IV. 10 shows the evolution of bainite plate thickness as a function of temperature determined by Singh et al. [31] on a 0.12C-2.03Si-2.96Mn steel.

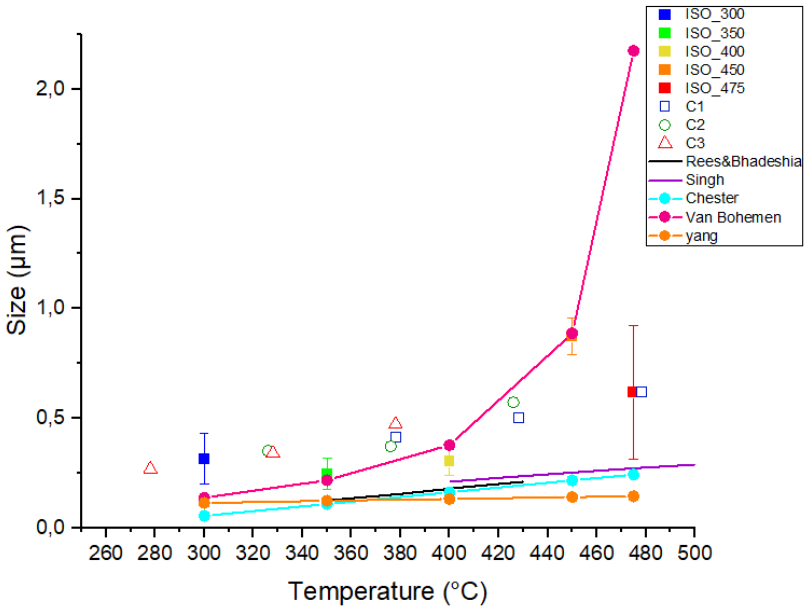

Figure. IV. 10: Comparison between our experimental measurements by EBSD and the prediction of different models found in the literature; Rees & Bhadeshia on the Fe-Mn-Si-C steel [16], Singh et al. on the 0.12C-2.03Si-2.96Mn alloy [17], the modeled evolution of bainite sub-unit width by Chester et al. [18], Van Bohemen [27] and Yang et al. [29].

All the models from literature predict a linear increase of the sizes with the temperature except the one of Van Bohemen, which shows a parabolic increase. Our experimental findings seems to be close to such empirical prediction, except maybe for the highest transformation temperature (475 °C) since it is difficult to have a precise measurement of bainite lath thickness due to the presence of a high fraction of fresh martensite (58 wt.%).

It also appears that the linear models from the literature explicitly or implicitly described the evolution of the sub-unit size. As a consequence, their predictions are lower than the sizes we measured. However, a proportionality factor of about 3 seems to be respected. It thus means that lath size corresponds almost to 3 sub-units in width. This ratio maybe increase with transformation temperature which could explain the parabolic trend we reported.

I.3.Conclusion

In this section, we have observed and analyzed the evolution of microstructures obtained after different isothermal holdings. The microstructures have been first observed using SEM after nital etching (post-mortem). The microstructures after these heat treatments show a lamellar morphology whatever the transformation temperature but the fraction of each components (bainite, austenite, tempered/fresh martensite and carbides) is dependent strongly on this temperature. At low transformation temperatures (300 °C and 350 °C), some carbides are visible on micrographs (Figure. IV. 1 a) and c)) in agreement with HEXRD results in Chapter III. Moreover, the proportion of fresh martensite decreases with the decreasing of isothermal holding temperature (stabilization of austenite by carbon partitioning).

By coupling SEM and EBSD, it was possible to go deeper in the microstructural characterization of bainite. The microstructures obtained after an heat treatment at 300 °C is composed of tempered martensite and bainite formed during the isothermal holding, but it was not possible to identity ambiguously tempered martensite and bainite on the maps. The microstructures obtained after heat treatments at 350 °C and 400 °C show a high proportion of high density angular boundaries which delimit different self-accommodating variants of bainitic packets. In contrast, the microstructures obtained after a heat treatment at 450 °C and 475 °C show a low density of HABs but a high proportion of LABs, with a single variant per bainitic packets. EBSD maps confirm the presence of an higher proportion of fresh martensite with the increase in transformation temperature. The fresh martensite was characterized by a high proportion of HABs.

The obtained bainite microstructure were classified using the Zajac's nomenclature based on the histograms of misorientations. The microstructures transformed after at 300 °C, 350 °C and 400 °C are classified as lower bainite, while the microstructures obtained at 450 °C and 475 °C are upper bainite from the crystallographic point of view.

The bainitic ferrite sizes were determined for each transformation temperature using the line intercept method with a variation of the critical angle. The line intercept grain size increase with the increase of the critical misorientation angle for all microstructures obtained after an isothermal holding. The measured sizes were compared to previous studies of the literature, our results show a relatively agreement with the results of Hell [5], which used the same characterization method. However, for others studies, our results are three times higher than the sub-unit width measurements determined by some authors [22], [27], [30], [31].

In the next section, we will present with the results using the same methodology for the multistep holding sequences.

II. Characterization of microstructures obtained in anisothermal treatments

In this section, the EBSD analysis of the samples annealed following multistep or continuous cooling schedules will be present successively and discussed with respect to the results obtained after isothermal holdings.

II.1. Multistep holding sequences

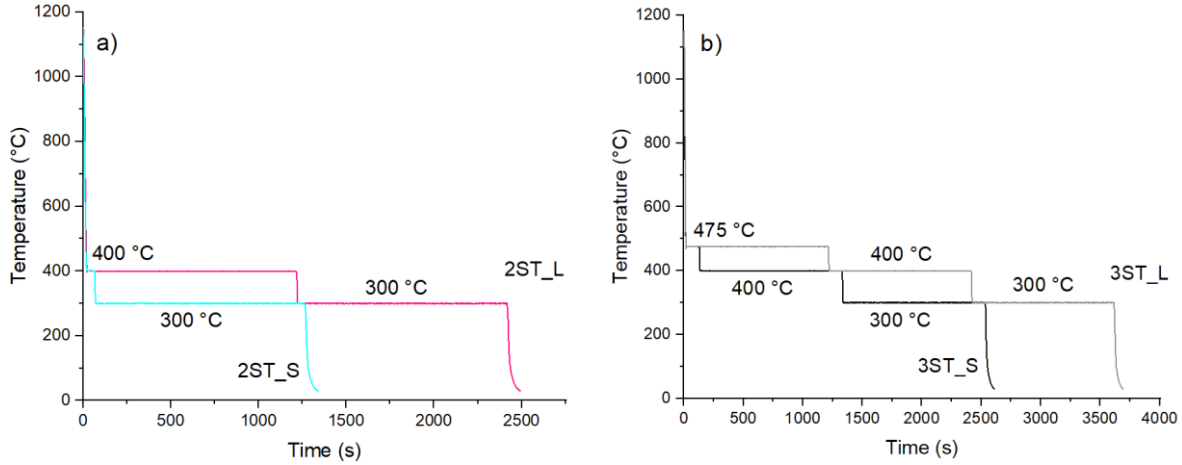

Figure. IV. 11: Heat treatments for multistep holding sequences a) two-step holding sequences b) three-step holding sequences.

As a reminder of Chapters II and III, Figure. IV. 11 a) and b) recalls the evolution of the temperature as function of the time for the two-step and three-step holding sequences respectively. Please refer to Chapter II Section II.1.c. for more details.

II.1.a. Two-step holding sequences

As discussed in Chapter III, the microstructures after the two-step treatments are composed of bainite obtained at 400 °C and bainite formed at 300 °C, tempered and fresh martensite and retained austenite as well.

For the 2ST_L experiment, during the second step at 300 °C, the transformation does not restart and less than 1 wt.% of bainite is formed at 300 °C. The microstructure is thus expected to be very similar to the one observed after isothermal holding at 400 °C. The microstructure is composed by high fraction of bainite formed at 400 °C (84 wt.%) and retained austenite. For the 2ST_S experiment, the duration time of the first step at 400 °C is reduced and the fraction of bainite does not reach the stasis value. At the end of the first step, 75 wt.% of untransformed austenite remains. During intermediate cooling between 400 °C and 300 °C, high fraction of martensite forms which will be further tempered. During the second isothermal step at 300 °C, the bainite transformation restarts. The fractions of austenite, martensite (fresh and tempered) and bainite at room temperature measured by HEXRD (Chapter III) are summarized in Table 10. The recall of these results is important because they will allow

to interpret the progressive entanglement of microstructures obtained along non-isothermal experiments.

Table 10: Summary of the microstructures compositions (in wt.%) at room temperature by HEXRD for two-step treatments.

	2ST_L	2ST_S
Bainite formed at 400 °C (wt.%)	84	25
Tempered martensite (wt.%)	0	43
Bainite formed at 300 °C (wt.%)	< 1	22
Retained austenite (wt.%)	15	10
Fresh martensite (wt.%)	< 1	< 1

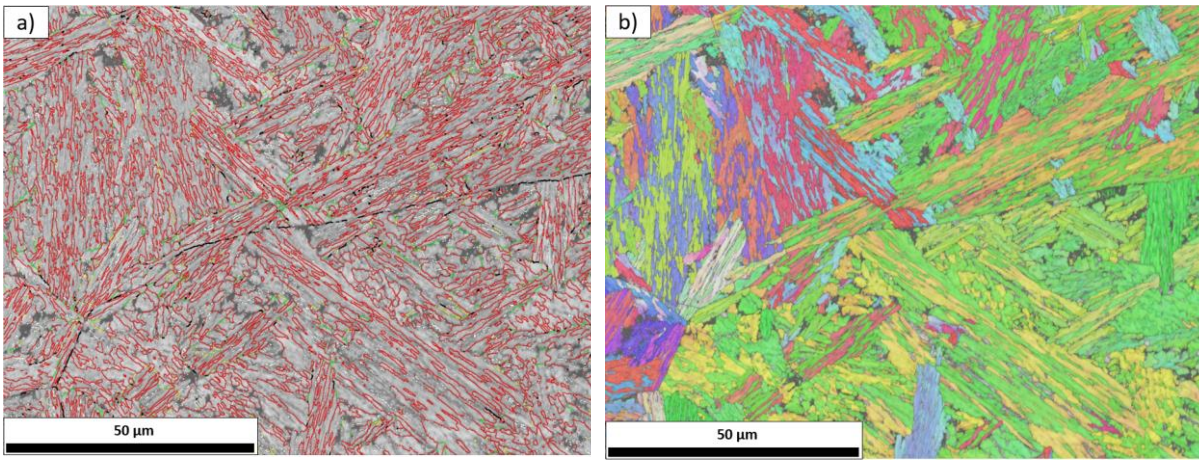

Figure. IV. 12: a) Image Quality maps and boundaries according to the nomenclature described in the text; b) IPF map of ferritic phases for experiment 2ST_L.

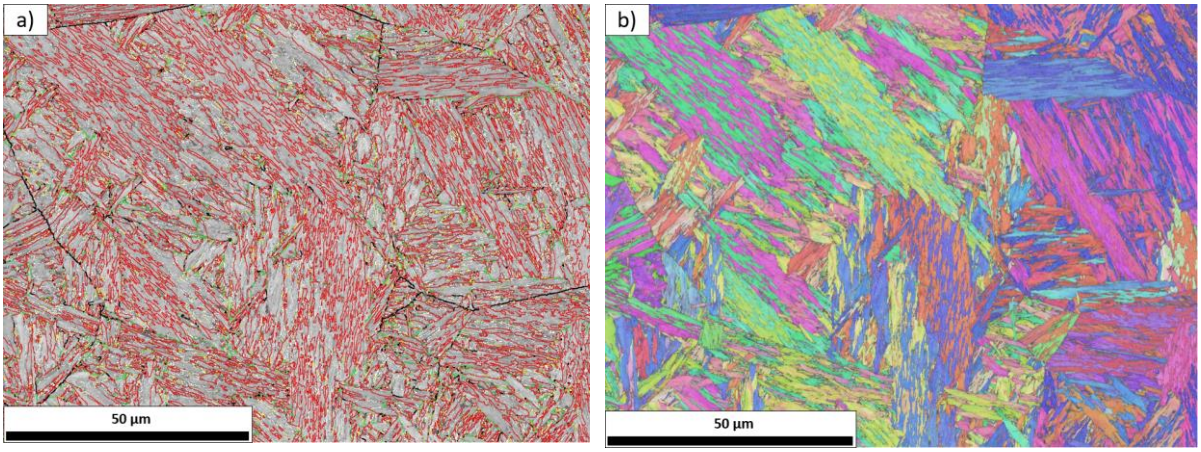

Figure. IV. 13: a) Image Quality maps and boundaries according to the nomenclature described in the text; b) IPF map of ferritic phases for experiment2ST_S.

Figure. IV. 12 and Figure. IV. 13 show the Image Quality and the IPF maps of ferritic phases (as in Figure. IV. 3 and Figure. IV. 4). Both microstructures shown in Figure. IV. 12 a) and Figure. IV. 13 a) present a high density of high misorientation angle > 50 ° (red lines) corresponding to the misorientation between self-accommodating variants inside a packet. As for isothermal experiments, some PAG boundaries appears on IQ maps misoriented between 20 ° and 50 ° (black lines).

The EBSD maps after treatment 2ST_L (Figure. IV. 12) looks like strongly to the one obtained in isothermal experiment at 400 °C solely (Figure. IV. 4 c)) which is consistent with the phase transformation processes observed by HEXRD.

The distinction between the 3 microstructure constituents (bainite formed at 400 °C, tempered martensite and bainite formed at 300 °C) expected after the 2ST_S path is difficult in Figure. IV. 13 as discussed in the preceding section. The presence of bainite obtained at 400 °C can neither be clearly put into evidence in terms of sizes or microtextures. Moreover, when comparing Figure. IV. 12 and Figure. IV. 13, Figure. IV. 12 reveals larger laths compared to Figure. IV. 13.

In both cases, the packet microstructures are highly entangled confirming an intergranular nucleation of the packets (not only at PAG boundaries) which could be the sign of an autocatalytic process for bainite and martensite transformations as well.

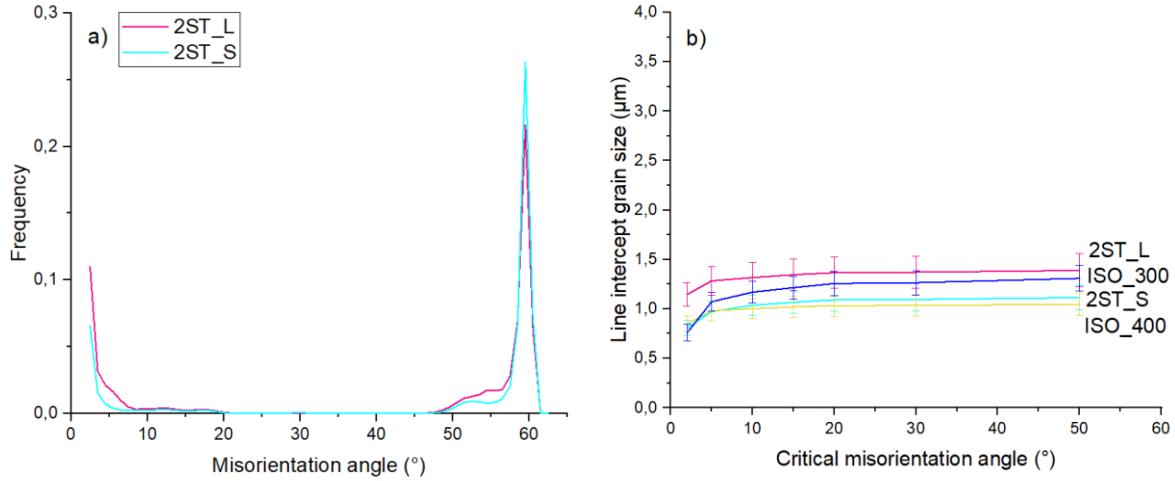

Figure. IV. 14: a) Histograms of misorientations after two-step experiments b) size distribution as a function of critical misorientation angle.

Figure. IV. 14 shows the histogram of misorientations of the microstructures after two-step sequences (a)) and the size distribution as a function of the critical misorientation angle (b)) measured with the methodology explained in the previous sections. The sizes determined previously after the annealing treatment at 400 °C (yellow) and 300 °C (blue) are recalled in Figure. IV. 14 b). The different schedules are represented in pink for the 2ST_L and cyan for the second 2ST_S treatment. Both microstructures presents as discussed above a high density of 50 °/60 ° misorientation angles (Figure. IV. 14 a)). The distributions are characteristics of a lower bainite (or martensite) from the crystallographic point of view. The proportion of boundaries with low misorientation angle (15 °) is however a bit higher in the case of the 2ST_L than in the 2ST_S treatment as it contains less low temperature components. As expected, the observed differences in terms of sizes fall into the resolution limits of the method. The bainite obtained at 400 °C or after the 2ST_L should have presented a similar distributions of lengths. It is thus impossible to discuss reasonably the observed differences between the experiments. It is not possible to distinguish both microstructures based on sizes and misorientations.

II.1.b. Three-step holding sequences

The constituting phases of the microstructures at the end of each three-step treatments obtained by HEXRD (heat treatments presented in Figure. IV. 11 b)) are recalled in Table 11.

The microstructure at the end of the 3ST_L treatment is composed of a high fraction of bainite obtained at 475 °C (48 wt.%), 26 wt.% bainite obtained at 400 °C and less than 1 wt.% of bainite obtained at 300 °C. It remains 18 wt.% of retained austenite which is unstable as 7 wt.% of fresh martensite is formed during the final cooling. The microstructure at the end of the 3ST_S treatment is composed of 22 wt.% of bainite obtained at 475 °C, 59 wt.% of bainite obtained at 400 °C, less than 1 wt.% of bainite obtained at 300 °C and 18 wt.% of retained austenite. The microstructure formed in the 3ST_L is meanly composed with bainite formed at 475 °C. However, when the duration time for the first step is reduced, the bainite transformation is favored at 400 °C and the transformation at 300 °C is again inhibited.

Table 11: Summary of the microstructures compositions (in wt.%) at room temperature by HEXRD for three-step treatments.

	3ST_L	3ST_S
Bainite formed at 475 °C (wt.%)	48	22
Bainite formed at 400 °C (wt.%)	26	59
Bainite formed at 300 °C (wt.%)	1	< 1
Retained Austenite (wt.%)	18	18
Fresh Martensite (wt.%)	7	< 1

Figure. IV. 15 and Figure. IV. 16 show the Image Quality a), the IPF maps of the ferritic phases b) acquired on samples 3ST_L and 3ST_S respectively.

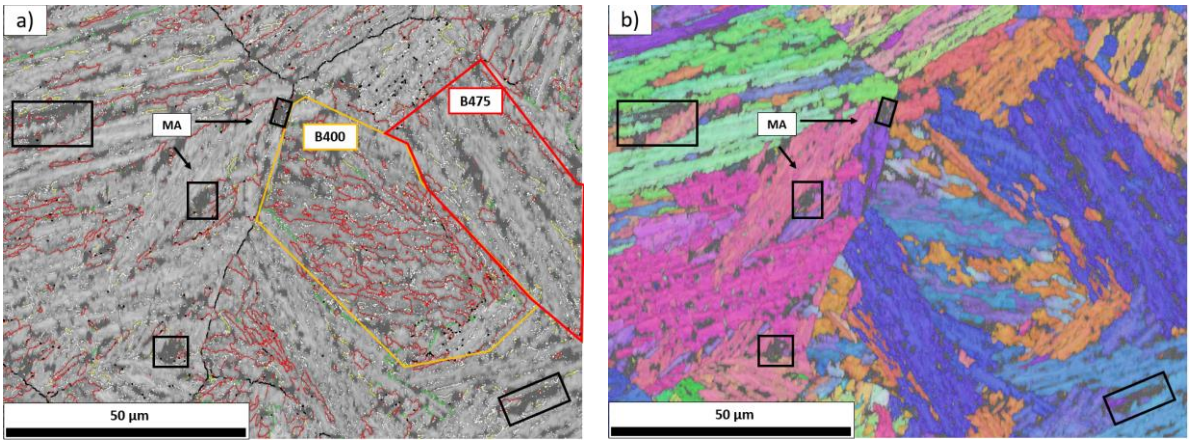

Figure. IV. 15: a) Image quality maps and boundaries according to the nomenclature described in the text; b) IPF map of the ferritic phases for experiment 3ST_L.

The Image Quality map presented in Figure. IV. 15 a) shows some areas of the microstructure with high densities of HAB (> 50 ° appearing in red). These domains obviously contain different variants in a given packet of laths on the IPF map. In contrast, the areas with the lowest densities contains one single variant per packet. It is very likely that the first type of domains corresponds in fact to the bainite formed at 400 °C (indicated by a yellow domain as B400 in Figure. IV. 15 a)) and the second type to the bainite formed at 475 °C (indicated by a red domain as B475 in Figure. IV. 15 a)). From the

crystallographic point of view, some of these typical packets are of lower and upper type respectively. Whatever the transformation temperature, the blocks of a given packet all appears almost simultaneously. It means that the bainite formed successively is not entangled in the existing packets but appears in retained austenite domains of sufficient size. The IQ map also clearly puts into evidence islands with a darker contrast located in between packets. As in Figure. IV. 3, they should correspond to MA islands. Some of these MA islands have been highlighted in Figure. IV. 15 (black boxes).

The microstructure is thus clearly made of two types of bainites, an upper bainite formed at 475 °C and a lower bainite of at 400 °C in addition to MA islands and residual austenite films (not detectable by EBSD). All these constituents can be more or less identified on the microstructures contrary to the previous study on two-step schedules.

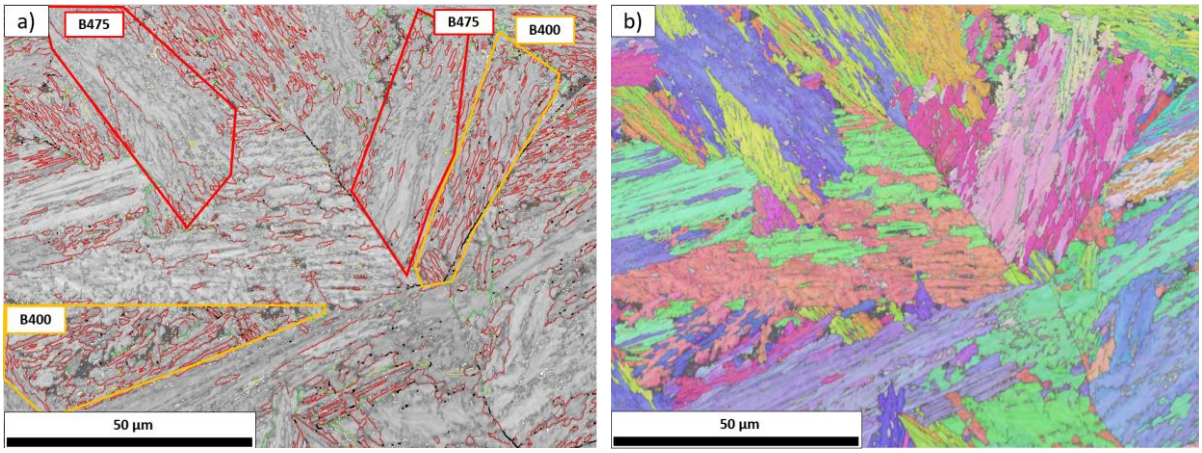

Figure. IV. 16: a) Image quality maps and boundaries according to the nomenclature described in the text; b) IPF map of the ferritic phases for experiment 3ST_S.

Maps on experiment 3ST_S show the same constituents discussed above except that the fraction of bainite formed at 475 °C and the fraction of MA islands is lower in accordance with the HEXRD results. In Figure. IV. 16 a), we have indicated on the microstructure the different areas of bainite formed at 475 °C by red domains (B475) and bainite formed at 400 °C by yellow domains (B400). The discrimination of the two types of bainite is realized on the basis of misorientation grain boundaries as explained above.

Figure. IV. 17 a) shows the histogram of misorientations corresponding to experiment 3ST_L (grey) and experiment 3ST_S (black). The distributions show a higher density of HAB in the 3ST_S than in the 3ST_L. As the Zajac classification has been developed to classify the homogenous microstructures, it is not directly applicable to microstructures composed by a mixture of different bainites as observed here. However, the distribution of misorientation angles for 3ST_S experiment is comparable to the one of upper bainite (as ISO_475 condition for instance in Figure. IV. 5). The sole observation of the distribution could have led to a misleading conclusions as it doesn't permit to put into evidence the two microstructure components obviously revealed by the detailed analysis of the maps.

Figure. IV. 17 b) shows the size distribution as a function of the critical misorientation angle measured for 3ST_L (grey), 3ST_S (black), ISO_475 (red) and ISO_400 (yellow) experiments. The size is smaller whatever the critical angle for the 3ST_S than the one measured for the 3ST_L. Those results are consistent with the constituting components of both microstructures. In the case of 3ST_S, the

microstructure is mostly composed of bainite formed at 400 °C with a thinner size. However, the size measured in this condition is higher than the pure isothermal holding at 400 °C due to the presence of 22 wt.% of bainite formed at 475 °C. The bainite formed during the first step at 475 °C present a larger size than bainite formed at 400 °C. For experiment 3ST_L, the size is larger than the pure isothermal ISO_475 and comparable with the one measured for ISO_450. As shown Table 11, the microstructure is yet composed with a mixture of bainite formed at 475 °C and bainite formed at 400 °C.

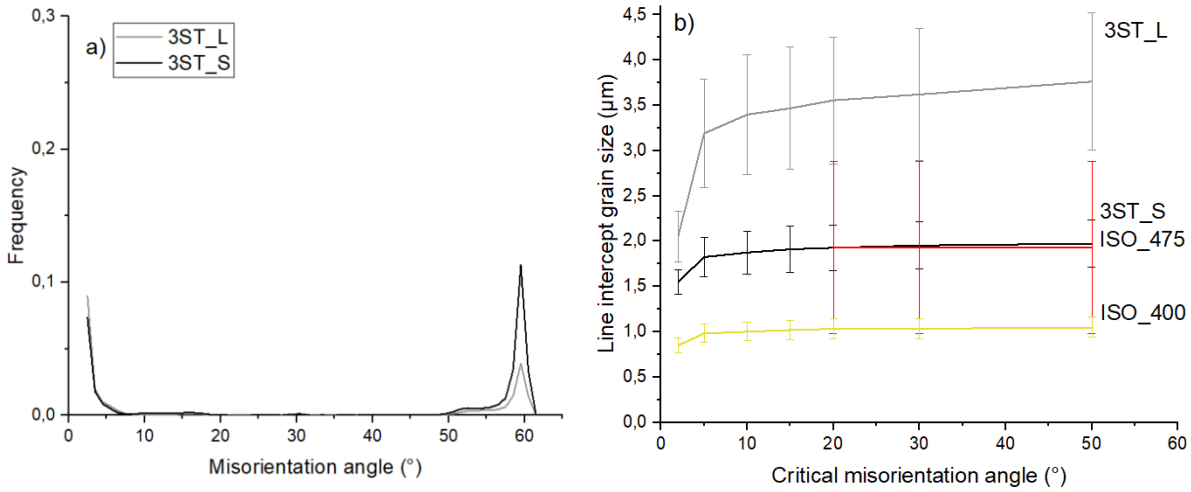

Figure. IV. 17: a) Histograms of misorientations after three-step experiments b) size distribution as a function of critical misorientation angle.

In conclusion, the microstructures obtained after the 3ST_L and 3ST_S holding sequences were characterized using SEM-EBSD. For both experiments, it was possible to distinguish the upper (bainite formed at 475 °C) and lower (bainite formed at 400 °C) components based on the IQ and grain boundary maps. As presented in the previous part, the bainite formed at high temperature is characterized by a low proportion of HABs, whereas the bainite formed at low temperature contain a high proportion of HABs. Using Zajac's classification both microstructures were classified as upper bainite comparable to the distribution of misorientation determined for the ISO_450 and ISO_475 experiments. Whatever the transformation temperature, the blocks of a given packet all appears almost simultaneously. It means the bainite formed successively is not entangled in the existing packets but appears in retained austenite blocks of sufficient sizes. Moreover, the measured line intercept grain sizes are comparable to the ones measured for high temperature experiments. It is difficult to have a direct comparison of sizes due to the formation of a mixture of different type of bainites, nevertheless the observed trend remain consistent with the observations made on the microstructures obtained after isothermal heat treatments.

As presented in Chapter I, microstructures obtained in continuous cooling conditions are composed with mixture of different types of bainite formed along the cooling. In the next section, we will present the characterization of microstructures obtained after a continuous cooling schedule with a low cooling rate (0.3 °C/s) and its associated multistep twin.

II.2. Continuous cooling treatment and the associated multistep holding sequence

In this section, the ESBD characterizations of the microstructure obtained after continuous cooling at 0.3 °C/s (CC_0.3) and after its multistep twin (ST_0.3) will be presented. The corresponding thermal treatments are presented in Figure. IV. 18 as reminder.

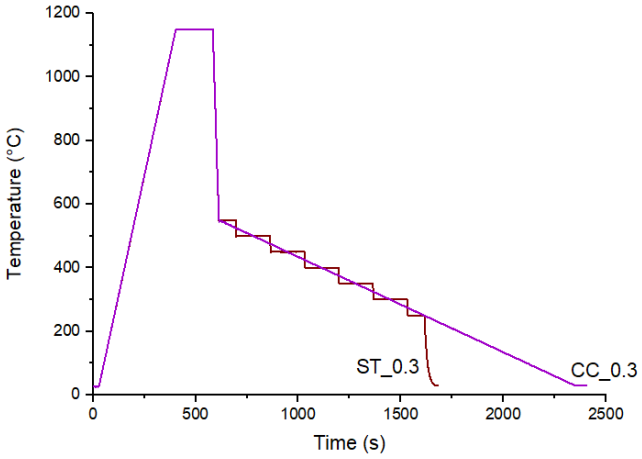

Figure. IV. 18: Heat treatments for ST_0.3 and CC_0.3 experiments.

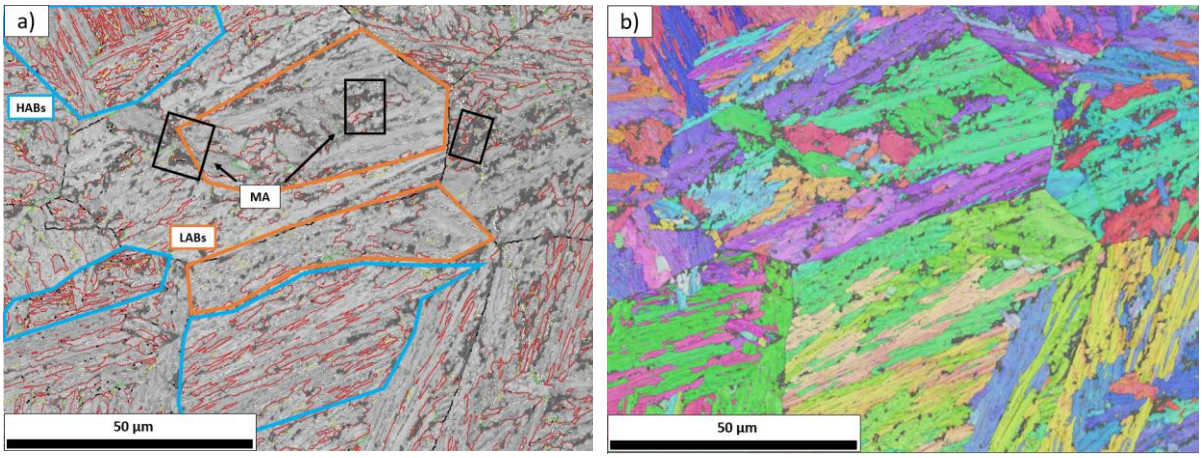

Figure. IV. 19: a) Image Quality maps and boundaries according to the nomenclature described in the text; b) IPF map of the ferritic phases for the continuous cooling condition (CC_0.3).

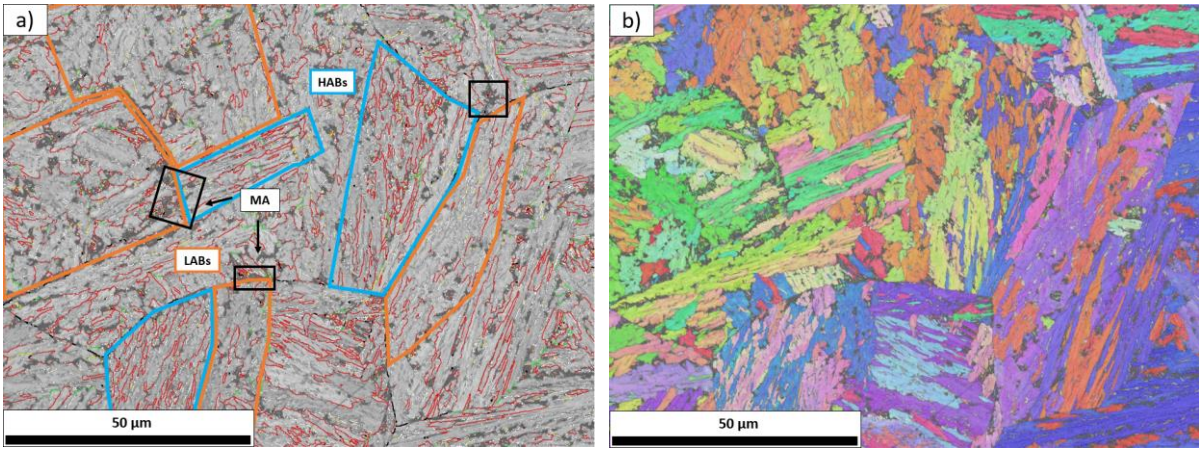

Figure. IV. 20: a) Image Quality maps and boundaries according to the nomenclature described in the text; b) IPF map of the ferritic phases for the multistep holding sequence ST_0.3.

Figure. IV. 19 and Figure. IV. 20 show the Image Quality and the IPF maps of the ferritic phases for the continuous cooling at 0.3°C/s and the multistep sequence respectively.

On both microstructures, the shape of the PAG can be guessed with boundaries drawn in black with a misorientation angle between 20 ° and 50 ° in Figure. IV. 19 a) and Figure. IV. 20 a). Moreover, some areas of the microstructure with a high density of HABs (> 50 ° appearing in red) and a high density of LABs are highlighted with blue boxes and orange boxes, respectively. As previously, the areas presenting the highest densities of HABs present different variants in a given packet of laths as shown in the IPF maps in Figure. IV. 19 a) and Figure. IV. 20 b). These areas correspond presumably to the bainite formed at low temperature (lower bainite). In contrast, the areas with the lowest densities contains one single variant per packet should correspond to the bainite formed at high temperature (upper bainite). In both microstructures, few MA islands are present (highlighted by black boxes at PAG boundaries). The HEXRD analysis shows that around 2 wt.% of fresh martensite and 4 wt.% of fresh martensite is formed at the end of the CC_0.3 and ST_0.3 experiments respectively. The rest of microstructure is made of bainite laths (presumably) as the presence of austenite cannot be revealed at such magnifications (x 1000).

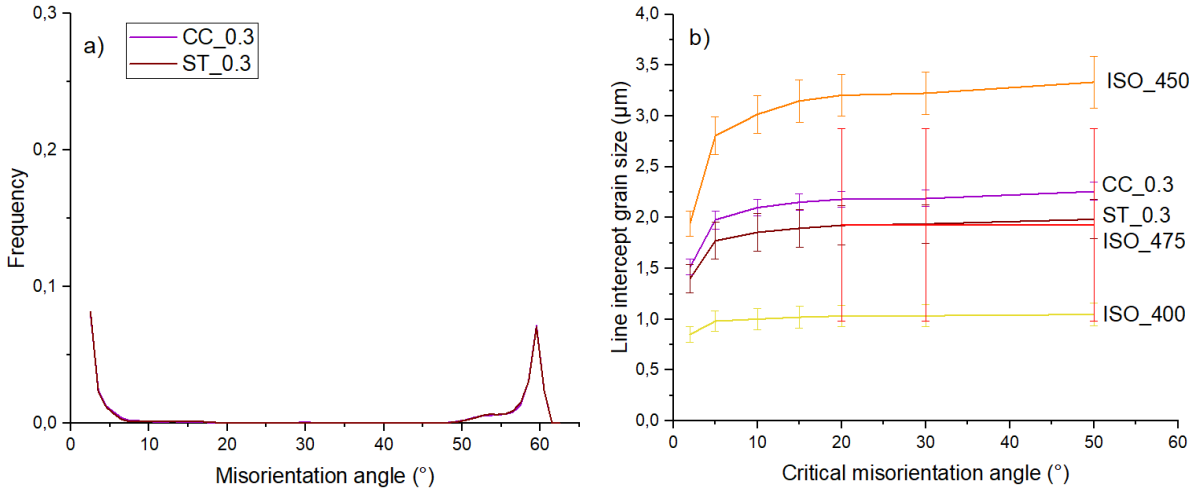

Figure. IV. 21: a) Histograms of misorientations after continuous cooling and multistep experiment ST_0.3 ; b) size distribution as a function of critical misorientation angle.

Figure. IV. 21 a) shows the histograms of misorientations corresponding to CC_0.3 (purple) and ST_0.3 (dark red). Figure. IV. 21 b) shows the corresponding size distribution as a function of the critical misorientation angle compared with the ones obtained for isothermal holdings ISO_475 (red), ISO_450 (orange) and ISO_400 (yellow). In both experiments, the distribution of boundary angles are quasi-identical. Using Zajac's classification, both can be defined as upper bainite because peaks at high angle misorientation are not intense as bainite formed at high temperatures. Those results are consistent with previous studies [5], [32]. The microstructures are composed with a mixture of different bainites and a high fraction of retained austenite (HEXRD) (progressive fragmentation of the microstructure [6], [33]).

The measured sizes for both anisothermal experiments are similar for all the critical misorientation angles (around 2 µm). Sizes are comparable to the one measured on sample ISO_475. The bainite lath sizes measured in continuous cooling and multistep experiments were reported in Figure. IV. 22

compared with isothermal sizes using the same analysis method. The bainitic laths sizes are comparable to the sizes measured for high temperature ISO_475 and considered as upper bainite.

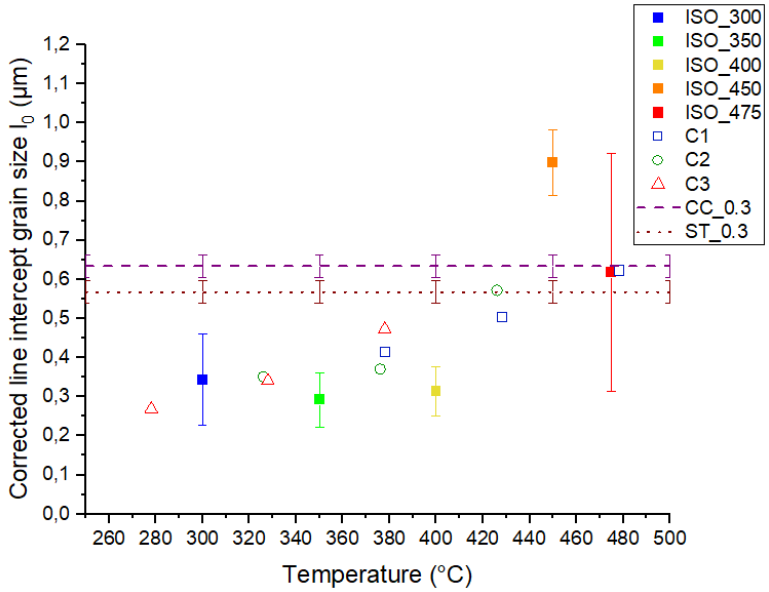

Figure. IV. 22: Bainite laths sizes as function of transformation temperature (isothermal experiments) or after continuous cooling experiments.

II.3. Conclusion

We have been able to show that the CFB microstructures are gradually formed during anisothermal transformations, and that it is possible to distinguish the bainites formed at different temperatures on the basis of their microtextures (upper and lower bainite). It is however impossible to distinguish the blocks below 400 °C (lower bainite or tempered martensite). Fresh martensite can only be distinguished on the basis of a low IQ contrast when the carbon content is high. For lower carbon content, martensite is resolved by ESBD and the indexed domain cannot be distinguished from lower bainite.

During continuous cooling experiments, upper bainitic domains appearing at high temperature above 450 °C (and 475 °C) are characterized by a low density of HABs but contain LABs (laths are obviously resolved). As in the microstructures obtained isothermally at high temperature, the bainite has a single variant per packet. For lower bainite domains appearing at low temperatures between 400 °C to 300 °C, the bainite is characterized by a high density of HABs delimiting often different self-accommodating variants inside a packet. With this study, we have reached the limits of Zajac's classification when considering bainitic component, even if bainite appearing as upper bainite with this classification, it hides different constituting populations of packets of lower and upper bainite.

The measured line intercept grain size distributions for the ST_0.3 and CC_0.3 are close to each other. The measured size reveals also a mean value close to the size measured for the ISO_475 condition.

This mean value is more sensitive to the presence of large microstructure features, and thus to different types of bainite.

The observation of the repartition of upper and lower bainitic structures after step cooling shows that all the laths of given packet appear probably at the same time (at least rapidly, at the same temperature). This is the reason why different domains can be easily identified on the maps and it sustains the view which consider that bainitic transformation is an autocatalytic process.

III. Microstructures and properties

The previous Chapter III details the transformation kinetics explaining the formation of the CFB microstructures as well as the relative stability of the austenite through carbon balances. The beginning of this Chapter IV proposes a quantitative analysis of the bainitic structure in terms of sizes and microtextures. All these features are necessary to understand the origins of the mechanical performances of these microstructures (tensile, toughness, fatigue …).

In the frame of this thesis, only Vickers hardness measurements have been conducted due to time constraints. Figure. IV. 23 shows the Vickers hardness (HV0.1) of the microstructures as function of the holding temperature for 1200 s isothermal treatments (squares) and after continuous cooling (purple line).

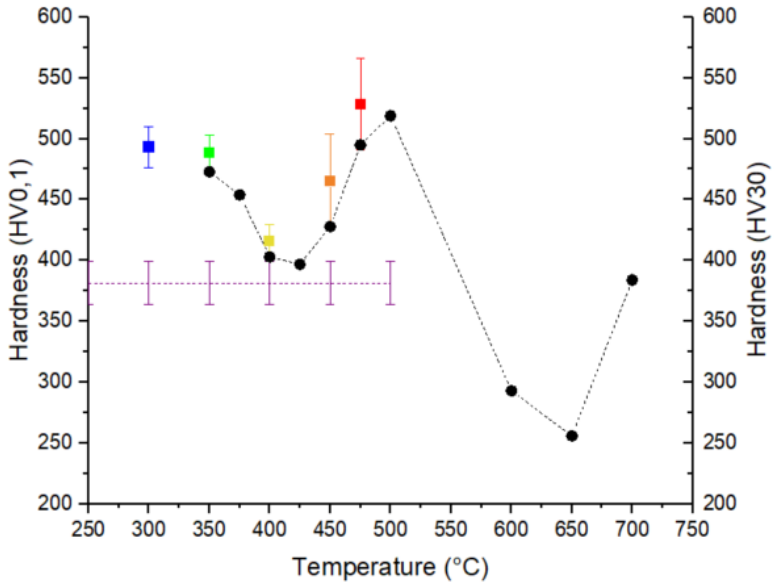

Figure. IV. 23: Hardness (HV0.1) of the samples as function of transformation temperature after 1200 s isothermal (squares) and continuous cooling (purple line) experiments. The error bar corresponds to the experimental statistical scattering. Hardness of the samples (HV30) as function of temperature (black circles) measured by Ascometal when elaborating the TTT diagram presented in Chapter III.

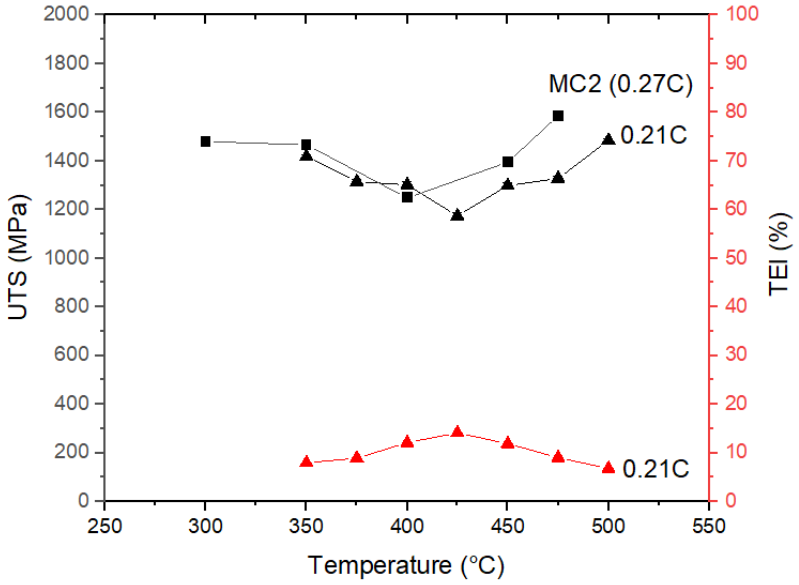

Figure. IV. 24: Ultimate Tensile Strength (UTS), Total Elongation (TEI) as a function of austempering temperature (°C) for a 0.21C steels, reproduced from [34] and the estimated UTS of the studied steel (studied alloy).

Figure. IV. 23 shows the Vickers hardness (HV0.1) of the microstructures as function of the transformation temperature for 1200s isothermal treatments (squares) and after continuous cooling (purple line) compared with the Vickers hardness of the samples (HV30) determined by Ascometal to make the TTT diagram in Chapter III. The hardness first decreases when increasing the holding temperature up to 400 °C. A minimal hardness is reached at 400 °C and the hardness then increases when increasing the holding temperature in the studied range. It is likely than above 500 °C, the hardness will decrease again due the presence of ferrite and pearlite when phase transformation take place above B_S (as shown in Figure. IV. 23). Such evolution of the hardness with the holding temperature is consistent with the evolution reported in previous studies [35], [36].

Figure. IV. 24 present a comparison between the tensile performance (UTS and UEL) of the 0.2C-1.5Si-2.5Mn steel studied by Sugimoto et al. [34] (already shown in Chapter I) and our hardness values as a function of the transformation temperature. Our values have been multiplied by a factor 3.0 to compare UTS and hardness values. Except that Sugimoto et al. report that the minimum in terms of strength is switched to 425 °C, the slope of the two branches below and above the minimum are rather similar.

As explained in the bibliography (Chapter I), the behavior at low temperature (below 400 °C) is mainly controlled by a size effect related to bainite and tempered martensite in the absence of fresh martensite (retained austenite is very stable). The higher the temperature, the higher the lath thickness and thus the lower the strength is. On the contrary, in the high temperature range (above 400 °C), the austenite is less enriched and thus less stable. The behavior is the controlled by the MA fraction (composite effect). Our microstructure observations summarized in Table 12 sustains this interpretation.

Table 12: Thickness of bainite lath measured by EBSD (with critical angle of 5 °) and the MA fraction determined by HEXRD measurement at room temperature for each isothermal treatment.

Temperature (°C)	Thickness (µm)	Fraction MA (wt.%)
300	0,31	10
350	0,25	10
400	0,30	17
450	0,87	40
475	0,62	65

This interpretation is also sustained by the careful observations of the hardness distribution on the samples annealed at 450 °C and 475 °C. First of all, it appears that the scattering of the measurements on a single sample increases with the transformation temperature. Figure. IV. 25 shows the statistical hardness distribution at 475 °C which is obviously bimodal corresponding to the two constituting phases, i.e. a bainitic phase obtained at 400 °C and fresh martensite (35 wt.% / 58 wt.% respectively according to Table 2). The second peak at about 550 and 600 HV corresponds to the hardness expected in a martensite phase with a carbon content of 0.36 wt.%. (cf. Krauss [37]).

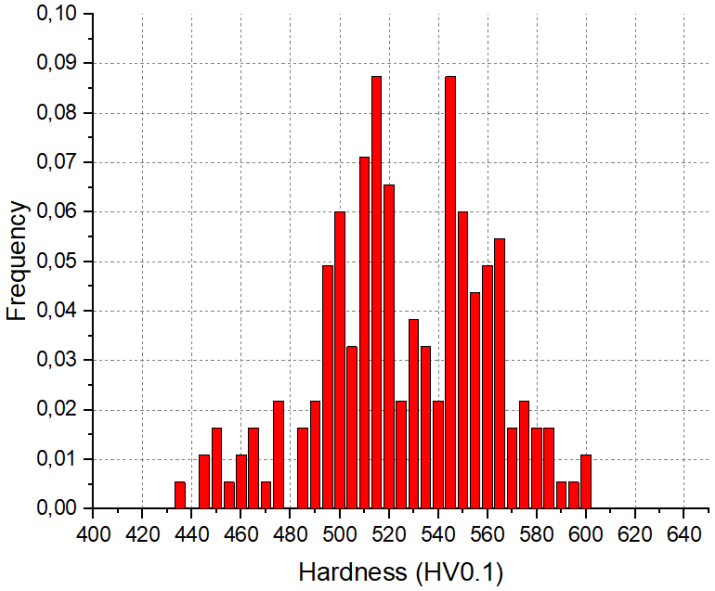

Figure. IV. 25: Distribution of hardness (HV0.1) for experiment ISO_475.

The measured hardness of the microstructure after a continuous cooling (0.3 °C/s) is also reported in Figure. IV. 23. The value is lower than the minimum value reported in isothermal experiment at 400 °C. This surprising result is related to the singular morphogenesis of the microstructure during continuous cooling. In fact, the size of the bainitic structure is far higher than the microstructure obtained at 400 °C and is comparable to the ones obtained at 450 °C and at 475 °C as the first bainitic laths appears at high temperature. In the meanwhile, the bainite transformation rates is far higher than at 450 °C or 475 °C, leading to a better enrichment and stabilization of retained austenite. As a consequence, the fraction of MA islands is lower after continuous cooling than after an isothermal holding at high temperature, reducing in turn their hardening potential. Hence, the microstructure after continuous

cooling can benefit neither from the hardening potential of the size effect of bainite nor from the second phase hardening.

The presence of bainitic structure obtained at different temperatures, and thus with different sizes explains why the scattering of the hardness measurement is also higher than the ones reported on the microstructure after isothermal holding at 400 °C, without being comparable to the ones reported after isothermal holding at higher temperatures which are more related to the presence of hard martensite.

Conclusions

In this Chapter, we have characterized the microstructures obtained after the different heat treatments detailed in Chapter 3 using state-of-the-art SEM coupling with EBSD. Reference post-treatments techniques of the literature were discussed and applied.

The main scientific results of this Chapter are:

- The size of bainitic laths increases with the increase in the transformation temperature in isothermal conditions. However, the observed evolution is not as linear as shown by Hell. Our results were compared with models found in the literature. The difficulty appeared that the objects described in the literature are often different in practice (thickness/volume, lath/sub-unit). This work allowed us to show that there is probably a factor 3 between lath and sub-unit sizes.
- The microstructures obtained after low temperature annealings (at 300 °C, 350 °C and 400 °C) show a high density of HABs which delimit different self-accommodating variants inside bainitic packets. This type of microstructure can be classified as lower bainite using Zajac's classification.
- The microstructures obtained after high temperature annealings (at 450 °C and 475 °C) show a low density of HABs but a high proportion of LABs, with a single variant per bainitic packet. These microstructures can be classified as upper bainite using Zajac's classification, even if they contain a high fraction of MA islands.
- The microstructures obtained after anisothermal schedules are composed with different types of bainite formed all along the cooling. It was possible to distinguish different domains in the maps composed with a high proportion of LABs and a high proportion of HABs, corresponding to the domains of bainite formed at high temperature and formed at low temperature respectively. The diversity of bainites in the microstructures make difficult their classification. Zajac's classification reaches its limits.
- The microstructures formed after continuous cooling treatments show a far larger variability of sizes. Their mean size is close to the one measured at high temperature in isothermal conditions.
- We have put into evidence that whatever the studied conditions, the microstructures are highly entangled confirming an intergranular nucleation of the packets (not only at PAG boundaries), which could be the sign of an autocatalytic process for bainite and martensite transformations as well.

- The hardness was measured to characterize the mechanical properties of the different microstructures. The hardness measured after isothermal conditions follow the evolution shown in the literature by Sugimoto et al. [34]. The minimal hardness measured is around 400 °C. The behavior at low temperature (below 400 °C) is mainly controlled by a size effect related to bainite and tempered martensite in the absence of fresh martensite (retained austenite is very stable). The increase at higher temperature is associated to the increase in the MA fraction. The hardness after experiment CC_0.3 is lower than the hardness measured for the ISO_400. This surprising result is related to the singular morphogenesis of the microstructure during continuous cooling.

Based on the in situ investigations of bainite transformation, shown in Chapter III, and the microstructure characterizations, shown in this Chapter, we have chosen to implement and improve a “diffusionless” model from the literature, which will be presented in the next Chapter.

References

[1] H. Kitahara, R. Ueji, N. Tsuji, and Y. Minamino, "Crystallographic features of lath martensite in low-carbon steel," *Acta Mater.*, vol. 54, no. 5, pp. 1279–1288, Mar. 2006, doi: 10.1016/j.actamat.2005.11.001.

[2] J. Mondal, K. Das, and S. Das, "Isothermal transformation kinetics, microstructure and mechanical properties of a carbide free bainitic steel," *Mater. Charact.*, vol. 177, p. 111166, Jul. 2021, doi: 10.1016/j.matchar.2021.111166.

[3] A. Navarro-López, J. Hidalgo, J. Sietsma, and M. J. Santofimia, "Characterization of bainitic/martensitic structures formed in isothermal treatments below the M s temperature," *Mater. Charact.*, vol. 128, pp. 248–256, Jun. 2017, doi: 10.1016/j.matchar.2017.04.007.

[4] M. Ben Haj Slama, N. Gey, L. Germain, K. Zhu, and S. Allain, "Key Parameters to Promote Granularization of Lath-Like Bainite/Martensite in FeNiC Alloys during Isothermal Holding," *Materials*, vol. 11, no. 10, p. 1808, Sep. 2018, doi: 10.3390/ma11101808.

[5] K. Zhu, O. Bouaziz, C. Oberbillig, and M. Huang, "An approach to define the effective lath size controlling yield strength of bainite," *Mater. Sci. Eng. A*, vol. 527, no. 24–25, pp. 6614–6619, Sep. 2010, doi: 10.1016/j.msea.2010.06.061.

[6] Gourgues A.-F., H. M. Flower, and T. C. Lindley, "Electron backscattering diffraction study of acicular ferrite, bainite, and martensite steel microstructures," *Mater. Sci. Technol.*, vol. 16, no. 1, pp. 26–40, Jan. 2000, doi: 10.1179/026708300773002636.

[7] H. K. D. H. Bhadeshia and J. Christian, "Bainite in steels," *Metall. Trans. A*, vol. 21, no. 3, pp. 767–797, 1990.

[8] J.-C. Hell, "Aciers bainitiques sans carbure: caractérisations microstructurale multi-échelle et in situ de la transformation austénite-bainite et relations entre microstructure et comportement mécanique," PhD Thesis, Metz, 2011.

[9] M. B. H. Slama, "Étude multi-échelle et in situ des évolutions microstructurales en conditions isothermes d'aciers bainitiques en lattes," PhD Thesis, Université de Lorraine, 2018.

[10] S. Morito, J. Nishikawa, and T. Maki, "Dislocation Density within Lath Martensite in Fe-C and Fe-Ni Alloys," *ISIJ Int.*, vol. 43, no. 9, pp. 1475–1477, 2003, doi: 10.2355/isijinternational.43.1475.

[11] G. Miyamoto, N. Takayama, and T. Furuhara, "Accurate measurement of the orientation relationship of lath martensite and bainite by electron backscatter diffraction analysis," *Scr. Mater.*, vol. 60, no. 12, pp. 1113–1116, Jun. 2009, doi: 10.1016/j.scriptamat.2009.02.053.

[12] J. Zhao *et al.*, "Transformation behavior and microstructure feature of large strain ausformed low-temperature bainite in a medium C - Si rich alloy steel," *Mater. Sci. Eng. A*, vol. 682, pp. 527–534, Jan. 2017, doi: 10.1016/j.msea.2016.11.073.

[13] G. Mao, R. Cao, C. Cayron, X. Mao, R. Logé, and J. Chen, "Effect of cooling conditions on microstructures and mechanical behaviors of reheated low-carbon weld metals," *Mater. Sci. Eng. A*, vol. 744, pp. 671–681, Jan. 2019, doi: 10.1016/j.msea.2018.12.035.

[14] S. Zajac, V. Schwinn, and K. H. Tacke, "Characterisation and Quantification of Complex Bainitic Microstructures in High and Ultra-High Strength Linepipe Steels," *Mater. Sci. Forum*, vol. 500–501, pp. 387–394, Nov. 2005, doi: 10.4028/www.scientific.net/MSF.500-501.387.

[15] X. Y. Long, J. Kang, B. Lv, and F. C. Zhang, "Carbide-free bainite in medium carbon steel," *Mater. Des.*, vol. 64, pp. 237–245, Dec. 2014, doi: 10.1016/j.matdes.2014.07.055.

[16] F. G. Caballero, S. Allain, J. Cornide, J. D. Puerta Velásquez, C. Garcia-Mateo, and M. K. Miller, "Design of cold rolled and continuous annealed carbide-free bainitic steels for automotive application," *Mater. Des.*, vol. 49, pp. 667–680, Aug. 2013, doi: 10.1016/j.matdes.2013.02.046.

[17] P. P. Suikkanen, C. Cayron, A. J. DeArdo, and L. P. Karjalainen, "Crystallographic Analysis of Isothermally Transformed Bainite in 0.2C–2.0Mn–1.5Si–0.6Cr Steel Using EBSD," *J. Mater. Sci. Technol.*, vol. 29, no. 4, pp. 359–366, Apr. 2013, doi: 10.1016/j.jmst.2013.01.015.

[18] S. Kang, J. G. Speer, R. W. Regier, H. Nako, S. C. Kennett, and K. O. Findley, "The analysis of bainitic ferrite microstructure in microalloyed plate steels through quantitative characterization of

intervariant boundaries," *Mater. Sci. Eng. A*, vol. 669, pp. 459–468, Jul. 2016, doi: 10.1016/j.msea.2016.05.111.

[19] E. P. Da Silva *et al.*, "Isothermal transformations in advanced high strength steels below martensite start temperature," *Mater. Sci. Technol.*, vol. 31, no. 7, pp. 808–816, May 2015, doi: 10.1179/1743284714Y.0000000719.

[20] L. Rancel, M. Gómez, S. F. Medina, and I. Gutierrez, "Measurement of bainite packet size and its influence on cleavage fracture in a medium carbon bainitic steel," *Mater. Sci. Eng. A*, vol. 530, pp. 21–27, Dec. 2011, doi: 10.1016/j.msea.2011.09.001.

[21] I. Pushkareva *et al.*, "The Influence of Vanadium Additions on Isothermally Formed Bainite Microstructures in Medium Carbon Steels Containing Retained Austenite," *Metals*, vol. 10, no. 3, p. 392, Mar. 2020, doi: 10.3390/met10030392.

[22] N. A. Chester and H. K. D. H. Bhadeshia, "Mathematical Modelling of Bainite Transformation Kinetics," *J. Phys. IV*, vol. 07, no. C5, pp. C5-41-C5-46, Nov. 1997, doi: 10.1051/jp4:1997506.

[23] L. C. Chang, "Bainite transformation and novel bainitic rail steels.," PhD Thesis, University of Cambridge, 1995.

[24] C. Garcia-Mateo *et al.*, "Analyzing the scale of the bainitic ferrite plates by XRD, SEM and TEM," *Mater. Charact.*, vol. 122, pp. 83–89, Dec. 2016, doi: 10.1016/j.matchar.2016.10.023.

[25] A. B. Cota, S. W. Ooi, W. Solano-Alvarez, and H. K. D. H. Bhadeshia, "Infusion of hydrogen into nanostructured bainitic steel," *Mater. Charact.*, vol. 134, pp. 96–102, Dec. 2017, doi: 10.1016/j.matchar.2017.10.006.

[26] M. Soliman and H. Palkowski, "Ultra-fine Bainite Structure in Hypo-eutectoid Steels," *ISIJ Int.*, vol. 47, no. 12, pp. 1703–1710, 2007, doi: 10.2355/isijinternational.47.1703.

[27] S. M. C. van Bohemen, "Exploring the correlation between the austenite yield strength and the bainite lath thickness," *Mater. Sci. Eng. A*, vol. 731, pp. 119–123, Jul. 2018, doi: 10.1016/j.msea.2018.06.041.

[28] K. Irvine, "The strength of austenitic stainless steels," *J Iron Steel Inst*, vol. 207, pp. 1017–1028, 1969.

[29] Z. Yang *et al.*, "Accelerating nano-bainite transformation based on a new constructed microstructural predicting model," *Mater. Sci. Eng. A*, vol. 748, pp. 16–20, Mar. 2019, doi: 10.1016/j.msea.2019.01.061.

[30] G. I. Rees and H. K. D. H. Bhadeshia, "Bainite transformation Part 1 Modified model," *Mater Sci Technol*, vol. 8, p. 965, 1992.

[31] S. B. Singh and H. K. D. H. Bhadeshia, "Estimation of bainite plate-thickness in low-alloy steels," *Mater. Sci. Eng. A*, vol. 245, no. 1, pp. 72–79, Apr. 1998, doi: 10.1016/S0921-5093(97)00701-6.

[32] S. N. Panpurin, N. Y. Zolotorevsky, Y. F. Titovets, A. A. Zisman, and E. I. Khlusova, "Crystallographic Features of Low-Carbon Bainite Formed under Non-Isothermal Conditions," *Mater. Sci. Forum*, vol. 762, pp. 110–115, Jul. 2013, doi: 10.4028/www.scientific.net/MSF.762.110.

[33] M. Sinha, B. Syed, A. Karmakar, and S. Ghosh, "Diffusional and displacive transformations in interstitial-free steel within the scope of a critical assessment of the mechanical property," *Mater. Sci. Eng. A*, vol. 787, p. 139519, Jun. 2020, doi: 10.1016/j.msea.2020.139519.

[34] K. Sugimoto, K. Nakano, S.-M. Song, and T. Kashima, "Retained austenite characteristics and stretch-flangeability of high-strength low-alloy TRIP type bainitic sheet steels," *ISIJ Int.*, vol. 42, no. 4, pp. 450–455, 2002.

[35] K. Sugimoto, A. Kanda, R. Kikuchi, S. Hashimoto, T. Kashima, and S. Ikeda, "Ductility and Formability of Newly Developed High Strength Low Alloy TRIP-aided Sheet Steels with Annealed Martensite Matrix.," *ISIJ Int.*, vol. 42, no. 8, pp. 910–915, 2002, doi: 10.2355/isijinternational.42.910.

[36] J.-C. Hell, M. Dehmas, S. Allain, J. M. Prado, A. Hazotte, and J.-P. Chateau, "Microstructure – Properties Relationships in Carbide-free Bainitic Steels," *ISIJ Int.*, vol. 51, no. 10, pp. 1724–1732, 2011, doi: 10.2355/isijinternational.51.1724.

[37] G. Krauss, "Martensite in steel: strength and structure," *Mater. Sci. Eng. A*, vol. 273–275, pp. 40–57, Dec. 1999, doi: 10.1016/S0921-5093(99)00288-9.

APPENDIX

APPENDIX 4: Image Quality (IQ) and Inverse Pole Figure (IPF) maps of FCC phase

Figure. IV. 26 shows the Image Quality (IQ) and Inverse Pole Figure (IPF) maps of FCC phase (austenite) for isothermal treatments obtained at x 2500 magnification.

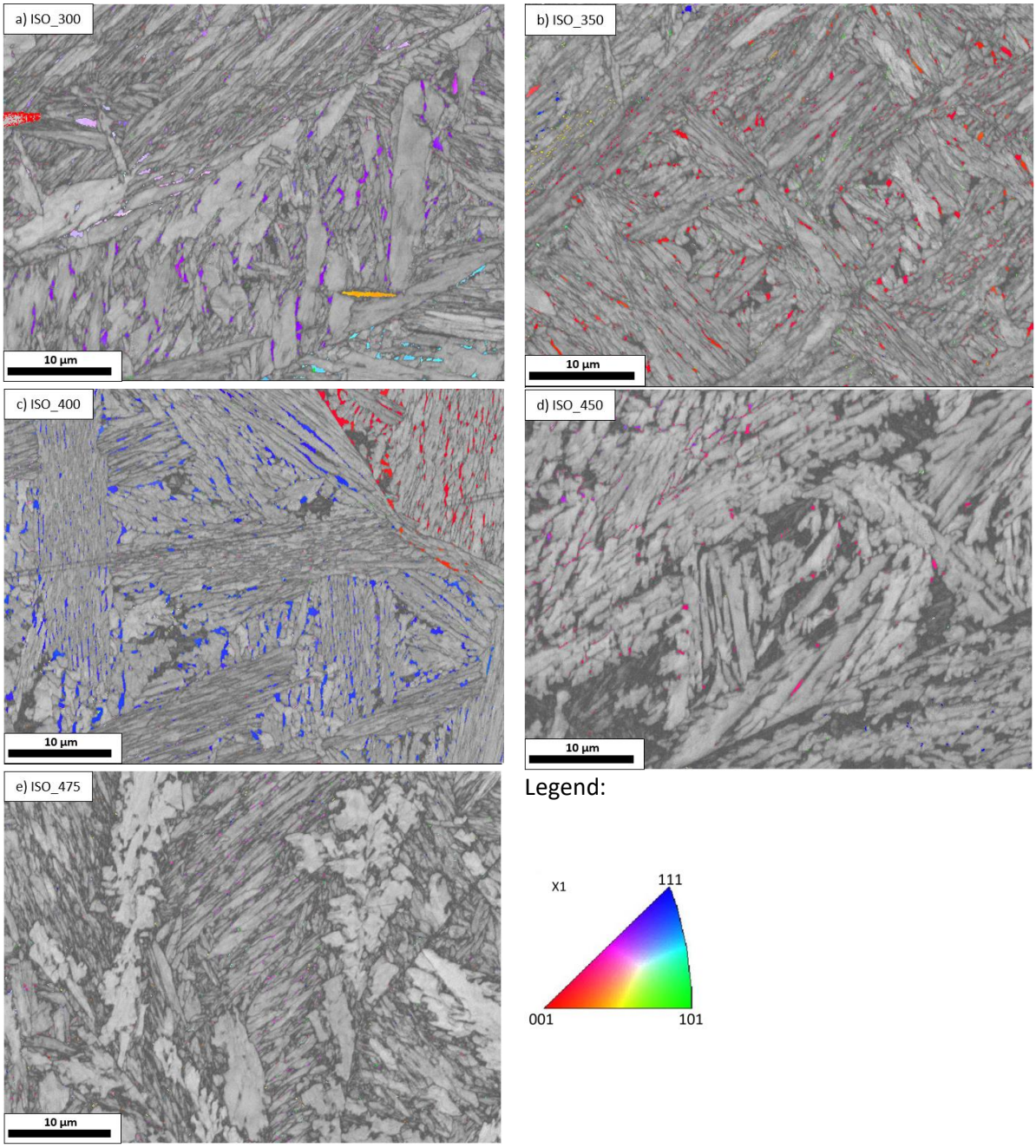

Figure. IV. 26: Image Quality and Inverse Pole Figure maps of austenite in X direction at a) 300 °C, b) 350 °C, c) 400 °C, d) 450 °C, e) 475 °C.

Chapter V: Modeling of bainite formation with a displacive model

Introduction

As presented in Chapter I there's still a controversy with the mechanisms of bainite formation between "diffusive" or "diffusionless" approaches [1]. In this Chapter, we will discuss the modeling of bainite formation following a "diffusionless" approach with the application of one model of the literature [2]. One of the stated objectives is the development of an industrial tool to predict the kinetics of microstructure formation (bainite/martensite transformation kinetics, stability of retained austenite) during customer processes (continuous cooling). However, through this development, we sought to better understand the actuators of this transformation and test the limits of the best "diffusionless" models. Most of them have been developed for isothermal transformations and not for continuous cooling schedules.

In this Chapter, we will first review different "diffusionless" models and show the particular position of the different versions of Van Bohemen's models. Secondly, we will describe the model used in this study based on Van Bohemen 2019 [2] and explain how it has been calibrated. The third part will be devoted to the presentation of the simulation results, with a particular attention paid to the carbon balances between phases. Different additional hypothesis compared to the original model have been tested in that sense (direct carbon balance, experimental input, effect of the mechanical stabilization). The model will be systematically compared to the experimental findings presented in Chapters III and IV (single isothermal holdings and continuous cooling schedules).

I. Principles of "Diffusionless" models

As recalled in Chapter I, the diffusionless approach assumes that the bainite transformation occurs by the nucleation of ferrite laths according to a displacive mechanism, which shares common points with the one of martensite. The bainite transformation global kinetics is limited by the nucleation rate of the bainitic ferrite laths. The nucleation sites are the grain boundaries of prior austenite grains and the ferrite laths already formed during the transformation. The bainitic ferrite laths inherit in a first stage the carbon composition of the parent austenite phase. The carbon can then leave the ferrite matrix by the precipitation of carbides or by partitioning into the surrounding austenite. The latter phenomenon is favorized in high-silicon steels, where the precipitation of carbides is slowed down. The partition of the carbon to austenite is one of the main origins of the stasis phenomenon, and this has been dealt with in several modeling studies and largely discussed already in Chapter III.

In this section, the principal features of bainite transformation models based on the non-diffusive assumption are summarized and critically assessed: thermodynamics of nucleation and growth of bainitic ferrite laths, nature of nucleation sites, nucleation rate and overall transformation kinetics with emphasis on the stasis phenomenon. Only the most important equations are recalled, whereas the reader is referred to the original papers for more detailed presentations.

I.1. Thermodynamics of nucleation and growth

This section presents the two thermodynamic driving forces which control in large extent the kinetics of bainitic ferrite nucleation and growth.

The nucleation consists in the formation of a nucleus of bainitic ferrite having a small volume. The nucleation driving force, denoted ΔG_m , is the change of Gibbs energy associated with the transformation of the parent austenite phase to ferrite having the composition in carbon of the nucleus. As schematized in Figure. V. 1, this change of Gibbs energy depends on the composition of the nucleus. It is assumed that the latter is such that ΔG_m takes the maximum possible value (common tangent construction). In practice, it means that the nucleus has a carbon content close to zero. This apparently contradicts the assumption of a phase transformation without diffusion. However, the depletion in carbon of the nucleus is conceivable in view of its small size. By analyzing a large number of experiments, Bhadeshia [3] established that ΔG_m should be higher than some critical value to allow the nucleation of ferrite and that this critical value depends on the temperature. This condition is formulated as follows [4]:

$$\Delta G_m < G_N \qquad \textit{Eq. 15}$$

The nucleation driving force ΔG_m has to be higher (in absolute value) than G_N, a "universal nucleation function" [4], which defines the minimum driving force necessary to trigger the bainite transformation. G_N only depends on the temperature and is calculated with the following empirical equation (Eq. 16):

$$G_N(J.mol^{-1}) = C_1(T - 273.18) - C_2 \qquad \textit{Eq. 16}$$

Where C_1 and C_2 are constant values equal to $3.637 \pm 0.2\, J.mol^{-1}.K^{-1}$ and $2540 \pm 120\, J.mol^{-1}$ respectively, T the temperature in Kelvin (in the range of 670-920 K). This relationship has been re-estimated in [5], [6] with more recent thermodynamic database.

The temperature at which $\Delta G_m = G_N$ is denoted T_h, which corresponds also to B_S for the bainite transformation.

In most studies, the nucleation of bainitic ferrite is assumed to occur according to a mechanism similar to the one proposed for martensite by Olson and Cohen [7] and then adapted by Bhadeshia [3]. The nucleus forms by the dissociation of dislocations already present in the austenite. This nucleation mechanism implies that its activation energy, which controls the nucleation rate (Section I.3.), follows the relationship [8]:

$$Q^* = Q_0 - K_1 \Delta G_m \qquad \textit{Eq. 17}$$

where Q_0 is the activation energy in the limit where the driving force becomes zero [8], and K_1 is a constant of proportionality. Both latter parameters depend on the material considered. Their physical meaning is discussed in [9].

The proportionality between Q^* and ΔG_m was put into evidence by analyzing a large number of experiments [3], [8], [10], [11]. Nevertheless, it should be mentioned that some studies considered the classical nucleation theory for diffusive transformations, according to which Q^* should be proportional to $1/\Delta G_m^2$ [12], [13].

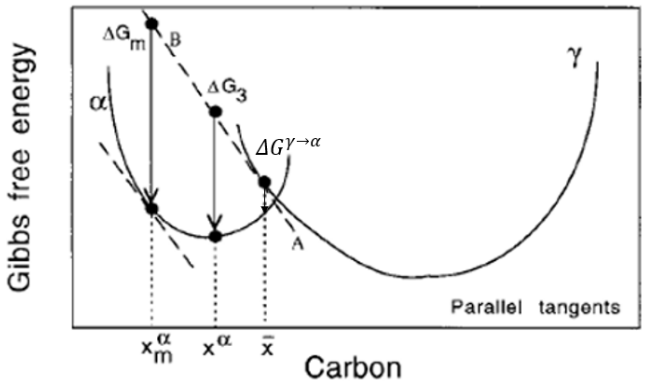

Figure. V. 1: Schematic of Gibbs free energy curves of bainitic ferrite (α) and austenite (γ), with driving forces for displacive growth $\Delta G^{\gamma\to\alpha}$ and for nucleation ΔG_m (reproduced from [4]).

Diffusionless models assume that the bainitic ferrite laths lengthen very fast because of the high mobility of the ferrite/austenite interface. Each lath stops to grow because of the defects introduced in the austenite as a result of the phase transformation strain. The bainite transformation then goes on by the nucleation of new ferrite laths. Contrary to the nucleation stage, the growth stage involves no change in carbon content between austenite and ferrite (the lath is much larger than the nucleus). The growth driving force, denoted $\Delta G^{\gamma\to\alpha}$, is the change of Gibbs energy associated with the transformation of austenite to ferrite, without any change of composition (see graphical

representation in Figure. V. 1). Bhadeshia [3] and numerous authors established that this driving force has to be higher than some critical value (G_{SB}), which corresponds to the elastic strain energy stored in the bainitic ferrite upon the transformation:

$$\Delta G^{\gamma\rightarrow\alpha} < -G_{SB} \qquad \textit{Eq. 18}$$

$G_{SB} = G_e$ is the elastic energy stored in bainitic ferrite, usually considered to be equal to 400 J.mol^{-1} [4]. This condition on the growth of bainitic ferrite is at the origin of the T_0 and T_0' criteria for the stasis of the bainite transformation. If the austenite gets enriched in carbon during the transformation, it stabilizes the austenite (i.e. it decreases its Gibbs energy), thereby decreasing $\Delta G^{\gamma\rightarrow\alpha}$. The temperatures at which $\Delta G^{\gamma\rightarrow\alpha} = 0$ and $\Delta G^{\gamma\rightarrow\alpha} = -G_{SB}$ are denoted T_0 and T_0' respectively. Both latter temperatures can be represented in an phase diagram as a function of the carbon concentration, as shown in Figure. I. 16.

I.2. Nucleation sites

The nucleation sites are the microstructural features which control the bainite transformation kinetics, whereas the driving forces mentioned in previous section give essentially the dependence of the kinetics to the temperature and the parent austenite phase composition. The nature of the nucleation sites for ferrite have been largely studied in diffusionless models, because the global bainite transformation kinetics is thought to be limited by the nucleation rate in diffusionless approaches. Two nucleation sites are considered: the grain boundaries of prior austenite grains (PAG) and the already formed bainitic ferrite laths (autocatalytic nucleation). In nearly all studies [14]–[16], the initial density of nucleation sites on the grain boundaries is assumed to be proportional to the surface per unit volume of PAG boundaries. This assumption is supported by studies on the effect of PAG size on kinetics ([4], [8], [17], [18]). Hence, the bainite transformation kinetics increases for decreasing PAG size. However, when the PAG size is too small, the opposite effect occurs because the grain boundaries may hinder the growth of the sheaves [3].
Some studies consider that the density of nucleation sites located at PAG boundaries does not depend on the temperature [2], [8], [15]. In such case, the number of nucleation sites per unit volume is expressed as:

$$N_i = \frac{6N_S}{d^{\gamma}} \qquad \textit{Eq. 19}$$

where d^{γ} is the prior austenite grain size (diameter), 6 a geometrical factor assuming that the austenite grains have a spherical geometry and N_S the number of nucleation sites per unit surface of austenite grain boundary.

In other studies as [19] for example, a temperature dependence is taken into account. For instance, in 2008, Van Bohemen et al. [8] adapted Magee's assumption regarding martensitic transformation [19], where the density of nucleation sites is proportional to the increase of the driving force due to the undercooling. The number density of potential nucleation sites located at grain boundaries, at the temperature T, can be expressed as a function of the net driving pressure at T (Eq. 20):

$$N_i = \varphi\big(G_N(T_h) - \Delta G_m(T)\big) = \varphi\Gamma(T_h - T) \quad \textit{Eq. 20}$$

Where: Γ is the slope $d(\Delta G_m)/dT$.

The number density of potential nucleation sites is equal to zero at $T = T_h$ and increases almost linearly with the undercooling, as the driving force itself is also nearly proportional to the undercooling. The factor φ is expressed with the following equation (Eq. 21) according to Magee's martensite nucleation model.

$$\varphi = \frac{\alpha}{V_b \Gamma} \quad \textit{Eq. 21}$$

Where V_b is the average volume of bainite sub-units (here considered as constant) and α is a constant. As shown in Chapter IV, the lath size is dependent to the temperature, the average volume of bainite sub-unit should be then considered as dependent on the temperature (Chapter IV, Section I.2.d.3.).

Autocatalytic nucleation consists of the nucleation of bainitic ferrite at the interface between austenite and already formed bainitic ferrite laths (thus inside the PAGs). In a large number of studies, the number of autocatalytic nucleation sites is assumed to be proportional to the volume fraction of already formed bainite. By adding the nucleation sites at grain boundaries, the total number of nucleation sites reads:

$$N = N_i(1 + \lambda f) \quad \textit{Eq. 22}$$

where λ is the autocatalysis factor and f the volume fraction of bainite. Other ways to account for the density of autocatalysis nucleation sites are presented in [15], [21].

The autocatalytic parameter λ is frequently a "fitting" parameter in bainite transformation models and its estimation on physical grounds has still to be established [20]. This is a weakness of these models, because the parameter λ has a strong influence on the calculated kinetics. Indeed, in many cases, autocatalytic nucleation prevails over nucleation on PAG boundaries. Different attempts have been done to estimate how λ can vary with the carbon content of the steel, the temperature, the presence of carbides, the lath size or the nature of the bainite transformation product (lower/upper bainite).

Rees and Bhadeshia [17] considered that the build-up of carbon at ferrite/austenite interfaces causes a local decrease in the driving force for the transformation of austenite to ferrite. The partition of carbon is expected to be more important with increasing carbon content of the steel. In this study [17], the autocatalysis factor, is calculated by (Eq. 23) as a function of the carbon content of the steel (noted $\bar{x}$). (No enrichment of austenite upon bainite transformation is considered in [17]).

$$\lambda = \lambda_1(1 - \lambda_2 \bar{x}) \quad \textit{Eq. 23}$$

Where λ_1 and λ_2 are empirical constants.

The dependence of the autocatalytic parameter on the carbon content in the steel has been confirmed by Singh in his studies [16]. According this relationship, the autocatalysis parameter would decrease with increasing carbon content. However, [10] mentions that the opposite was observed in other studies.

Later on, Van Bohemen et al. [8] introduce a dependence of the autocatalysis factor on the temperature, the austenite grain size and the length of the bainitic sub-unit. Figure. V. 2 shows the λ/d^{γ} factor as a function of temperature for 10 alloys. For lower bainite (noted LB on Figure. V. 2) the λ/d^{γ} factor increases with the decreasing of temperature. This behavior can be justified by the decrease of bainite lath thickness which increases the volume density of interface boundaries and by the increase in dislocation density.

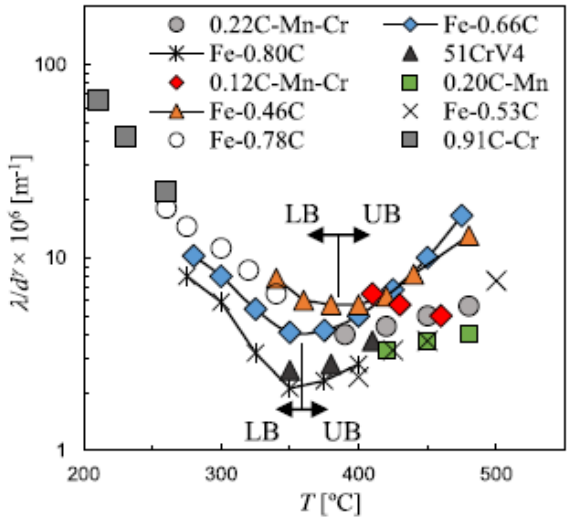

Figure. V. 2: The temperature dependence of λ/d^{γ} values evaluated from the bests fits for alloys 1-10 [2].

The autocatalytic parameter λ can in fact be expressed as (Eq. 24):

$$\lambda = \frac{2d^{\gamma}}{S\xi u_l} \qquad \textit{Eq. 24}$$

Where d^{γ} is the average austenite grain size, S is a geometrical factor dependent of the shape of the austenite grain, ξ is the fraction of the initially-nucleated bainitic sub-units on the grain boundaries (≈ 0.4), and u_l is the typical length of a bainitic sub-unit (2 µm). This relationship reflects the fact that the autocatalytic nucleation becomes more important than the nucleation on grain boundaries when the grain size is increased. Reducing the bainite sub-unit size makes increases the density of autocatalytic nucleation sites.

For upper bainite (noted UB in Figure. V. 2), on the contrary, the λ/d^{γ} factor increases with the increasing of temperature. This increase can be attributed to the increase in volume fraction of cementite precipitates in austenite (near to the interface austenite/ferritic bainite) which can stimulate the nucleation (comparable to acicular ferrite nucleation). Van Bohemen [2] assumes that the combination of these two mechanisms of bainite formation for upper and lower bainite can justify the evolution of λ/d^{γ} factor with the temperature.

As for the activation energy for autocatalytic nucleation, most straightforward assumption is to take the same as for the nucleation on grain boundaries. But in other studies, a different value is considered for the respective nucleation sites. This was investigated in particular by Ravi et al. [15], but also in [18], [21], [22]. For example, Ravi et al. [15] came to the following expression of the autocatalysis parameter:

$$\lambda = \exp(\frac{\Delta Q^*}{kT}) \quad \textit{Eq. 25}$$

Where ΔQ^* is the difference between activation energies for nucleation at grain boundary and autocatalytic, k the Boltzmann constant and T the temperature. This formula represents the fact that nucleation is easier by autocatalysis than on grain boundaries.

I.3. Bainite transformation kinetics

The growth of bainitic sub-unit is considered to take place very quickly, and therefore the prediction of the bainite transformation kinetics is mostly based only on the nucleation rate. In diffusionless models the volume of bainite sub-units is considered to be constant along the transformation in isothermal conditions (see the discussion in Chapter IV).

The fraction of bainite along the transformation is then directly calculated from the nucleation rate:

$$\frac{df}{dt} = V_b \frac{dN}{dt} \quad \textit{Eq. 26}$$

where V_b is the lath volume.

Most models of the literature estimate the bainite nucleation rate in a similar way. Equation below (Eq. 27), taken from Van Bohemen [8], is a good example.

$$\frac{dN}{dt} = \frac{kT}{h}(1-f)N_i(1+\lambda f)\exp\left(-\frac{Q^*}{kT}\right) \quad \textit{Eq. 27}$$

where h is Planck's constant.

In this example, the nucleation rate is assumed to be proportional to $\exp\left(-\frac{Q^*}{kT}\right)$, like in most studies. Another dependence to the activation energy was assumed in [23], where an influence of the driving force for growth, $\Delta G^{\gamma\to\alpha}$, was also taken into account. The factor $\frac{kT}{h}$ gives an estimate of the nucleation attempt frequency. In other studies, the latter is assumed constant. The factor $(1-f)$ represents the exhaustion of nucleation sites when the bainite transformation progresses, in the same manner as in JMAK models (extended volume concept). On this latter point of the geometrical representation of the microstructure, more detailed descriptions were carried out, for instance in [24] in order to take account of the transformation starting from grain boundaries, by using approaches introduced in [24], [25]. Other models also calculate separately the nucleation rate at grain boundaries and autocatalytic, with or without the same activation energy [15], [18], [21], [22]. Last equation is actually the simplest expression of the nucleation rate. Its advantage is to reduce the number of model parameters, but to the detriment of the precision with which the bainite transformation is described. Despite this limitation, an excellent agreement between simulations and experiments is presented in references [2], [8], [9], [20]. As evoked previously, main possible model refinements regard a better geometrical representation of the microstructure, and considering specifically the nucleation at grain boundaries or autocatalytically. Final essential feature regards the carbon distribution.

I.4. Carbon distribution and stasis phenomenon

As explained in Section I.1., during the bainite transformation, the sub-units grow without any change in composition. In high-silicon steels, the carbon then leaves the ferrite matrix by partitioning to the remaining austenite (some carbides may also precipitate). Although it has been shown that the bainitic ferrite remains largely supersaturated (e.g. [26]) the carbon content of austenite will increase. As a result, the driving force for partition-less growth $\Delta G^{\gamma\to\alpha}$ will decrease down to some critical value, corresponding to the elastic energy stored in bainitic ferrite (see Eq. 18). This is known as the T_0' criterion.

It can be seen that the expression of the nucleation rate (Eq. 27) cannot predict the stasis on the basis of the T_0' criterion. In fact, $\Delta G^{\gamma\to\alpha}$ does not appear in this expression. In [10], [24] a maximum fraction of bainite was defined as:

$$v_{\alpha B-max} = \frac{x_{T_0'} - \bar{x}}{x_{T_0'} - x^{\alpha\gamma}} \qquad \textit{Eq. 28}$$

where $x_{T_0'}$ is the carbon concentration corresponding to the T_0' curve, $\bar{x}$ average carbon concentration of the steel, and the $x^{\alpha\gamma}$ is the paraequilibrium carbon concentration. The computation of the overall bainite transformation kinetics was modified accordingly. More recently, Van Bohemen took differently into account driving force $\Delta G^{\gamma\to\alpha}$ which was included in the calculation of a genuine growth factor [2]. This will be discussed in the next Section.

In many examples, the T_0' criterion did not give a satisfactory prediction of the stasis (e.g. [6]). One of the origins proposed for this discrepancy is that the carbon concentration is not uniform inside the austenite, because of the limited rate of diffusion (as discussed already in Chapter III). Near the ferrite laths, the austenite tends to get enriched beyond the T_0' value, while it will remain poorer farther from the first-formed laths. The final microstructure may contain films of austenite located between the bainitic ferrite laths and enriched in carbon beyond the T_0' criterion. On the contrary, the regions which remained poor in carbon undergo the transformation to ferrite. As a result, the final fraction of ferrite will be beyond the value expected by the T_0' criterion. The consequences on the overall kinetics were investigated by simulation [27], and later on with more detailed studies which considered the competition between carbon diffusion rate and new bainitic ferrite laths nucleation (one aim of these models was to predict the thickness of austenite films). See for instance [6], [15], [28], [29]. These heterogeneities are more pronounced at lower transformation temperature due to the slower diffusion. The effect of carbon heterogeneities is also more pronounced in low C steels, as the carbon trapped in austenite films will represent a higher proportion of the overall carbon content of the steel [27]. We have shown in chapter III, with the help of long time experiments (5h) at low transformation temperatures that the enrichment of austenite reaches a composition close to T_0'. This heterogeneity phenomenon is thus less marked on these experiments. However, we have shown strong heterogeneities at higher transformation temperatures. At these high temperatures the enrichment is done concomitantly with the bainitic transformation.

I.5. Conclusion

The literature provides a sound basis to carry out a simulation study of the bainite transformation based on the diffusionless assumption. Best established features of these models regard the thermodynamics of ferrite nucleation and growth, the nucleation at two different sites (grain boundaries, already formed ferrite) and the sensitivity to metallurgical parameters such as the PAG size, the influence of transformation temperature or the alloy composition. Different degrees of precision have been considered to describe geometrically the microstructure and to deal separately with the nucleation on grain boundaries and other bainite units. Even the simplest formulations allowed to find a good agreement between simulations and experiments. Remaining issues regard how to estimate the autocatalysis on a more physical basis, and how to deal with the stasis phenomenon. The effects of carbon redistribution have been studied extensively, but their proper accounting remains an open issue. Finally, another origin of the stasis could be the mechanical stabilization of the austenite upon the bainite transformation progression. This was not addressed in the models presented in this Section. In following Section, a model introduced recently which takes account of both stabilizations, mechanical and by the carbon will be presented.

II. Diffusionless model from literature with transformation stasis

This section presents the model that we have chosen for our simulation study. Compared to other simulations studies based on the diffusionless approach, this model addresses specifically the issue of the phase transformation stasis, which is at the center of our study. This model is based on different versions already developed by Van Bohemen in [8], [9], and whose parameters were established on a large set of experimental data. But as mentioned in last Section, the drawback of such previous models is that the effect of the driving force for diffusionless transformation ($\Delta G^{\gamma\rightarrow\alpha}$) does not appear explicitly in the kinetic equations, whereas it controls the stasis due to carbon enrichment of austenite. The original model introduced by Van Bohemen in [2], [30]–[34] improves this by introducing a thermodynamic growth factor, which takes account not only of the carbon enrichment of austenite, but also of the mechanical stabilization of austenite upon bainite formation, the two origins of the transformation stasis that we want to consider.

II.1. Nucleation

The nucleation rate of bainite sub-units is calculated with (Eq. 29):

$$\frac{dN}{dt} = \nu^* \frac{ZN_S}{d^\gamma}(1-f)(1+\lambda f)exp\left(-\frac{Q^*}{RT}\right) \quad \textit{Eq. 29}$$

where ν^* is the nucleation attempt frequency assumed constant ($10^{13}\ s^{-1}$), N_S the number density of nucleation sites available per unit austenite grain boundaries area, Z a geometrical factor equal to 6 for a spherical austenite grain, d^γ the prior austenite grain size, f the bainite volume fraction, λ the autocatalysis factor, Q^* the activation energy for nucleation, R the perfect gas constant. Q^* decreases linearly with the maximum driving force ΔG_m, as shown in previous Section I.1. (Eq. 17).

The maximum driving force can be written as follows:

$$\Delta G_m = \Gamma(T_3 - T) \quad \textit{Eq. 30}$$

where T_3 is the temperature at which ΔG_m becomes equal to zero and Γ is a constant determined using thermodynamic databases. This proportionality relationship is of course a simplification but which represents well the evolution of ΔG_m.

Another activation energy, Q_b, was introduced by Van Bohemen and defined as:

$$Q_b = Q_0 - K_1 \Gamma T_3 \quad \textit{Eq. 31}$$

Combining the equations (Eq. 17), (Eq. 29) and (Eq. 31), the nucleation rate writes (Eq. 32):

$$\frac{dN}{dt} = \nu^* \frac{6N_S}{d^\gamma}(1-f)(1+\lambda f)exp\left(-\frac{K_1\Gamma}{R}\right)exp\left(\frac{-Q_b}{RT}\right) \quad \textit{Eq. 32}$$

where Q_b appears as an effective activation energy, because it gives its temperature dependence to the nucleation rate equation.

II.2. Thermodynamic growth criterion

The overall transformation rate is described by the equation (Eq. 33), combining the nucleation rate $\frac{dN}{dt}$, the volume of bainite lath V_b and a growth factor B_g, introduced in [2].

$$\frac{df}{dt} = \frac{dN}{dt} V_b B_g \qquad \textit{Eq. 33}$$

where B_g reads:

$$B_g = \frac{V_n \Delta G_{net}}{V_b G_e} \qquad \textit{Eq. 34}$$

where: V_n is the critical volume of nucleus considered as a constant ($2.10^{-25}\ m^3$), ΔG_{net} the net driving force and G_e the elastic strain energy stored in bainite (typically taken equal to 400 J/mol). The net driving force is the difference between the driving force $\Delta G^{\gamma \to \alpha}$ and G_e: $\Delta G_{net} = \Delta G^{\gamma \to \alpha} - G_e$.

The Figure. V. 3, reproduced from [2], shows schematically the definition of $\Delta G^{\gamma \to \alpha}$, which is plotted as a function of temperature. The driving force $\Delta G^{\gamma \to \alpha}$ is also linearized using the following relationship:

$$\Delta G^{\gamma \to \alpha} = \Gamma_B (T_2 - T) \qquad \textit{Eq. 35}$$

At the start temperature B_{s0} we can define the initial elastic stain energy as $G_{e0,Bs}$ (the schematically description is shown in [2]) which the strain energy in bainite when forming the first lath of bainite at temperature B_{s0}. It is evaluated with (Eq. 36):

$$G_{e0,Bs} = \Gamma_B (T_2 - B_{s,0}) \qquad \textit{Eq. 36}$$

where the parameters Γ_B and T_2 define a linear approximation of $\Delta G^{\gamma \to \alpha}$ evolution as a function of the temperature.

If the transformation temperature is lower than $B_{S,0}$, the strain energy necessary to form bainite is higher because the parent austenite phase has a too high yield strength. The corresponding increase of the strain energy is denoted $\Delta G_{e0,\sigma}$. If the first lath of bainite forms at $T < B_{S,0}$, the initial elastic energy reads:

$$G_{e0} = G_{e0,Bs} + \Delta G_{e0,\sigma} \qquad \textit{Eq. 37}$$

Upon the progression of the bainite transformation, the austenite then gets stabilized mechanically. The corresponding increase in the elastic strain energy is denoted $\Delta G_{e,b}$. The total elastic strain energy stored in bainite eventually reads:

$$G_e = G_{e0,Bs} + \Delta G_{e0,\sigma} + \Delta G_{e,b} \qquad \textit{Eq. 38}$$

An equivalent expression of the growth factor defined by the equation (Eq. 34) can be written as follows (Eq. 39):

$$B_g = \frac{V_n}{V_b}\left(\frac{\Gamma_B(B_{S*} - T)}{G_{e0} + \Delta G_{e,b}}\right) \quad \textit{Eq. 39}$$

where B_{S*} is the modified bainite-start temperature, which accounts for the mechanical stabilization of austenite and the effect of the yield strength. B_{S*} is calculated using the equation (Eq. 40).

$$B_{S*} = B_{S,0} - \Delta B_S \quad \textit{Eq. 40}$$

where ΔB_S reads:

$$\Delta B_S = \frac{(\Delta G_{e0,\sigma} + \Delta G_{e,b})}{\Gamma_B} \quad \textit{Eq. 41}$$

$$\Delta G_{e0,\sigma} = p_1 V_m \Delta \sigma_y^{\gamma} \quad \textit{Eq. 42}$$

where p_1 is as a constant $p_1 = 1$, but which can be adjusted, $V_m = 7.1 \times 10^{-6}\ m^3 mol^{-1}$ is the molar volume of austenite and $\Delta\sigma_y^{\gamma}$ is the increase in yield strength of austenite due to the decrease of temperature below $B_{s,0}$.

$$\Delta \sigma_y^{\gamma} = \sigma_{y,T}^{\gamma} - \sigma_{y,B_{S,0}}^{\gamma} \quad \textit{Eq. 43}$$

where $\sigma_{y,T}^{\gamma}$ and $\sigma_{y,B_{S,0}}^{\gamma}$ are the yield strength of austenite at the temperature T and $B_{S,0}$, respectively.

The calculation of the yield strength of austenite at the temperature T ($\sigma_{y,T}^{\gamma}$) is given by:

$$\sigma_{y,T}^{\gamma} = \sigma_{y,25\,^\circ C}^{\gamma}\left(1 - \frac{2.2(T-25)}{10^3} + \frac{4.2(T-25)^2}{10^6} - \frac{3.0(T-25)^3}{10^9}\right) \quad \textit{Eq. 44}$$

where T is the transformation temperature in °C and $\sigma_{y,25\,^\circ C}^{\gamma}$ corresponds to the yield strength of austenite a room temperature calculated from (Eq. 45)

$$\sigma_{y,25\,^\circ C}^{\gamma} = 87.8 + 254x_C + 15.1x_{Si} + 2.5x_{Cr} + 14.5x_{Mo} + 18.5x_V + 4.5x_W + 40x_{Nb} + 5.4x_{Al} + 26.2x_{Ti} + \frac{10.5}{\sqrt{d^{\gamma}}} \quad \textit{Eq. 45}$$

Where x_X is the component *X* composition in wt.% and d^{γ} is the average austenite grain size in mm

As bainite forms, the driving force for bainite formation is decreased by $\Delta G_{e,b}$ due to the mechanical stabilization of austenite. Different contributions are considered:

$$\Delta G_{e,b} = \Delta G_{ds} + \Delta G_{gc} + \Delta G_{hp} \quad \textit{Eq. 46}$$

where ΔG_{ds} is the stabilization energy due to the dislocation strengthening; ΔG_{gc} is the stabilization energy due to the geometrical constraints; ΔG_{hp} is the stabilization energy due to the hydrostatic

pressure. In present study, the latter will be neglected because it becomes significant when the bainite fraction is higher than 0.88, which did not occur in our experiments.

$\Delta G_{e,b}$ is estimated as follows, as fully developed in [2]:

$$\Delta G_{e,b} = p_2 \Delta G_{Ms,b} \quad \textit{Eq. 47}$$

where p_2 is a proportionality factor $p_2 = 0.7$ (which can be adjusted) and $\Delta G_{Ms,b}$ is the increase of the driving force required to initiate martensite formation as a consequence of prior bainite formation. It is calculated with:

$$\Delta G_{Ms,b} = -\Gamma_m \frac{\ln(1-f)}{\beta_{Ms,b}} \quad \textit{Eq. 48}$$

Where Γ_m is equal to 7.22 J.mol^{-1}.K^{-1} and $\beta_{Ms,b}$ is calculated with:

$$\beta_{Ms,b} = [p_C(T - M_S) + 1]\alpha^m \quad \textit{Eq. 49}$$

Where α^m is the parameter related to law of Koistinen-Marburger for martensitic formation [34], [35].

Where p_C is a proportionality factor is calculated using:

$$p_C = 0.051 - 0.044[1 - exp(-3x_C)] \quad \textit{Eq. 50}$$

Where x_C is the carbon concentration in wt.%.

II.3. Overall transformation kinetics

The overall transformation kinetics can be calculated by combining the nucleation and growth equations as (Eq. 51):

$$\frac{df}{dt} = (1-f)(1+\lambda f)\nu^* \frac{6N_S}{d^\gamma} V_n \left(\frac{\Gamma_B(B_{S*} - T)}{G_{e0} + \Delta G_{e,b}}\right) exp\left(-\frac{K_1 \Gamma}{R}\right) exp\left(\frac{-Q_b}{RT}\right) \quad \textit{Eq. 51}$$

One can notice that the volume of the bainite lath (V_b) no longer appears in the equation. On the contrary, V_n the nucleus volume appears explicitly, because of the newly introduced growth factor, B_g. In the model of [2] V_n is assumed constant, as mentioned previously. The growth factor B_g is a dimensionless factor (and is smaller than the unit because $V_n \ll V_b$). The growth factor B_g is proportional to the $\frac{V_n}{V_b}$ ratio, since a larger V_b corresponds to a large glissile interface movement during the displacive growth from the critical nucleus (with a volume V_n) and thus the strain hardening of the surrounding matrix is more important, which opposes the transformation, as Van Bohemen exposed in his paper [2] according to [3], [30].

II.4. Model data

The computation of thermodynamic parameters (driving force $\Delta G^{\gamma\to\alpha}$, maximum driving force ΔG_m) was done by using the TCFE9 database from Thermocalc software, by considering the FCC and BCC phases of the database. Only the main alloying elements (C, Mn, Si and Cr) were considered in the calculations for the sake of simplification. It was checked that the other alloying elements with lower concentration have a weak influence on these thermodynamic properties. Figure. V. 3 shows the driving forces $\Delta G^{\gamma\to\alpha}$ and ΔG_m as a function of temperature, considering that the austenite has the initial carbon concentration of the steel, 0.27 wt.%. For temperatures below B_S (noted $B_{S,0}$) temperature, a linear approximation could be done without significant discrepancy. The slopes of the linearized curves, denoted Γ_B (Eq. 35) and Γ (Eq. 30) respectively, are also parameters of the model, and the intersections with the temperature axis are denoted T_2 and T_3 respectively. As will be explained later, the model of [2] will be used to consider the effect of the enrichment in carbon of the austenite during the bainite transformation. Hence, the driving forces $\Delta G^{\gamma\to\alpha}$ and ΔG_m were calculated as a function of the carbon concentration in austenite (up to 7 at.%). More specifically, the parameters Γ_B, Γ, T_2 and T_1 were tabulated as a function of the carbon concentration in austenite. Figure. V. 3 shows some examples of the effect of carbon concentration in austenite on the driving forces.

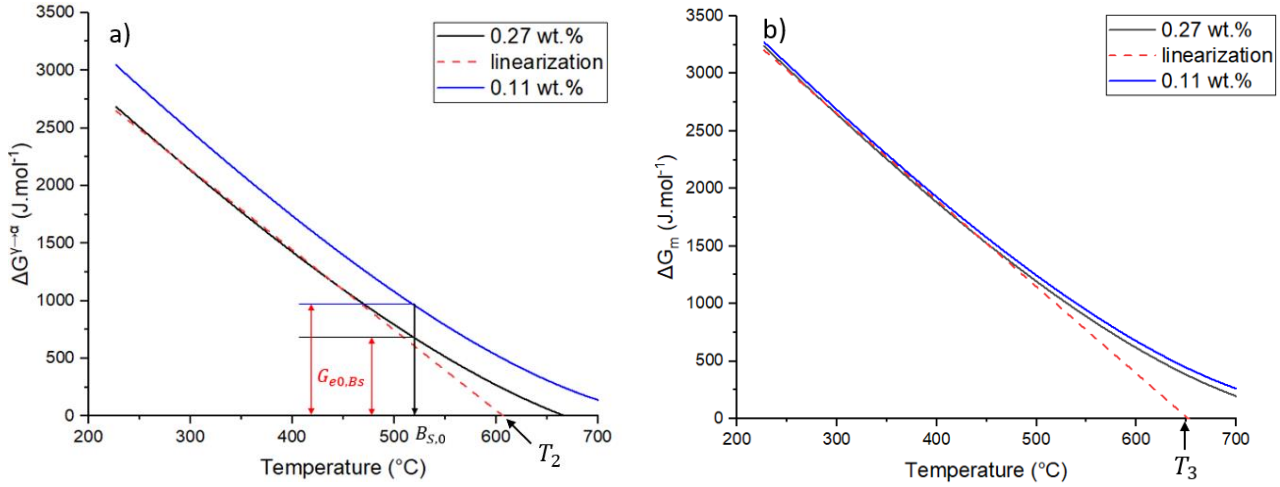

Figure. V. 3: a) Driving forces $\Delta G^{\gamma\to\alpha}$ and b) ΔG_m as a function of temperature (continuous lines: black curve corresponds to the 0.27 wt.% and blue curve corresponds to the 0.11 wt.% carbon composition) and proposed linear models (dotted red lines) according to the equations.

Microstructural parameters of the model are related to the nucleation of the bainitic ferrite on the prior austenite grain (PAG) boundaries: these are the austenite grain size d^{γ} and the number of nucleation sites per unit surface of PAG boundary, N_S (Table 13). The former is known from experiment (see Chapter IV, Section I.1.). The latter is assumed to be constant, like in [2], and as discussed in previous Section I.2.. In the same manner, the volume of the critical nucleus V_n and the nucleation attempt frequency ν^* are assumed constant. The values of N_S , V_n and ν^* are taken from [2].

Table 13: Parameters of the model.

Parameters taken from [2]	v^*	$1 \times 10^{13}\ s^{-1}$
	N_S	$1 \times 10^{16}\ m^{-2}$
	V_n	$2 \times 10^{-25}\ m^3$
	Z	6
Microstructural parameter	$d^\gamma (\mu m)$	74
Adjustable parameters	$K_1\Gamma$ (J.mol^{-1}.K^{-1})*	213
	Q_b^0 (kJ.mol^{-1})*	20
	$B_{S,0}$ (°C)*	520
	$G_{e0,Bs}$ (J.mol^{-1})*	670
	λ (part III.1.a)	100
	λ (part III.1.b)	125
	λ (part III.1.c)	200

**$K_1\Gamma$ and Q_b^0 are interrelated, as well as $B_{S,0}$ and $G_{e0,Bs}$.*

The parameters $B_{S,0}$, K_1 and Q_b^0 depend on the material. The temperature $B_{S,0}$ is not known with precision from our experiments. According to the TTT diagram established by Ascometal from dilatometry experiments (see Section I.1. in Chapter III), the possible range of $B_{S,0}$ is between 500 °C and up to 550 °C. A value of 520 °C was found to give the best agreement between simulations and experiments, as will be discussed in the Results Section. The $B_{S,0}$ temperature is associated with an important parameter of the model, $G_{e0,Bs}$, the elastic strain energy necessary to form the first laths of bainite (Eq. 36).

Parameters Q_b and K_1 are interrelated according Van Bohemen et al. [9] who have considered a wide range of alloy compositions to establish the following empirical relationship, whose parameters can thus be considered as material-independent:

$$Q_b = Q_d - K_1\Gamma T_d \qquad \textit{Eq. 52}$$

where Q_d = 170 kJ.mol^{-1} and T_d = 705 K. This relationship is represented in Figure. V. 4, reproduced from [9]. As discussed in [9], this relationship leads to an expression of the activation energy for nucleation Q^* (Eq. 17) which is in good agreement with Olson and Cohen's theory [7], [36], [37] for the nucleation of martensite involving the dissociation of dislocations and later adapted for bainitic ferrite nucleation [3].

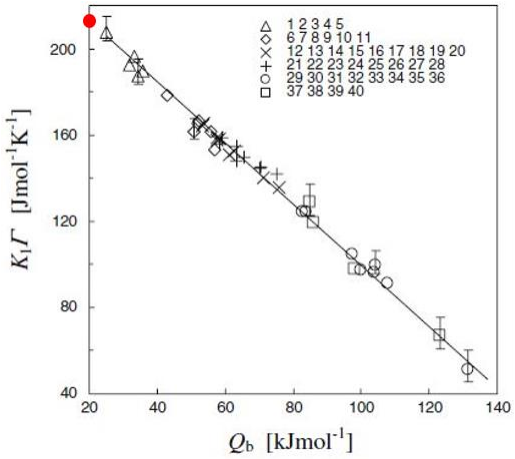

Figure. V. 4: Values of $K_1\Gamma$ as function of Q_b (points) from [9] and current study (red points), $K_1\Gamma$ = (170 kJ.mol^{-1}-Q_b)/(705K) (line).

As explained in [9], the couple of parameters Q_b and K_1 can be selected on the basis of the TTT diagram of the alloy and more specifically thanks to the transformation start curves, as illustrated in Figure. V. 5, reproduced from [9]. The parameter K_1 shifts the C curves towards shorter or longer times, independently on the temperature, whereas the effective nucleation driving force Q_b gives the temperature dependence. (These effects can also be seen in Eq. 52). The higher Q_b is, the longer is the time of transformation start below the "nose temperature".

As discussed in next Section, we will use the model of [2] to estimate the effects of a carbon enrichment of austenite upon the bainite transformation. The apparent activation energy Q_b will increase with increasing carbon content of the austenite. In the following, we define Q_b^0 as its value before the start of the transformation (i.e. when the austenite composition is equal to the nominal carbon content of the steel). Notations $Q_b\left(x_C^\gamma\right)$ or Q_b stands for its value which will increase with the enrichment in carbon. Due to the variation of Q_b, the product $K_1\Gamma$ will also decrease, because we assume that the empirical (Eq. 52) remains fulfilled. For the sake of simplicity, no specific notation is used for the initial value of $K_1\Gamma$ and its evolution.

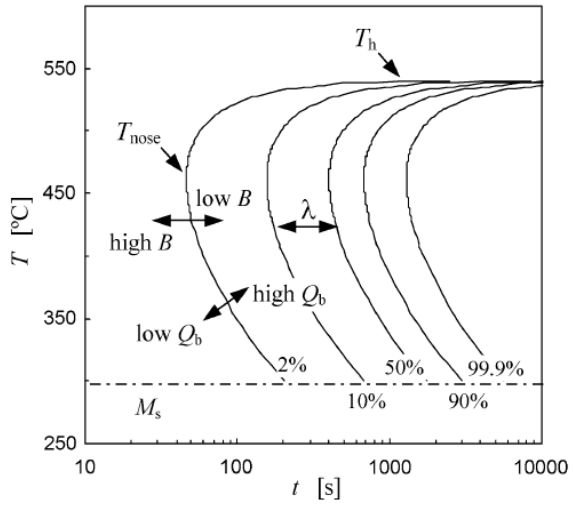

Figure. V. 5: TTT diagram showing the effect of B($\propto exp\left(-\frac{K_1\Gamma}{R}\right)$), λ and Q_b on the transformation times (reproduced from [9]).

In this study, we have chosen to select the value of the apparent activation energy Q_b^0 on the basis of our experimental TTT diagram. The latter, obtained by dilatometry experiments, is plotted in Figure. V. 6 a). One reminds that the kinetics at short times could not be established by HEXRD, because of the issue of the large austenite grains (see Chapter III). The TTT diagram shows that the transformation rate increases with decreasing transformation temperature. There is actually no identifiable "nose temperature", which seems lower than the M_S of the steel, 346 °C. Good agreement with the experiments was thus found with parameters Q_b^0 = 20 kJ.mol^{-1} and $K_1\Gamma$ = 210 J.mol^{-1}.K^{-1}.

The corresponding times for 2 %, 10 % and 50 % of transformation progression are represented in Figure. V. 6 b). To compute these times, isothermal treatment simulations were performed by using the version of the model of [2] that will be presented in Section III.1.a. and the parameters mentioned above (The autocatalysis nucleation parameter λ has not yet been discussed, but it has a weak influence on the 2 % and 10 % transformation times). With this value of Q_b^0, the calculated TTT diagram has a shape in agreement with the experiment, with decreasing transformation times for decreasing temperature. (Note that at this stage, we only consider the shape of the TTT diagram, not the exact transformation times). The selected values of Q_b^0 and $K_1\Gamma$ are represented in Figure. V. 4, along with the values established by Van Bohemen for other steels. It can be seen that the pair of values Q_b^0 and $K_1\Gamma$ that we selected is inside the range established in [9], but at one extremity corresponding to lowest values of Q_b. This low value of Q_b^0 for our studied steel is related to the shape of the experimental C curves, which is different from most of the steels investigated in [9]. Indeed, most of the latter exhibited a more pronounced "C shape" with a well-identifiable "nose", and increasing transformation times for decreasing temperature (like e.g. in Figure. V. 5). Let us mention that an empirical formula was established in [9] to compute Q_b as a function of the steel composition. For the studied steel, it gives a value of 55 kJ.mol^{-1}, which is far higher than the one that we used. If assuming this value of Q_b^0, the shape of the TTT diagram would be far from our experiments, as represented in Figure. V. 6 b) (red lines).

As explained in [9], the temperature corresponding to the "nose" of the bainite's C curve can also be evaluated with the formula:

$$T_{nose} = -\frac{Q_b}{2R} + \frac{1}{2}\sqrt{\left(\frac{Q_b}{R}\right)^2 + 4\frac{Q_b}{R}T_h} \qquad \textit{Eq. 53}$$

By assuming Q_b = 20 kJ.mol^{-1} , this yields a T_{nose} value of 369 °C. Although the experimental value of T_{nose} is not clearly identifiable from our experiments, this value does not contradict our data on kinetics. In contrast, the value of T_{nose} found if assuming that Q_b = 55 kJ.mol^{-1} is equal to 446 °C, which is much too high, in view of our experimental TTT diagram.

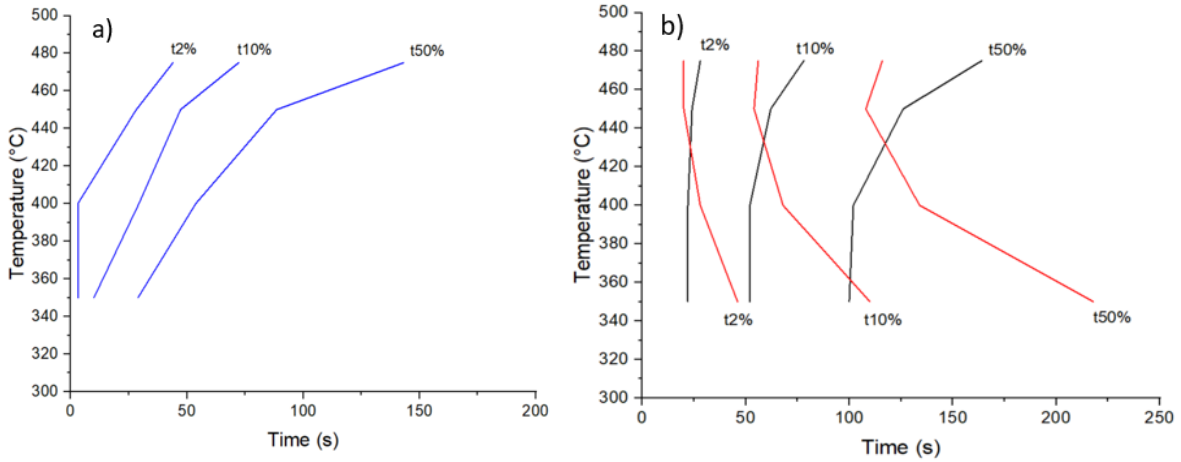

Figure. V. 6. a) TTT diagram of the studied steel according to the dilatometry experiment; b) Calculated times for 2 %, 10 % and 50 % of bainite transformation progression (normalized on max ferrite fraction) according to the simulation and considering an initial value of Q_b of 20 kJ/mol (black lines) or 55 kJ/mol (red lines).

As for the autocatalysis factor λ, a large range of values is reported in literature, from 3 to 500 [8,10,15]. As we have shown in the previous part (I.3.), λ depends on the temperature, the steel carbon composition, the dislocation density, the type of bainite formed (upper or lower bainite) and the prior austenite grain size [20]. Currently, λ cannot be calculated on physical grounds, and only trends could be established in literature.

In view of our microstructural observations (Chapter IV), we could have assumed an increase of λ with decreasing transformation temperature as proposed by Van Bohemen [2], [20]. Indeed, we observed a transition from upper to lower bainite at ca. 450 °C, a decrease of the bainite lath thickness with decreasing transformation temperature and we detected carbides only at low temperatures (Chapter IV). However, we chose to keep λ constant, because we want to assess the ability of the model of [2] to capture the influence of temperature. So, we have not considered, as many authors do, λ as a free adjustment parameter. Keeping λ constant will also simplify the analysis of the influence of the temperature. λ values ranging between 100 and 200 will be used in the successive versions of the model.

To conclude on the model parameters, one can notice that only three of these are adjustable: the temperature $B_{S,0}$ which is not known with precision from experiment, the initial value of the apparent activation energy Q_b^0 and the autocatalysis nucleation parameter λ. All others either come from thermodynamic data ($\Delta G^{\gamma\to\alpha}$, ΔG_m), from experiment (austenite grain size d^γ) or are assumed constant (N_S, ν^*, V_n) with values found in the literature.

II.5. The consideration of the carbon enrichment of the austenite

As shown in Chapter III, the austenite gets enriched in carbon during the bainite transformation. We will investigate in this study how the model introduced in [2] can take account of this enrichment in carbon, although the model has been applied so far mostly to low-Si steels (i.e. with carbide precipitation). An important focus of our work has been to systematically investigate the effect of this enrichment through the model, in relation to the experimental results.

First, the rate at which the austenite gets enriched in carbon has to be estimated. As presented in Chapter III, a simple mass balance, where the carbide precipitation is neglected, can be used:

$$x_C^0 = x_C^\alpha f + x_C^\gamma (1 - f) \quad \textit{Eq. 54}$$

where x_C^0 is the nominal carbon content in the steel, x_C^α and x_C^γ are respectively the carbon content in bainite and austenite and f is the fraction of bainite. For simplicity, it is assumed that the ferrite and austenite phases have the same density and the same molar volume.

The carbon content in bainitic ferrite (Table 14) is considered as directly dependent to the transformation temperature and to be constant during isothermal treatments, as shown by HEXRD experiments (Chapter III). Conversely, for continuous cooling treatments, a constant mean value of 0.12 wt.% is considered, also on the basis of experiments (CC_0.1, CC_0.3 and CC_0.5).

Table 14: Bainitic ferrite carbon content (x_C^α) as a function of function of treatments determined by HEXRD.

Treatment	ISO_350	ISO_400	ISO_450	ISO_475	CC_0.1 CC_0.3 CC_0.5
Bainite carbon content (wt.%) x_C^α	0.15	0.14	0.11	0.09	0.12

Another way will be to consider directly the experimental data, while knowing the limits discussed in Chapter III (i.e. the possible heterogeneities of composition).

The enrichment of austenite in carbon will have several impacts on the rate equation. A slow-down of the kinetics will occur, firstly because of the increase of the bainitic ferrite nucleation barrier Q^*. This effect is evaluated with the following equation, deduced from (Eq. 17) and (Eq. 52) (see [2], [9]):

$$Q^* = Q_b + K_1 \Gamma T \quad \textit{Eq. 55}$$

Upon carbon enrichment, Q_b will become higher than its initial value Q_b^0, corresponding to the initial carbon content of the austenite, as explained above. Meanwhile, $K_1\Gamma$ will decrease because, as mentioned above, we assume that Q_b and $K_1\Gamma$ remain interrelated by the empirical (Eq. 52).

For an isothermal transformations, the impact of the former will be the highest and Q^* will increase. The influence of the carbon concentration on the effective activation energy Q_b is estimated as follows:

$$Q_b(x_C^\gamma) = Q_b(x_C^{\gamma 0}) + 89.10^3 (x_C^\gamma - x_C^{\gamma 0}) \quad \textit{Eq. 56}$$

This formula is based on the empirical formula established in [9] to calculate Q_b as a function of the steel composition, which includes the effect of carbon. Although this formula did not give a value of $Q_b(x_C^{\gamma 0})$ in good agreement with our TTT diagram (see previous Section), it is assumed that it allows

to take account of the carbon concentration increase in the austenite. The factor $K_1\Gamma$ is then calculated during the transformation as a function of Q_b by using the material-independent relationship [9]:

$$K_1\Gamma = \frac{(Q_d - Q_b)}{T_d} \qquad \textit{Eq. 57}$$

The bainite transformation will slow down upon carbon enrichment of the austenite also because of the decrease of the growth factor B_g determined using (Eq. 39). In [2] B_{S*} represents the value of B_S which is decreased due to mechanical stabilization effects. We now consider the enrichment in carbon as an additional source of austenite stabilization. Eq. 41 is thus reformulated as follows:

$$\Delta B_S = \Delta B_{S,C} + \Delta B_{S,\sigma} + \Delta B_{S,b} \qquad \textit{Eq. 58}$$

where $\Delta B_{S,\sigma}$ and $\Delta B_{S,b}$ have been defined above. The decrease of Bs due to carbon enrichment is estimated as:

$$\Delta B_{S,C} = \frac{\left(\Delta G^{\gamma\to\alpha}\left(x_C^{\gamma 0}\right) - \Delta G^{\gamma\to\alpha}\left(x_C^{\gamma}\right)\right)}{\Gamma_B} \qquad \textit{Eq. 59}$$

where $\Delta G^{\gamma\to\alpha}\left(x_C^{\gamma 0}\right)$ and $\Delta G^{\gamma\to\alpha}\left(x_C^{\gamma}\right)$ are the driving force in austenite having the initial carbon content and the current (higher) carbon content, respectively. The computation of $\Delta G^{\gamma\to\alpha}$ was presented above. Upon bainite transformation, B_{S*} will decrease until it reaches the transformation temperature, *T*. Once achieved, it means that the bainite transformation has reached its stasis according to the model.

Let us mention finally the model parameters for which we assume no dependency to the carbon concentration: N_S, the number of nucleation sites per unit surface of austenite grain boundaries and V_n, the volume of the critical nucleus. This assumption is in line with [2], where no variation was also assumed (but in this study, carbon enrichment of austenite was not considered). The elastic energy of first-formed bainite, $G_{e0,Bs}$ could also depend on the carbon concentration in austenite, as it impacts the phase transformation strain (different values of $G_{e0,Bs}$ for various steel compositions are reported in [2]). For the sake of simplicity, this parameter is assumed to be constant.

The mechanical stabilization effects will also be modified because of the enrichment in carbon of the austenite. The dependency to carbon concentration of the parameters related to mechanical stabilization is already presented in [2], [35].

II.6. Conclusion

The model which will be used for the simulations is essentially the one introduced by Van Bohemen in reference [2]. We extended this model to take account of the austenite enrichment by the carbon, which decreases $\Delta G^{\gamma\rightarrow\alpha}$ and also modifies some model parameters. (One can mention that in ref. [2], this model was used to consider a high-Si steel, but without detailing how the effect of carbon is accounted for).

Let us summarize the main differences between this model and the previous ones from the literature. First one concerns the growth factor B_g, which takes account of how the available driving force for displacive growth ($\Delta G^{\gamma\rightarrow\alpha}$) is consumed by mechanical stabilization effects. This factor is actually introduced without detailed physical justification. (For example, B_g should increase with ΔG_{net}, so it is assumed that B_g is proportional to ΔG_{net}). But its advantage is to include all origins of the austenite stabilization (chemical, mechanical), which can cause the stasis phenomenon, at the center of our study. Another difference regards how the density of nucleation sites at the prior austenite grain boundaries (N_S) is handled. In [2], it is assumed to be constant, whereas previous simulation works assume that this density increases linearly with the undercooling below B_S (Magee's assumption, see Section I.2.). In fact, the model of [2] keeps the linear dependence of the nucleation rate with the undercooling, because of the growth factor B_g (see Eq. 39). But instead of being related to the nucleation stage like in previous works, this linear dependence with the undercooling is now related to the displacive growth stage. Final difference regards the definition of the B_s temperature. In [2], it is the temperature at which the growth factor B_g is equal to zero, i.e. when $\Delta G^{\gamma\rightarrow\alpha} = G_{e0,Bs}$. Hence, it is a criterion related to the displacive growth stage. Conversely, in previous similar models, B_s is related to the nucleation stage, via the relationship $\Delta G_m = G_N$ (cf. Eq. 15). This latter relationship is actually never used in the model of [2].

Despite these differences with previous simulations works, we think that the way in which the growth factor B_g was introduced is relevant. At least numerically, this model is expected to behave like the previous ones from literature (proportionality of nucleation rate with undercooling, stasis when $\Delta G^{\gamma\rightarrow\alpha}$ reaches some critical value…). Finally, as mentioned, this model and its parameters were assessed and calibrated by using an experimental database covering a large variety of steel compositions [2], [8], [9], [20], which gives confidence on its predictions.

III. Results

The purpose of the simulation study presented in this section is to examine how the model introduced in [2] can be used to predict the effects of austenite enrichment in carbon as well as the effect of mechanical stabilization on the slow down of the bainite transformation kinetics and its stasis. We will consider first isothermal treatments in order to investigate the influence of the transformation temperature (between 350 °C and 475 °C). Continuous coolings at rates from 0.1 °C/s to 0.5 °C/s will then be discussed. The results will be compared to the experimental kinetics obtained using HEXRD (cf. Chapter III).

III.1. Isothermal treatments

In this part, we will present the simulation results regarding isothermal treatments. The effects of the stabilization by the carbon and of mechanical stabilization will be considered successively, thus separately. The reason is that most models of bainite transformation in literature do not consider mechanical stabilization effects.

In a first stage, the effect of austenite stabilization by the enrichment in carbon alone will be considered (parts III.1.a and III.1.b), before adding the mechanical stabilization effects (part III.1.c). Two different methods will be used successively, in parts a and b, to estimate the evolution of the carbon concentration in austenite. On the whole, three sub-versions of the model will be considered, in parts III.1.a, III.1.b and III.1.c..

III.1.a. Austenite chemical stabilization: carbon partition estimated by mass balance

In this section, the model of [2] is simplified by suppressing the effects of mechanical stabilization. This means that the elastic strain energy necessary to form a new bainite lath will remain equal to $G_{e0,Bs}$, its value for the first bainite formed at temperature $B_{S,0}$. (Note that $G_{e0,Bs}$ does not depend on temperature). The growth factor B_g then reduces to (Eq. 60):

$$B_g = \frac{V_n}{V_b}\left(\frac{\Gamma_B(B_{S*} - T)}{G_{e0,Bs}}\right) \qquad \textit{Eq. 60}$$

The values of B_{S0} and $G_{e0,Bs}$ are given in Table 13.

The calculation of B_{S*} as a function of the carbon enrichment of austenite is presented in Section II.2.. In this section, the evolution of carbon concentration in austenite is estimated by applying a mass balance (Eq. 54). It was shown in Chapter III that this mass balance is well verified at the end of the isothermal treatments, but not necessarily at the beginning due to the heterogeneous distribution of carbon. We assume here that it is also the case during the whole duration of the bainite transformation (no carbide, homogenous distribution of carbon). To calculate the mass balance, it is assumed that the carbon concentration in bainitic ferrite is constant during isothermal treatments. The experimental values are given in Table 14.

Figure. V. 7 shows the simulated bainite transformation kinetics at 350, 400, 450 and 475 °C respectively (above M_S). For all temperatures, the calculated curves show the same stages: a sluggish start followed by fast kinetics, then a progressive slow down and finally a stasis. These stages are consistent with the experimental behaviors.

For increasing temperature, the kinetics decreases and the final fraction of ferrite decreases. This effect of temperature on kinetics comes in part from the low initial apparent activation energy Q_b^0 of 20 kJ/mol that we selected, which allows to predict lower times of transformation start with decreasing temperature (Section II.4.). The acceleration of the kinetics for decreasing temperature also comes from the increase of the driving force $\Delta G^{\gamma\to\alpha}$ (and hence of the growth factor B_g) and the decrease of the nucleation barrier Q^*. Let us remind that we kept the autocatalytic nucleation parameter λ independent on temperature, in order to observe more easily the influence of the temperature on the model predictions. In these simulations, a value of λ = 100 is used.

For all temperatures, the final slow-down of the kinetics is due to the enrichment in carbon of the austenite, which increases the nucleation barrier $Q^*$and decreases the growth factor B_g. The decrease of B_g down to zero is the dominant factor, whereas Q^* undergoes a weak increase, whatever the temperature. The stasis is reached when the actual B_S temperature, B_{S*} , approaches the transformation temperature, i.e. when the driving force $\Delta G^{\gamma\to\alpha}$ approaches $G_{e0,Bs}$, the elastic energy necessary to form a bainitic ferrite lath. As the driving force increases with decreasing temperature, the final fraction of ferrite increases, as well as the final enrichment in carbon of the austenite. The latter is represented in Figure. V. 7 for each temperature, along with the T_0 and T_0' (400 J/mol) curves. The points are superposed to the T_0' curve corresponding to strain energy of 670 J/mol. This version of the model actually stops the bainite transformation in agreement with the T_0' criterion [4], except that the elastic energy is equal to $G_{e0,Bs}$ (670 J/mol), instead of the more usual value of 400 J/mol.

Figure. V. 7 also shows the experimental bainite transformation kinetics obtained by HEXRD experiments and presented in Chapter III. Due to the repeatability issues which occurred at 450 °C and 475 °C, three experiments are presented for each of these temperatures. The kinetics and the plateaus are well predicted by the model at 450 °C and 475 °C, but these are underestimated at 350 °C and 400 °C. These discrepancies are better seen at shorter times (Figure. V. 7 b). In agreement with the too low plateaus predicted at 350 °C and 400 °C, the final carbon concentrations in austenite predicted are underestimated at these temperatures, compared to the experiment (Figure. V. 7 c). The agreement seems better at 450 °C and 475 °C, although the experiments show some scatter, especially at 450 °C.

These simulations show that this version of the model is not able to capture accurately the influence of the temperature in the range considered, 350-475 °C. This does not come simply from the adjustable parameters ($B_{S,0}$, Q_b, λ) that we selected. Parameter Q_b is linked to the start C curve of studied alloy's IT diagram, and cannot really be changed. By increasing $B_{S,0}$, it would have been possible to obtain a better description of the kinetics at temperatures 350 °C and 400 °C but in such case, the kinetics and the plateaus at 450 and 475 °C would have been overestimated. Moreover, the corresponding value of $B_{S,0}$ would be unrealistically high, at about 650 °C. We could also have chosen a specific value of the autocatalytic nucleation parameter λ for each transformation temperature, as was done in previous studies [2], [8], [9], [20]. In fact, λ probably increases with decreasing temperature (higher density of nucleation sites due to finer bainite laths, more dislocations due to plastic accommodation [2]). But

changing the values of λ would not have changed the values of the plateaus, even if it would have improved the global kinetics.

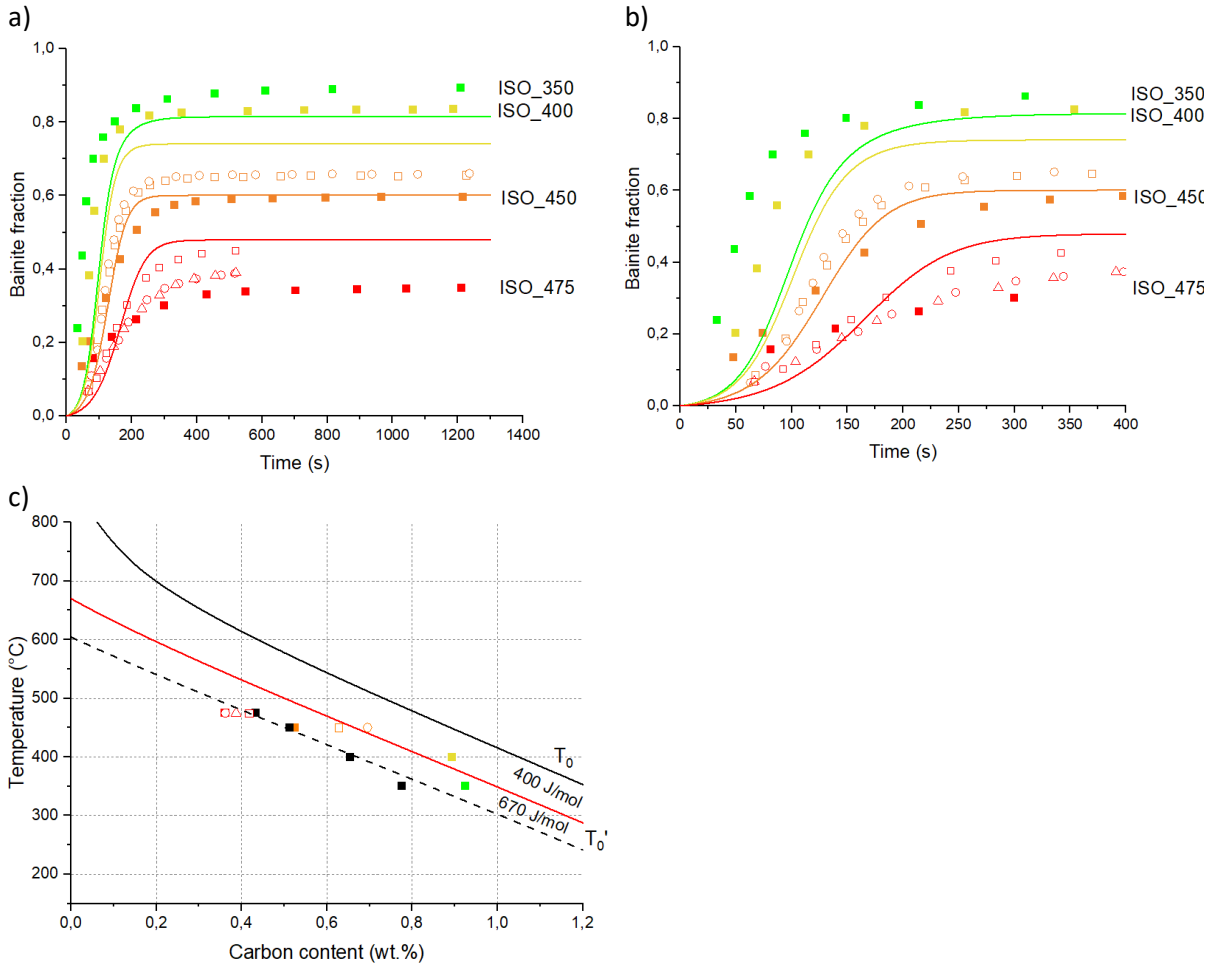

Figure. V. 7: a) Bainite transformation kinetics according to simulation (continuous lines) and HEXRD experiments (dots), during isothermal transformation at 350 °C (green), 400 °C (yellow), 450 °C (orange), 475 °C (red). b) Same as a) with zoom on shorter times; c) Carbon content in austenite at the end of isothermal holdings, for each transformation temperature, according to experiment (colored squares) or the simulation (black squares), along with T_0 curve and T_0' curves for elastic strain energy in ferrite 400 J/mol or 670 J/mol. (Note that in figure c, some symbols are superimposed).

The discrepancies between simulations and experiments in present work are rather unexpected, in view of the nearly perfect agreement which is presented e.g. in reference [2] regarding simulations on a large number of other steels, including one high-Si steel. These are not though to come from the mechanical stabilization effects that we suppressed in this Section. Indeed, a very good match between simulation and experiment is possible without these effects and over a large range of temperatures, as shown by the simulations in [8], where a previous version of this model was used.

As the main modification we brought to the model regards the effect of austenite enrichment in carbon, the origins of the discrepancies may be found in this part of the model. Reference [2] provides the data and equations necessary to take account of the carbon concentration in austenite, as elaborated in Section II.5.. However, there are more uncertainties about the rate at which the carbon actually

partitions from bainitic ferrite to austenite. In the simulations presented above, we estimated the carbon concentration in austenite with the mass balance (Eq. 54). This assumes that the carbon is immediately rejected into austenite by the forming bainitic ferrite (which remains supersaturated, see Table 14) and that the carbon concentration in austenite is homogenized by diffusion in a very short time. This approach gives an upper limit of the carbon concentration in austenite. Although the carbon content evolutions in austenite were presented in Chapter III, the mass balance that we used was verified only at the end of the isothermal treatments. We need to consider now whether or not the mass balance is verified for the whole duration of the bainite transformation.

Figure. V. 8 compares the experimental (continuous lines) and the calculated (dashed lines, according to the simulations presented above) austenite carbon content evolution during isothermal holdings at 350 °C, 400 °C, 450 °C and 475 °C. The discrepancies between the simulations and the experiment are significant, regarding both kinetics and plateau values. These come in part from the discrepancies regarding the ferrite fractions discussed previously. But it seems that at 350 °C and 400 °C, the carbon partitions more slowly than predicted by the mass balance. Even if this can be explained in part by the precipitation of carbides at 350 °C, the kinetics of carbon partitioning should be modified in the model.

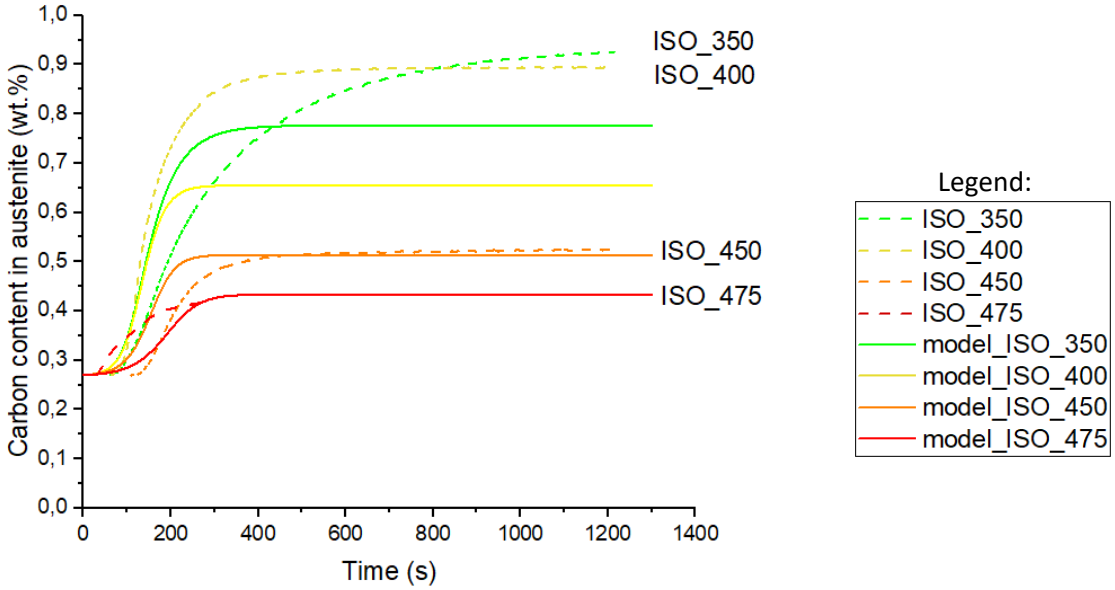

Figure. V. 8: Evolution of austenite carbon content obtained experimentally (dashes) and by a simple carbon mass balance in the model (lines).

Figure. V. 9 a) shows the carbon concentration in austenite as a function of the bainitic ferrite mass fraction according to the HEXRD experiments for the four transformation temperatures. These evolutions are compared with the evolutions which would have occurred if the mass balance (Eq. 54) had been verified. (There is one calculated curve for each temperature, because of the bainitic ferrite carbon content, which depends on temperature, see Table 14). One can clearly see that at 400 °C and 350 °C, the experiment shows a strong delay compared to the prediction from the mass balance. At 400 °C and 350 °C, the carbon concentration in austenite starts to increase only once about 60 % and 70 % of ferrite has formed, respectively. In contrast, at 450 °C and 475 °C, the carbon mass balance seems to give a better estimate of the actual carbon concentration in austenite (Figure. V. 9 b)). At 450 °C, the carbon concentration actually goes beyond the mass balance, although the latter should give an upper limit.

There can be several origins for the slower carbon partitioning at low temperature. First one is the time necessary for carbon to diffuse out the bainitic ferrite into the austenite. However, the nearly constant c/a ratios presented in Chapter III (Figure. III. 8) suggest that this partition occurs in a short time after the formation of each bainitic ferrite lath. Other HEXRD in situ studies of bainite transformation suggest the same behavior [38]. Second origin can be the time necessary for carbon to diffuse in austenite. One can assume that at 350 °C and 400 °C, the austenite remains heterogeneous in a first stage, with the vicinity of bainite laths being enriched in carbon and the remaining keeping the initial carbon concentration. Such heterogeneities were put into evidence in Chapter III in the case of continuous cooling treatments (Chapter III, Section III.1.c.1), by showing the asymmetry of the austenite diffraction peaks. However, it must be mentioned that such asymmetries could not be observed clearly in the case of isothermal treatments. As mentioned in Chapter III, the first stages of austenite enrichment would not be detected because of the low fraction of enriched austenite. The eventual increase of the austenite cell parameter can come from two mechanisms: either the diffusion of carbon inside the austenite, or the transformation to ferrite of the poorer austenite. In this latter scenario, the average concentration in austenite would increase because the austenite which does not transform is the one which is the richest in carbon.

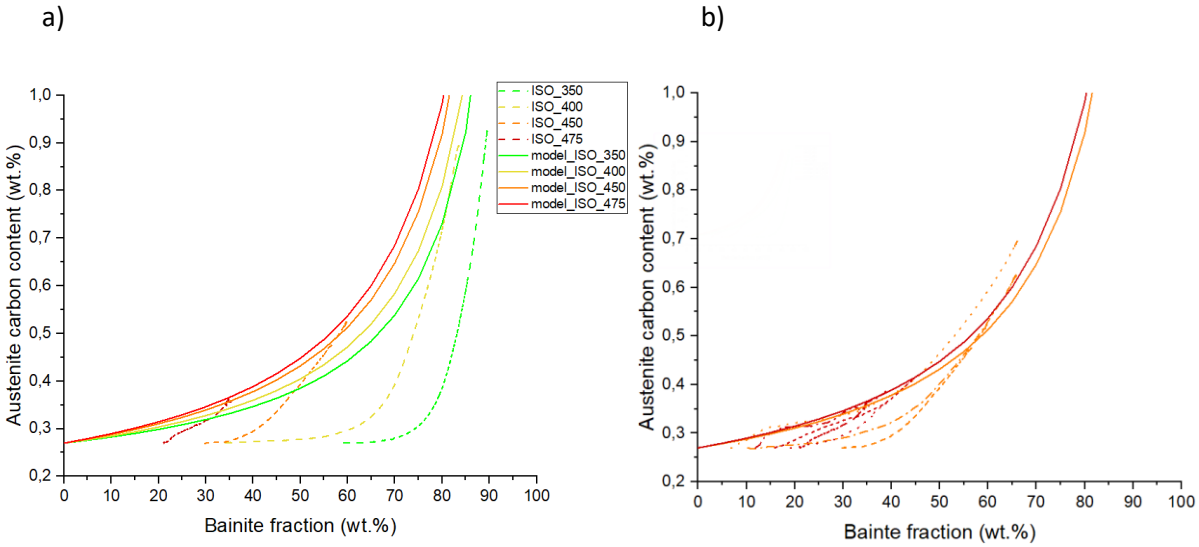

Figure. V. 9: Austenite carbon content as a function of the bainitic ferrite fraction according to HEXRD experiments (dotted lines) and calculated by assuming the carbon mass balance Eq. 54 (continuous lines). a) isothermal treatments at 475 °C, 450 °C, 400 °C and 350 °C; b) 475 °C and 450 °C, with three experiments for each temperature.

From these experimental results regarding the carbon partition/diffusion kinetics at 350 °C and 400 °C, it comes out that the version of the model presented above overestimates the rate of increase of the carbon concentration in austenite at these temperatures. This may explain why the kinetics, the plateau (Figure. V. 7 a-b)) and the final carbon concentration in austenite (Figure. V. 7 c)) are underestimated, whereas the predictions are correct at 450 °C and 475 °C. Indeed, a too fast increase of the carbon concentration will stabilize the austenite too early. In terms of model parameters, the driving force $\Delta G^{\gamma \to \alpha}$ and thus the growth factor B_g, which is the predominant factor influenced by the carbon concentration, will decrease too fast. In next section, the carbon content of austenite will be evaluated differently.

III.1.b. Austenite chemical stabilization: carbon partition estimated from HEXRD experiments

As shown in previous part (III.1.a.), the kinetics of carbon partition to austenite is overestimated at 350 °C and 450 °C, which leads to discrepancies between simulations and experiments. In this part, we will use the same model as in the previous part (i.e. mechanical stabilization effects are still suppressed), but the evolution of austenite carbon enrichment along the transformation will be directly imposed from experiment at 350 °C and 400 °C. One can mention that different studies were conducted in literature regarding carbon partitioning (see Section I.4.), but detailed modeling of this phenomenon is out of scope of present study. As for isothermal treatments at 450 °C and 475 °C, the carbon concentration in austenite is still estimated with a mass balance, as it gives partitioning kinetics in good agreement with the experiment.

Figure. V. 10 a) and b) show the simulated kinetics for the four isothermal treatment temperatures. At temperatures 350 °C and 400 °C, it can be seen that delaying the carbon partition largely increased the kinetics and the plateau values, compared to previous simulations. Looking more closely at the kinetics calculated at 400 °C, there is a sharp stop of the transformation at time 170 s. This behavior differs from simulations of previous section, where the kinetics slowed-down smoothly and progressively. This is due to the imposed the carbon concentration in austenite taken directly from experiments. At time t = 170 s, the decreasing driving force $\Delta G^{\gamma\rightarrow\alpha}$ becomes lower than $G_{e0,Bs}$. We impose then a value of zero to the growth factor B_g. In previous model version, the ferrite fraction and the carbon content of austenite were interrelated, making thus the growth factor B_g approach zero, but without ever reaching this value. The same sharp stop occurs at 350 °C at 428 s, but it is less visible in the calculated curve. In fact, the partition of carbon has been such strongly delayed that the ferrite fraction reaches almost 100 %, at 350 °C. At all temperatures, when the transformation stops, i.e. when $B_g = 0$ the carbon concentration in austenite is such that $\Delta G^{\gamma\rightarrow\alpha} = G_{e0,Bs}$. This is why the corresponding carbon concentrations are the same as those reported in previous section (Figure. V. 7 c)).

In this version of the model, the respective kinetics of ferrite formation and austenite carbon enrichment are now a priori independent. As a result, the time at which the stasis starts and the value of the final ferrite fraction plateau depend on the difference between both kinetics. This is why the values of the plateaus now depend on the autocatalytic parameter λ. Increasing it makes increase the rate of ferrite formation with respect to the rate of carbon partitioning. As a result, the plateau will be higher when increasing λ, whereas it was not the case in previous model's version.

Experimental ferrite fractions evolutions are also plotted in Figure. V. 10 a) and b). At 400 °C, the agreement between simulation and experiment is better than with previous model's version, thanks to the delayed enrichment in carbon of austenite, which has been imposed from experiments. But at 350 °C, the simulation predicts simultaneously a too slow kinetics and a too high value of the plateau. Hence, the reduction of the carbon partitioning rate was not sufficient to increase the nucleation rate of bainitic ferrite, but this reduction was too important to predict correctly the stasis. At the end of the transformation, the bainite nucleation was not sufficiently impeded by carbon enrichment.

It must be mentioned that, like in previous section, we kept the same value of the autocatalytic parameter λ in the temperature range 350-475 °C, in order to highlight the effects of temperature at the expense of a perfect description of kinetics. A value of 125 was chosen instead of 100, because as

explained above, λ has an influence on the calculated plateau, in present version of the model. This does not change much the predictions at 450 and 475 °C, which remain close to the experiments. In fact, with this version of the model, it seems not possible to describe simultaneously the kinetics and the stasis at the lowest transformation temperature, 350 °C.

These simulations highlight that an accurate knowledge of the carbon partition kinetics from ferrite to austenite is necessary to predict the bainite transformation kinetics and its stasis. Two concurrent kinetics have to be considered a priori separately: the one of bainite nucleation and the one of carbon partition. Contrary to what was assumed in previous section, both kinetics are not fully coupled (via the mass balance). In the example investigated here at 350 °C and 400 °C, carbon partition tends to be slower than ferrite nucleation. It was already visible from experiments: for example, at 400 °C, the stasis can be considered to be reached at ca. 267 s, whereas the carbon partition then goes on (i.e. Figure. III. 3, Figure. III. 12 and Figure. IV. 10). Regardless of the accuracy of the carbon composition measurements (discussed in Chapter III), this may put into question the assumption that we did, regarding the fact that the bainitic ferrite would release its carbon in a very short time into austenite. The increase of measured carbon content in austenite after the stasis could also come from the homogenization by diffusion of the carbon in austenite.

These results also allow to reconsider how to interpret the final carbon concentration in austenite reported in Figure. V. 10 c. Instead of the values measured long after the stasis, it would be more relevant to consider the values at the time when the stasis is reached. For example at 400 °C, the stasis occurs between 183 s and 267 s. The corresponding values of carbon concentration measured at these times are reported in Figure. V. 10 (with an horizontal error bar), and the same was done at 350 °C (the stasis occurs between 427 s and 576 s). It can be seen that the values are now better aligned in the full temperature range 350-475 °C, in agreement with the classical T_0' analysis (still considering an elastic energy in ferrite of $G_{e0,Bs}$ = 670 J/mol).

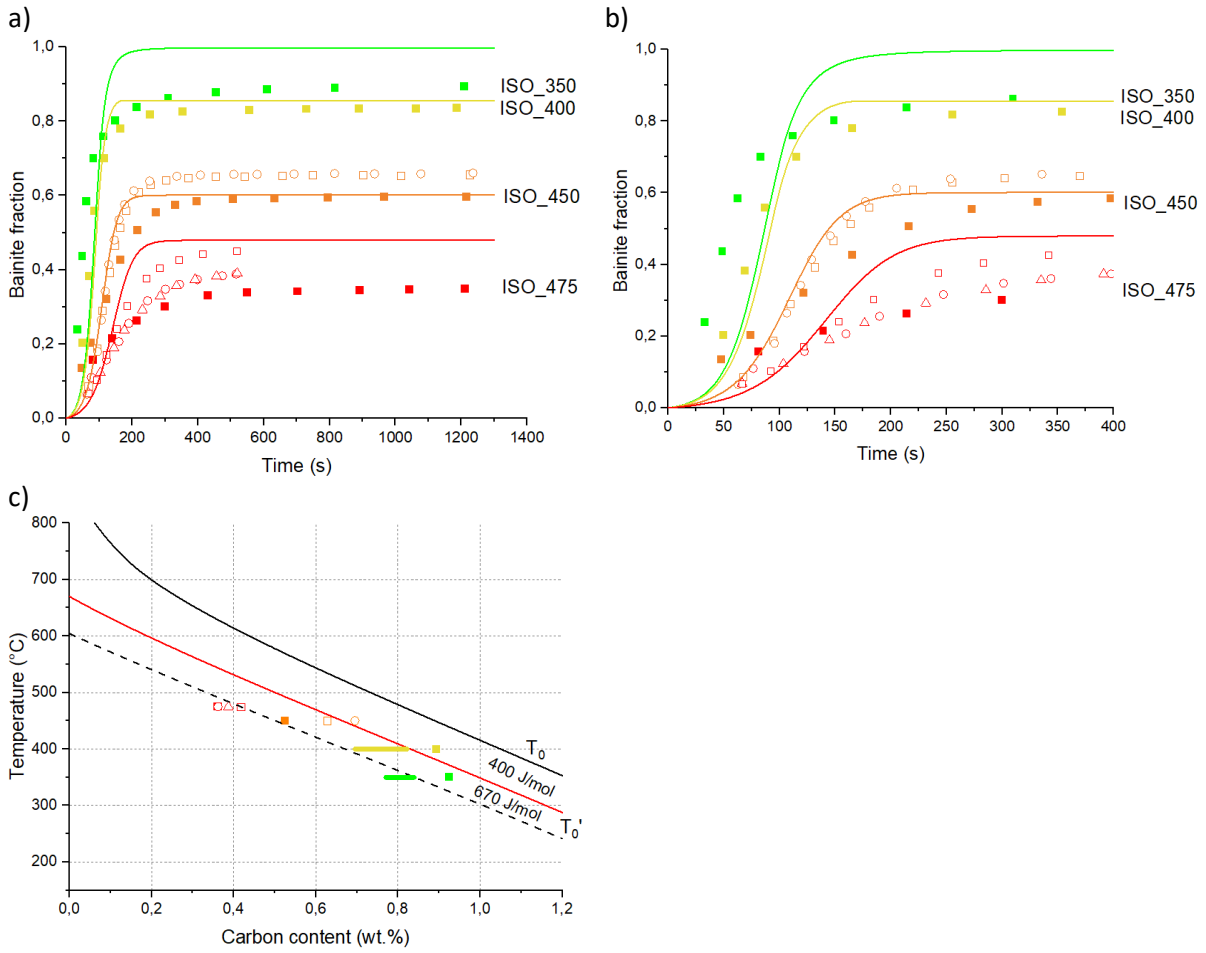

Figure. V. 10: a) Bainite transformation kinetics according to simulation (continuous lines) and HEXRD experiments (dots), during isothermal transformation at 350 °C (green), 400 °C (yellow), 450 °C (orange), 475 °C (red). b) Same as a) with zoom on shorter times; c) Carbon content in austenite at the end of isothermal holdings, for each transformation temperature, according to experiment, and at the stasis of bainite transformation at 400 °C and 350 °C (represented by horizontal bars), along with T_0 curve and T_0' curves for elastic strain energy in ferrite 400 J/mol or 670 J/mol.

To conclude on this part, this version of the model is able to predict isothermal bainite transformation kinetics in a larger temperature range (400-475 °C) than the previous version (450-475 °C), thanks to the introduction of a carbon partition kinetics in better agreement with the experiment. However, at 350 °C, no stasis is predicted because of the slower carbon partitioning introduced. In next section, mechanical stabilization effects will be considered in addition to the stabilization by the carbon.

III.1.c. Accounting of carbon partitioning and mechanical stabilization of austenite

In this section, the full model of [2] is considered, by adding the effects of mechanical stabilization to the effects of enrichment by the carbon. The growth factor is now calculated as follows:

$$B_g = \frac{V_n}{V_b}\left(\frac{\Gamma_B(B_{S*} - T)}{G_{e0,Bs} + \Delta G_{e0,\sigma} + \Delta G_{e,b}}\right) \qquad \textit{Eq. 61}$$

As recalled in Section II.2., two effects are accounted for, which increase the elastic energy necessary to form a bainitic ferrite lath: first one is the increase of the austenite yield strength with decreasing temperature ($\Delta G_{e0,\sigma}$). Second one comes from the dislocation strengthening and the geometrical constraints, gathered in $\Delta G_{e,b}$. The calculation of the actual B_S temperature, B_{S*}, also takes account of the mechanical stabilization (see (Eq. 40) and (Eq. 58)), in addition to the stabilization of austenite by the carbon. The calculation of $\Delta G_{e0,\sigma}$ and $\Delta G_{e,b}$ is recalled in Section II.2., as well as the influence of the carbon content in austenite. Like in previous section, the kinetics of carbon partitioning is directly imposed from the experiment at 350 °C and 400 °C, as it gave better comparisons between simulation and experiment than when using a mass balance. (At 450 °C and 475 °C, we always used a mass balance, because it gives a good agreement with the experiment). All the model parameters remain the same, apart from the autocatalysis parameter λ (= 200), which is still assumed to be the same at all temperatures.

Figure. V. 11 a) and b) show the kinetics obtained by the model with the addition of mechanical stabilization of austenite for all isothermal experiments. At all temperatures, the addition of mechanical stabilization effects leads to a slowdown of the kinetics and a reduction of the final bainite mass fraction on the plateau, compared to previous simulations. At 350 °C, a satisfactory outcome is the prediction of the stasis, in agreement with the experiment. Indeed, we showed in last section that the stabilization by carbon partitioning was not sufficient to explain the stasis, because the carbon partitions too slowly. However, the effect of mechanical stabilization seems too strong at 475 °C and even more at 450 °C. The effect on the kinetics is more difficult to comment as it depends in large part on the autocatalysis parameter λ, that we assumed to be constant.

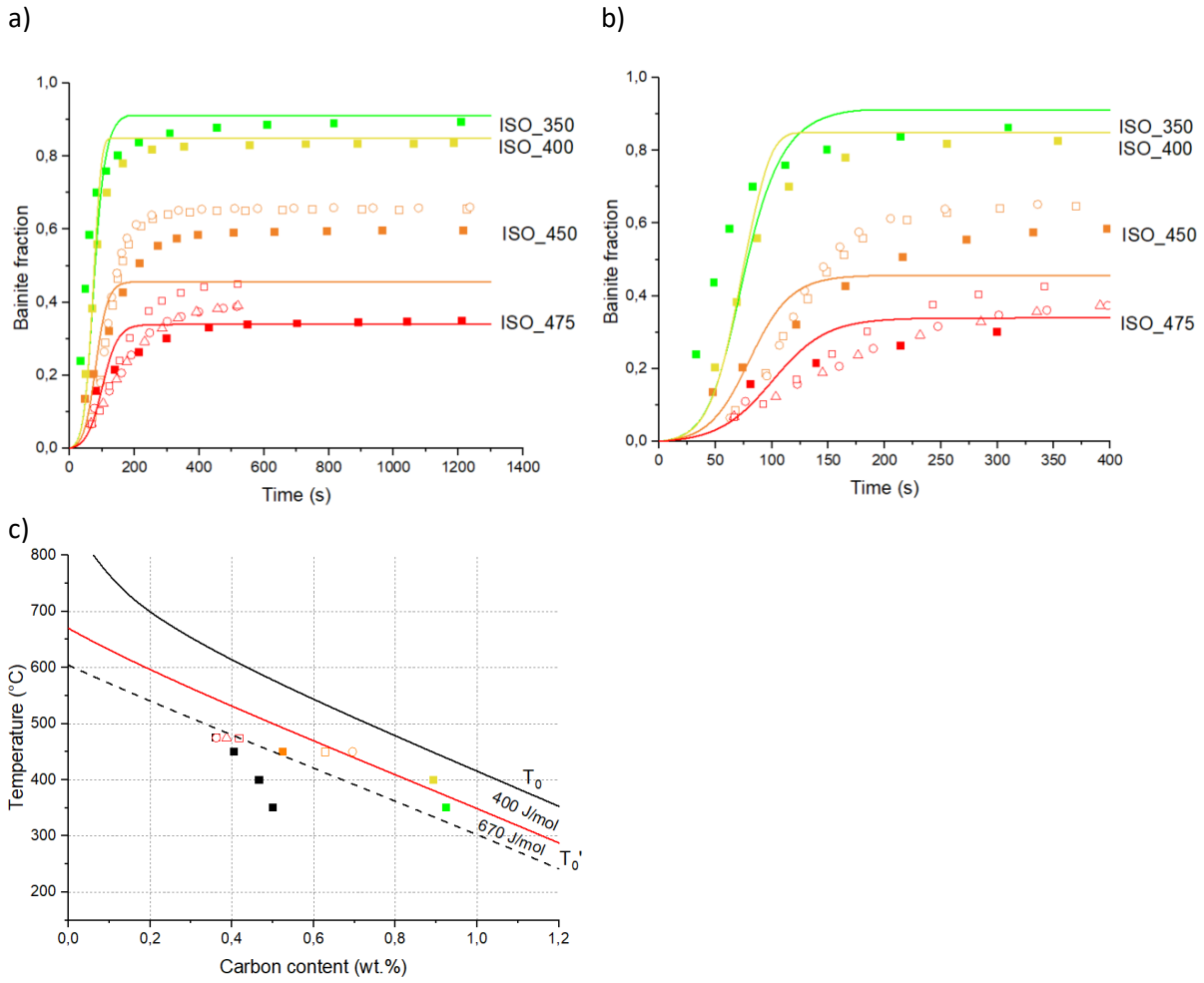

Figure. V. 11: a) Bainite kinetics in isothermal conditions: ISO_350 (green), ISO_400 (yellow), ISO_450 (orange), ISO_475 (red). Line models, dots experimental; b) Initial kinetics in short time of transformation c) Carbon content in austenite at the end of isothermal holdings: ISO_350, ISO_400, ISO_450 and ISO_475 (colored squares). Black squares results from the model when transformation stops.

In order to examine further the effects of the mechanical stabilization, both contributions $\Delta G_{e,b}$ and $\Delta G_{e0,\sigma}$, are plotted as a function of time in Figure. V. 12, for each temperature. At the start of the transformation, $\Delta G_{e,b}$ is equal to zero (by definition), whereas $\Delta G_{e0,\sigma}$ starts with some initial value, which takes account of the temperature dependence of $\sigma_{y,T}^{\gamma}$. $\Delta G_{e,b}$and $\Delta G_{e0,\sigma}$ then increase during the bainite transformation. The evolutions of $\Delta G_{e,b}$ and $\Delta G_{e0,\sigma}$ present different behaviors at high temperature (450 °C, 475 °C) and low temperature (350 °C, 400 °C). At high temperatures, both $\Delta G_{e,b}$ and $\Delta G_{e0,\sigma}$ increase simultaneously. $\Delta G_{e0,\sigma}$ increases because of the carbon enrichment of the austenite (effect of carbon on the austenite yield strength (Eq. 43, Eq. 44, Eq. 45)). $\Delta G_{e,b}$ increases with the bainitic ferrite fraction, in agreement with the model of [2]. The total increase of the elastic strain energy required to form a bainitic ferrite lath is about 300 J/mol at 450 °C and 200 J/mol at 475 °C, which is significant, as the initial strain energy, $G_{e0,Bs}$, is equal to 670 J/mol. This is why the plateaus are lower than in previous simulation (Section III.1.b.), where mechanical stabilization effects were not considered.

At low temperatures (350 °C, 400 °C), the evolutions of $\Delta G_{e,b}$ and $\Delta G_{e0,\sigma}$ are different: $\Delta G_{e0,\sigma}$ undergoes a much higher increase than $\Delta G_{e,b}$. But this actually has a weak impact on the simulation,

because the largest part of the $\Delta G_{e0,\sigma}$ increase occurs after that the stasis has been reached, at times 576 s and 267 s respectively. This is due to the delayed partition of the carbon, which has been imposed in the simulations. Hence the main origin of the mechanical stabilization comes from the term $\Delta G_{e,b}$, related to dislocations strengthening and geometrical constraints. As expected, $\Delta G_{e,b}$ increases for decreasing temperature: it is equal to about 350 J/mol at 400 °C and 525 J/mol at 350 °C. Hence, although there is no significant contribution of the term $\Delta G_{e0,\sigma}$ before the stasis at 350 °C and 400 °C, the mechanical stabilization reached at the stasis is higher at 350 °C and 400 °C than at higher temperature. Considering the whole investigated temperature range, from 350 °C to 475 °C, the mechanical stabilization increases for decreasing temperature. At 450 °C and 475 °C, there is a similar contribution of both $\Delta G_{e0,\sigma}$ and $\Delta G_{e,b}$ terms. At 350 °C and 400 °C, $\Delta G_{e,b}$ is much larger than $\Delta G_{e0,\sigma}$.
Figure. V. 11 c) shows the carbon concentration in austenite when the stasis is reached (black squares) according to the model, (i.e. when the growth factor B_g reaches zero). These concentrations are lower than for the simulations of the two last sections. (The latter were aligned with the T_0' line corresponding to 670 J/mol, see Figure. V. 7 c). The main reason is that the stasis tends to be reached earlier because of the mechanical stabilization. But one should also consider the kinetics of carbon partitioning, which has been estimated differently at high temperature (450 °C, 475 °C) and at low temperature (350 °C, 400 °C). At high temperature, we used a mass balance, because it gives a good agreement with the carbon concentrations in austenite obtained by HEXRD (see Figure. V. 9). The lower concentrations in austenite calculated at the stasis are consistent with the lower plateaus predicted by the simulation. At low temperature, we imposed the evolution of carbon concentration directly from the HEXRD experiments. Hence, the respective evolutions of carbon concentration in austenite and of the mechanical stabilization ($\Delta G_{e,b}$, the preponderant parameter at 350 °C and 400 °C) are less dependent, whereas these were correlated at 450 °C and 475 °C. Due to the mechanical stabilization, the stasis occurred earlier than in previous simulations, and the carbon had less time to partition to the austenite.
Put together, the concentrations at the end of the stasis from 350 °C to 475 °C predicted by the model have now nothing to do with the measured concentrations, which are plotted again in Figure. V. 11 c). Both the too low plateaus predicted at high temperature and the too low carbon concentrations in austenite in the whole temperature range (350-475 °C) represent significant discrepancies between the simulations and the experiments.

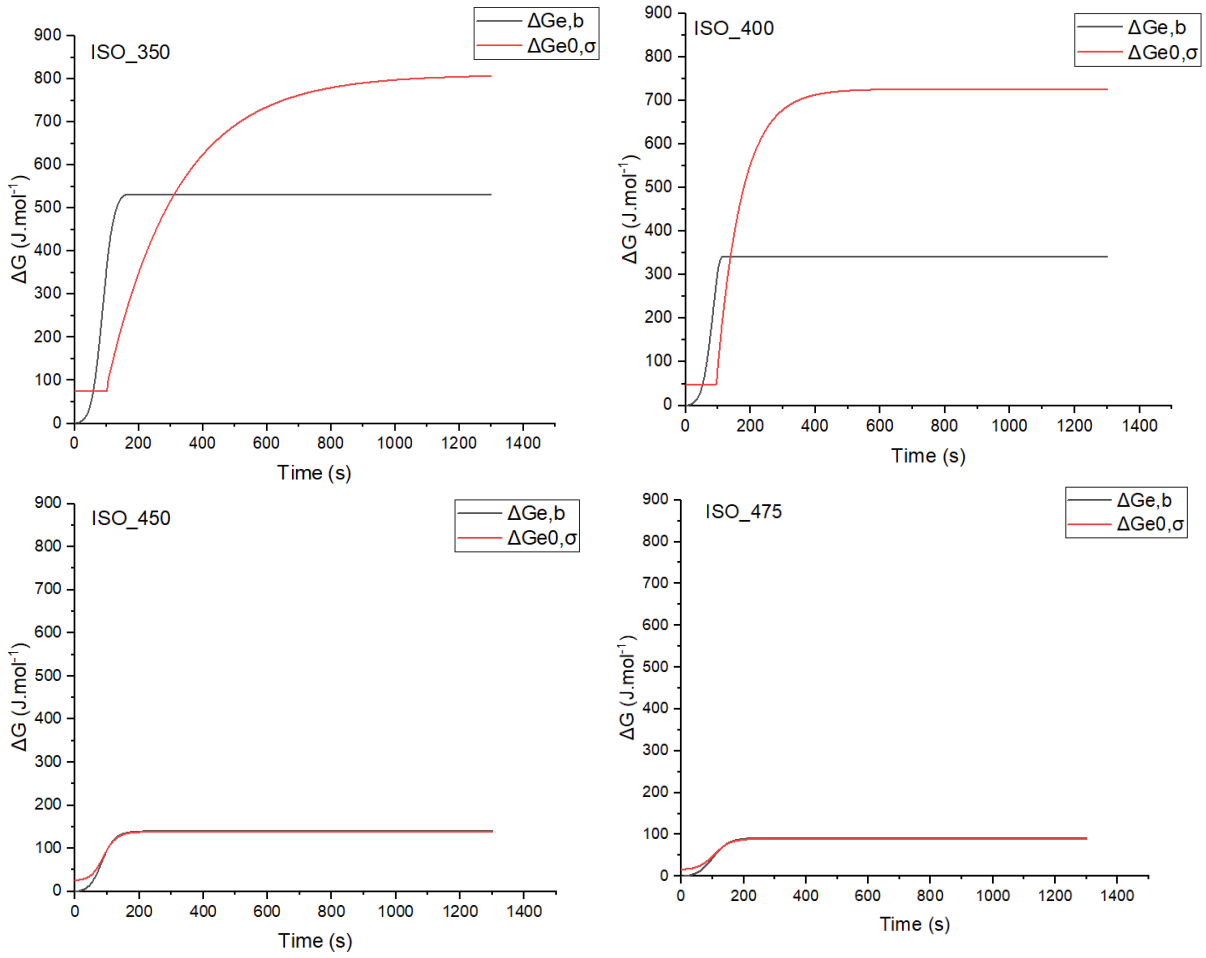

Figure. V. 12. Mechanical stabilization as a function of time, from the increase of $\sigma_{y,T}^{\gamma}$ ($\Delta G_{e0,\sigma}$) and from the dislocation strengthening and geometrical constraints ($\Delta G_{e,b}$), according to the simulation of isothermal transformation at 350 °C, 400 °C, 450 °C and 475 °C.

First obvious conclusion regarding mechanical stabilization effects is that these effects are drastic on the calculated kinetics. Therefore, these should probably not be neglected in future modeling. As for the agreement between simulations and experiment, two opposite effects are experienced: on the one hand, a satisfactory result is the prediction of the stasis at 350 °C, which seemed not possible with the accounting of the effect of carbon enrichment alone. On the other hand, the discrepancies mentioned above (carbon concentration, low plateaus at high temperature) are too important. These discrepancies come in part from the model parameters ($B_{S,0}$, Q_b^0), that we did not change (except the autocatalysis parameter λ) for the three versions presented in present Section and both preceding, in order to analyze successively the effects of carbon enrichment and mechanical stabilization. The parameters related to the calculation of the mechanical stabilization could also be reconsidered specifically for the alloy investigated. Finally, allowing also λ to increase with decreasing temperature would also permit a better agreement. The corresponding results are not shown here.

III.2. Continuous cooling

In this section, we will simulate three continuous coolings at 0.1 °C/s, 0.3 °C/s and 0.5 °C/s and compare the simulations to the experiments which were presented in Chapter III. Among the three versions of the model presented in previous section on isothermal transformations, we have chosen the first one (Section III.1.a.): mechanical stabilization effects are neglected and the carbon enrichment of austenite is estimated by a mass balance. The same model parameters as in Section III.1.a. have been used. Contrary to the case of isothermal treatments (Section III.1.a.), the carbon concentration in bainitic ferrite is assumed to not depend on the temperature, and to be the same for all three cooling rates (x_C^{α} = 0.12 wt.%). This simplification is based on the mean determination of the carbon concentration in ferrite upon continuous cooling (Chapter III).
The calculated ferrite fraction is plotted in Figure. V. 13 a) and b) as a function of temperature and in Figure. V. 13 c) as a function of time. The initial time was taken at the beginning of the slow cooling (at 550 °C) during the experiment (see Chapter III). As expected, faster cooling shifts the bainite transformation to lower temperatures and longer times. At about 375 °C, the three curves seem to converge towards one single master curve, but there are actually differences of about 1 % in ferrite fraction. Figure. V. 13 a) and b) also show the maximum fraction of ferrite that would be obtained if assuming that the composition in carbon in austenite follows the maximum value (Eq. 28) given by the T_0' line (strain energy $G_{e0,Bs}$ = 670 J/mol). For all three cooling rates, the calculated bainite fraction remains below this maximum value except at 0.1 °C/s, for which this limit is reached temporarily.

The kinetics at 0.1 °C/s and 0.5 °C/s show two different behaviors [39]. At 0.1 °C/s, the kinetics shows two stages: a fast stage down to 450 °C, followed by a sharp slow-down. The latter is due to the enrichment in carbon of austenite (x_C^{γ} almost reaches the T_0' curve), whereas the driving force $\Delta G^{\gamma\rightarrow\alpha}$ remains low due to the high temperature. In contrast, the kinetics calculated at 0.5 °C/s is more progressive, with a final slow down at about 300 °C. In this case, the carbon concentration in austenite increases more slowly with decreasing temperature, while the driving force increases. The kinetics calculated at 0.3 °C/s shows intermediate behavior.

The carbon enrichment in austenite is plotted as a function of temperature in Figure. V. 13 d), along with the T_0' curves. These evolutions are the direct consequence of the calculated bainite transformation kinetics, as we used the mass balance (Eq. 54) to estimate the carbon concentration. Hence, the enrichment of austenite is shifted to lower temperatures for increasing cooling rates. The curves of carbon concentration for the three cooling rates never become superimposed. This might be unexpected, as the ferrite fraction curves are almost superimposed below about 375 °C. This apparent discrepancy comes from the expression of the mass balance (Eq. 54). When the ferrite fraction is high, the carbon concentration in austenite varies very fast, even for a low variation of ferrite fraction. Below about 350 °C, differences of about 1 % in ferrite fraction exist between the curves calculated at 0.1 °C/s, 0.3 °C/s and 0.5 °C/s. These differences explain the large differences between the corresponding carbon concentrations. Actually, the calculation of the carbon composition lacks of precision when the ferrite fraction is high, and this happens below about 375 °C in these simulations.

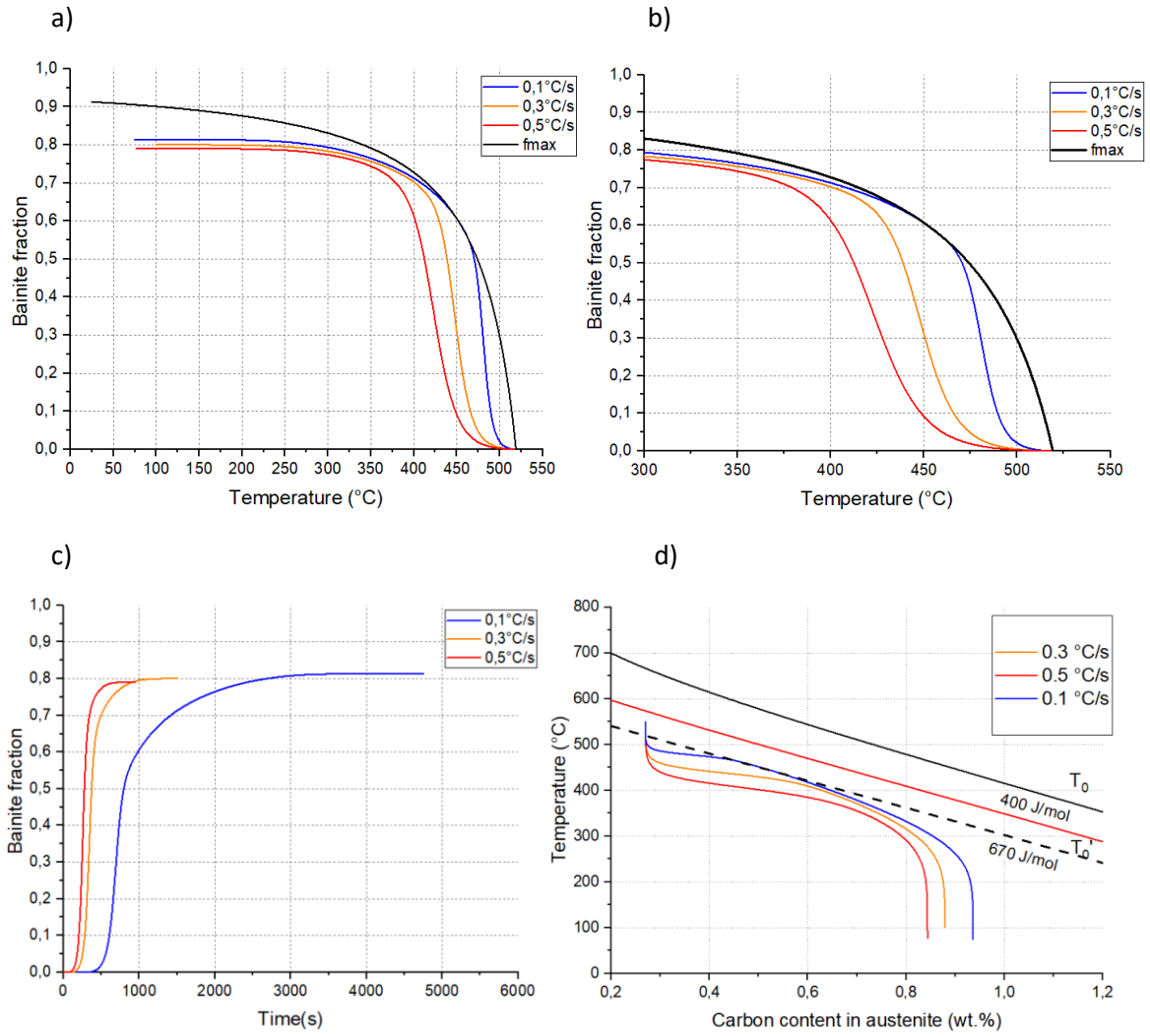

Figure. V. 13: CCs simulation results a) and b) Bainite fraction as a function of temperature; c) Bainite transformation kinetics; d) Carbon content in austenite along coolings: 0.5 °C/s (red), 0.3 °C/s (orange), 0.1 °C/s (blue).

Simulations are compared to the HEXRD experiments (see Chapter III) in
Figure. V. 14. The predicted time evolutions of the bainite fractions show a good agreement with the experimental curves (
Figure. V. 14 c), but the model does not capture the slow-down of the kinetics, beyond 70 % of ferrite at 0.3°C/s and beyond 30 % of ferrite at 0.1 °C/s. (CC at 0.5 °C/s shows less discrepancy in final fraction). Considering the ferrite fractions plotted as a function of temperature, larger discrepancies are put into evidence. Kinetics is correctly predicted at 0.3 °C/s, but it is overestimated at 0.1 °C/s and underestimated at 0.5 °C/s. On the whole, the shift of the transformation to lower temperatures with increasing cooling rate is too high. Nevertheless, the convergence of the three calculated curves towards close values below about 350 °C is in good agreement with the experiment, except the fact that the final bainite fraction is overestimated at 0.1 °C/s and 0.3 °C/s, as mentioned above.

Regarding the evolutions of carbon concentration, two features of the experimental curves are well reproduced. In a first stage, x_C^γ remains nearly constant. According to the model, this is due to the

expression of the carbon mass balance (Eq. 54), which gives a weak dependence of the x_C^γ on the ferrite fraction when the latter is low. (See for example the calculated curves of Figure. V. 13).

Another satisfactory prediction regards the influence of the cooling rate: increasing it shifts the enrichment to lower temperatures. The predicted kinetics of enrichment are satisfactory at 0.3 °C/s and 0.5 °C/s down to ca. 400 °C. But this kinetics is clearly overestimated at 0.1 °C/s. Moreover, below 400 °C, the model does not capture a slow-down of the carbon enrichment kinetics, which is more pronounced with decreasing cooling rate. As a result, the carbon concentration in austenite ends with a lower value at 0.1 °C/s than at 0.3 °C/s, and at 0.5 °C/s, according to the experiment. The model predicts the opposite trend.

Some of the differences and similarities between these simulations and the experiments can be interpreted on the basis of the simulations in isothermal conditions presented in previous sections. The best agreement between simulation and experiment is obtained for the cooling rate 0.3 °C/s. The reason may be that most part of the transformation occurs near 450 °C, the isothermal treatment temperature at which the chosen version of the model (presented in Section III.1.a.) gave the predictions in best agreement with the experiment. The too slow kinetics predicted at 0.5 °C/s may be due to the use of the mass balance to estimate the carbon concentration in austenite. Indeed, a large part of the bainite transformation takes place below 450 °C, a temperature under which the mass balance may overestimate the carbon partitioning kinetics, as discussed in Section III.1.a.. As for the cooling rate 0.1 °C/s, the overestimation of the kinetics by the model can be related to the overestimation of the kinetics at 475 °C in isothermal conditions, as a large part of the bainite transformation occurs near 475 °C, according to the experiment. Also, the model was not assessed in isothermal conditions at temperatures above 475 °C, whereas an important part of the bainite transformation also takes place in this temperature range. Let us also recall the lack of reproducibility of the experiments that we pointed out in this temperature range, when studying isothermal treatments.

Finally, the largest discrepancies between the simulations and the experiments occurred at 0.1 °C/s: below about 475 °C, the predicted kinetics is much too fast. This does not come from a lack of precision in the predicted carbon partitioning kinetics, because the model predicts a kinetics of carbon enrichment which is faster than the experiment. Hence, improving this would lead to predict an even faster kinetics of bainite transformation, thereby worsening the discrepancy between simulation and experiment.

It obviously seems that the model does not capture an effect which was put into evidence in Chapter III: prior transformation at high temperature tends to inhibit further bainite transformation at lower temperature. This was well showed by the “step treatments”. The highest temperature considered for the first step was 475 °C. During the CC at 0.1 °C/s, the bainite transformation starts above this temperature, and the effect of inhibition at lower temperature could thus be even stronger than for the step treatments. Let us mention that in a previous study, it was also attempted to use a similar model to predict the bainite transformation kinetics upon cooling [40]. At lower investigated cooling rate, the model also tended to predict faster kinetics than the experiment. This had been ascribed to the mechanical stabilization by the bainite formed at high temperature. Therefore, one could investigate whether applying the model of [2] with the mechanical stabilization effects could improve the prediction of kinetics upon cooling. But the predictions regarding isothermal transformations would need to be improved first.

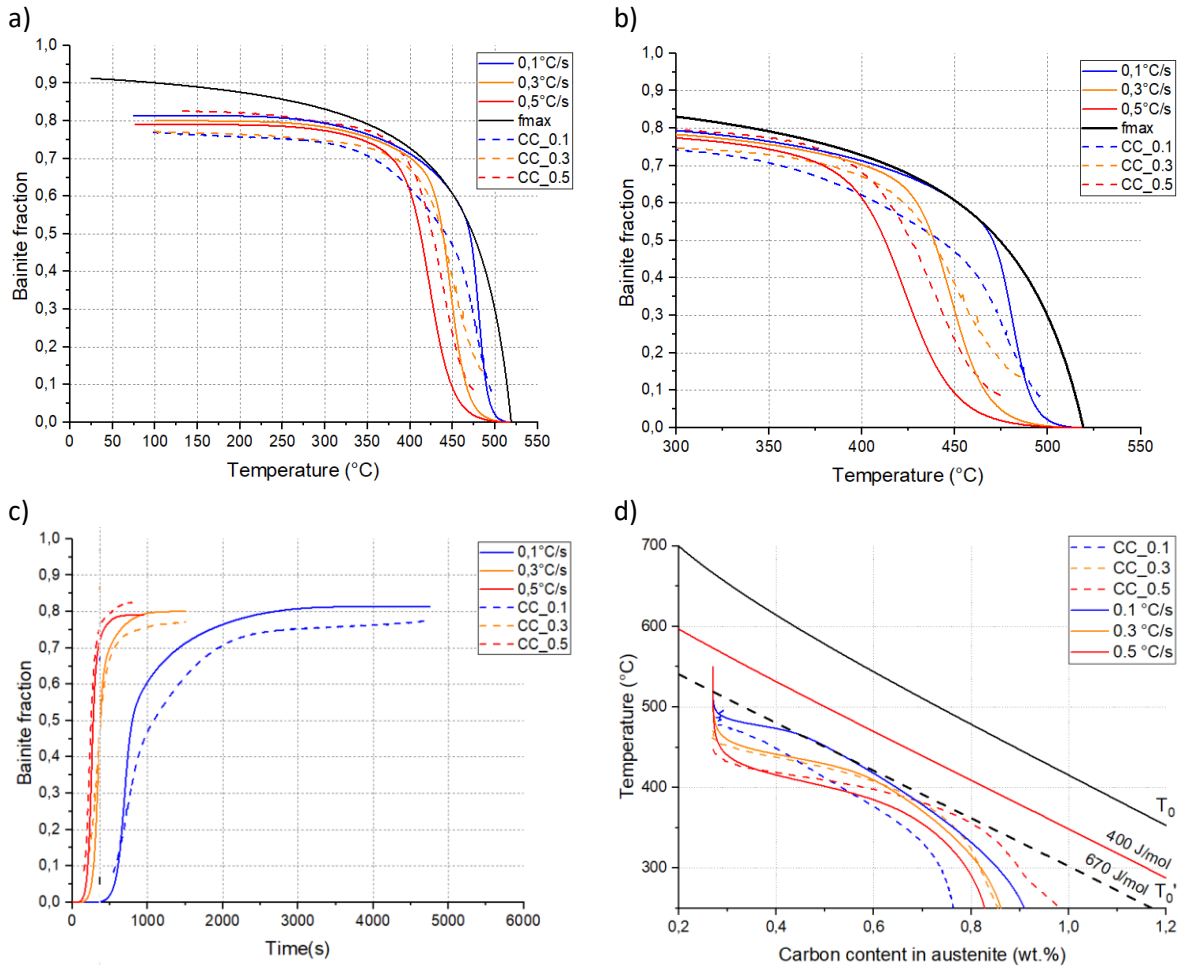

Figure. V. 14: a) and b) Bainite fraction as a function of temperature; c) Bainite kinetics; Experimental dots, models in lines; d) Carbon content in austenite along coolings: in continuous cooling sequences: 0.5 °C/s (red), 0.3 °C/s (orange), 0.1 °C/s (blue).

Conclusion

In this Chapter, the bainite transformation kinetics has been simulated by using a model of the literature and introduced in [2]. This model is based on the "diffusionless" approach [2], which assumes that the bainitic ferrite laths form with a displacive mechanism and that their nucleation rate is the limiting factor controlling the bainite transformation kinetics. Originality of this model was to introduce the effects of austenite mechanical stabilization upon the last stages of the bainite transformation, which increase the elastic strain energy necessary to form a new bainitic ferrite lath.
One key feature of the experiments presented in Chapter III was the stasis phenomenon upon isothermal or continuous cooling treatments. First aim of this simulation work was to use the model of [2] to evaluate two possible origins for this phase transformation stasis: the mechanical stabilization of the austenite, but also its enrichment by the carbon, which partitions from the bainitic ferrite. The latter origin of the austenite stabilization is not explicitly addressed in reference [2], where mostly low-Si steels were considered. However, reference [2] provides all the data necessary to modify the model parameters as a function of the austenite composition in carbon. Besides studying the origin of the stasis, more practical objective of this simulation work was also to assess the ability of the model to predict the bainite transformation kinetics upon isothermal and continuous cooling treatments.

It was found that both mechanical and chemical stabilizations have a significant effect and should be accounted for in order to obtain accurate prediction of the kinetics and the stasis. Neglecting the mechanical stabilization effects led to significant discrepancies. As for the chemical stabilization, a precise knowledge of the evolution of carbon composition in austenite is necessary. At lower transformation temperature, the carbon partitioning kinetics tends to be slower than the global bainite transformation kinetics. If this is neglected, the austenite gets stabilized too early by the carbon, and the model then tends to underestimate the bainite transformation kinetics and to predict the stasis too early. The provisory solution that we found was to impose in the simulations the evolution of austenite carbon content in austenite that we measured by in situ HEXRD.

Once both effects of mechanical stabilization and precise time evolutions of austenite carbon content are implemented, the model properly predicts the kinetics in isothermal conditions in the whole temperature range considered (350-475 °C), but also when simulating continuous cooling. However, it should be recognized that significant discrepancies remain between calculated and experimental bainite transformation kinetics. Actually, these discrepancies contrast with the very good comparisons between simulation and experiment presented in [2].
First origin of these discrepancies is that we voluntarily limited to the minimum the number of adjustable model parameters. This allowed us to better interpret the effects of temperature, carbon partition and mechanical stabilization, but to the detriment of the model predictability. For instance, if we allow the autocatalytic nucleation parameter (λ) to depend on temperature, better agreement with experiment is obtained (corresponding results were not shown). Nevertheless, significant discrepancies would subsist.
Two of the model parameters, the number of nucleation sites per unit surface of grain boundaries (N_S) and the volume of the nucleus (V_n) are assumed constant, like in [2], and this may be an oversimplification.

Another simplifying assumption regards the carbon distribution in austenite. We always assumed that the carbon is distributed homogeneously in austenite. The experiments (Chapter III) show the contrary, at least during continuous cooling, as well as [39]. Last possible origin of the discrepancies is that in [2], kinetics from dilatometry experiments were used to assess the model, but also to calibrate its parameters, whereas we used HEXRD data. In Chapter III, we showed that kinetics established by dilatometry and HEXRD may differ significantly.

Regarding continuous cooling treatments, the current version of the model of bainite transformation gives satisfactory predictions at 0.3 °C/s and 0.5 °C/s, but it does not allow to predict accurately the bainite transformation kinetics at the lowest cooling rate considered, 0.1 °C/s. This is because it does not take account of the fact that the bainite transformation gets itself inhibited if a large fraction of bainite is formed at high temperature. This is was showed Chapter III by the step treatments, but the mechanisms of inhibition have yet to be established. Possible mechanisms are the mechanical stabilization or the effect of the bainite lath sizes on the autocatalysis.

Future work could consist in fully exploiting the experimental data of Chapter III: the evolutions of carbon concentration obtained from experiments upon continuous coolings (CCs) have not been considered in the simulations so far, like we did for isothermal treatments. Mechanical stabilization effects have not been considered either for CCs. The step treatments have also not been simulated yet. In the longer term, future developments could be focused on a better description of carbon distribution both at the scale of an individual ferrite lath and its surrounding and at the scale of the prior austenite grain (blocky untransformed austenite). For the moment, the mechanical stabilization effects are obviously too strong, with current parametrization of this part of the model, and this could be reconsidered in future work.

References

[1] L. C. D. Fielding, “The Bainite Controversy,” *Mater. Sci. Technol.*, vol. 29, no. 4, pp. 383–399, Apr. 2013, doi: 10.1179/1743284712Y.0000000157.

[2] S. M. C. van Bohemen, “Bainite growth retardation due to mechanical stabilisation of austenite,” *Materialia*, vol. 7, p. 100384, Sep. 2019, doi: 10.1016/j.mtla.2019.100384.

[3] H. K. D. H. Bhadeshia, *Bainite in steels: transformations, microstructure and properties*, 2. ed. London: IOM Communications, 2001.

[4] H. K. D. H. Bhadeshia and J. Christian, “Bainite in steels,” *Metall. Trans. A*, vol. 21, no. 3, pp. 767–797, 1990.

[5] Z. Li *et al.*, “Effect of Austenitizing Temperature and Prior Martensite on Ultra-Fine Bainite Transformation Kinetics,” *Metals*, vol. 9, no. 12, p. 1309, Dec. 2019, doi: 10.3390/met9121309.

[6] S. Li, R. Zhu, I. Karaman, and R. Arróyave, “Development of a kinetic model for bainitic isothermal transformation in transformation-induced plasticity steels,” *Acta Mater.*, vol. 61, no. 8, pp. 2884–2894, May 2013, doi: 10.1016/j.actamat.2013.01.032.

[7] G. B. Olson and M. Cohen, “A general mechanism of martensitic nucleation: Part III. Kinetics of martensitic nucleation,” *Metall. Trans. A*, p. 9.

[8] S. M. C. van Bohemen and J. Sietsma, “Modeling of isothermal bainite formation based on the nucleation kinetics,” *Int. J. Mater. Res.*, vol. 99, no. 7, pp. 739–747, 2008, doi: doi:10.3139/146.101695.

[9] S. M. C. Van Bohemen, “Modeling Start Curves of Bainite Formation,” *Metall. Mater. Trans. A*, vol. 41, no. 2, pp. 285–296, Feb. 2010, doi: 10.1007/s11661-009-0106-9.

[10] M. J. Santofimia, F. G. Caballero, C. Capdevila, C. García-Mateo, and C. G. de Andrés, “Evaluation of displacive models for bainite transformation kinetics in steels,” *Mater. Trans.*, vol. 47, no. 6, pp. 1492–1500, 2006.

[11] G. Sidhu, S. Srinivasan, and S. Bhole, “A Model for Bainite Formation at Isothermal Heat Treatment Conditions,” *J. Therm. Sci. Eng. Appl.*, vol. 12, no. 1, Feb. 2020, doi: 10.1115/1.4042861.

[12] D. Quidort and Y. J. Brechet, “A model of isothermal and non isothermal transformation kinetics of bainite in 0.5% C steels,” *ISIJ Int.*, vol. 42, no. 9, pp. 1010–1017, 2002.

[13] W. F. Lange, M. Enomoto, and H. I. Aaronson, “The kinetics of ferrite nucleation at austenite grain boundaries in Fe-C alloys,” *Metall. Trans. A*, vol. 19, no. 3, pp. 427–440, Mar. 1988, doi: 10.1007/BF02649256.

[14] S. B. Singh and H. K. D. H. Bhadeshia, “Estimation of bainite plate-thickness in low-alloy steels,” *Mater. Sci. Eng. A*, vol. 245, no. 1, pp. 72–79, Apr. 1998, doi: 10.1016/S0921-5093(97)00701-6.

[15] A. M. Ravi, J. Sietsma, and M. J. Santofimia, “Exploring bainite formation kinetics distinguishing grain-boundary and autocatalytic nucleation in high and low-Si steels,” *Acta Mater.*, vol. 105, pp. 155–164, Feb. 2016, doi: 10.1016/j.actamat.2015.11.044.

[16] S. B. Singh, “Phase transformations from deformed austenite,” PhD Thesis, University of Cambridge, 1998.

[17] G. I. Rees and H. K. D. H. Bhadeshia, “Bainite transformation Part 1 Modified model,” *Mater Sci Technol*, vol. 8, p. 965, 1992.

[18] A. M. Ravi, A. Kumar, M. Herbig, J. Sietsma, and M. J. Santofimia, “Impact of austenite grain boundaries and ferrite nucleation on bainite formation in steels,” *Acta Mater.*, vol. 188, pp. 424–434, Apr. 2020, doi: 10.1016/j.actamat.2020.01.065.

[19] C. Magee, “The nucleation of martensite,” *Phase Transform.*, 1970.

[20] S. M. C. van Bohemen, “Autocatalytic nature of the bainitic transformation in steels: a new hypothesis,” *Philos. Mag.*, vol. 93, no. 4, pp. 388–408, Feb. 2013, doi: 10.1080/14786435.2012.721570.

[21] M. Shah, S. K. Das, and A. Pastor, “Phenomenological kinetic model of the nano-bainitic steels to characterize the dynamics of the autocatalytic nucleation process,” *SN Appl. Sci.*, vol. 2, no. 4, Apr. 2020, doi: 10.1007/s42452-020-2395-y.

[22] A. M. Ravi, A. Navarro-López, J. Sietsma, and M. J. Santofimia, “Influence of martensite/austenite interfaces on bainite formation in low-alloy steels below M,” *Acta Mater.*, vol. 188, pp. 394–405, Apr. 2020, doi: 10.1016/j.actamat.2020.02.003.
[23] D. Gaude-Fugarolas and P. J. Jacques, “A New Physical Model for the Kinetics of the Bainite Transformation,” *ISIJ Int.*, vol. 46, no. 5, pp. 712–717, 2006, doi: 10.2355/isijinternational.46.712.
[24] H. Matsuda and H. K. D. H. Bhadeshia, “Kinetics of the bainite transformation,” *Proc. R. Soc. Math. Phys. Eng. Sci.*, vol. 460, no. 2046, pp. 1707–1722, Jun. 2004, doi: 10.1098/rspa.2003.1225.
[25] J. W. Cahn, “The kinetics of grain boundary nucleated reactions,” *Acta Metall.*, vol. 4, no. 5, pp. 449–459, 1956.
[26] F. G. Caballero, M. K. Miller, and C. Garcia-Mateo, “Carbon supersaturation of ferrite in a nanocrystalline bainitic steel,” *Acta Mater.*, vol. 58, no. 7, pp. 2338–2343, Apr. 2010, doi: 10.1016/j.actamat.2009.12.020.
[27] G. I. Rees, “Bainite transformation kinetics Part 2 Non-uniform distribution,” p. 3.
[28] L. C. Chang, “Austenite films in bainitic microstructures,” vol. 11, p. 10, 1995.
[29] P. Retzl, S. Zamberger, and E. Kozeschnik, “Computational analysis of austenite film thickness and C-redistribution in carbide-free bainite,” *Mater. Res. Express*, vol. 8, no. 7, p. 076502, Jul. 2021, doi: 10.1088/2053-1591/ac0d6f.
[30] S. Chatterjee, H.-S. Wang, J. R. Yang, and H. K. D. H. Bhadeshia, “Mechanical stabilisation of austenite,” *Mater. Sci. Technol.*, vol. 22, no. 6, pp. 641–644, Jun. 2006, doi: 10.1179/174328406X86128.
[31] H. K. D. H. Bhadeshia, “Developments in martensitic and bainitic steels: role of the shape deformation,” *Mater. Sci. Eng. A*, vol. 378, no. 1–2, pp. 34–39, Jul. 2004, doi: 10.1016/j.msea.2003.10.328.
[32] S. M. C. van Bohemen, “Relationship between acoustic emission energy and the kinetics of martensite formation in plain carbon steels,” *Philos. Mag.*, vol. 95, no. 2, pp. 210–223, Jan. 2015, doi: 10.1080/14786435.2014.994574.
[33] B. Edmondson and T. Ko, “Spontaneous deformation of austenite during martensitic transformations,” *Acta Metall.*, vol. 2, no. 2, pp. 235–241, Mar. 1954, doi: 10.1016/0001-6160(54)90164-9.
[34] S. M. C. Van Bohemen and J. Sietsma, “Martensite Formation in Partially and Fully Austenitic Plain Carbon Steels,” *Metall. Mater. Trans. A*, vol. 40, no. 5, pp. 1059–1068, May 2009, doi: 10.1007/s11661-009-9796-2.
[35] S. M. C. van Bohemen, “Bainite and martensite start temperature calculated with exponential carbon dependence,” *Mater. Sci. Technol.*, vol. 28, no. 4, pp. 487–495, Apr. 2012, doi: 10.1179/1743284711Y.0000000097.
[36] G. B. Olson and M. Cohen, “A General Mechanism of Martensitic Nucleation= Part I. General Concepts and the FCC HCP Transformation,” *Metall. Trans. A*, p. 8.
[37] G. B. Olson and M. Cohen, “A General Mechanism of Martensitic Nucleation- Part II. FCC ---,-BCC and Other Martensitic Transformations,” *Metall. Trans. A*, p. 10.
[38] R. Rementeria *et al.*, “Carbon concentration measurements by atom probe tomography in the ferritic phase of high-silicon steels,” *Acta Mater.*, vol. 125, pp. 359–368, Feb. 2017, doi: 10.1016/j.actamat.2016.12.013.
[39] S. Reisinger *et al.*, “Strain energy contributions on the bainitic phase transformation in a CrMoV steel during continuous cooling,” *Mater. Des.*, vol. 155, pp. 475–484, Oct. 2018, doi: 10.1016/j.matdes.2018.06.014.
[40] S. M. C. van Bohemen and J. Sietsma, “The kinetics of bainite and martensite formation in steels during cooling,” *Mater. Sci. Eng. A*, vol. 527, no. 24–25, pp. 6672–6676, Sep. 2010, doi: 10.1016/j.msea.2010.06.091.

General conclusions and outlooks

This thesis aimed at a better understanding of the CFB phase transformation mechanisms of an industrial steel during a forging process. One of the major scientific challenges was to investigate the transformations in conditions of continuous cooling that were much less studied in the literature than the transformations in isothermal conditions.

To do so, Carbide Free Bainitic transformations were investigated by in situ High Energy X-Ray Diffraction (HEXRD). **This latter technic was shown to be probably the best in class available to metallurgists to study such transformations.** The experiments permit quantifying the phases in presence all along isothermal holdings, multistep holding sequences and continuous cooling sequences, which were chosen to be representative of the forging process conditions. The composition of phases are concomitantly determined and tracked using the austenite lattice parameter and the tetragonality of the bainite lattice. The absence of BCT peak splitting or asymmetry could make this latter determination controversial. However, the same major conclusions on the carbon distributions could have been drawn without this determination. **These coupled results have served to establish accurate time-resolved carbon mass balances between phases for each treatment**. The precision and robustness of our approach has allowed us to identify the conditions in which part of the carbon is also precipitated (transition carbides at low transformation temperatures).

The obtained transformation kinetics during isothermal holdings were comparable to similar steels studied in the literature, i.e. the lower the temperature is, the faster the transformation and the higher the fraction of austenite at stasis. **One of our major results is to have undoubtedly confirmed that bainitic ferrite is still supersaturated in carbon**, even for transformations at high temperature. Our experiments do not allow however us to prejudge the spatial distribution of these atoms (solid solution, segregated on defects). This result is key for the development of the model in Chapter V. In fact, the carbon atoms trapped in bainite are not available for austenite enrichment and thus it limits in turn the possible fraction of retained austenite.

The austenite carbon content at the end of the holding was compared to the displacive criterion T_0' line. **The experimental values at the end of isothermal holdings are close to the conventional T_0' line however this criterion is not respected for high temperature transformations**; even if we take into account the lack of repeatability of our experiences in this temperature range.

For continuous cooling experiments, **we have also developed an original methodology to analyze austenite enrichment and validated on a multistep twin experiment** [1]. This latter method is thought to be more reliable than the ones previously followed in the literature based on the sole bainite tetragonality. In accordance with the literature, the transformation starts at high temperature but never reach the stasis criterion. The kinetics show also different enrichment stages, which were discussed in Chapter III. The stage 1 is shown to be related to an heterogeneous carbon distribution but the second onset of transformation, observed at low cooling rate, is not explained so far.

The characterization of microstructures using SEM-EBSD allow us to study systematically the sizes and microtextures of the microstructures after our in situ experiments. **For microstructures formed after isothermal treatments the bainite lath size increases with the increase of transformation temperature**. The different bainitic microstructures were also categorized at the light of the Zajac's

classification which is based on the histograms of misorientations [2]. For microstructures formed at low temperature, our CFB microstructures can be classified as lower bainite, while microstructures formed at high temperatures can be classified as upper bainite.

By comparison, **the microstructures obtained after continuous cooling sequences show a far larger variability of sizes and microtextures than the one obtained after isothermal treatments**. Their mean size are comparable to bainites formed at high transformation temperatures and they can be classified as upper bainite from the crystallographic point of view, even if it contains significant fraction of highly misoriented domains. **The limits of the actual classifications for these latter microstructures formed progressively at different temperatures have thus been discussed.**

Furthermore, we have shown that the packet microstructures are highly entangled confirming an intergranular nucleation of the packets (not only at PAG boundaries) which could be **the sign of an autocatalytic process for bainite and martensite transformation as well**. This autocatalytic process is an important component of the model developed in Chapter V.

Based on the in situ investigations of bainite transformation and the microstructure characterizations we have chosen to implement and improve a “diffusionless” model from the literature. **The bainite transformation kinetics were simulated taking into account of carbon partitioning between austenite and bainitic ferrite and the mechanical stabilization of austenite**. For isothermal transformations, we have shown that **a precise knowledge of the evolution of carbon composition in austenite is necessary**. For the low temperature transformations, it was necessary to take into account the experimental carbon content of the austenite determined by HEXRD, as the experimental carbon partitioning kinetics tend to be slower than the bainite transformation kinetics. In this study, we deliberately chose not to seek a systematic and perfect adjustment of experimental results in favor of understanding the relative effects of the parameters. This is the case, for example, of the autocatalytic factor, which has been kept constant as a function of temperature.

Once calibrated on isothermal experiments, it was possible to use the model to simulate bainite kinetics for anisothermal transformations. The model reproduce quite well the observed overall trend without any additional adjustment (in particular the absence of stasis criterion). However, it is not able to simulate properly the sensitivity of the transformation to the cooling rates. Our in situ experiments reveal in deed an unexpected trends in the studied range of cooling rate; **the higher the cooling rate, the higher the fraction of stabilized retained austenite**. Our multistep experiments in Chapter III proved that it comes from the fact that the bainite transformation gets itself inhibited if a large fraction of bainite is formed at high temperature. **The bainite transformation does not respect the additivity rule**. The bainitic transformation can restart if the transformation is not enough advanced. Even if the transformation restarts, the kinetics at a given temperature is also lowered. The bainite transformation is thus dependent on the history and previous transformations. **The mechanisms of inhibition have yet to be established and modeled** and could be related to the austenite stability (local carbon distribution), the nucleation processes (size effect, autocatalysis) or the mechanical stabilization. This is the reason why the actual version of the model is not able so far to model all the inheritance effects of the bainite formation.

This work was therefore able to identify avenues for future works:

- Going deeper in the understanding why the stasis criterion (T_0') is not respected at high transformation temperatures. This behavior have been also observed in other studies as [3] but remains misunderstood. It could mean that diffusionless theory does not apply at such temperatures, keeping in mind however that we have clearly established that bainite is still supersatured at such temperatures. Other models based on diffusional approaches could be tested in this frame.
- Understanding the origin of the inheritance mechanism in continuous cooling is certainly one of the most important challenges in the future of this study. Different hypotheses have been discussed in Chapters III and V and they should be assessed critically, either through the bias of dedicated experiments (interrupted tests) and advanced characterization methods (EELS) or by improving model by implementing additional size or mechanical stabilization effects.
- By determining its tetragonality, we were able to show that the bainitic ferrite remains supersaturated in carbon whatever the treatment (as observed by other authors [3]–[7]). Thanks to this estimation we could show that our carbon balances are perfectly consistent. However, the peaks of the ferritic phases we recorded are not asymmetric which leaves a question: is bainite really tetragonal ? It is also not clear if this estimation of the carbon content also encompasses carbon clusters or carbon segregated at defects [5], such as dislocations or bainitic lath boundaries [8]–[10]. Some 3D atom probe tomography (3D APT) experiments would have allowed us to have an idea of the distribution of the carbon as the following authors have done [11]–[13]. Additional experiments were carried out by Frederic Danoix (GPM Rouen) within the framework of this thesis but are not yet exploited.
- Our HEXRD method does allow to follow mean carbon composition in austenite and show its limits when dealing with the local chemical composition. We have evidenced that when studying the asymmetry of austenite diffraction peak which probably reveal an heterogeneous distribution of carbon in austenite (continuous cooling). The measurements of carbon heterogeneities at the micron scale in austenite islands (for instance by EELS mapping in TEM) could bring valuable information to describe better the heterogeneity at a statistically relevant scale and could help to improve the models introducing additional scales (carbon diffusion distance in austenite for instance).
- In Chapter IV, we have shown that it is very difficult to uncouple the contribution of the ferritic phases in presence (bainite/ martensite) especially at high temperature. Some authors such as [14]–[16] are interested in the study of bimodal structures but their methodology has not been deployed in the framework of this thesis.
- There is therefore a challenge to standardize practices in the measurement of the bainite size in the literature [17]–[21]. This question is all the more important as the size of bainitic features is a key input of the models and the current “diffusionless” models do not consider the temperature dependence of the lath sizes.

References

[1] S. M. C. van Bohemen, “The nonlinear lattice expansion of iron alloys in the range 100–1600K,” *Scr. Mater.*, vol. 69, no. 4, pp. 315–318, Aug. 2013, doi: 10.1016/j.scriptamat.2013.05.009.

[2] S. Zajac, V. Schwinn, and K. H. Tacke, “Characterisation and Quantification of Complex Bainitic Microstructures in High and Ultra-High Strength Linepipe Steels,” *Mater. Sci. Forum*, vol. 500–501, pp. 387–394, Nov. 2005, doi: 10.4028/www.scientific.net/MSF.500-501.387.

[3] L. Guo, H. K. D. H. Bhadeshia, H. Roelofs, and M. I. Lembke, “In situ synchrotron X-ray study of bainite transformation kinetics in a low-carbon Si-containing steel,” *Mater. Sci. Technol.*, vol. 33, no. 17, pp. 2147–2156, Nov. 2017, doi: 10.1080/02670836.2017.1353669.

[4] J. W. Christian, “Tetragonal Martensites in Ferrous Alloys — A Critique,” *Mater. Trans. JIM*, vol. 33, no. 3, pp. 208–214, 1992, doi: 10.2320/matertrans1989.33.208.

[5] Y. Lu, H. Yu, and R. D. Sisson, “The effect of carbon content on the c/a ratio of as-quenched martensite in Fe-C alloys,” *Mater. Sci. Eng. A*, vol. 700, pp. 592–597, Jul. 2017, doi: 10.1016/j.msea.2017.05.094.

[6] Z. Nishiyama, *Martensitic transformation*. Elsevier, 2012.

[7] C. S. Roberts, “Effect of Carbon on the Volume Fractions and Lattice Parameters Of Retained Austenite and Martensite,” *JOM*, vol. 5, no. 2, pp. 203–204, Feb. 1953, doi: 10.1007/BF03397477.

[8] R. Rementeria *et al.*, “Quantitative assessment of carbon allocation anomalies in low temperature bainite,” *Acta Mater.*, vol. 133, pp. 333–345, Jul. 2017, doi: 10.1016/j.actamat.2017.05.048.

[9] R. Rementeria *et al.*, “Carbon concentration measurements by atom probe tomography in the ferritic phase of high-silicon steels,” *Acta Mater.*, vol. 125, pp. 359–368, Feb. 2017, doi: 10.1016/j.actamat.2016.12.013.

[10] S. Gaudez, “Kinetics and microstructural evolutions during the tempering of martensitic and nano-bainitic low alloyed steel: in situ experimental study and modelling,” PhD Thesis, Université de Lorraine, 2021.

[11] I. Pushkareva *et al.*, “The Influence of Vanadium Additions on Isothermally Formed Bainite Microstructures in Medium Carbon Steels Containing Retained Austenite,” *Metals*, vol. 10, no. 3, p. 392, Mar. 2020, doi: 10.3390/met10030392.

[12] F. G. Caballero, M. K. Miller, and C. Garcia-Mateo, “Carbon supersaturation of ferrite in a nanocrystalline bainitic steel,” *Acta Mater.*, vol. 58, no. 7, pp. 2338–2343, Apr. 2010, doi: 10.1016/j.actamat.2009.12.020.

[13] C. Garcia-Mateo *et al.*, “Low temperature bainitic ferrite: Evidence of carbon super-saturation and tetragonality,” *Acta Mater.*, vol. 91, pp. 162–173, Jun. 2015, doi: 10.1016/j.actamat.2015.03.018.

[14] E. P. Da Silva *et al.*, “Isothermal transformations in advanced high strength steels below martensite start temperature,” *Mater. Sci. Technol.*, vol. 31, no. 7, pp. 808–816, May 2015, doi: 10.1179/1743284714Y.0000000719.

[15] A. Navarro-López, J. Hidalgo, J. Sietsma, and M. J. Santofimia, “Characterization of bainitic/martensitic structures formed in isothermal treatments below the M s temperature,” *Mater. Charact.*, vol. 128, pp. 248–256, Jun. 2017, doi: 10.1016/j.matchar.2017.04.007.

[16] L. Qian, Z. Li, T. Wang, D. Li, F. Zhang, and J. Meng, “Roles of pre-formed martensite in below-Ms bainite formation, microstructure, strain partitioning and impact absorption energies of low-carbon bainitic steel,” *J. Mater. Sci. Technol.*, vol. 96, pp. 69–84, Jan. 2022, doi: 10.1016/j.jmst.2021.05.002.

[17] G. I. Rees and H. K. D. H. Bhadeshia, “Bainite transformation Part 1 Modified model,” *Mater Sci Technol*, vol. 8, p. 965, 1992.

[18] S. B. Singh and H. K. D. H. Bhadeshia, “Estimation of bainite plate-thickness in low-alloy steels,” *Mater. Sci. Eng. A*, vol. 245, no. 1, pp. 72–79, Apr. 1998, doi: 10.1016/S0921-5093(97)00701-6.

[19] N. A. Chester and H. K. D. H. Bhadeshia, “Mathematical Modelling of Bainite Transformation Kinetics,” *J. Phys. IV*, vol. 07, no. C5, pp. C5-41-C5-46, Nov. 1997, doi: 10.1051/jp4:1997506.

[20] S. M. C. van Bohemen, "Exploring the correlation between the austenite yield strength and the bainite lath thickness," *Mater. Sci. Eng. A*, vol. 731, pp. 119–123, Jul. 2018, doi: 10.1016/j.msea.2018.06.041.

[21] Z. Yang *et al.*, "Accelerating nano-bainite transformation based on a new constructed microstructural predicting model," *Mater. Sci. Eng. A*, vol. 748, pp. 16–20, Mar. 2019, doi: 10.1016/j.msea.2019.01.061.

Characterization and modeling of Carbide-Free Bainite transformations along isothermal and anisothermal heat treatments

Carbide-Free Bainites are multiphase microstructures obtained from austenite decomposition at low temperatures (typically between 450 °C and 200 °C) in alloyed steels. These microstructures are very attractive owing to their high mechanical properties and good toughness especially for forged parts dedicated to the automotive market. They are made of a fine ferritic matrix without carbide thanks to a judicious chemical composition, retained austenite stabilized by carbon partitioning during the transformation and martensite. The high fraction of retained austenite may transform in martensite during further mechanical solicitations at room temperature (strain induced transformation). These microstructures have been studied since many years, but their formation mechanisms are still a subject that continues to divide the metallurgy community, between diffuse and diffusionless approaches. The incomplete transformation phenomenon encountered in this process is one of the bones of contention. One of the great novelties of this work was to elucidate the mechanisms of formation of these microstructures in continuous cooling conditions.

In this work, we have investigated the evolution of microstructures along different thermal treatments (isothermal holdings, multistep and continuous cooling treatments) by in situ High Energy X-Ray Diffraction (HEXRD) on synchrotron beamlines. Such experiments make possible the simultaneous measurement of phase transformation kinetics, of the lattice parameters of the different phases and the detection of possible carbide precipitation processes. On this basis, very precise carbon mass balances between the constituting phases have been established for the first time leading to the conclusions that the ferritic bainite is even more supersaturated in carbon that expected. The multistep and continuous cooling experiments have also proved that the bainitic transformation doesn't respect the additivity rule of purely diffusive transformations and is highly sensitive to the transformation sequences. The microstructures after thermal treatments have been systematically studied post mortem by Scanning Electron microscopy (SEM) coupled with Electron Back Scattered Diffraction (EBSD). It has served to explain the observed microstructures after continuous cooling which show large distributions of size, morphology and microtexture as they are formed progressively at different temperatures.
A phase transformation model based on the diffusionless-type approach of Van Bohemen (2019) was finally developed and calibrated on available experimental data. This model is not only able to simulate bainite kinetics along isothermal holding and continuous cooling but also the respective compositions of the phases. The capabilities and limits of the new approach are analyzed and discussed.

Keywords: Steels, Bainite, Austenite, Synchrotron, EBSD, Phase transformation.

Caractérisation et modélisation des transformations de la bainite sans carbure au cours de traitements thermiques isothermes et anisothermes

Les bainites sans carbure sont des microstructures multiphasées obtenues par décomposition de l'austénite à basse température (généralement entre 450 °C et 200 °C) dans les aciers alliés. Ces microstructures sont très intéressantes en raison de leurs propriétés mécaniques élevées et de leur bonne ténacité, notamment pour les pièces forgées destinées au marché automobile. Grâce à un choix judicieux de leur composition chimique, elles sont constituées d'une fine matrice ferritique sans carbure, d'austénite résiduelle stabilisée par enrichissement en carbone lors de la transformation et de martensite. L'austénite résiduelle peut se transformer en martensite lors de sollicitations mécaniques ultérieures à température ambiante (*strain induced transformation*). Une des grandes nouveautés de ce travail a été de comprendre les mécanismes de formation de ces microstructures en conditions de refroidissement continu. Ces microstructures ont été étudiées depuis de nombreuses années, mais leurs mécanismes de formation restent un sujet qui continue de diviser la communauté métallurgique, entre approches « diffusive » et « diffusionless ». Le phénomène de transformation incomplète rencontré dans ce processus est l'un des points de discorde.

Dans ce travail, nous avons étudié l'évolution des microstructures au cours de différents traitements thermiques (maintiens isothermes, traitements étagés et traitements de refroidissement continu) par Diffraction des Rayons X à Haute Energie (DRXHE) *in situ* sur ligne de lumière synchrotron. Ces expériences permettent la mesure simultanée de la cinétique de transformation de phase, des paramètres de maille des différentes phases et la détection d'éventuels processus de précipitation des carbures. Sur cette base, des bilans massiques de carbone très précis entre les phases constituant la microstructure ont été établis pour la première fois, ce qui a permis de conclure que la bainite ferritique est encore plus sursaturée en carbone que prévu. Les expériences par traitements étagés et de refroidissement continu ont également prouvé que la transformation bainitique ne respecte pas la règle d'additivité des transformations purement diffusives et est très sensible aux séquences de transformation. Les microstructures après traitements thermiques ont été systématiquement étudiées *post mortem* par microscopie électronique à balayage (MEB) couplée à la diffraction des électrons rétrodiffusés (EBSD). Cela a permis d'expliquer les microstructures observées après un refroidissement continu, qui présentent des distributions étendues de taille, de morphologie et de microtexture du fait de leur formation à différentes températures.
Un modèle de transformation de phase basé sur l'approche sans diffusion de Van Bohemen (2019) a finalement été développé et calibré sur les données expérimentales disponibles. Ce modèle est non seulement capable de simuler la cinétique de la transformation bainitique le long d'un maintien isotherme et de refroidissements continus, mais aussi les compositions respectives des phases. Les capacités et les limites de la nouvelle approche sont analysées et discutées.

Mots clés : Aciers, Bainite, Austénite, Synchrotron, EBSD, Transformation de phase.